2011-12-08

Extended Depth Optical Coherence Tomography for Anterior Segment and Accommodation Imaging in Real-Time.

Marco Ruggeri
University of Miami, mr.marcoruggeri@gmail.com

UNIVERSITY OF MIAMI

EXTENDED DEPTH OPTICAL COHERENCE TOMOGRAPHY FOR ANTERIOR SEGMENT AND ACCOMMODATION IMAGING IN REAL-TIME

By

Marco Ruggeri

A DISSERTATION

Submitted to the Faculty
of the University of Miami
in partial fulfillment of the requirements for
the degree of Doctor of Philosophy

Coral Gables, Florida

December 2011

UNIVERSITY OF MIAMI

A dissertation submitted in partial fulfillment of
the requirements for the degree of
Doctor of Philosophy

EXTENDED DEPTH OPTICAL COHERENCE TOMOGRAPHY FOR ANTERIOR SEGMENT AND ACCOMMODATION IMAGING IN REAL-TIME

Marco Ruggeri

Approved:

Fabrice Manns, Ph.D. Associate Professor of Biomedical Engineering and Ophthalmology	Terri A. Scandura, Ph.D. Dean of the Graduate School
Jean-Marie Parel, Ph.D. Henry and Flore Lesieur Chair in Ophthalmology, Research Associate Professor of Ophthalmology and Biomedical Engineering	Jorge Bohorquez, Ph.D. Assistant Professor of Professional Practice
Giovanni Gregori, Ph.D. Research Assistant Professor of Ophthalmology	Arthur Ho, B.Optom. (Hon.) M.Optom., Ph.D., FAAO Chief Technologist Brien Holden Vision Institute Professorial Visiting Fellow School of Optometry and Vision Science, University of New South Wales, Sydney, Australia
Sonia H. Yoo, M.D. Professor of Ophthalmology	Weizhao Zhao, Ph.D. Associate Professor of Biomedical Engineering

RUGGERI, MARCO (Ph.D., Biomedical Engineering)
(December 2011)

Extended Depth Optical Coherence Tomography for Anterior Segment and Accommodation Imaging in Real-Time.

Abstract of a dissertation at the University of Miami.

Dissertation supervised by Professor Fabrice Manns.
No. of pages of text. (190)

The changes in the human crystalline lens shape and its internal structure during accommodation and with aging are a fundamental component of the dynamic mechanism of accommodation and presbyopia, the loss of near vision with age. A better understanding of the crystalline lens changes during accommodation will help in developing new treatments to correct for presbyopia. The goal of this dissertation is to design and develop an imaging system to study the dynamic changes in lens shape during accommodative response. An imaging system based on spectral domain optical coherence tomography (SD-OCT) was developed with long axial range, high axial and lateral resolution and high speed for *in vivo* imaging the anterior segment along its entire length at video-rate. A slit-lamp mounted optical delivery scanning device for the extended depth SD-OCT system was developed. The delivery system was combined with a custom made unit that provides accommodation and disaccommodation step stimuli. A method to correct for the distortions of the OCT images was also developed that provides corrected two dimensional biometric data at different accommodative states.

I dedicate this dissertation to my family

ACKNOWLEDGEMENTS

I would like to express my sincere gratitude to my supervisors, Fabrice Manns, Ph.D. and Jean-Marie Parel, Ph.D., for giving me the opportunity to pursue a Ph.D. career at the Ophthalmic Biophysics Center of Bascom Palmer Eye Institute, a great professional and yet friendly environment. Dr. Manns and Dr. Parel supported me with patience, guidance and dedication throughout my graduate career. I would also like to thank Stephen Uhlhorn, Ph.D., for his important contribution to this project as well as his guidance. I am grateful to Carolina de Freitas, B.S., whose assistance and technical support has been essential to this project and Mariela Aguilar, M.S. for her constant help and endless patience. A special thank is extended to my dissertation committee members, Jorge E. Bohorquez, Ph.D., Giovanni Gregori Ph.D., Arthur Ho, M.Optom., Ph.D., F.A.A.O., Sonia Yoo, M.D., and Weizhao Zhao, Ph.D., for their willingness to participate and review this dissertation.

I would like to thank the former graduate students at the Ophthalmic Biophysics Center, David Borja, Ph.D., and Raksha Urs, Ph.D., and the current graduate students Victor Hernandez, M.S. and Bianca Maceo, M.S., for their contributions to this project. Special thanks are due to Izuru Nose, William G. Lee, Cor Rowaan and Alex Rodriguez at the Ophthalmic Biophysics Center for their technical support. I would like to thank the President and CEO of Bioptigen Inc., Eric Buckland, Ph.D. and his staff for the technical support provided to this project. I would like to acknowledge financial support from National Eye Institute grants (2R01EY14225, 2R43EY018021 and P30EY14801 Center Grant), Australian Government CRC Scheme (Vision CRC), Florida Lions Eye Bank, Research to Prevent Blindness and The Henri and Flore Lesieur Foundation (JMP).

TABLE OF CONTENTS

LIST OF FIGURES

LIST OF TABLES

PUBLICATION NOTE

The following are peer-reviewed articles, conference proceedings, presentations, and posters on the work described in this dissertation:

Peer-Reviewed Publications:

T.-H. Chou, O.P. Kocaoglu, D. Borja, **M. Ruggeri**, S.R. Uhlhorn, F. Manns, and V. Porciatti. Postnatal Elongation of Eye Size in DBA/2J Mice Compared with C57BL/6J Mice: In vivo Analysis with Whole-eye OCT. Invest. Ophthalmol. Vis. Sci., May 2011, 52:2604-3612

Patent application:

S. Uhlhorn, **M. Ruggeri**, F. Manns and J-M Parel. Intraoperative Imaging System and Apparatus for Anterior Segment Ocular surgery. Application pending

Conference Proceedings and Presentations:

M. Ruggeri, S. Jiao, J. Major Jr.,C. Cebulla, P. Rosenfeld, G. Gregori, G. Tsechpenakis, J. Wang, T. Murray, V. Porciatti. Ultra High-Resolution Optical Coherence Tomography for Ocular Imaging of Small Animals. 25th Southern Biomedical Engineering Conference, 2009: Miami, FL.

M. Ruggeri, P. Kocaoglu, S. Uhlhorn, D. Borja, R. Urs, T.-H. Chou, V. Porciatti, J.-M. Parel, and F. Manns. Small Animal Ocular Biometry Using Optical Coherence Tomography. Ophthalmic Technologies XX Session, Program 7550-42, Photonic West Conference, 2010: San Jose, CA. Spie conference.

M. Ruggeri, O. P. Kocaoglu, S. Uhlhorn, D. Borja, R. Urs, T.-H. Chou, V. Porciatti, J.-M. Parel, and F. Manns In Vivo Quantitative Analysis of Ocular Biometric Parameters in the C57BL/6J Mouse Invest. Ophthalmol. Vis. Sci. 2010 51: E-Abstract 6363.

M. Ruggeri, S. Uhlhorn, F. Manns, J.-M.Parel, V. Porciatti. Whole Eye Imaging of Small Animals with Spectral Domain Optical Coherence Tomography. EOS Topical Meeting: 5th European Meeting on Visual and Physiological Optics (EMVPO), Stockholm, Sweden, 2010

M. Ruggeri, S. Uhlhorn, F. Manns, J.-M. Parel. Extended-Depth Optical Coherence Tomography for Anterior Segment Imaging. Technologies XXI Session, program [7885-29], Photonic West Conference, 2011: San Jose, CA.Spie conference.

C. P. de Freitas, **M. Ruggeri**, B. Maceo, S. Uhlhorn, E. Arrieta, F. Manns, R. Augusteyn, A. Ho, and J.-M. Parel. Internal Crystalline Lens Structure Imaging using Long Range Optical Coherence Tomography. ARVO Meeting Abstracts April 22, 2011 52:818

M. Ruggeri, S. Uhlhorn, C. De Freitas, F. Manns, and J.-M. Parel. Real-Time Imaging of Accommodation using Extended Depth Spectral Domain OCT. ARVO Meeting Abstracts April 22, 2011 52:3402

Other related works published during the course of my doctoral studies:

Peer-Reviewed Publications:

M. Ruggeri, G.Tsechpenakis, S. Jiao, M. E.Jockovich, C. Cebulla, E. Hernandez , T. G. Murray , P. J. Rosenfeld and C. A. Puliafito. Retinal Tumor Imaging and Volume Quantification in Mouse Model using Optical Coherence Tomography. Optics Express, Vol. 17, Issue 5, pp. 4074-4083 (2009).

J. Wang, S. Jiao, C. A. Puliafito, **M. Ruggeri.** In Situ Visualization of Tears on Contact Lens using Ultra High Resolution Optical Coherence Tomography. Eye & Contact Lens: Science & Clinical Practice: Volume 35(2) (2009) pp 44-49.

J. Guy, X. Qi, R. D. Koilkonda, T. Arguello, T-H.Chou, **M.Ruggeri**, V.Porciatti, A. S. Lewin and W. W. Hauswirth. Efficiency and Safety of AAV Mediated Gene Delivery of the Human ND4 Complex I Subunit in the Mouse Visual System. Invest. Ophthalmol. Vis. Sci. Apr 22, 2009 50:4205-4214

C. M. Cebulla, **M. Ruggeri**, T. G. Murray, W. J. Feuer, E. Hernandez. Spectral Domain Optical Coherence Tomography in a Murine Retinal Detachment Model, Experimental Eye Research, Vol. 90, Issue 4521-527, , 2010.

C. C. Wykoff, A. M. Berrocal, A. C. Schefler, S. R. Uhlhorn, **M.Ruggeri,** D. Hess. Case Report: Intraoperative OCT of a Full-Thickness Macular Hole Before and After Internal Limiting Membrane Peeling. Ophthalmic Surgery, Lasers and Imaging, Vol. 41, No. 1 2010.

M. Ruggeri, J. C. Major Jr., C.McKeown, H.Wehbe, R.W. Knighton, S.Jiao and C.A. Puliafito . Retinal Structures of Bird of Prey Revealed by Ultra-High Resolution Spectral-Domain Optical Coherence Tomography. Invest. Ophthalmol. Vis. Sci. June 2010. 51:5789-5795

A. Camp, **M. Ruggeri**, G. C. Munguba, M. L. Tapia, S. W.M. John, S. K. Bhattacharya, R. K. Lee. Structural Correlation between the Nerve Fiber Layer and Retinal Ganglion Cell Loss in Mice with Targeted Disruption of the Brn3b gene. Invest. Ophthalmol. Vis. Sci., July 2011, 52:5226-5232

H. A. Aziz, MD; **M. Ruggeri;** A. M. Berrocal, Intraoperative OCT of Bilateral Macular Coloboma in a Child With Down Syndrome. J Pediatr Ophthalmol Strabismus, July/August 48:e37-e39

R. A. Oechsler, R. A. Santos, M. A. Shousha, A. Iovieno, J. Maestra**, M. Ruggeri**, M. E. Fini, V. L Perez, D. Miller, E. Alfonso, M. Bajenaru, Spectral Domain-Optical Coherence Tomography (SD-OCT) for the Diagnosis of Fusariumkeratitis in a rat contact lens model Invest. Ophthalmol. Vis. Sci., *In preparation*.

Conference Proceedings and Presentations:

M. Ruggeri, B. Sinicrope, C. Medina, J. Wang, S. Jiao and V.Perez. Anterior Segment Spectral Domain OCT for Imaging Cornea Transplant in Mice. Ophthalmic Technologies XIX Session, program [7163-01], Photonic West Conference, 2009: San Jose, CA.Spie conference.

S.Jiao, **M. Ruggeri**. Polarization and the Depth Resolution of Optical Fiber based Optical Coherence Tomography. Optical Coherence Tomography and Coherence Domain Optical Methods in Biomedicine XIII session, program [7168-43], Photonic West Conference, 2009: San Jose, CA.Spie conference.

M. Alegret, A. C. Schefler, Y. Pina, H. Boutrid, E. Hernandez, **M. Ruggeri**, S. Jiao, and T. G. Murray. Recent Advancements in 532 Green Laser Technology and Probe Enhancement: Clinical Assessment and Laboratory Evaluation. Invest. Ophthalmol. Vis. Sci. 2009 50: E-Abstract 2082.

C. M. Cebulla, **M. Ruggeri**, T. G. Murray, and E. Hernandez. Optical Coherence omography in a Murine Retinal Detachment Model. Invest. Ophthalmol. Vis. Sci. 2009 50: E-Abstract 3798.

A. S. Camp, **M. Ruggeri**, G. C. Munguba, S. K. Bhattacharya, and R. K. Lee In vivo Retinal Thickness Quantification in brn3b -/- Mice Using Optical Coherence Tomography Segmentation Invest. Ophthalmol. Vis. Sci. 2010 51: E-Abstract 2145.

W.-H. Lee, **M. Ruggeri**, R. W. Knighton, and S. Jiao Dispersion Compensation Improves Spectral Domain Optical Coherence Tomography (SDOCT) Depth Resolution in Silicone Oil-Filled Eye Invest. Ophthalmol. Vis. Sci. 2010 51: E-Abstract 292.

A. De La Zerda, J. Wang, V. Perez, **M. Ruggeri**, S. S. Gambir, R. Awdeh. Optical Coherence Molecular Imaging using Gold Nanorods in Living Mice Eyes. Imaging Instrumentation and Methodology. Program 0387A. World Molecular Imaging Congress, 2010, Kyoto, Japan.

M. C. Aguilar, **M. Ruggeri**, I. Nose, W. Lee, C. Rowaan, A. Bernal, C. De Freitas, S. Uhlhorn, Byron L. Lam, and J-M. A. Parel. Supine SD-OCT for Pediatric Patients. ARVO Meeting Abstracts April 22, 2011 52:4026

R. D. Koilkonda, T-H. Chou, **M. Ruggeri**, V. Porciatti, W. W. Hauswirth, V. Chiodo, S. L. Boye, and J. Guy. Early Functional and Long-term Rescue of the LHON Mouse With

Wild-type Human ND4 Gene Delivery. ARVO Meeting Abstracts April 22, 2011 52:1416

X. Yang, M. S. Hernandes, T.-H. Chou, **M. Ruggeri**, and V. Porciatti. A New Mouse Model Of Retinal Ganglion Cell (RGC) Dysfunction: Chronic Effects Of Superior Colliculus (SC) Lesion On Inner Retina. ARVO Meeting Abstracts April 22, 2011 52:4584

CHAPTER 1. AIMS OF THE STUDY

The changes in the human crystalline lens shape and its internal structure during accommodation and with aging are a fundamental component of the dynamic mechanism of accommodation and presbyopia, the loss of near vision with age. A better understanding of the crystalline lens changes during accommodation and with age will help in developing new treatments to correct for presbyopia. Studies of the dynamic changes in lens shape during accommodative response require an instrument that provides high-resolution quantitative *in vivo* images of the human crystalline lens at video-rate.

The primary goal of this project is to build a OCT system with long axial range for imaging the anterior segment along its entire length and perform biometry. The design will allow for real time display of the images at 20 frame/sec and high acquisition speed (up to 40,000 depth scans/sec), making the system suitable for observing the dynamic accommodation mechanism *in vivo* and in real-time. The system will feature high axial resolution and sensitivity. An optical delivery system will be designed to efficiently deliver the OCT beam into the crystalline lens. The optical head will be mounted on a slit-lamp so *in vivo* quantitative experiments of human accommodation can be performed.

The specific aims of the project are:

Aim 1: To design, build and bench-test a spectral domain (SD) OCT engine with extended depth for *in vivo* imaging of the whole anterior segment at video rate. The main purpose of this aim is to design and test an SD-OCT system with high speed and high axial range that enables cross-sectional imaging of the entire anterior segment.

The tasks of Aim 1 include:

Task 1.1: Design an OCT spectrometer with long axial range for entire crystalline lens imaging at high speed.

Task 1.2: Develop a setup and procedure for spectrometer calibration.

Task 1.3: Design and build an OCT interferometer.

Task 1.4: Test the performance of the system.

Task 1.5: Design an optical switching technique that extends the axial imaging range to the entire anterior segment.

Task 1.6: Interface the system to a commercial acquisition and processing software.

Aim 2: To develop a slit-lamp mounted optical delivery probe to study accommodation

An optical system to deliver the OCT beam will be developed for studying accommodation. The delivery system will be mounted on a slit-lamp and it will deliver the OCT beam into the eye while providing a visible accommodation stimulus to the subject.

The tasks of Aim 2 include:

Task 2.1: To design and evaluate a transverse scanning mechanism and focusing optics to efficiently deliver the OCT beam to the anterior segment of the eye.

Task 2.2: To design and develop a slit-lamp mounted delivery system that combines OCT and a visible accommodation stimulus.

Aim 3: Imaging of the lens and accommodation. Tests will be performed to show that the system can quantify changes of the crystalline lens shape *in vivo* and during

accommodation. The data obtained from this study will be compared to the existing data and will be used to validate the OCT system as a tool for dynamic studies of accommodation.

Task 3.1: To test the imaging capability of the system in imaging *in vivo* the crystalline lens and the anterior segment.

Task 3.2: To build and validate a method for correcting optical distortions of the OCT ocular images of the anterior segment due to refraction of the beam through the consecutive surfaces.

Task 3.3: To test the capability of the system in imaging and quantifying the dynamic changes occurring in the crystalline lens during accommodation.

CHAPTER 2. BACKGROUND AND SIGNIFICANCE

2.1. Anterior segment imaging: Introduction

The anterior segment of the eye is the front portion of the eye that encompasses all the structures between the cornea outermost surface and the front surface of the vitreous humor (Figure 2.1). In this introduction, it will be assumed that the expression "*anterior segment imaging*" refers to any ophthalmic imaging modality that is able to display a representative cross-sectional or three-dimensional (3D) image of the entire or just a specific part of the anterior segment, regardless of the method used to obtain the image. In clinical practice anterior segment imaging is an integral part of the standard ophthalmic examination and is used to improve diagnostic accuracy and to perform biometry of typical landmarks of the most common disorders.

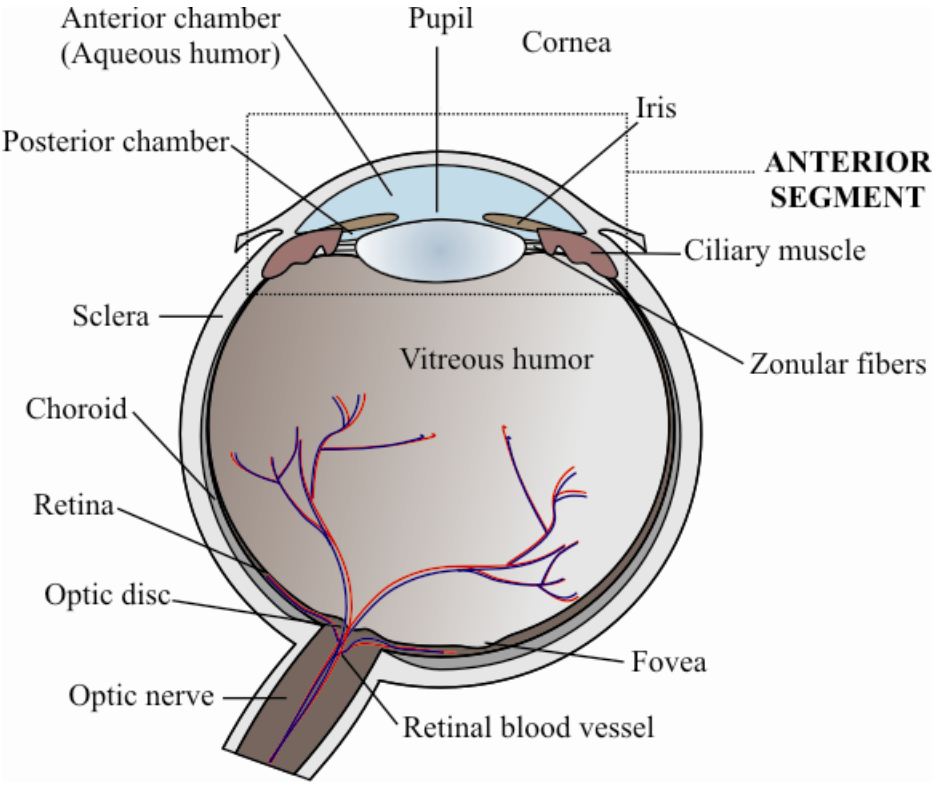

Figure 2.1: A schematic representation of the human eye. The anterior segment of the eye is marked.

Biometry of the cornea is key for the detection of pathological conditions such as for example keratoconus (Rao et al, 2002; Arntz et al, 2003; de Sanctis et al, 2008), which involves degenerative changes to the corneal structure. With the recent advances in refractive surgery, there has been an increasing need for tools for cornea imaging. In fact, quantifying shape and thickness of the cornea is necessary to assess the effects and stability of the refractive correction procedures (Hashemi et al, 2007), control of astigmatism after cornea transplantation and partial-thickness corneal transplantation (DSEAK) (Prasher et al, 2010; de Sanctis et al, 2007) as well as contact lens fitting. In the management of glaucoma, the anterior chamber angle is a key anatomical parameter involved in the progression of the degenerative disease. Anterior segment imaging has being used for iridocorneal angle evaluation (Nolan et al, 2006; Allouch et al, 2002). Routine ocular examinations of the angle width in glaucoma patients is crucial. Other clinical general applications of anterior segment imaging are screening of the anterior eye to locate and evaluate the extent of the effect of trauma (Ozdal et al, 2003), tumor (Bianciotto et al, 2011) and the presence of foreign bodies (Arora et al, 2010). An imaging modality that provides *in vivo* real time images of the crystalline lens would help to understand the processes of accommodation and to investigate the pathophysiology of conditions like presbyopia. Anterior segment imaging in surgery provides a different perspective of the surgical field, displaying areas that are otherwise hardly visible with a conventional operation microscope. In cataract surgery for example, the guidance of anterior segment surgery with OCT is currently investigated to help clinicians in creating openings in the anterior lens capsule (capsulotomy) and fragmenting and evacuating of the lens tissue with femto-second lasers (Palanker et al, 2010) (Figure 2.2A).

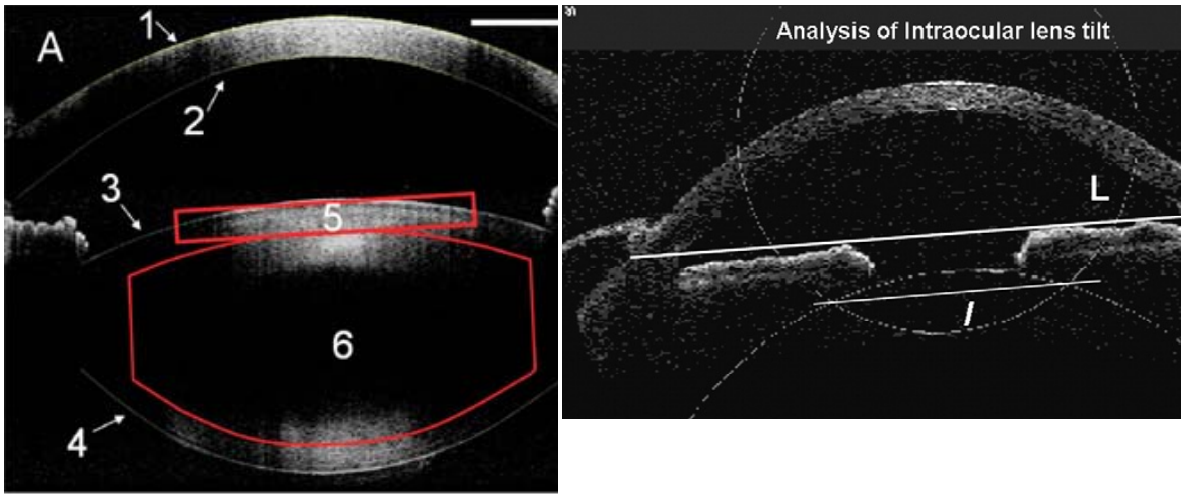

(A) **(B)**

Figure 2.2: (A) In the study presented by Palanker et al (2010), the system overlays the prospective capsulotomy and the lens segmentation patterns (red) onto the OCT data for the physician's review on a graphical user interface (GUI). **(B)** In the study presented by Kumar et al the intraocular lens (IOL) tilt was evaluated with OCT after surgery.

The position of IOLs after cataract surgery has also been evaluated with OCT (Kumar et al, 2011). In this application, OCT potentially helps to improve the refractive outcome of the treatment intra-operatively (Figure 2.2B).

Among the main research interests of the Ophthalmic Biophysics Center, at Bascom Palmer Eye Institute, are the study of the phenomena of accommodation and presbyopia, which at present are not completely understood. The ultimate goal of this study is the development of presbyopia correction using the lens-refilling technique, Phaco-Ersatz, developed by Parel et al (1986). Accommodation is the ability of the crystalline lens of the eye to change its optical power to maintain near objects in focus. The loss of near visual function that results from the progressive decline of this ability with age is referred to as presbyopia. The human eye accommodates by changing the lens shape. Therefore, quantitative information of the change in shape of the crystalline lens

during accommodation and with aging are the key factors to understand presbyopia. Quantifying the lens shape response requires an anterior segment imaging modality that provides high-resolution in vivo images of the entire anterior segment at video-rate. In the case of lens refilling for restoration of accommodation, a real time cross-sectional view of the anterior segment would also greatly help the clinician to complete the refilling.

2.2. Anterior segment imaging: Modalities

Slit-lamp biomicroscopy is the conventional tool used in clinical practice for observing the anterior segment of the eye. Slit lamp biomicroscopy uses a high intensity light source to illuminate a section of the anterior segment with a slit light beam that can be adjusted in width, intensity and direction. A binocular microscope that provides a magnified view of the eye to the operator is combined to the illumination device. The viewing path and the illumination path are positioned at an angle to each other and intersect in the area to be examined (Figure 2.3A). The angle must be sufficiently wide so that the specular reflections are not directed into the field of view of the microscope. The light backscattered by the ocular structures at the intersection point of the paths creates an optical section of the examined area (Figure 2.3B). Slit-lamp biomicroscopy provides images with limited resolution, contrast and depth of focus and it is primarily used for qualitative screening of the cornea, iris, and lens.

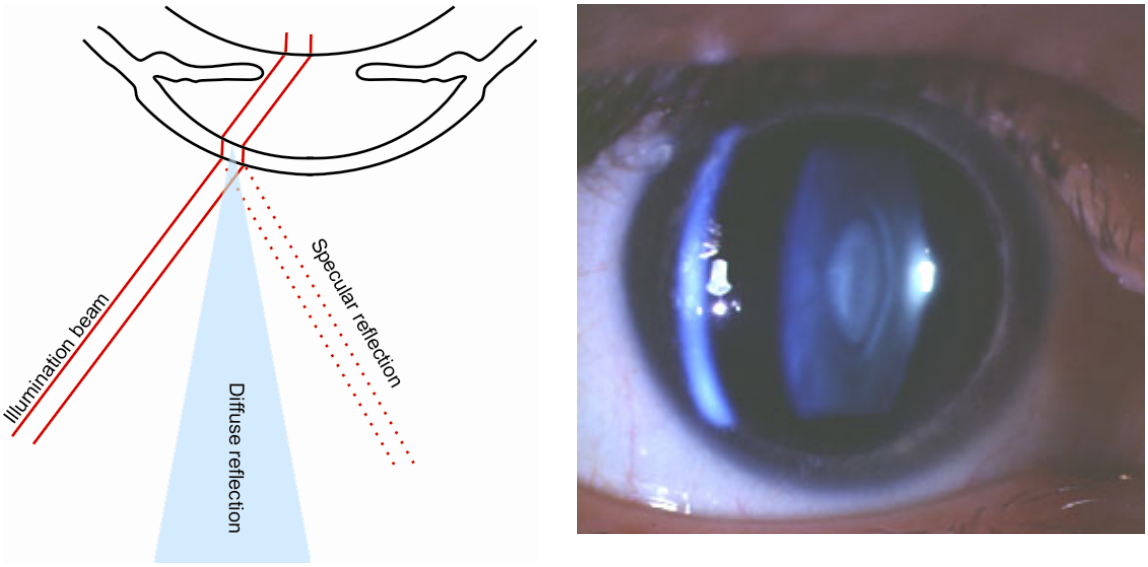

(A) **(B)**

Figure 2.3: (A) A schematic presentation of direct illumination in slit-lamp examination. **(B)** Photograph of the optical section of the human anterior segment obtained with slit-lamp examination. Image modified from opt.indiana.edu

Scheimpflug imaging (Hockwin et al, 1983; Muller-Breitenkamp et al, 1992; Koretz et al, 2004) is a special implementation of a slit-lamp biomicroscope with a modified configuration. A slit beam is also used to illuminate the anterior segment of the eye (Figure 2.4A). However, the camera plane is tilted according to the Scheimpflug principle, which allows for increased depth of focus. The essential principle can be explained considering three planes: the image plane upon which the camera sensor is positioned, the imaging lens plane passing through the center of the imaging lens and perpendicular to the optical axis and the object plane positioned such that an object lying on it will be imaged sharply on the image plane. The Scheimpflug principle states that a sharp image of the object is obtained when the image plane, lens plane and object plane intersect in one common line.

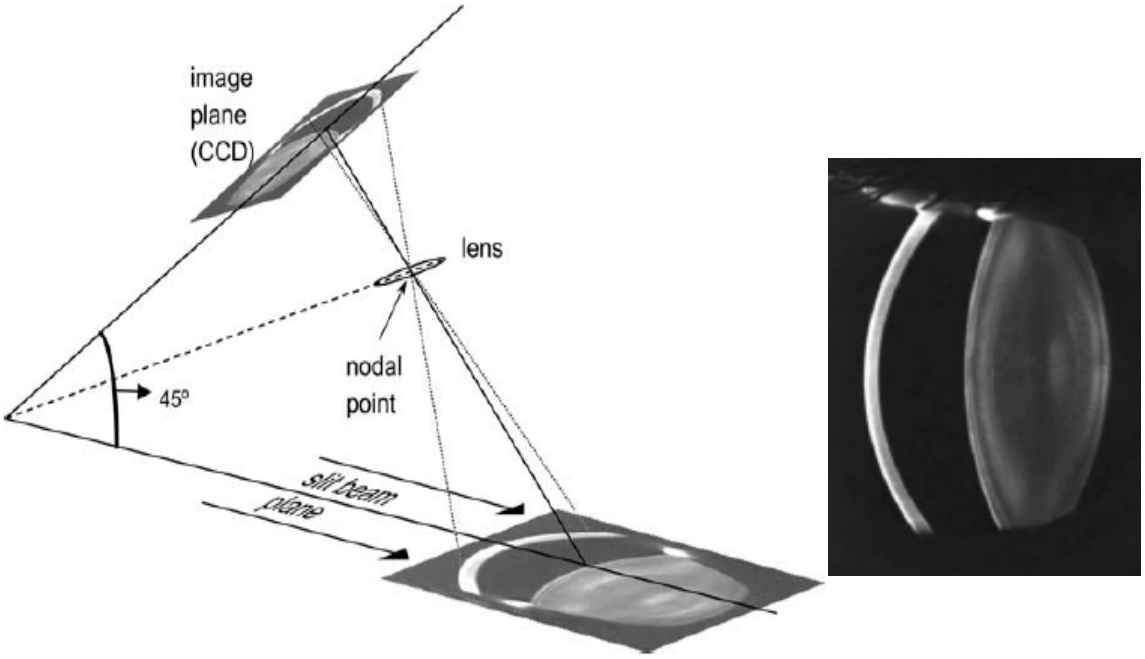

(A) **(B)**

Figure 2.4: (A) A schematic presentation of the Scheimpflug imaging principle (Dubbelman et al, 2005). **(B)** Scheimpflug image of the human anterior segment (Dubbelman et al, 2005).

A typical image of the anterior segment acquired with a Scheimpflug system is shown in Figure 2.4B. 3D scans are obtained by mechanically revolving the camera around the optical axis of the eye. Scheimpflug imaging suffers of strong optical distortions resulting from tilt of the image, lens and object planes and from the refraction through the ocular surfaces. In slit-lamp biomicroscopy the direction of the illumination path and viewing path is adjustable. In a Scheimpflug system, on the other hand, the optical layout is known and fixed. Hence, the imaging distortions of the Scheimpflug images can be corrected and accurate biometry of the anterior segment can be obtained. Scheimpflug photography is suitable for biometry of the anterior segment with high axial resolution (~15 µm) and high speed up to 50 slit images in 2s. However, the requirements

for a correct alignment are strict due to the spatial constraints involved in imaging the anterior segment, making the method difficult for imaging at video-rate. Another limitation of Scheimpflug imaging is that during pupil constriction the visibility of the posterior part of the lens is limited. This modality is mainly used for non contact assessment of cataract, corneal haze (Sparrow et al, 1986) and biometry of the crystalline lens and/or cornea (Dubbelman et al, 2003; Rosales et al, 2006). Commercial devices have been recently developed to capture multiple images with high speed and create three-dimensional images of the anterior segment (Buehl et al, 2006).

Ultrasound biomicroscopy (UBM) (Pavlin et al, 1995; Liebmann et al, 1996; Silverman, 2009; Nolan et al, 2008) works on the principle of an ultrasound but employs ultrasound transducers at high frequency (30-50 MHz) to produce images of ocular structures with finer resolution than lower frequency transducers. The transducer is incorporated in a mechanical scanner to allow cross-sectional images or 3D images to be constructed (Figure 2.5A). A limitation of Slit-lamp and Scheimpflug imaging for anterior segment examination is that light is blocked by the iris, preventing imaging behind it. Ultrasound allows images to be recorded even if the structures are not transparent to light. Commercial devices provide high penetration up to 5 mm in tissue. However, the axial and lateral resolutions of approximately 25 μm and 50 μm respectively, are lower than the ones obtained with optical methods. For current commercial anterior segment scanners the imaging speed is limited to 13 frames/s, slower than optical imaging techniques. A drawback of UBM is that it requires contact with the patient's eye through the use of topical gel or fluid bath. The imaging procedure is less comfortable to the patient and requires a local anesthetic.

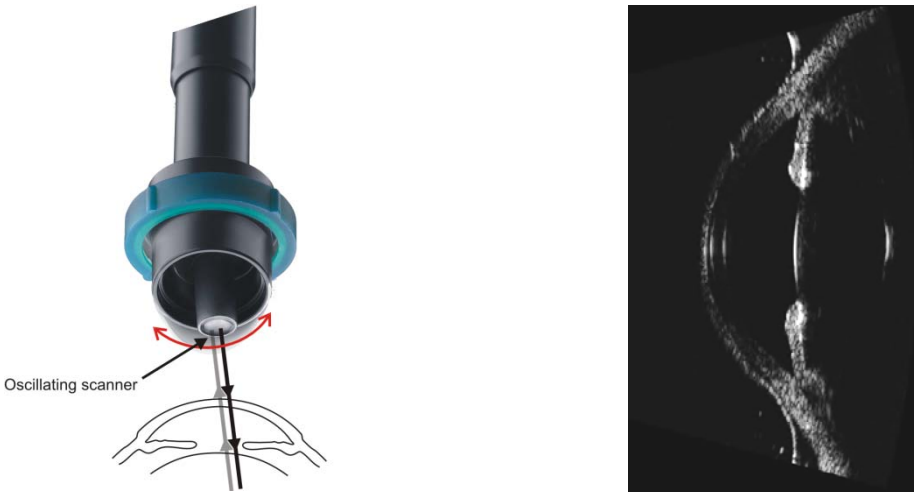

(A) **(B)**

Figure 2.5: (A) A schematic presentation of the UBM scanning principle. **(B)** UBM image of the human anterior segment. Image were modified from www.ellex.com.

UBM has been used in many clinical and research applications such as, iridocorneal angle estimation, abnormalities of ciliary body and iris detection, ocular trauma and tumor visualization and management, IOL positioning. Figure 2.5B shows a typical section of the human anterior segment acquired with a commercial UBM system.

Optical coherence tomography (OCT) (Huang et al, 1991; Fercher et al, 1996; Häusler et al, 1998) is a non-contact optical cross-sectional imaging technique with micrometer resolution. OCT is analogous to ultrasound, measuring the echo delay and intensity of backscattered light from the internal tissue microstructure. Because the echo time delays propagate at the speed of light and thus are too fast to be electronically detected, an optical correlation technique, known as low-coherence interferometry, is used. OCT uses low coherence light in the near infrared spectral region.

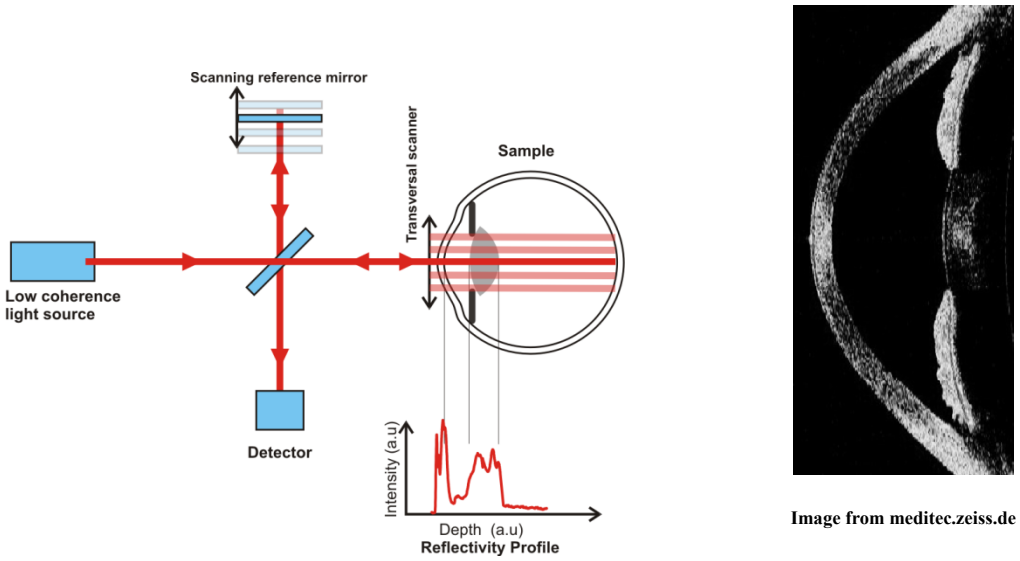

Figure 2.6: (A) A schematic presentation of the basic OCT implementation. **(B)** OCT image of the human anterior segment.

In the basic implementation, light from a sample beam is back scattered by the ocular structures and combined with a beam reflected by a scanning reference mirror causing interference. The coherent interference, which contains the information about the reflectivity and the position of the structures within the sample, is detected by an interferometer and a reflectivity profile of the sample is generated (Figure 2.6A). By transversally scanning the sample beam, reflectivity profiles are recorded at different lateral positions so that two and three -dimensional sectional images of the sample are constructed. Figure 2.6B shows an OCT image of the anterior segment recorded with a commercial instrument. As with Scheimpflug imaging, in OCT the light is blocked by the iris and therefore structures behind it cannot be optically accessed. Compared to the other techniques, OCT is promising for dynamic studies and to perform biometry because of its high recording speed and high resolution.

Modality	Manufacturer/Instrument	Axial Resolution (μm)	Frame rate (fps)	Scanning rate (Depth scans/s)	Axial Range (mm)
Scheimpflug	OCULUS/Penatacam HR	>15 *	50	>50,000 *	4.5
	ZIEMER/Galilei	>14*	~30	30,000*	N/A
UBM	PARADIGM/P60	27	8	2048	N/A
	ELLEX/Eyecube	23	13	3328*	12.5
OCT	BIOPTIGEN/3D SD-OCT	3-5	16 to 66**	17,000	~2
	OPTOVUE/iVue	5	25 to 100**	26,000	2-2.3

Table 2.1: Summary of the specifications of commercial imaging systems for anterior segment imaging. (* Estimated values, ** Values were calculated for 256 to 1024 depth scans per frame).

However, the main challenge in using OCT for imaging the crystalline lens and the anterior segment, which are about ~5 mm and ~9 mm in thickness, respectively, is that the commercial high speed OCT implementations have limited axial range. Current commercial systems for anterior segment imaging offer high speed up to 40,000 depth scans/s and high axial resolution of 3~5 μm but their axial range is limited to about 2 mm. Table 2.1 summarizes the specifications for some of the current commercial devices used for anterior segment imaging.

2.3. Anterior segment imaging: Challenges

Among the current challenges in anterior segment imaging is the design and development of new or improved imaging modalities capable of real-time imaging and biometry to study the dynamic process of accommodation and imaging for guiding ocular treatments to the anterior segment. Such an imaging system requires high speed, high resolution and long imaging depth. The human crystalline lens is, on average, approximately 5mm in thickness while the anterior segment depth is about 9mm. Imaging of accommodation requires a system with sufficient axial range to image the entire anterior segment. Accommodation is a dynamic process that occurs with relatively high

speed (0.2 to 0.6 sec, Kasthurirangan et al, 2003). Hence, recording the dynamic changes in lens shape during accommodative response requires an instrument that also provides high acquisition rates. While imaging accommodation, it is also necessary to provide a real-time feedback to the operator so correct alignment of the eye is maintained during image acquisition. In image assisted surgery, real-time feedback is also key to guide the physician during the intervention. Real time displaying (>10fps) is fundamental for these applications. To detect changes in the internal structure of the lens during accommodation high axial resolution (<10μm) is also preferable.

Although UBM has long axial imaging range and sufficient imaging speed, and allows imaging through the iris, it is less desirable than optical modalities because it requires contacting the cornea and it shows low axial resolution. Scheimpflug imaging, on the other hand, is a non contact technique that provides the required imaging range and speed. However, it is difficult to maintain a correct alignment with the subjects eye over time making real-time imaging complicated. In addition, Scheimpflug imaging is significantly affected by optical distortion and its integration in a surgical setting would be complex. While OCT appears to be the most promising technology in this context, the limitation of the current commercial systems that prevents imaging of accommodation and image guided surgery is the limited axial range. Increasing the OCT axial range would benefit these applications.

2.4. Scope of the thesis

The goal of this project is to build an OCT system for accommodation studies in human subjects. The system will feature high imaging speed (>10 fps), high axial resolution (between 5 μm and 10 μm) and superior imaging depth (> 12mm) for anterior

segment visualization along its whole depth. For this purpose a spectrometer based system (SD-OCT) will be built. An optical system that delivers the OCT light and provides accommodation stimuli to the eye of the subject will be designed and mounted on a slit-lamp. Finally, a method to extract biometric information from the anterior segment images will be developed and tested.

CHAPTER 3. OPTICAL COHERENCE TOMOGRAPHY (OCT)

3.1. Brief history and overview of OCT

OCT technology has been first published in 1991 by Huang et al. The first commercial instrument for retinal imaging has been introduced by Carl Zeiss Meditech in 1996 (Duker et al, 2005). Today OCT is widely used in clinical practice and research to image the retina. Anterior segment (AS) OCT has first been published in 1994 (Izatt et al, 1994). The first commercial AS-OCT system become available in 2005 (Dartt et al 2011). AS-OCT has been used in a number of applications, such as, examination and measurement of the thickness of the cornea and its layers (Fukuda et al, 2009; Muscat et al, 2002) and the crystalline lens (Lehman et al, 2009), evaluation of corneal anatomy in refractive surgery (Li et al, 2007; Avila et al, 2006; Maldonado et al, 2000), evaluation of post-transplant corneal grafts (Genevois et al, 2007), imaging and measurement of intraocular lens parameters (Goldsmith et al, 2005; Tang et al, 2009) and measurement of anterior chamber depth (Goldsmith et al, 2005) and irido-corneal angle (Pekmezci et al, 2009; Radhakrishnan et al, 2005).

A brief overview of the OCT operation has been given in section 2.2. Two detection schemes are used in OCT instrumentation: Time Domain and Fourier Domain. The original method is time-domain OCT (TD-OCT), where a profile of the in-depth distribution of scatterers (A-scan) is extracted by varying the optical path length difference between the interferometer reference and sample arms in time. To achieve optical path variations between the two arms a number of scanning schemes with moving parts, namely optical delay lines, have been used in the reference arm. The main limitation of TD-OCT systems is that the imaging speed (~2 kHz A-line rate) is limited

by the slow movements of the delay line, which precludes its use for applications where high speed is needed, such as real-time displaying and recording volumes. In the last decade, frequency domain implementations of OCT have progressively replaced TD-OCT as they exhibit much higher speed and improved sensitivity compared to time domain implementations (Leitgeb et al., 2003; de Boer et al, 2003). Spectral domain OCT (SD-OCT) (Fercher et al, 1995; Häusler et al, 1998) and Swept Source OCT (SS-OCT) (Chinn et al, 1997; Haberland et al, 1997) are the two spectral discrimination solutions proposed for frequency domain OCT imaging.

3.2. Basic theory of Optical Coherence Tomography

3.2.1. Interferometry with a monochromatic light source

One of the most common embodiment used in interferometry is the Michelson interferometer (Figure 3.1). This interferometer consists of a light source, a beam splitter, a reference mirror, a sample and a single point photodetector. Monochromatic, or highly coherent, light consists of a finite bandwidth of wavelengths that are confined to an extremely narrow range. To simplify the understanding of the underlying physics, monochromatic light will be considered as ideally composed by a single wavelength, the interferometer will be in free space, the sample will be a perfectly reflecting mirror and the polarization of light will be ignored. For the sake of convenience and without loss of generality, geometrical lengths are considered in the theoretical analysis (i.e., the interferometer and sample are assumed to be located in air). However, the same results apply if geometrical lengths are replaced with optical lengths.

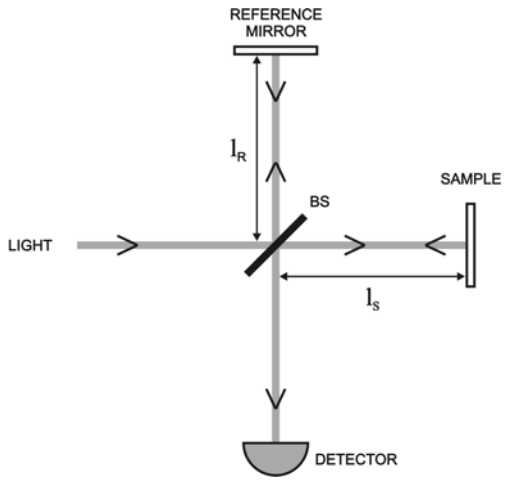

Figure 3.1: Setup of a Michelson interferometer.

Ideal monochromatic light emitted by the source is divided by the beam splitter into the reference and the sample arms. The light back reflected by the sample and by the mirror is recombined at the beam splitter and propagates toward the detector. The mirrors in the reference and the sample arms are positioned at distance l_R and l_S from the beam splitter, respectively. U_S and U_R represent the complex amplitudes of the monochromatic fields returning from the sample and the reference arms that are recombined at the beam splitter. The total instantaneous field at the detector can be written as the sum of the two complex fields U_S and U_R

$$U_D = U_S + U_R \tag{3.1}$$

The complex amplitudes of the monochromatic instantaneous fields can be expressed in the following form

$$U_S = A_{0S}\, e^{-i2kl_S},\ U_R = A_{0R}\, e^{-i2kl_R} \tag{3.2}$$

where $k = 2\pi/\lambda$ is the propagation constant, λ is the wavelength and A_{0S} and A_{0R} are the amplitudes of the monochromatic fields returning from the sample and the reference arms. The factor of two in the phase constant is generated by the double pass of

the light into the two arms. The intensity of the light collected by the detector during its integration time is proportional to the square modulus of the instantaneous field and can be written as

$$I \propto \langle |U_D|^2 \rangle = \langle [U_S + U_R][U_S + U_R]^* \rangle \quad 3.3$$

which is equivalent to

$$I \propto I_S + I_R + \langle U_S \cdot U_R{}^* \rangle + \langle U_S{}^* \cdot U_R \rangle = \quad 3.4$$

$$= I_S + I_R + 2Re[U_S \cdot U_R{}^*]$$

where I_S and I_R are DC terms that represent the constant intensities returned from the sample and the reference arms, respectively. The last term of equation 3.4 can be expressed using the field forms in equation 3.2, which yields

$$I \propto I_S + I_R + 2A_{0S}A_{0R}\cos[2\mathrm{k}(l_S - l_R)\,] = I_S + I_R + 2\sqrt{I_S I_R}\cos[2\mathrm{k}(l_S - l_R)\,] \quad 3.5$$

By defining $\Delta l = l_S - l_R$ as the mismatch between the path lengths of the reference and the sample arms and regrouping the DC components into the term $I_{DC} = I_S + I_R$, equation 3.5 reduces to

$$I \propto I_{DC} + 2\sqrt{I_S I_R}\cos\left(\frac{2\pi}{\lambda}\,2\Delta l\right) = I_{DC}\left(1 + 2\frac{\sqrt{I_S I_R}}{I_{DC}}\cos\left(2\pi\frac{\Delta l}{\lambda/2}\right)\right) \quad 3.6$$

The oscillatory term in equation 3.6. is known as cross-correlation term (Häusler et al, 1998) and contains the interference information. Maxima of intensity are found when the path length mismatches are equal to $\Delta l = m\frac{\lambda}{2}\,, m = 0, 1, 2, \ldots$and minima when $\Delta l = \left(m + \frac{1}{2}\right)\frac{\lambda}{2}\,, m = 0, 1, 2, \ldots$ The intensity of the interference oscillates with a period that is half of the wavelength relative to the path length difference Δl between the two arms. Figure 3.2 shows the normalized cross-correlation term seen with the superimposition of two monochromatic fields, when $I_S = I_R = I_{DC}/2$.

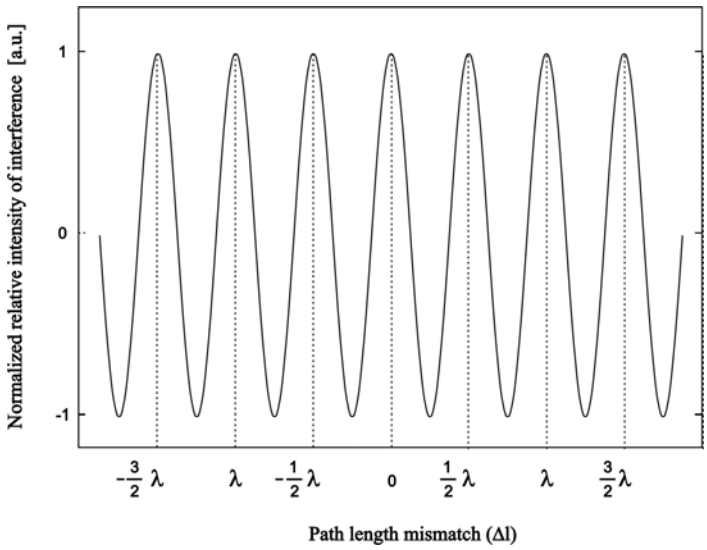

Figure 3.2: Cross-correlation term of the interference signal as a function of wavelength shown for $I_S = I_R = I_{DC}/2$

In the Michelson interferometer with a monochromatic light source, interference is obtained by moving the mirror in the reference arm along its optical axis. As the mirror translates, the path length difference between the arms varies and consequently the interference oscillations changes according to equation 3.6. The frequency of the oscillations is directly related to the translation speed. With ideal monochromatic light the interference fringes are observed for a infinite range of path length differences.

3.2.2. Low Coherence Interferometry (LCI)

Low coherence interferometry uses broadband light sources. A light source with broad bandwidth consists of a finite bandwidth of wavelengths, and can be described by its coherence length

$$l_c = \frac{\lambda_0^2}{\Delta\lambda} \qquad 3.7$$

where λ_0 is the central wavelength and $\Delta\lambda$ the spectral bandwidth of the light source. In LCI, interference occurs only when the distances that the light travels in the sample and reference arms match within a coherence length of the light source l_c.

The coherence length can be also written in terms of the propagation constant $k = 2\pi/\lambda$ as

$$l_c = \frac{2\pi}{\Delta k} \tag{3.8}$$

Light sources used in low-coherence interferometry usually have a Gaussian spectral distribution and their spectral intensity can be written as

$$i(k) = i_0 e^{-\frac{4ln2(k-k_0)^2}{\Delta k^2}} \tag{3.9}$$

where Δk is the Full-Width at Half-Maximum (FWHM) of the spectral distribution, k_0 is the center of the Gaussian spectrum and i_0 is the intensity at k_0 (Figure 3.3).

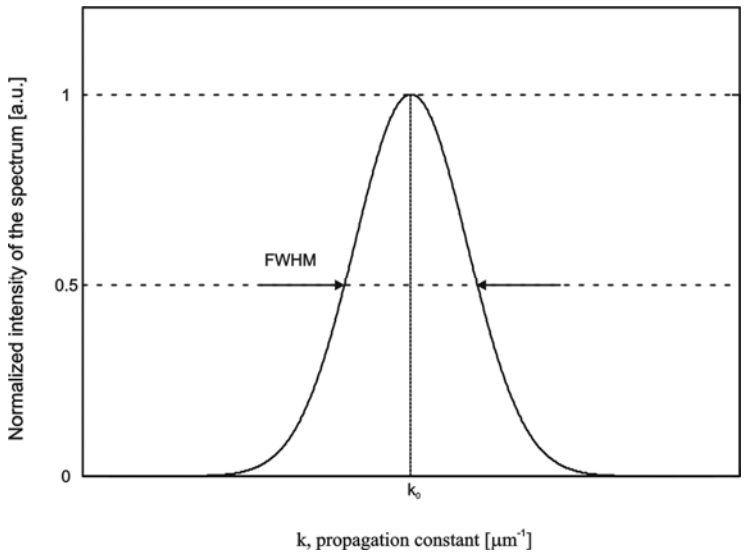

Figure 3.3: Typical Gaussian shaped low-coherence light spectrum.

By combining equation 3.8 and equation 3.9 the spectral intensity of the light source can be written in term of its coherence length as

$$i(k) = i_0 e^{-\frac{ln2}{\pi^2} l_c{}^2 (k-k_0)^2} \tag{3.10}$$

In a low-coherence interferometer the total instantaneous field at the detector is the sum of two complex fields $u_S(k)$ and $u_R(k)$ that are frequency dependent. The interference signal at the detector is the sum of the contributions from all frequencies. According to equation 3.5 the intensities of the interference signals of each spectral component can be written as

$$i(k, \Delta l) = i_S(k) + i_R(k) + 2\sqrt{i_S(k) i_R(k)} \cos(2\mathrm{k}\Delta l) \tag{3.11}$$

The resulting interference signal can be then calculated by integrating the interferences for all spectral components

$$I(\Delta l) = \int_{-\infty}^{\infty} i(k, \Delta l)\, dk \tag{3.12}$$

With the assumption that the incident beam is divided equally between the reference and the sample arm $i_S(k) = i_R(k) = i_0(k)$, equation 3.12 can be written as

$$I(\Delta l) = \int_{-\infty}^{\infty} 2 i_0(k) \big(1 + \cos(2\mathrm{k}\Delta l)\big)\, dk \tag{3.13}$$

Assuming a Gaussian spectral distribution, the interference signal can be calculated according to equation 3.9 and written as

$$I(\Delta l) = \int_{-\infty}^{\infty} 2 i_0 e^{-\frac{ln2}{\pi^2} l_c{}^2 (k-k_0)^2} \big(1 + \cos(2\mathrm{k}\Delta l)\big)\, dk \tag{3.14}$$

The integral in equation 3.14 is the sum of a DC component and a term containing the interference information

$$I(\Delta l) = 2i_0 \int_{-\infty}^{\infty} e^{-\frac{ln2}{\pi^2} l_c{}^2 (k-k_0)^2}\, dk + 2i_0 \int_{-\infty}^{\infty} e^{-\frac{ln2}{\pi^2} l_c{}^2 (k-k_0)^2} \cos(2k\Delta l)\, dk \qquad 3.15$$

The first term is the well known Poisson integral while the second term is the real part of the Fourier transform of the Gaussian function that represents the spectral distribution of the light source. By calculating the two integrals with known mathematical relations (Abramowitz et al, 1972), the interference signal can be written as

$$I(\Delta l) = 2i_0 \frac{\sqrt{\pi}}{\alpha} \left(1 + \cos(2k_0 \Delta l) e^{-\frac{(2\Delta l)^2}{4\alpha^2}} \right) \qquad 3.16$$

where $\alpha = \frac{\sqrt{ln2}}{\pi} l_C$. The interference signal contains a DC component and a modulation term $C(\Delta l)$ that is named "coherence function". The envelope of the coherence function is Gaussian and can be expressed in function of the coherence length of the light source as

$$\nu(\Delta l) = e^{-\frac{(2\Delta l)^2}{4\alpha^2}} = e^{-\frac{\pi^2}{4ln2\, l_c{}^2}(2\Delta l)^2} \qquad 3.17$$

Figure 3.4 shows a typical interference signal and its envelope for a Gaussian shaped spectrum optical source with low-coherence length ($l_c = 14\mu m$). The Gaussian envelope of the interference signal is reported with its FWHM. This analysis shows that if low-coherence light is used, interference is only observed when the path lengths of the reference and sample arms are matched within a distance approximately equal the coherence length. According to equation 3.16 the period of the interference signal is equal to the central wavelength $\lambda_0 = 2\pi/k_0$ of the optical source.

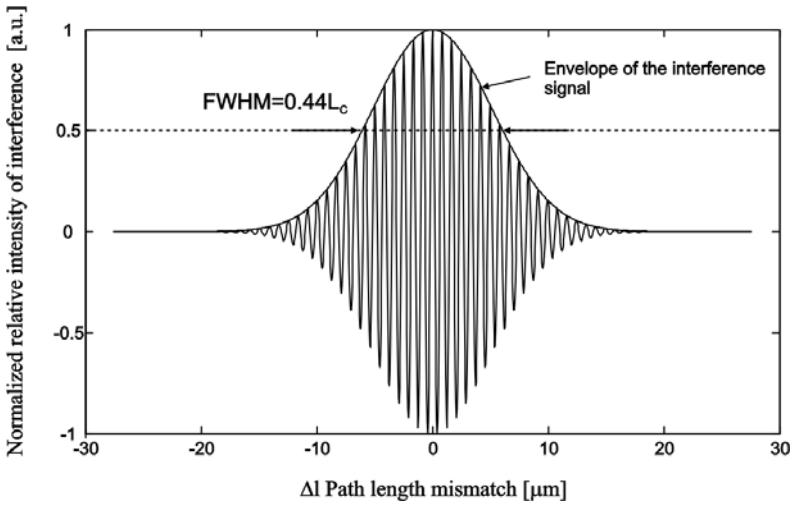

Figure 3.4: The interference signal and its envelope with a low-coherence interferometer (λ_0=830nm, $\Delta\lambda$=50nm).

Compared to interferometry with monochromatic light, low-coherence interferometry show an interference gating property that is used in many practical applications for measurements of absolute distances and dimensions of structures of a material or a tissue. The position of the reflector in the sample arm corresponds to the center of the envelope of the interference signal. This position is named "zero delay position" ($\Delta l = 0$). Normally, in ranging applications the reference mirror is scanned along its optical axis to match the position of multiple structures along the sample axis and the magnitude and relative distances of the envelope peaks are registered at the detector (Figure 3.5).

3.2.3. LCI for multiple reflectivity boundaries

To derive equation 3.16 the sample was treated as a single reflecting mirror. However, this is an unrealistic situation and in normal applications the light is partially reflected from layers with different reflectance located at different positions within a

sample. If we assume a sample with $j = N$ layers and neglect the interference between different boundaries of the sample, the interference signal can be written as

$$i(k, l_R) = i_R(k) + \sum_j i_S(k,j) + \sum_j 2\sqrt{i_R(k) i_S(k,j)}\cos\left(2\mathrm{k}\Delta l_\mathrm{j}\right) \qquad 3.18$$

where l_R is the position of the reference mirror, l_j is the position of the j^{th} layer, $\Delta l_\mathrm{j} = l_R - l_j$ is the path difference between the j^{th} layer and the reference reflector and $i_S(k,j)$ is the spectral intensity returning from the j^{th} boundary. The interference signal $I(l_R)$ is the integral of the components $i(k, l_R)$ over the entire spectrum. Let R_j be the fraction of power reflected from the layer located at position l_j within the object. The normalized sample reflectivity vs. depth or reflectivity profile of the sample can be written as

$$R(l_R) = \sum_{j=1}^{N} \delta\left(l_R - l_\mathrm{j}\right) R_j \qquad 3.19$$

where δ is the Dirac function. Assuming again that the incident beam is divided equally between the reference and the sample arm $i_S(k) = i_R(k) = i_0(k)$, the intensity given in equation 3.18 can be written as (Kulkarni et al 1997, Pan et al 1995, Schmitt et al,1999)

$$I(l_R) = 2i_0 \frac{\sqrt{\pi}}{\alpha}\left(1 + \sqrt{R(l_R)} \otimes \mathrm{C}(l_R)\right) \qquad 3.20$$

where $\mathrm{C}(l_R)$ is the coherence function that defines the interferometer response to path resolved reflectance variations and $\otimes$ denotes the convolution operation (Figure 3.4). Figure 3.5 depicts an example of normalized reflectivity profile of a sample with three reflecting layers.

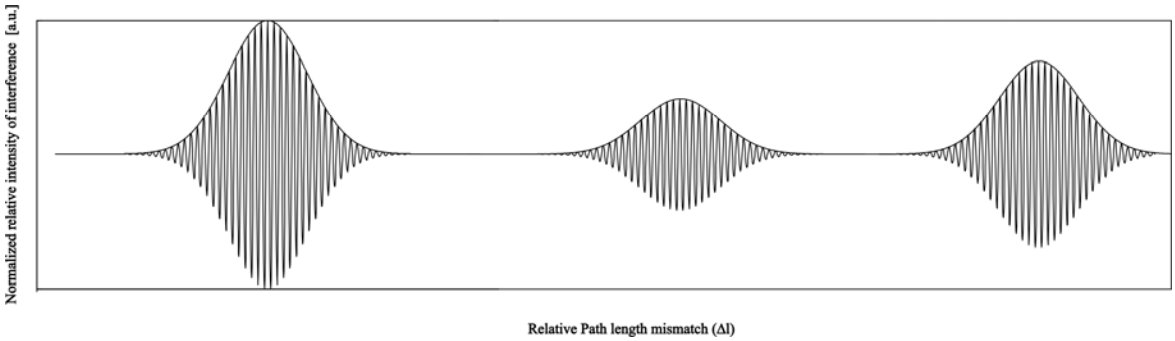

Figure 3.5: Example of the interference signal and its envelope generated in a low-coherence interferometer through the scan of a sample with three surfaces at different depth and with different reflectance.

3.2.4. Axial resolution of LCI

The axial resolution expresses the degree of separation between peaks associated to neighboring reflecting sites that is sufficient to produce two distinct peaks rather than one large peak. The greater the space between the peaks, the easier it is to resolve them (Figure 3.6A). One of the most common definitions of spatial resolution for Gaussian distributions is the Rayleigh criterion (Figure 3.6B). According to the Rayleigh definition, the distributions are considered resolved if their centers are separated by more than one FWHM. Figure 3.6C shows the sum of the Gaussian lineshapes if their separation is shorter than a FWHM. The lineshapes cannot be separated. The FWHM of the interference signal in a free space interferometer using a light source with Gaussian spectral distribution can be calculated by setting its envelope (equation 3.17) equal to 1/2

$$\Delta l_{\mathrm{FWHM}} = \frac{2ln2}{\pi} l_c = 0.44 l_c \simeq 0.44 \frac{\lambda_0^2}{\Delta\lambda} \qquad 3.21$$

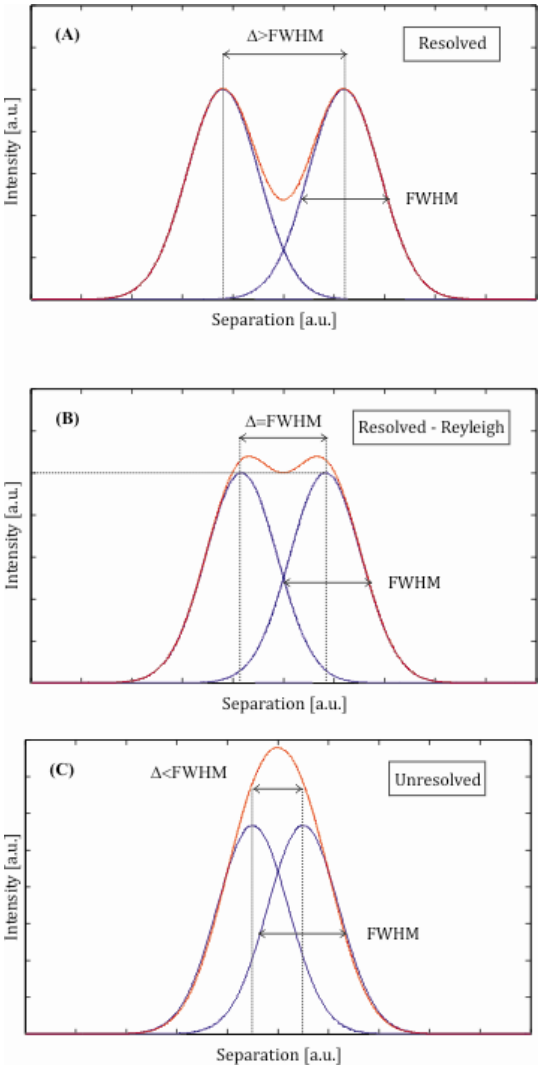

Figure 3.6: Large separation between the Gaussian lineshapes (blue lines). The peaks are resolved (red line) **(A)**. Rayleigh condition. The separation between the Gaussian lineshapes (blue lines) is equal to their FWHM. The peak are resolved (red line) **(B)**. The separation between the Gaussian lineshapes (blue lines) is smaller than their FWHM. The peaks are not resolved (red line) **(C)**.

For an optical source with Gaussian shape spectral distribution, equation 3.21 represents the spatial or axial resolution of a low-coherence interferometer in term of the coherence length, or equivalently, of the spectral characteristics of the light source. To achieve high spatial resolution, optical sources with wide spectral bandwidth are desired. For non-Gaussian shaped spectrum optical sources, the coherence length and therefore

the spatial resolution can be estimated by the FWHM of the Fourier transform of the spectral intensity distribution. Compared to a Gaussian spectrum, non-Gaussian spectra normally produce side lobes of the interference envelope, reducing the axial resolution and contrast. According to this definition of axial resolution, in a multi-layer sample, if the distance between consecutive layers is larger than 0.44 times the coherence length of the light source, all the layers can be resolved and distinguished as individual peaks in the reflectivity profile.

Low-coherence interferometry allows for detecting the reflectivity profile of a sample along one axis. The limitation of LCI lies in the fact that is only a one-dimensional ranging technique similar to A-mode ultrasound. OCT is based on LCI and produces two-dimensional images by transversally scanning the beam into the sample arm (similarly to B-mode ultrasound). Reflectivity profiles are recorded at different lateral positions so that two and three -dimensional sectional images of the sample can be constructed.

3.3. Time Domain OCT

In the basic implementation of Time Domain OCT (TD-OCT), the interference signal is recorded with a single point detector while the length of the reference arm is modulated with a delay line. The delay line matches the delay of the light back reflected from the various layers in the sample (Figure 3.7) with the light back reflected by the reference arm. The interference signal is then electronically and numerically processed to produce a reflectivity profile of the sample (a-scan, a-line or depth scan). A plane mirror mounted on a translation stage is the simplest form of delay line. Numerous more complex delay line schemes characterized by different axial ranges and speed have been

reported at the earliest stage of the Time Domain implementations as reviewed by Rollins et al (2002). The limiting factor for the axial range is the maximum extension that the optical path of the delay line can reach. A transversal scanner in the sample arm, which is typically comprised of mirrors mounted on galvanometer actuators, scans a focused beam across the sample to allow acquisition of signals from different transverse locations. At each lateral position, the transversal scanner is maintained stationary while an axial scan is acquired. To generate a two-dimensional image the multiple depth scans acquired at different lateral locations are placed side by side and displayed with an intensity scale map. The typical speed of TD-OCT systems is about 2,000 Alines/sec. TD-OCT sensitivity varies between 75-100dB (Rollins et al, 2007; Podoleanu, 2000).

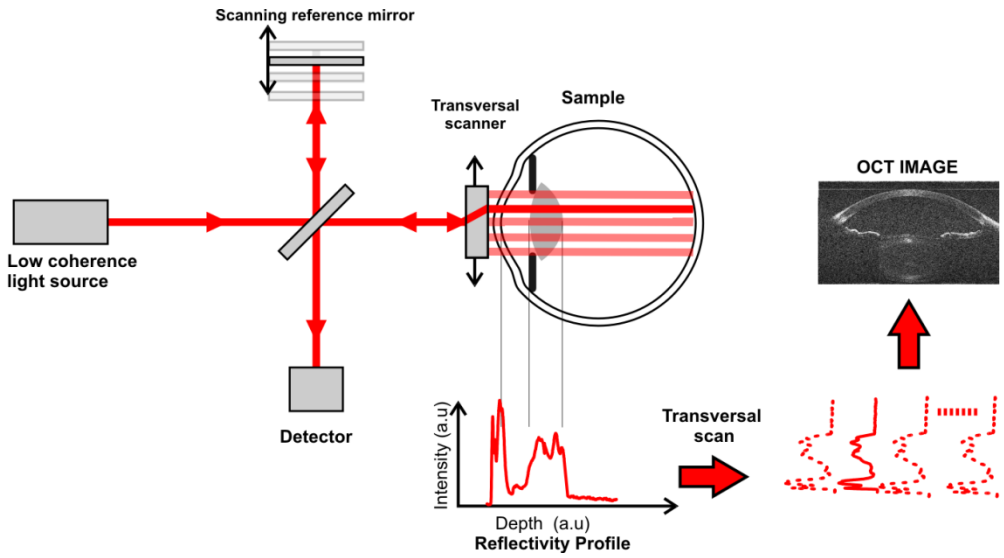

Figure 3.7: Schematic of a Time Domain OCT system.

3.4. Fourier Domain OCT

3.4.1. Basic theory

In recent years, new OCT methods named Fourier domain or Frequency domain methods found their place as they exhibit advantages in terms of imaging speed and sensitivity compared to the earlier time domain methods (Leitgeb et al, 2003; Choma et al, 2003; De Boer et al, 2003). The main limitation of the time domain implementations is the low scanning speed of the delay lines, which limits the overall acquisition speed of the system. Another limitation of TD-OCT is that the speed of the delay line defines the frequency of the interference signal. An increase of speed corresponds to an increase of the signal bandwidth. On the other hand, an increase of bandwidth decreases the SNR and consequently it lowers the sensitivity of the system. The increased imaging speed of FD-OCT system is due to the fact that no modulation of the reference arm length is needed to record a reflectivity profile. In FD-OCT an axial scan is obtained by Fourier transforming the spectrum of the light reaching the detector while the reference arm is maintained stationary. Let us consider a sample with N layers. In Fourier Domain OCT the intensity of the signal as a function of the propagation constant can be expressed according to equation 3.18 as

$$i(\mathrm{k}) \propto i_R(\mathrm{k}) + \sum_{\mathrm{i}} i_S(\mathrm{k},\mathrm{i}) + \sum_{\mathrm{i}} 2\sqrt{i_R(\mathrm{k}) i_S(\mathrm{k},\mathrm{i})}\cos(2\mathrm{k}\Delta z_{\mathrm{i}}) \qquad 3.22$$

$$+ \sum_{\mathrm{i}} \sum_{\mathrm{i}\neq\mathrm{j}} 2\sqrt{i_S(\mathrm{k},\mathrm{i}) i_S(\mathrm{k},\mathrm{j})}\cos\left(2\mathrm{k}\Delta z_{\mathrm{ij}}\right)$$

where $i_R(\mathrm{k})$ and $i_S(\mathrm{k},\mathrm{i})$ are the wavelength dependent intensities reflected by the reference arm and the i^{th} layer and Δz_{i} is the path length difference between the reference arm and the i^{th} boundary and Δz_{ij} is the path length difference between the i^{th} and j^{th}

internal layers of the sample. The signal can be rewritten in term of the spectral intensity distribution of the light source and the reflectivity profile of the sample

$$i(\mathrm{k}) \propto s(\mathrm{k})\left[R_R + \sum_{\mathrm{i}} \mathrm{R_i} + 2\sqrt{R_R}\sum_{\mathrm{i}} \sqrt{\mathrm{R_i}}\cos(2\mathrm{k}\Delta \mathrm{z_i}) + 2\sum_{\mathrm{i}}\sum_{\mathrm{i}\neq\mathrm{j}} \sqrt{\mathrm{R_i R_j}}\cos\left(2\mathrm{k}\Delta \mathrm{z_{ij}}\right)\right] \quad 3.23$$

where $s(\mathrm{k})$ is the spectral intensity distribution of the light source, R_R is the reflectivity of the reference mirror and R_i is the reflectivity of the i^{th} boundary. The first and second term are DC terms. The third term in the brackets of equation 3.23, commonly referred as the spectral interferogram or spectral fringes in OCT terminology, contains the information about the reflectivity profile of the sample. The fourth term is the mutual interference among the light returning from any two layers within the sample. The reflectivity profile can be calculated by performing the Inverse Fourier transform of the signal in equation 3.23 (Häusler et al, 1998)

$$|\mathcal{F}^{-1}[I(\mathrm{k})]| \propto \Gamma(\mathrm{z}) \otimes \left[\left(R_R + \sum_{\mathrm{i}} \mathrm{R_i}\right)\delta(0) + 2\sqrt{R_R}\sum_{\mathrm{i}} \sqrt{\mathrm{R_i}}\,\delta(\mathrm{z} \pm \Delta \mathrm{z_i}) + 2\sum_{\mathrm{i}}\sum_{\mathrm{i}\neq\mathrm{j}} \sqrt{\mathrm{R_i R_j}}\,\delta\left(\mathrm{z} \pm \Delta \mathrm{z_{ij}}\right)\right] \quad 3.24$$

where δ is the Dirac function and $\Gamma(\mathrm{z})$ is the Fourier transform of the source spectrum, which represents the envelope of the coherence function. The first term in the brackets is a DC term that is located at $\mathrm{z} = 0$ depth, or zero delay. The second term encodes the depth information of the object and the third term describes the cross-correlation noise from the mutual interference between the layers within the sample. The

third term is normally near to the zero delay position if the intra-layer distances in the sample are relatively short compared to the reference arm length. In practice, the third term is negligible because the reflectance of the reference arm R_R is usually orders of magnitude higher than the reflectance of the sample layers R_i. Neglecting the cross-correltation term, the interference signal in the domain of the spectrum can be rewritten as

$$|\mathcal{F}^{-1}[I(\mathrm{k})]| \propto \Gamma(\mathrm{z}) \otimes \left[\left(R_R + \sum_{\mathrm{i}} \mathrm{R_i} \right) \delta(0) + 2\sqrt{R_R} \sum_{\mathrm{i}} \left(\sqrt{\mathrm{R_i}}\delta(\mathrm{z} + \Delta \mathrm{z_i}) + \sqrt{\mathrm{R_i}}\delta(\mathrm{z} - \Delta \mathrm{z_i}) \right) \right] \quad 3.25$$

Assuming the source spectrum to be Gaussian shaped

$$s(k) = \mathrm{i}_0 e^{-\frac{4ln2(k-k_0)^2}{\Delta k^2}} \quad 3.26$$

the Fourier transform of the spectral intensity distribution can be written as

$$\Gamma(\mathrm{z}) = 2\mathrm{i}_0 \frac{\sqrt{\pi}}{\alpha} e^{-\frac{(2z)^2}{4\alpha^2}} \quad 3.27$$

where $\alpha = \frac{\sqrt{ln2}}{\pi} l_C$ and i_0 is related to the total intensity of the source. $\Gamma(\mathrm{z})$ is also Gaussian shaped. The spectral fringes corresponding to the i^{th} boundary at Δz_i are displayed in Figure 3.8 (Top). The original spectrum is modulated with frequency $\frac{\pi}{\Delta z_i}$ in the wavenumber domain. The Fourier transform in equation 3.25 produces two Gaussian terms with intensity peaks that are located at $\pm\Delta z_i$ (Figure 3.8, Bottom). The constant term of equation 3.25 is a Gaussian term $\Gamma(\mathrm{z})$ with intensity peak centered at the zero depth.

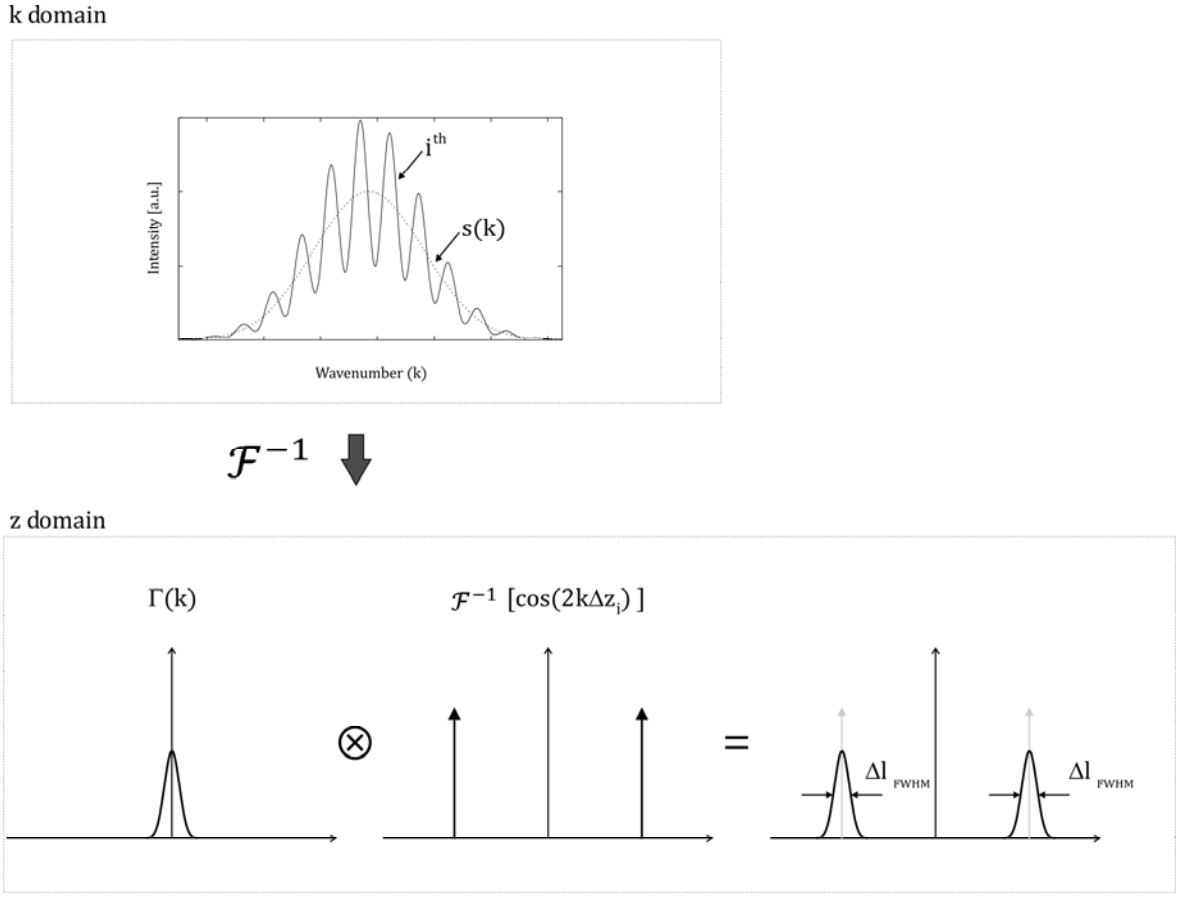

Figure 3.8: FD-OCT signal reconstruction from the wavenumber domain to the depth domain.

The axial resolution in FD-OCT is the same as for TD-OCT

$$\Delta l_{\mathrm{FWHM}} = \frac{2ln2}{\pi}\frac{\lambda_0^2}{\Delta\lambda} \approx 0.44\frac{\lambda_0^2}{\Delta\lambda} \qquad 3.28$$

Note that the depth information about each i^{th} layer is reported twice in the depth space because of the symmetrical delta functions $\delta(\mathrm{z} + \Delta\mathrm{z_i})$ and $\delta(\mathrm{z} - \Delta\mathrm{z_i})$ in equation 3.22. The Fourier transform of a real valued function, such as the spectral interferogram in equation 3.23, is Hermitian symmetric and thus produces a complex conjugate artifact that mirrors the depth space about the zero delay. Because of this artifact, the reflectivity profile of the sample appears on either sides of the depth space. FD-OCT generates two images of the sample symmetrical to the zero depth position (Figure 3.9). FD-OCT

instruments normally display only one of these images. If the sample is not positioned entirely within the positive (or negative) space there is overlap of the two images (Figure 3.9A). The part of the sample that overlaps the displayed image is named "mirror image" or "complex conjugate artifact". During a normal imaging procedure, the operator carefully positions the sample entirely within the positive (or negative) space so that there is no overlap between the two images, making the final image unambiguous (Figure 3.9B).

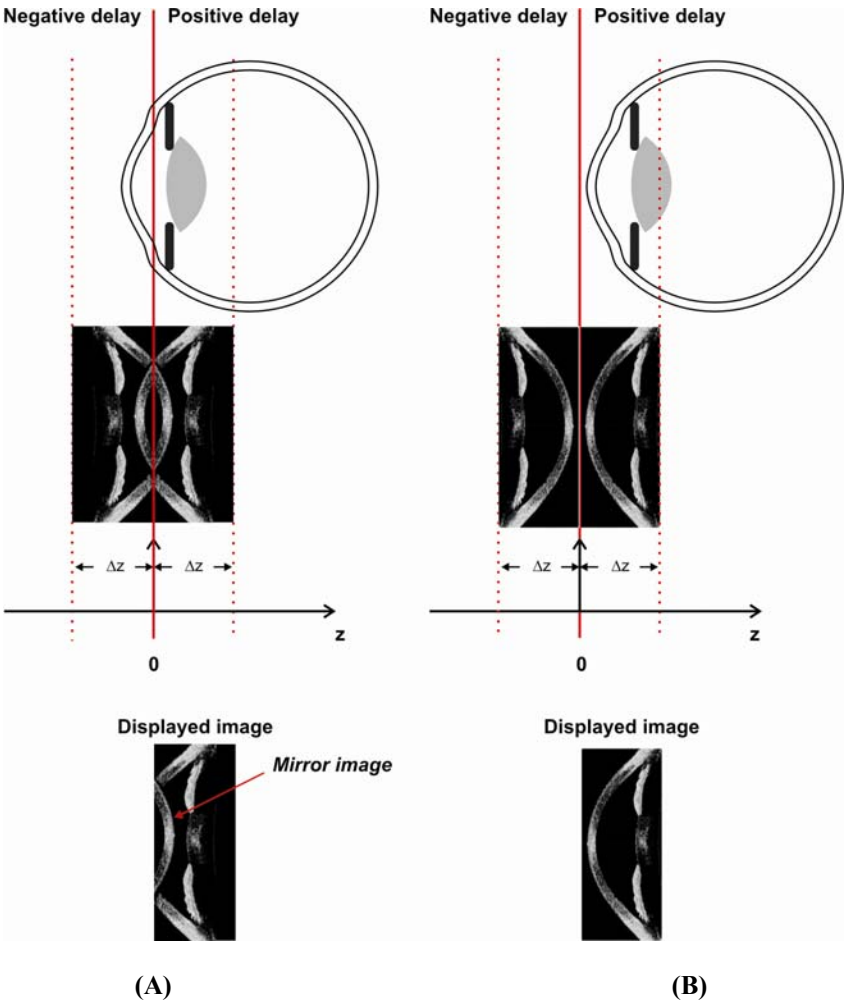

Figure 3.9: The sample is not entirely positioned on either the positive or the negative space. The FD-OCT processing generates a mirror image that overlaps the displayed image **(A)**. The sample is entirely positioned on the positive space. The FD-OCT processing generates a mirror image that does not overlap the displayed image **(B)**.

The complex conjugate artifact has been extensively investigated and approaches for using the entire axial range have been exploited (Wojtkowski et al, 2002; Leitgeb R.A., Hitzenberger C. K. et al, 2003; Choma et al, 2003; Yun et al, 2004; Sarunic et al, 2005; Davis et al, 2005; Zhang et al, 2005; Targowski et al, 2005; Yasuno et al, 2005; Sarunic et al, 2006; Vakoc et al, 2006; Vakhtin et al, 2006; Baumann et al, 2007; Hofer et al, 2009). Although these methods allow a twofold increase of the axial range and enhance the detection sensitivity, they exhibit some disadvantages. In fact, doubling the axial range and avoiding the mirror image requires more data to be acquired and extra post processing, which in turn reduces the imaging speed. Finally, implementing such a method may require additional hardware that increases the overall system complexity and most of the time, some artifacts remain in the image.

Fourier Domain implementations: SD-OCT and SS-OCT

In FD-OCT, the spectral distribution of the light backscattered from the sample is obtained by either spectral interferometry techniques (Spectral Domain OCT) or by wavelength tuning techniques (Swept Source OCT). SD-OCT operates with a low coherence light source. In the basic implementation of SD-OCT the depth scan data from the sample is obtained by recording the spectral fringes with a spectrometer (Figure 3.10). The recorded spectral fringes are then Fourier transformed to produce the reflectivity profile (a-scan, a-line or depth scan). The transversal scanning operation is similar to the one in TD-OCT implementations. At each lateral location, spectral fringes are acquired and Fourier transformed. The depth scans are then placed side by side to form a two-dimensional image.

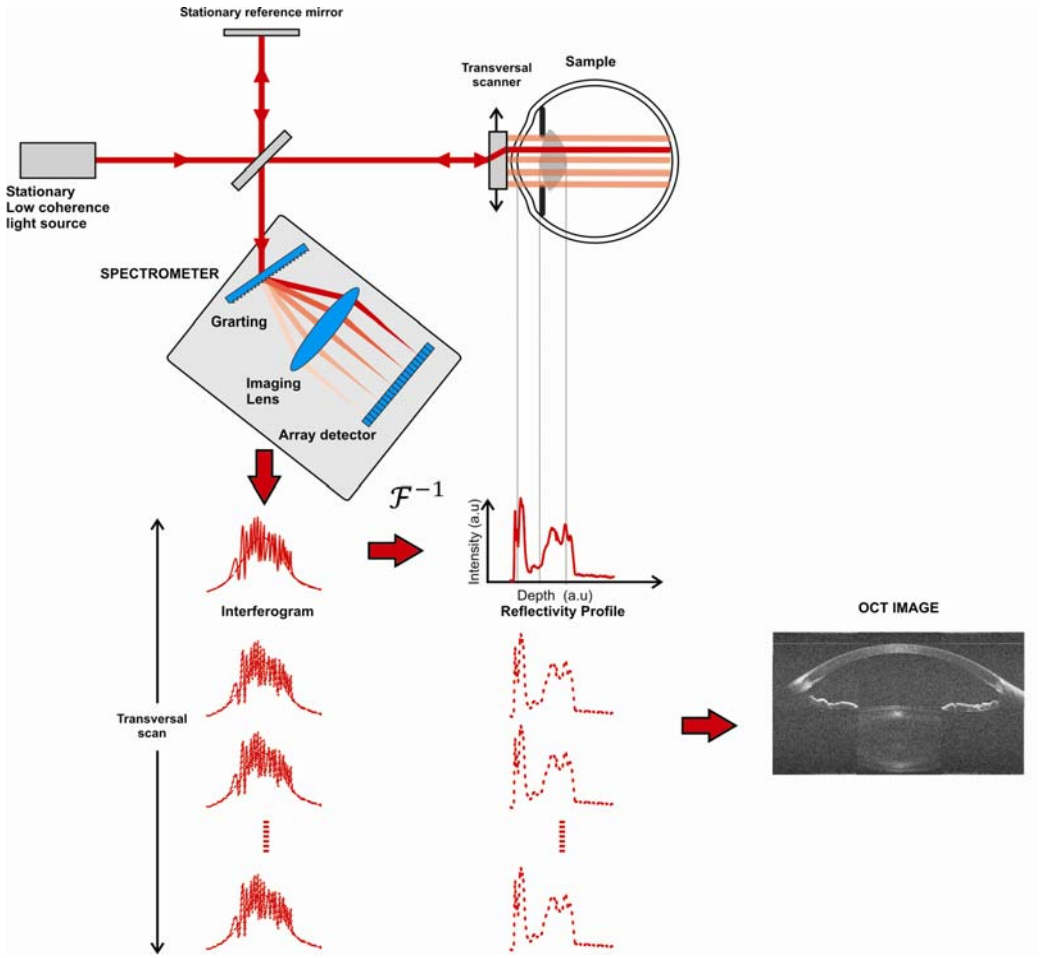

Figure 3.10: Schematic of a SD-OCT system

SS-OCT (Figure 3.11) uses a rapidly tunable laser source and a single point detector. In SS-OCT, the interferogram is sequentially detected in the frequency domain by modulating a narrowband source over a range of wavelengths at a rapid rate. Once a spectral interferogram is sequentially acquired, it is Fourier transformed to obtain a reflectivity profile of the sample. The transverse scanning and image creation operations are analogous to the ones in TD-OCT and SD-OCT.

Between the two spectral discrimination solutions existing for FD-OCT imaging, SD-OCT was chosen as the imaging platform to build an imaging system with extended depth.

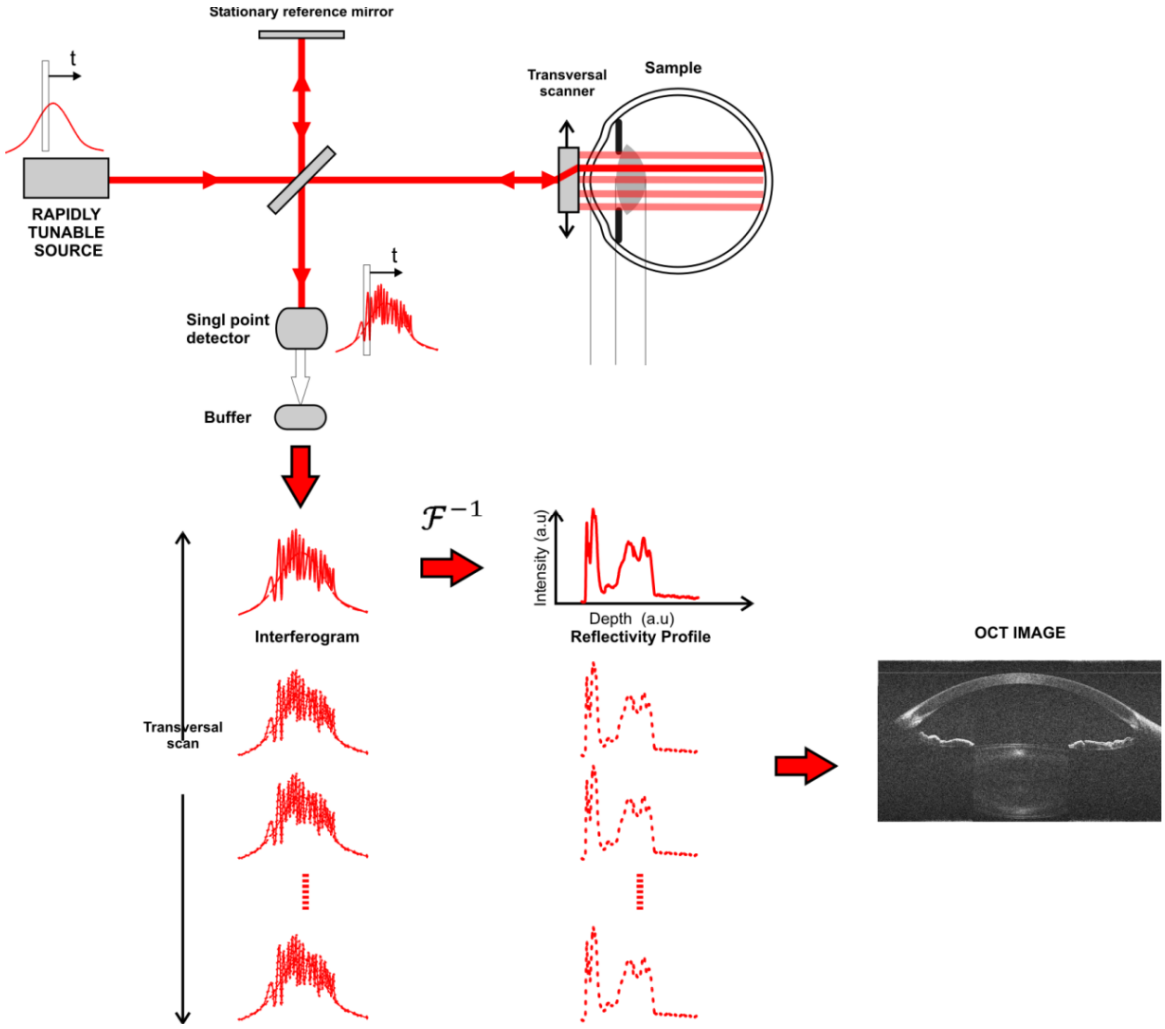

Figure 3.11: Schematic of a SS-OCT system.

SS-OCT is the most recent implementation of OCT imaging and allows higher imaging speed (SS-OCT) compared to earlier SD-OCT implementations (Gora et al, 2009; Potsaid et al, 2010). The choice of developing an imaging system based on SD-OCT rather than a SS-OCT system for this project holds several motivations. At the beginning of this project, in early 2009, the tunable sources suitable for extended depth imaging were not available. At that time, SD-OCT seemed to be the quickest solution to achieve extended depth imaging. Anterior segment imaging based on SS-OCT ranged

from the cornea to the anterior lens (Yasuno et al, 2005, Sarunic et al, 2008; Gora et al, 2009). Only more recently after 2009, the OCT research community worked to improve the performances of wavelength tunable light sources to make them suitable for extended depth imaging. Entire anterior segment image acquired with SS-OCT have been lately presented (Furukawa et al, 2010). Another motivation to prefer SD-OCT rather than SS-OCT, is the unavailability of a tunable light source with the desired wavelength and bandwidth, which will be further clarified in the next sections. Since SD-OCT is the method used in this project to achieve extended depth, only the fundamentals of SD-OCT design will be introduced in the next sections.

3.5. Spectral Domain OCT

3.5.1. Axial range

The spectral fringes $s(k)2\sqrt{R_R}\sqrt{\mathrm{R_i}}\cos(2\mathrm{k}\Delta\mathrm{z_i}), \mathrm{i} = 1,2, \ldots \mathrm{N}$ in equation 3.23 contain the depth information of the sample. Let us consider only the positive side of the depth space $\mathrm{z} > 0$. From equation 3.25, the Fourier transform of spectral fringes leads to a series of point spread functions that are centered at $\mathrm{z} - 2\Delta\mathrm{z_i} \quad \mathrm{i} = 1,2, \ldots \mathrm{N}$. The greater the mismatch between a layer of the sample and the reference arm, the higher the frequency of the spectral modulation. Figure 3.12 shows the OCT spectral modulation for a single boundary as a function of depth for three different frequency oscillations in the k domain.

In SD-OCT the spectral fringes are recorded with a one dimensional array of photodetectors.

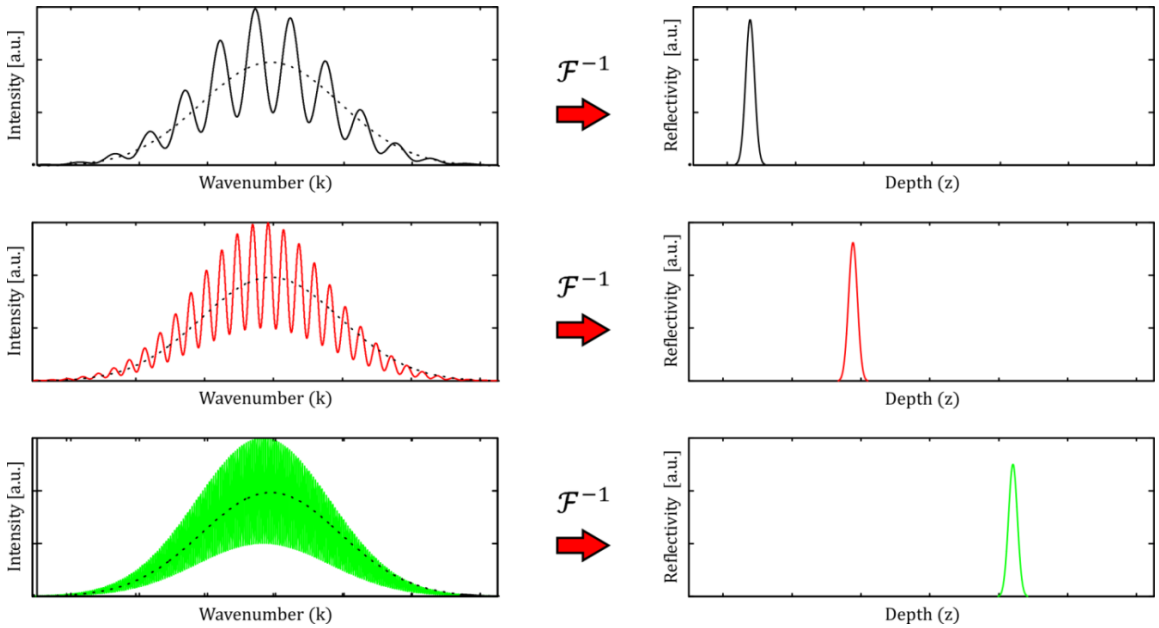

Figure 3.12: Effect of different frequency oscillations of the spectral fringes in the wavenumber on the depth domain.

The photodetector array has a finite number of pixels and a finite pixel size. We assume that the number of sampling points N of the spectral fringes is given by the number of pixels of the array. According to the Nyquist sampling criterion, the sampling period δk has to be less than twice the period of the fringe corresponding to the maximum depth Δz_{max} (Wojtkowski et al, 2002), At the maximum depth, the period is, from equation 3.23, $\pi/\Delta z_{max}$. The Nyquist criterion can be written as

$$\Delta z_{max} < \frac{1}{2}\frac{\pi}{\delta k} = \frac{1}{4}\frac{\lambda_0^2}{\delta\lambda} \qquad 3.29$$

where $\delta k = 2\pi\lambda_0^2/\delta\lambda$ was expressed in terms of the sampling interval $\delta\lambda$, which is the wavelength spacing between successive pixels of the spectrometer. The sampling interval is the ratio of the spectral range $\Delta\Lambda$ spread over the array and the number of pixels N. Equation 3.29 yields (Wotjtkowski et al, 2002; Häusler et al, 1998)

$$z_{\mathrm{MAX}} = \frac{1}{4}\frac{\lambda_0^2}{\Delta\Lambda}\mathrm{N} \qquad 3.30$$

Equation 3.30 determines the maximum depth in air in function of the central wavelength of the source, the number of pixels of the detector and the spectral range. The axial imaging range can be increased by reducing the sampling interval δλ, which in turn can be achieved either by increasing the number of pixels N used to detect the spectral range ΔΛ, or by decreasing ΔΛ.

As seen in section 3.4, the Fourier transform of a real valued function has conjugate symmetry about the zero delay, which means that only half of the bins in the depth domain contain exclusive depth information about the sample reflectivity. Equation 3.30 can then be rewritten as

$$z_{\mathrm{MAX}} = \frac{1}{2}\frac{\lambda_0^2}{\Delta\Lambda}\frac{\mathrm{N}}{2} = \delta\mathrm{z}\,\frac{\mathrm{N}}{2} \qquad 3.31$$

where δz is the bin spacing in the depth domain. To resolve two layers that are separated by the axial resolution Δl_{FWHM}, the bin spacing in the depth domain should be at least $\Delta l_{\mathrm{FWHM}}/2$ because of the Nyquist criterion. Equation 3.31 can be written as

$$z_{\mathrm{MAX}} = \frac{\Delta l_{\mathrm{FWHM}}}{2}\,\frac{\mathrm{N}}{2} \qquad 3.32$$

This equation shows that there is a trade-off between the theoretical axial resolution and the maximum axial range that can be achieved (Wotjtkowski et al, 2002): the imaging depth increased at the expense of a loss in axial resolution. Although the theoretical axial resolution is defined by the spectral characteristics of the light source in equation 3.28, the spectrum of the source needs to fit in the detected spectral range ΔΛ, or else the axial resolution would be inferior to the theoretical limit.

Combining equations 3.32, 3.28 and 3.30 shows that to achieve the resolution of equation 3.28, the spectral range must be

$$\Delta\Lambda = N\delta\lambda = \frac{1}{2}\frac{\lambda_0^2}{\frac{\Delta l_{FWHM}}{2}} = \frac{\pi}{2ln2}\Delta\lambda \qquad 3.33$$

3.5.2. Noise and Sensitivity

A requirement for OCT instrumentation is to detect extremely low signal intensities of light backscattered from the sample. One of the main advantage of FD-OCT, and in particular SD-OCT, compared to TD-OCT is the superior sensitivity (Leitgeb et al, 2003; De Boer et al, 2003; Choma et al, 2003). In SD-OCT the main noise sources include the shot noise, thermal noise, excess noise and receiver noise. Optimal sensitivity is achieved when the detection system is shot noise limited. In shot noise limited detection, when the reflectivity of the reference arm is larger than in the sample arm, the sensitivity of a SD-OCT system can be generally expressed in terms of the signal to noise ratio as follows (Nassif et al, 2004; De Boer et al, 2003; Leitgeb et al, 2003; Grulkowski et al, 2009; Choma et al, 2003)

$$S_{SD-OCT} = SNR_{SD-OCT} = \frac{\rho\ \Delta t\ P_S}{\frac{hc}{\lambda}} \qquad 3.34$$

where ρ is the efficiency of the optical system that comprises the losses and efficiency of each component and the spectrometer, P_S is the power returning from the sample, Δt is the integration time of the array detector and $\frac{hc}{\lambda}$ is photon energy. The power of the light delivered to the sample is limited to ensure that the light intensity delivered to the eye is safe for the anterior segment and retina according to the American National Standards Institute, *Safe Use of Lasers* (ANSI, 1993). The maximum safe power

for 830nm radiation is 0.75mW. The power returning from the sample P_S depends on the reflectivity R_S of the sample. In general, for biological tissues, shorter wavelengths produce higher scattering which results in higher diffuse reflectivity. Shorter wavelengths also correspond to higher photon energy, and therefore a higher sensitivity. Two parameters in the spectrometer design can be controlled to optimize the sensitivity of the system: the integration time and the spectrometer efficiency. Designing a spectrometer with reduced losses is key to reach high sensitivity. The acquisition speed of the system is defined by the readout speed of the line detector which is defined as the inverse of the integration time. Therefore, there is a tradeoff between the maximum speed and the maximum sensitivity that can be reached in a SD-OCT system. With a perfect reflector as a sample, the typical sensitivity of a SD-OCT system can be well above 100dB (Choma et al, 2003). With a light source centered at 830nm, a detector with integration time of 50 μs and assuming the efficiency of the spectrometer to be 80%, within the ANSI safety limits and with a perfect reflector, the sensitivity of the spectrometer is ~111dB.

3.5.3. Sensitivity fall-off with depth

One of the main drawbacks of FD implementations is the presence of a depth dependent decrease of sensitivity (Figure 3.13). Let us consider a reflector positioned at different depths $z_1 < z_2 < z_3$ in the sample arm. The spectral fringes associated to each of the three depths can be written as $s(k)\left[1 + 2\sqrt{R_R}\sqrt{\mathrm{R_i}}\cos(2\mathrm{kz_i})\right], \mathrm{i} = 1,2,3$ according to equation 3.27, where $\mathrm{z_i}$ is the path length difference between sample and reference arm. Since the reflectivity of the sample and of the reference mirror is constant and the spectral distribution $s(k)$ has a constant amplitude, one expects that the spectral fringes have the same amplitude at the three depths, as depicted in Figure 3.12. In reality, a decay

of the spectral fringe amplitude occurs as the frequency in the k domain increases (Left hand side of Figure 3.13). This effect leads to a drop of the point spread function amplitude with depth (Right hand side of Figure 3.13).

The decrease of sensitivity with depth depends on the implementation of the spectrometer and it is known in the OCT literature as sensitivity "fall-off" or "roll-off". The sensitivity fall-off limits the usable axial range defined by equation 3.30.

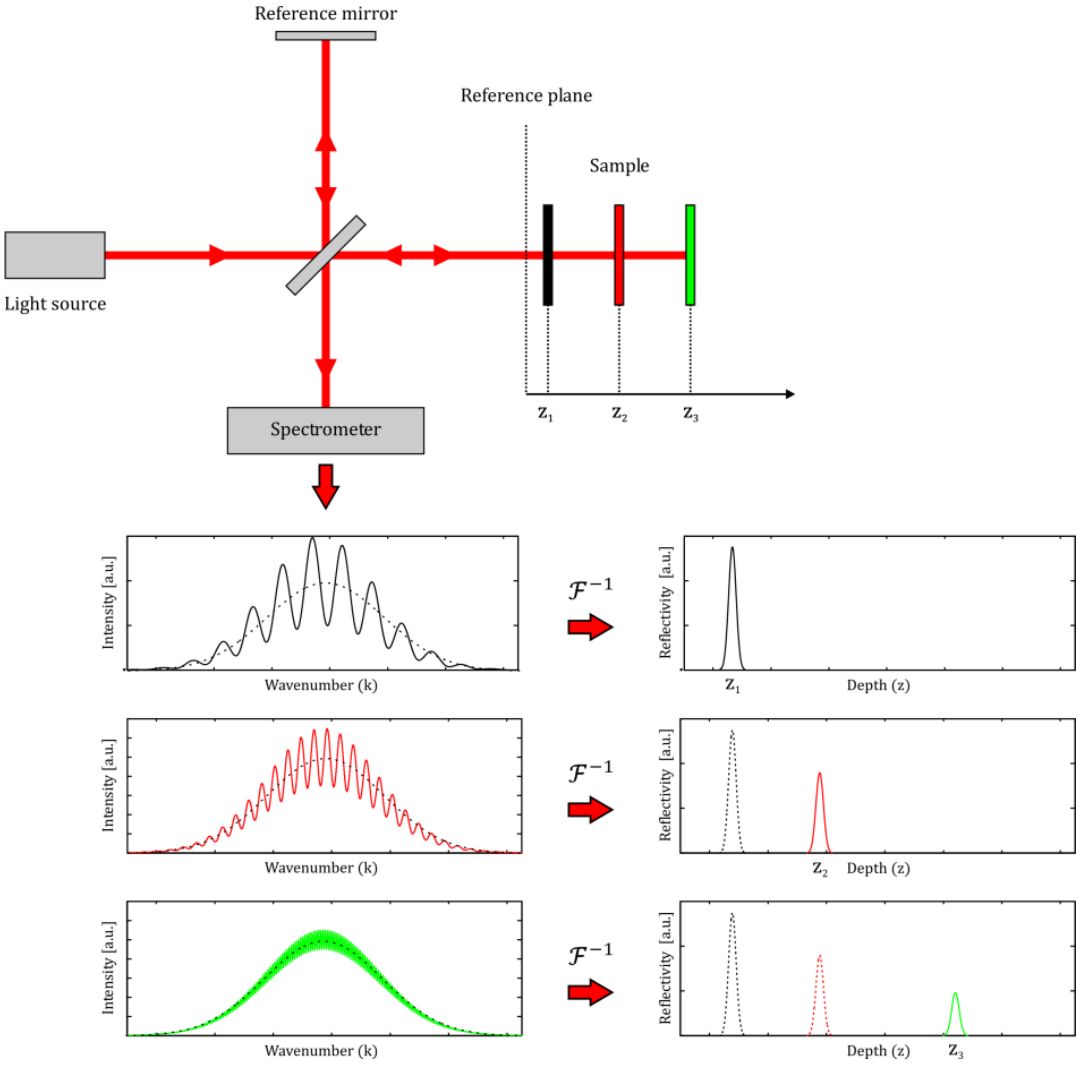

Figure 3.13: Decrease of the sensitivity in the wavenumber and depth domains. The signal amplitude decreases with depth even though the reflectivity of the sample is constant.

The sensitivity fall-off has been extensively investigated and the contribution of the causes have been included in general analytical models (Leitgeb et al, 2003; Yun et al, 2003; Nassif et al, 2004, Hu et al, 2007). The main sources of sensitivity decay are

- The finite width of the pixels of the array detector, which sets a fundamental limit for the sampling interval $\delta\lambda$
- The extended spot size produced on the detector array by the focusing optics of the spectrometer, which sets a practical limit for the sampling interval $\delta\lambda$
- The interferogram is not evenly spaced in the wavenumber domain

The first term is the result of the rectangular characteristic of the array pixel, which reduces the amplitude of high frequency oscillation of the interference signal. The spectral fringes are convolved with a *rect* function representing the pixel shape, which becomes a *sinc* function in the depth domain after Fourier transformation (Leitgeb et al, 2003). The sinc term has origin at the zero depth and suppresses the amplitude of the signal at longer depth. The second term is a Gaussian decay with depth that is the result of the Fourier transform of the Gaussian profile of the focused spot onto the array pixels (Yun et al, 2003). The third term occurs because the dispersion of light by the diffraction grating used in the spectrometer is almost evenly spaced in the wavelength domain and not in the wavenumber space. In order to perform Fourier transformation, the spectral fringes acquired in the wavelength domain need to be resampled to be evenly spaced in the wavenumber space. The typical resampling methods use in OCT processing employ interpolation algorithms, which introduce an interpolation error.

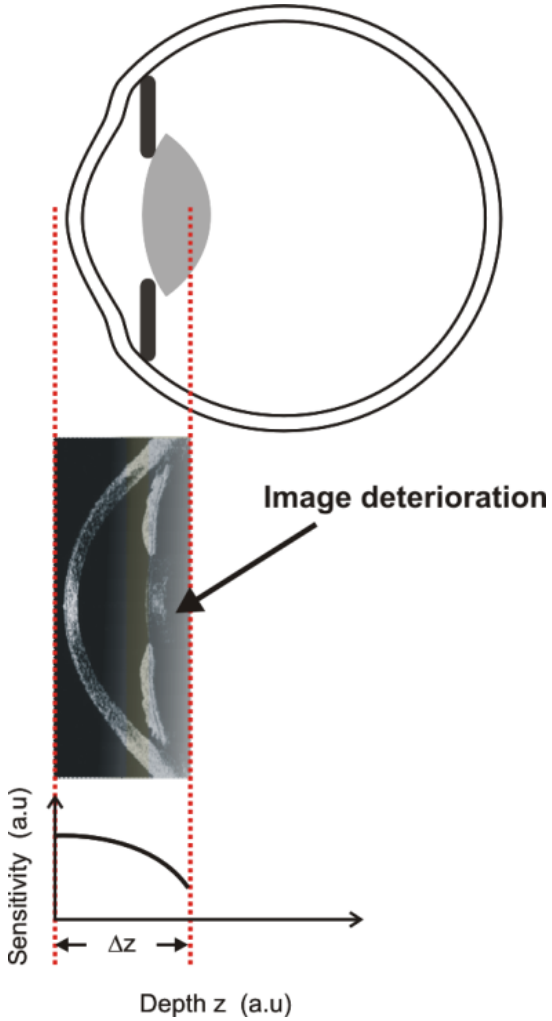

Figure 3.14: Falloff of the sensitivity with depth deteriorates the quality of the image at longer depth, which in turn limits the axial range Δz.

The degree of the interpolation error increases for higher signal frequencies, which in turn causes the sensitivity to decrease for signals originated at longer depths (Chan and Tang, 2010). In OCT instrumentation, fall-off of the sensitivity deteriorates the quality of the image at deeper reflections (Figure 3.14) limiting further the useful axial imaging range. A complex general model of sensitivity roll-off that takes into accounts the three factors has been previously proposed (Hu et al, 2007) and will be adopted in next chapter in the spectrometer design section.

3.5.4. Dispersion

In OCT, to achieve optimal axial resolution it is necessary to match the dispersion between the reference and the sample arm (Fercher et al, 2002; Wojtkowski et al, 2004). Dispersion causes frequency dependence of the propagation constant *k*. The propagation constant can be expressed as a Taylor series near the center frequency of the light source $\nu_0 = c/\lambda_0$ in vacuum,

$$k(\nu) = k(\nu_0) + \left.\frac{\partial k}{\partial \nu}\right|_{\nu_0} (\nu - \nu_0) + \left.\frac{1}{2}\frac{\partial^2 k}{\partial \nu^2}\right|_{\nu_0} (\nu - \nu_0)^2 + \left.\frac{1}{6}\frac{\partial^3 k}{\partial \nu^3}\right|_{\nu_0} (\nu - \nu_0)^3 + \ldots \qquad 3.35$$

where c is the speed of light in vacuum and $k(\nu_0)$ is the propagation constant at ν_0. The first order term $\left.\frac{\partial k}{\partial \nu}\right|_{\nu_0}$ is defined as the inverse group velocity. The first two terms do not affect the axial resolution of OCT. The second order term, $\left.\frac{\partial^2 k}{\partial \nu^2}\right|_{\nu_0}$ (group velocity variation) produces a broadening of the axial PSF. The third order term $\left.\frac{\partial^3 k}{\partial \nu^3}\right|_{\nu_0}$ (third order dispersion) produces asymmetry of the envelope of the interferometric signal in the depth domain. From equation 3.23 the interference signal can be written as (Wojtkowski et al, 2004)

$$I(\nu) \propto s(\nu) 2\sqrt{R_R} \sum_{\mathrm{i}} \sqrt{\mathrm{R_i}} \cos\left(\frac{2\pi}{\mathrm{c}} \nu \, 2\Delta \mathrm{z_i} + \psi(\nu, \Delta \mathrm{z_i})\right) \qquad 3.36$$

where the phase term $\psi(\nu, \Delta \mathrm{z_i})$ is dependent on frequency and depth and includes the higher order terms of the propagation constant. In OCT, the depth dependence is assumed to be negligible because of the limited axial range. With this assumption the phase can be expressed as

$$\psi(\nu) = \psi(\nu_0) + \left.\frac{\partial\psi}{\partial\nu}\right|_{\nu_0} (\nu - \nu_0) + a2\,(\nu - \nu_0)^2 + a3(\nu - \nu_0)^3 + \ldots \qquad 3.37$$

where $a2 = \frac{1}{2}\left.\frac{\partial^2\psi}{\partial\nu^2}\right|_{\nu_0}$ and $a3 = \frac{1}{6}\left.\frac{\partial^3\psi}{\partial\nu^3}\right|_{\nu_0}$ are coefficients for the second and third order dispersion. Figure 3.15 shows simulation results of the effect of the dispersion mismatch caused by 2mm of water. The second and third order dispersion coefficients of water at 800nm are about $a2 = 50fs^2$ and $a3 = 50fs^3$ (Coello et al, 2007). Figure 3.15A and B show the effect when the second order coefficient was set to $a2 = 50fs^2$ and the third order coefficient $a3 = 0$. Figure 3.15C and D show the effect when $a2 = 0$ and $a3 = 50fs^3$. In this simulation, the spectrum has Gaussian distribution centered at $\lambda_0 = 800nm$ and $FWHM = 50nm$. The group velocity dispersion and the third order coefficient are added to the interference fringes in equation 3.37. The effect of mismatch is noticeable in the spectral fringes (See arrows in Figure 3.15A and C). There is a broadening of the FWHM of the PSF and asymmetry of the PSF after Fourier transform. In OCT, dispersion effects are minimized by introducing an optical component in the reference arm that has near identical dispersion properties as the sample. When imaging the retina, for instance, the vitreous of the eye introduces significant dispersion mismatch. This dispersion is mostly compensated for by introducing in the reference arm a water cell of length equal to the average eye length. However, some residual dispersion remains due to the variability of the eye length in different subjects.

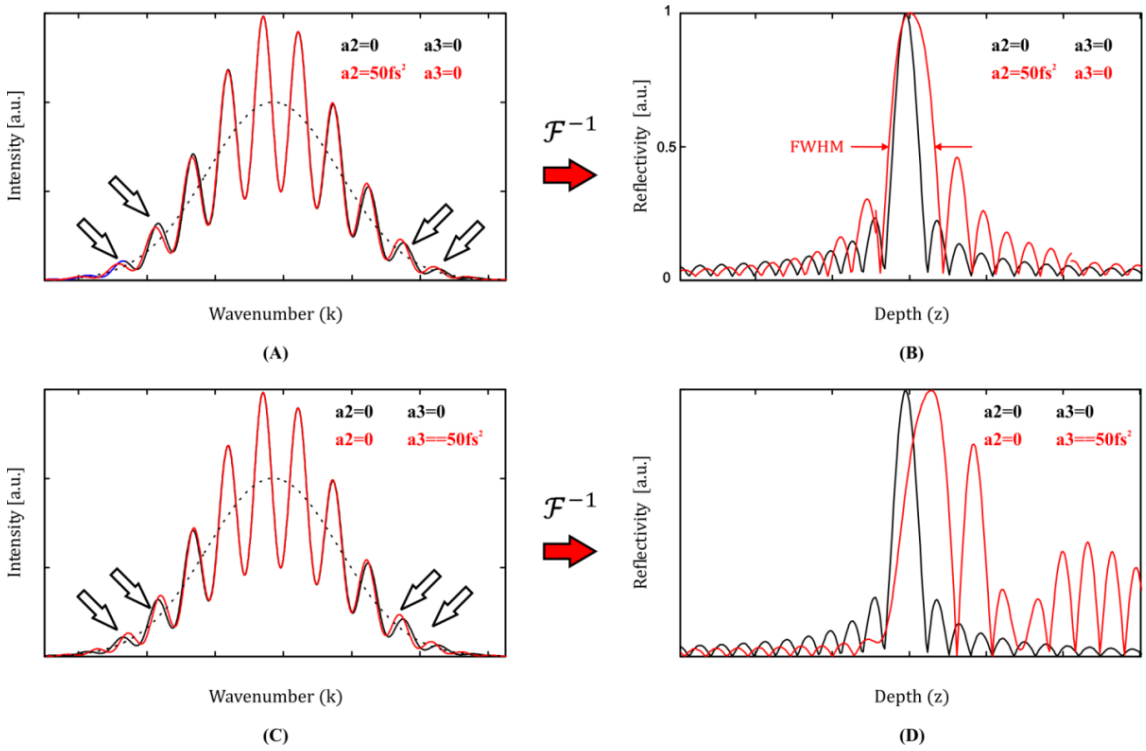

Figure 3.15: Effect of the dispersion mismatch to the spectral fringes and the FWHM of the PSF after Fourier transform (red lines). Effect of the second order coefficient $a2 = 50fs^2$ to the spectral fringes (arrows) **(A)** and relative broadening of the FWHM of the PSF **(B)**. Effect of the third order coefficient $a3 = 50fs^2$ to the spectral fringes (arrows) **(C)** and relative asymmetry of the FWHM of the PSF **(D)**.

In order to compensate for that residual compensation mismatch and for additional dispersion mismatch in the optical setup a phase correction function can be added to the signal in equation 3.38 to compensate for dispersion (Fercher et al, 2002; Wojtkowski et al, 2004)

$$\varphi(\nu) = -c2\,(\nu - \nu_0)^2 + c3(\nu - \nu_0)^3 \qquad 3.38$$

The coefficient $c2$ adjusts for the group velocity variation while the coefficient $c3$ for the third order dispersion coefficient. Normally, if the dispersion of the optical components in the arms of the OCT system is well matched, numerical compensation up to the third order is sufficient to achieve optimal axial resolution.

In OCT imaging of ocular structures, approximate dispersion compensation can be performed by calculating the second and third order dispersion coefficients of the ocular components of interest (Coello et al, 2007). The coefficients can then be manually fine tuned to reach high image quality. Numerical dispersion compensation methods are also available to automatically find the optimal dispersion coefficients (Wojtkowski et al, 2004).

3.6. FD-OCT of the AS with long axial range

Until recently, the axial range of FD-OCT systems was limited to 2-3mm. Recent technological advances have enabled the development of one dimensional CMOS cameras with a large number of pixels (N=4096, CMOS Basler Sprint spL4096-104k; Basler AG, Germany). Arrays with a larger number of pixels allow the construction of spectrometers with finer spectral sampling interval ($\delta\lambda$) and therefore longer axial depth (z_{MAX}). Grulkowski et al developed a SD-OCT system at 830nm for anterior segment imaging with unprecedented depth (5.2mm in tissue) (Grulkowski et al, 2009). They demonstrated that OCT images of the entire human lens can be acquired in a single frame with their system. However, the imaging depth was barely enough to image the lens of young subjects (less than 30 years of age). This design would not be suitable to image the thicker lens of older subjects in a single frame. After using a method to avoid the mirror image artifact and use the entire axial range, Grulkowski et al were able to image the entire anterior segment from cornea to posterior lens (Figure 3.16A). However, residual complex conjugate artifacts were present in the image. Other two significant OCT developments for imaging the entire anterior segment were recently demonstrated (Jungwirth et al, 2009; Furukawa et al, 2010).

Jungwirth et al used an approach similar to Grulkowski et al by developing a spectrometer based OCT system at the same wavelength (835nm) with a depth of 7mm in air. Imaging of the entire anterior segment was demonstrated after doubling the axial range to 14mm using a complex conjugate removal technique (Figure 3.16B). The design used for suppressing the mirror image artifact requires a specific scanning pattern with fixed speed and transversal range, which in turn limits the potential of the imaging system. The system showed a better suppression of the image artifacts compared to the one reported by Grulkowski et al while the overall image quality and sensitivity was comparable. Furukawa et al built a SS-OCT at 1300nm to extend the free space axial range to 12 mm with no use of any method to avoid the mirror image and use the entire axial range (Furukawa et al, 2010). With this implementation they demonstrate anterior segment OCT imaging of a young (33 year-old) subject eye in a single frame, including the entire depth from the cornea to the posterior lens (Figure 3.16C). The main limitation of this system is the lower axial resolution.

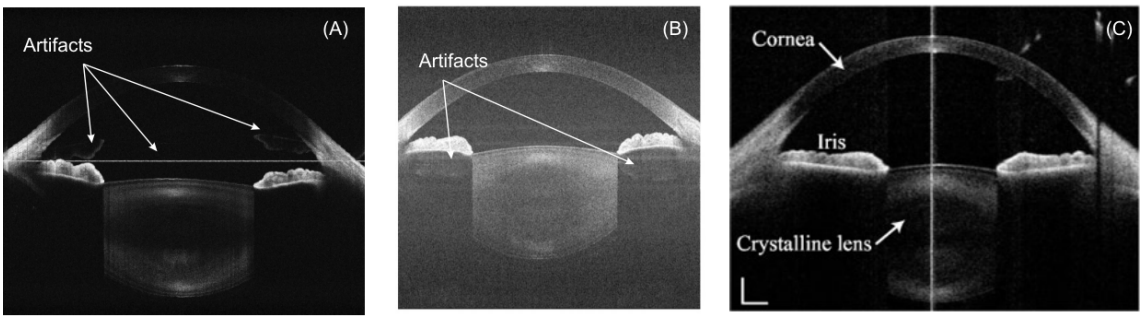

Figure 3.16: (A) Image modified by Grulkowski et al (2009). The image of the anterior segment is affected by artifacts. **(B)** Image modified by Jungwirth et al (2009). **(C)** Image obtained by Furukawa et al (2010).

3.7. Summary

In this chapter, we reviewed the literature and theory of SD-OCT that will be used to design a system for extended depth imaging of the anterior segment with high axial resolution and high speed. To achieve long axial range a spectrometer with very high spectral sampling interval needs to be built. Such design requires high spectral resolution and a detector with very high number of pixels N. The main tradeoff of such a system is the high spectral resolution of the spectrometer vs. high axial resolution and high speed. An important challenge in designing the spectrometer is the optimization of the sensitivity fall-off typical of Fourier Domain OCT, which affects the sensitivity of the system at longer depth, and limits the usable axial range. In the next chapter, a detailed design analysis taking into consideration the tradeoffs and the effects of the sensitivity fall-off will be performed to meet the requirements for imaging the whole crystalline lens and the whole anterior segment of the eye.

CHAPTER 4. DESIGN OF AN EXTENDED DEPTH SD-OCT SYSTEM

4.1. Objective

The purpose is to develop a SD-OCT system with extended axial range, high axial resolution and high speed, for fast cross-sectional imaging of the anterior segment. The axial resolution and sensitivity need to be sufficiently high to image changes in the lens internal structure during accommodation. Table 4.1 summarizes the specifications of two commercial and three experimental OCT devices used for anterior segment imaging together with the design specification for the proposed SD-OCT system. The SD-OCT setup (Figure 4.1) consists of several parts: an interferometer, a low coherence light source, a delay line, a scanning head and a spectrometer for detection. A computer is used to acquire the data and a control unit was developed to synchronize the devices. A commercial software package (Bioptigen, Inc. Research Triangle Park, NC) was modified and used for the real-time acquisition and display of the OCT data.

OCT Modality	Manufacturer/Author	Axial Resolution (μm)	Frame rate (fps)	Scanning rate (Depth scans/s)	Axial Depth (mm)
SD	BIOPTIGEN/3D SD-OCT	3-5	16 to 66**	17,000	~2
SD	OPTOVUE/iVue	5	25 to 100**	26,000	2-2.3
SD	Grulkowski et al (2009)	7-15	>20**	>20,000*	~7* (s)
SS	Furukawa et al (2010)	14	20 to 78**	20,000	12.5 (s)
SD	Jungwirth et al (2009)	17	20 to 78**	20,000	7 (s) 14 (d)
SD	**Proposed system**	**<10**	**>10**	**>20,000**	**>12**

Table 4.1: Summary of the specifications of commercial and experimental OCT systems for anterior segment imaging. Specification design of the proposed OCT system are reported ((s) single frame, (d) double frame with complex conjugate removal, * Estimated values, ** Values were calculated for 256 to 1024 depth scans per frame).

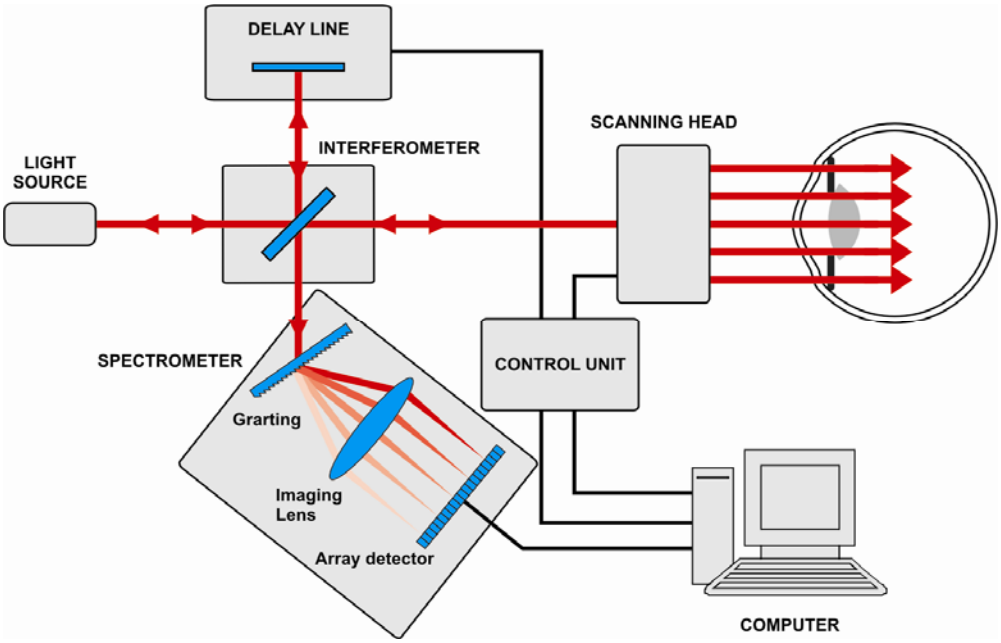

Figure 4.1: Schematic of the SD-OCT system

This chapter includes the description of the selection of the light source and the design of the interferometer, the spectrometer and the delay line. The OCT data processing algorithm is also described, and the system performance is evaluated.

4.2. Light source selection

Imaging with OCT requires a spatially coherent light source with broad bandwidth (low temporal coherence) to produce micrometric axial resolution. At present, in SD-OCT the most common approach to achieve high light coupling efficiency into a single mode fiber with broad bandwidth is using superluminescent diode (SLD) light sources. The key property of SLD that make them suitable for OCT imaging is the combination of high power (up to ~100mW), broad bandwidth (up to 100nm with a single diode) and high spatial coherence. SLD are available over a range of wavelengths between 680nm and 1600nm. Broad bandwidth versions of SLD that combine several modules have spectral bandwidth above 100nm.

There are three parameters that characterize the light source:

- central wavelength
- bandwidth
- power

Central wavelength: The central wavelength of the light source governs the penetration in tissue. Longer wavelength is indicated for higher penetration in tissue because of the reduced scattering. However, it is also important to consider absorption in tissue. Shown in Figure 4.2 is the absorption spectrum in the visible and near infrared wavelength for the common components of human soft tissue: water, oxy hemoglobin, de-oxy hemoglobin and melanin (Hamblin and Demidova, 2009). Proteins, such as collagen, are not included because their absorption is minimal in the spectral region of interest. Near infrared wavelengths between 800 and 1300nm are desirable in OCT to take advantage of the lower absorption and lower scattering compared to visible and longer infrared wavelengths.

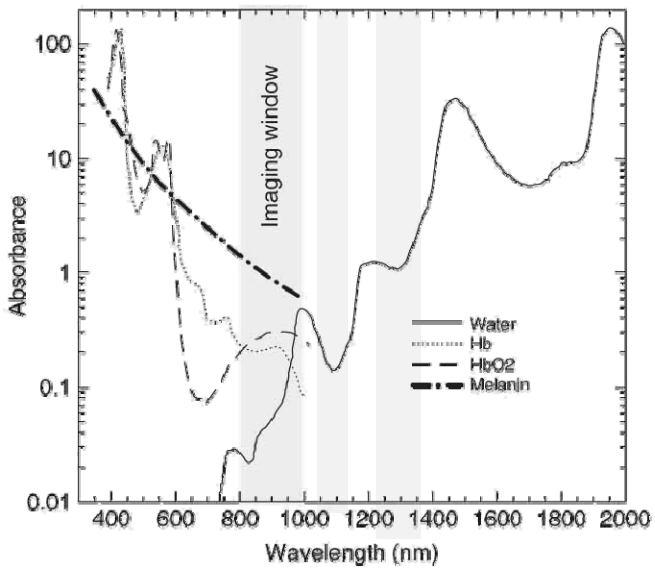

Figure 4.2: Absorption spectrum in the visible and near infrared wavelength range (Adapted from Hamblin and Demidova, 2009).

Near infrared wavelengths between 800 and 1300nm are desirable in OCT to take advantage of the lower absorption and/or lower scattering compared to visible and longer infrared wavelengths. The most common light sources used in OCT are centered in proximity of the water absorption windows around 850nm, ~1μm and ~1.3 μm. Detailed retinal imaging is normally performed in the 800nm range because there is deeper penetration in water (aqueous media) for these wavelengths. Posterior eye imaging at ~1μm has been used for deeper penetration in the retinal choroidal layers and optic nerve (Lee et al, 2006; Yasuno et al, 2007). The window at 1.3 μm has been mainly used for anterior segment imaging (Yun et al, 2004; Choma et al, 2005; Yasuno et al, 2005) and it is preferred when deeper penetration into more highly scattering tissue (sclera, ciliary body and iris) is needed.

The objective of this work is to obtain detailed images of the entire anterior segment with minimal loss and therefore shorter wavelengths are preferable. Using the absorption coefficient of water (Hale and Querry, 1973), the absorption loss is approximately 0.3dB/mm at 1300nm, 0.05dB/mm at 1060nm and 0.01 dB/mm at 825nm. If we assume that the anterior and posterior lens surfaces are located at 4 and 8mm from the anterior corneal surface, at 1300nm the returning signal will be attenuated by 2.4 dB for the anterior lens and 4.8 dB for the posterior lens. At 1060nm, the attenuation due to absorption is 0.4 dB for the anterior lens and 0.8 dB for the posterior lens. At 800nm, the attenuation due to absorption is negligible in this range of distances (less than 0.2dB), which makes this wavelength preferable for anterior segment imaging. Another reason why 800nm is preferable is that at this wavelength the scattering coefficient is higher than the one at 1060nm and 1300nm. Thus, at 800nm one expects that the back reflections

from the internal structure of the crystalline lens will be displayed with higher intensity in the OCT images. Another factor that governs the wavelength selection is the availability of line scan detectors (CCD or CMOS) in the spectral region of interest. Silicon based detectors have high responsivity in the spectral region between 600nm to 800nm and can have a very high number of pixels (N<8192). Indium Gallium Arsenide detectors (InGaAs) have higher responsivity in the region between 1μm and 1.6μm. However, InGaAs arrays have a relatively low number of pixels (N<1024), which prevents the construction of a spectrometer with high sampling density and therefore long axial range.

Bandwidth: Figure 4.3 reports the axial resolution of an OCT system as a function of the bandwidth $\Delta\lambda_{FWHM}$ and the central wavelength of the light source. At a given axial resolution, bandwidth requirements increase considerably for longer wavelengths. In order to achieve an axial resolution lower than 10μm at 830nm a bandwidth (FWHM) higher than approximately 30nm needs to be selected.

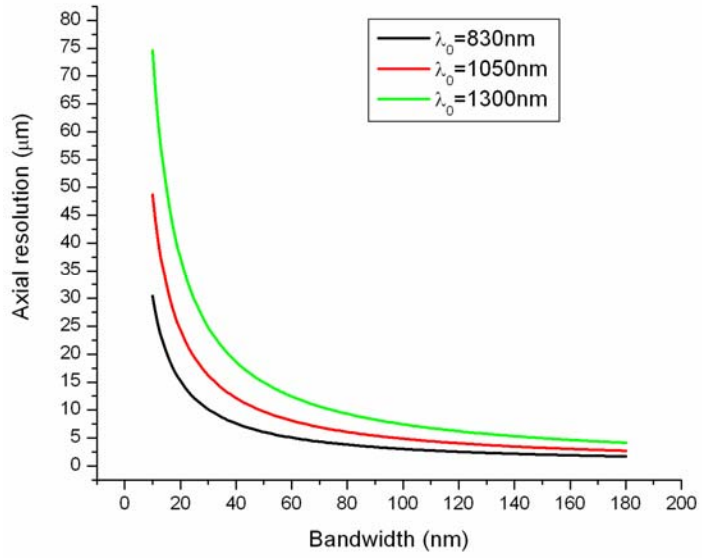

Figure 4.3: Axial resolution vs. bandwidth as a function of central wavelength of the light source.

Power: The power of the light on the sample is a constant parameter that is calculated to ensure that the light intensity delivered to the eye is safe for the anterior segment and retina according to the American National Standards Institute, Safe Use of Lasers (ANSI, 1993). According to this standard, the maximum power at 840nm that can be safely delivered to the anterior segment is 0.75mW.

SLD selection: A superluminescent diode with a center wavelength of 840 nm and a FWHM (full width at half maximum) bandwidth of 50nm (SLD-371-HP2, Superlumdiodes Ltd, Moscow, Russia) was selected as low coherence light source, which produces a theoretical axial resolution of about 6.2 μm. The SLD is coupled with a single mode fiber. The spectral distribution of the light source was measured, and is plotted in Figure 4.4A.

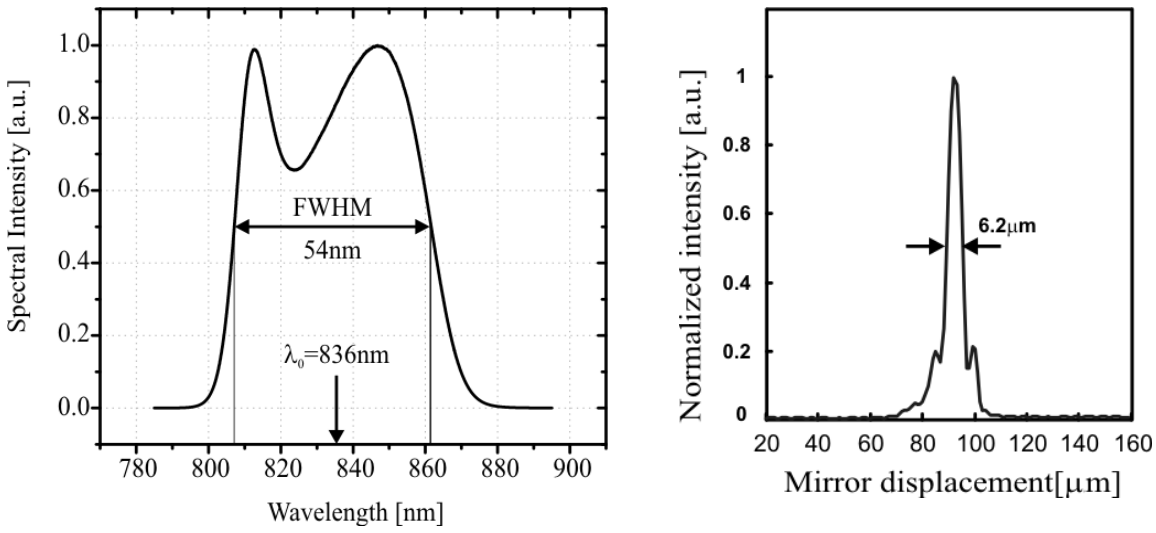

(A) **(B)**

Figure 4.4: Spectral distribution of the light source SLD 371 HP centered at 836nm and with 54nm FWHM **(A)**. Theoretical axial resolution of the light source at 90 μm **(B)**. The central wavelength and FWHM are 836nm and 54nm, respectively.

The optical power delivered through the fiber is 15mW. The mode field diameter of the fiber is 5µm. Figure 4.4B shows the theoretical point spread function generated using the measured spectral data of the light source for a mirror located at 90µm from the zero delay position.

4.3. Interferometer

Michelson interferometers used in OCT systems are typically realized by using 2×2 fiber couplers, which are the optical fiber versions of free space beam splitters. Fiber couplers offer several advantages compared to their free space version. Cable based connections offer more flexibility in terms of positioning of the system components and during imaging operations where the transversal scanner needs to be correctly aligned with the subject's eye. The great advantage of fiber couplers is that each arm becomes independent from the others. With a beam splitter, instead, the four arms need to be co-aligned.

The interferometer chosen consists of a 2×2 20/80 fiber coupler (FC850-40-20-APC, Thorlabs Inc, USA). The unbalanced splitting ratio (20/80) was chosen to optimize the coupling efficiency of the detection arm, as it will be briefly explained. The coupler uses a single mode fiber with a mode-field diameter of $5\,\mu m$ at 850nm and broad bandwidth (from 780nm to 970nm). Figure 4.5 shows the optical fiber based connections. The SLD light source is connected to a fiber coupled optical isolator (IO-F-830APC, OFR,USA) that prevents unwanted feedback into the light source and a fiber coupled optical variable attenuator (BB-500-11-830-5/125-S-40-3A3A-3-1, OZ Optics, Canada) that is used to adjust the power of light delivered to the interferometer.

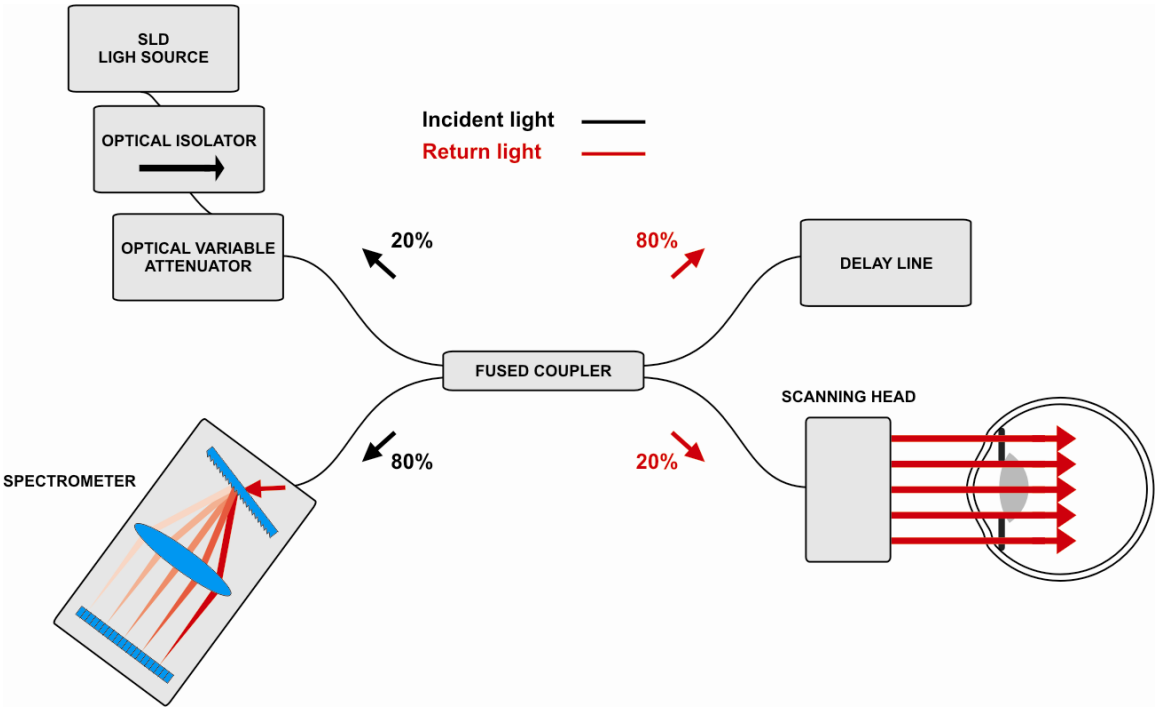

Figure 4.5: Optical fiber based interferometer and connections. The fraction of the incident light that is delivered to the delay line and sample is reported in red. The fraction of light that is returned to the spectrometer and the light source is reported in black.

The input of the fiber coupler is connected to the output of the optical attenuator. The fiber coupler transmits 20% of the SLD light into the sample arm and 80% into the reference arm. The light back reflected by the reference and sample arms is combined into the fiber coupler and 80% is directed to the spectrometer through the detection fiber end while the other 20% is directed to the source fiber end and blocked by the optical isolator.

4.4. Spectrometer

4.4.1. Axial Range requirements for human lens imaging

Originally, the project was aimed to image only the human crystalline lens instead of the entire anterior segment and therefore the spectrometer of the imaging system was

designed based on the maximum axial thickness that a human crystalline lens can reach. To estimate the axial range needed to image the crystalline lens at all ages with SD-OCT, published measurements of the optical thickness of isolated human crystalline lenses using TD-OCT (Uhlhorn et al, 2008) were used. In that study, OCT images of the isolated (i.e., fully accommodated) lens from donors of ages ranging from 6 to 82 years were acquired. A method was developed to measure their optical and geometrical thickness from the OCT images. The results are shown in Figure 4.6 together with eight additional previously unpublished data points obtained using the same method on isolated lenses ranging from 31 to 90 years of age. The approximate geometrical thickness of the new lenses was calculated assuming an equivalent group refractive index for all the lenses equal to 1.40 at the wavelength used to perform the measurements (825nm).

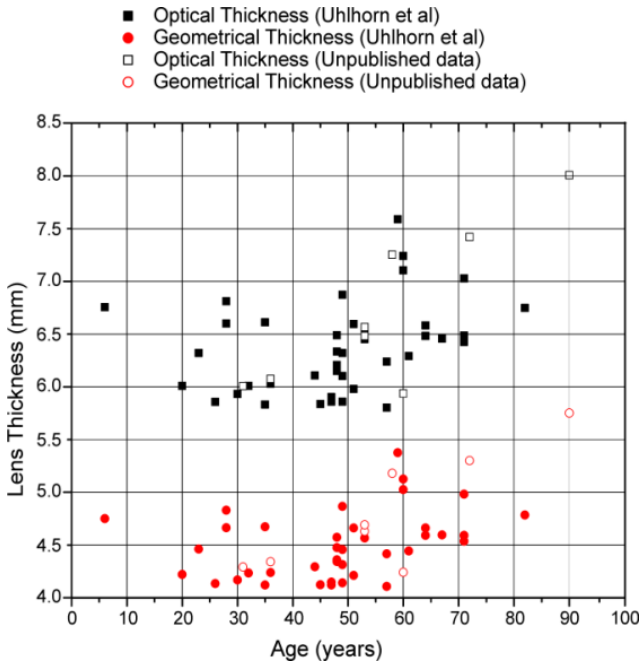

Figure 4.6: Human crystalline lens thickness vs. age. Geometrical thickness (red dots) and optical thickness (black squares) were calculated based on the results obtained on isolated lenses in a previous publication (filled dots and squares) (Uhlhorn et al, 2008) and from additional unpublished data obtained in our laboratory using the same setup and methods (empty dots and squares).

The maximum values were 8.01mm for the optical thickness and 5.75mm for the geometrical thickness. These parameters can be used to estimate that the axial range needed to image the whole *in vivo* crystalline lens over the entire human lifespan, is roughly 8mm ±2mm for tolerance in positioning.

4.4.2. General spectrometer configuration

The configuration of the spectrometer is the standard Czerny-Turner spectrometer design used in SD-OCT (Wojtkowski et al, 2002). Figure 4.7 shows a schematic of the spectrometer design. Light from the detection arm of the fiber interferometer in Figure 4.7 is collimated and directed to a transmission grating at an angle of incidence θ. Light is then dispersed by the grating into separate spectral components according to the grating equation (Loewen and Popov, 1997)

$$\mathrm{m}\lambda = d\sin\theta + d\sin\gamma \qquad 4.1$$

where d is the grating period, m the diffraction order and γ is the angle of diffraction at wavelength λ. The grating efficiency is the fraction of the incident radiation that is diffracted into a specific order (Schnopper et al, 1977). The efficiency of the grating depends upon many parameters, such as the power and polarization of the incident light, the angles of incidence and diffraction and the groove period. High efficiency is desirable to measure weak intensity transitions occurring in the spectral distribution of the diffracted light.

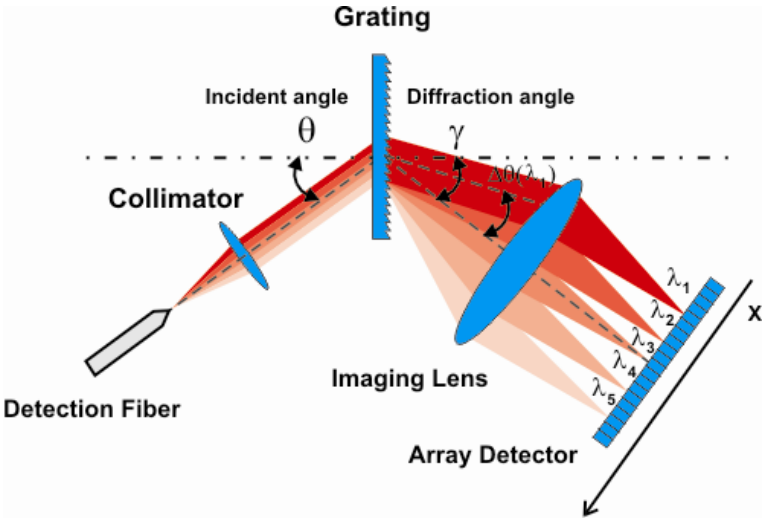

Figure 4.7: Spectrometer schematic. The spectrometer includes a detection fiber, a collimator, a transmission grating, an imaging lens and an array detector.

The most widely used rule of thumb to maximize the efficiency of a grating is orienting the grating in a special configuration named the Littrow condition (Loewen and Popov, 1997). In the Littrow configuration the light at given wavelength λ_L is diffracted at the same angle as the incident angle θ_L. The grating equation at the Littrow condition becomes

$$m\lambda_L = 2d \sin\theta_L \qquad 4.2$$

In a spectrometer for SD-OCT, to optimize the grating efficiency, the angle θ_L has to be selected so the wavelength λ_L is near to the central wavelength of the light source.

The imaging lens collects the dispersed spectral components and focuses them into the pixels of the linear detector. In the Littrow configuration the position of a specific spectral component λ onto the detector array is equal to

$$x(\lambda) = f \tan[\theta_L + \Delta\theta(\lambda)] \qquad 4.3$$

where f is the focal length, $\theta_L + \Delta\theta(\lambda)$ is the diffraction angle of the spectral component λ, dispersed according to equation 4.1. For the central wavelength $\lambda_0 = \lambda_L$ the angle $\Delta\theta(\lambda_0) = 0$.

If we consider an array sensor with horizontal pixel size Δx and number of pixel N, according to equation 4.2 and 4.3 the focal length necessary to disperse a spectrum ranging from λ_{min} to λ_{max} over the sensor is given by

$$f = \frac{\Delta x N}{|\tan(\theta_{max}) - \tan(\theta_{min})|} \qquad 4.4$$

where θ_{min} and θ_{max} are the dispersed angle for the minimum and maximum detected wavelengths λ_{min} and λ_{max}, respectively. Equations 4.1 and 4.2 yield

$$\Delta\theta_{min} = arc\sin\left[\frac{m}{d}\left(\lambda_{min} - \frac{\lambda_L}{2}\right)\right] - \theta_L, \qquad 4.5$$

$$\Delta\theta_{max} = arc\sin\left[\frac{m}{d}\left(\lambda_{max} - \frac{\lambda_L}{2}\right)\right] - \theta_L \qquad 4.6$$

The angle variation $\Delta\theta_{max} - \Delta\theta_{min}$ for a specific spectrum range increases with the order m of the grating. The higher the order, the broader the dispersion, but gratings designed for the first order ($m=1$) have the maximum efficiency. To simplify the spectrometer design and maximize the efficiency, the first order was used.

4.4.3. Selection of pixel number and array detector

According to equation 3.33 to achieve source limited axial resolution of ~10µm at $\lambda_0 = 836\text{nm}$ the array detector has to detect a spectral range $\Delta\Lambda = \lambda_{max} - \lambda_{min} \simeq 70\text{nm}$. The maximum axial range depends on the number of pixels of the array detector N (equation 3.31)

$$z_{\text{MAX}} = \frac{1}{2}\frac{\lambda_0^2}{\Delta\Lambda}\frac{\text{N}}{2} \qquad 4.7$$

Typical arrays of photodetectors (CCD and CMOS) have standard number of pixels N=512, 1024, 2048, 4096 and 8192. The maximum depth and average sampling density for $\lambda_0 = 836\text{nm}$ and $\Delta\Lambda \simeq 70\text{nm}$ in function of the standard number of pixels is reported in Table 4.2. Table 4.2 shows that to image the entire human crystalline lens, which is maximum 8mm in thickness, an array detector with N=4096 or 8196 is needed. At the time we started the project, the only available array detector with such a high number of pixel and featuring high speed was a CMOS camera (Basler Sprint spL4096-104k; Basler AG, Germany) with N=4096 pixels, a line rate up to 140,000 KHz and 10 micron pixel size. Later on, the same manufacturer started producing a newer detector (Basler Sprint spL8196-70k; Basler AG, Germany) with N=8196 pixels, 10 micron pixel size and featuring half of the line rate (70,000 KHz) than the previous version with N=4196 pixels.

N (pixels)	$\delta\lambda\ (\frac{\text{nm}}{\text{pixels}})$	z_{MAX} (mm)
512	0.0137	1.28
1024	0.068	2.55
2048	0.029	5.11
4096	0.017	10.22
8192	0.009	20.45

Table 4.2: Maximum depth and average sampling density for $\lambda_0 = 836\text{nm}$ and $\Delta\Lambda \simeq 70\text{nm}$ in function of the standard number of pixels of typical array detectors.

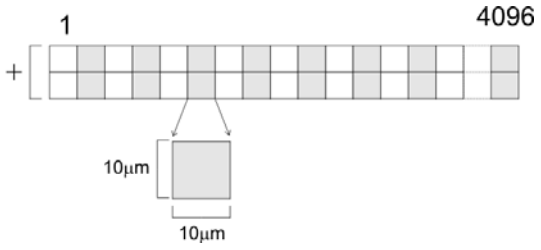

Figure 4.8: Geometry of the array detector operating in summing mode.

This detector has a large sensor width of 8196 ×10 µm = 8.196cm. Such a large sensor needs a focusing optics with comparable width, which would require a custom made design and therefore would complicate significantly the spectrometer design. The array detector selected for the spectrometer was the Basler Sprint CMOS camera with N=4196 pixels. This detector has been used in recent experimental SD-OCT systems for extended depth anterior segment imaging (Grulkowski et al, 2009) and for high speed retinal imaging (Potsaid et al, 2010). The sensor has two adjacent sensor lines of 4096 pixels each, with 10 micron pixel size. The camera can operate in summing mode between two detector lines. In summing mode, two vertical pixels that are located at the same horizontal position are binned together so that the equivalent pixel size is 10 μm × 20 μm (horizontal × vertical) (Figure 4.8). Although this operating mode halves the line rate frequency from 140,000 Khz to 70,000 Khz, the pixel size is enlarged in the vertical position, which allows to capture more light, thus increasing the coupling efficiency and therefore the system sensitivity. Figure 4.9 shows the quantum efficiency of the camera in function of the wavelength. The spectral response covers a wide range of wavelengths that includes the bandwidth of the light source selected for the design.

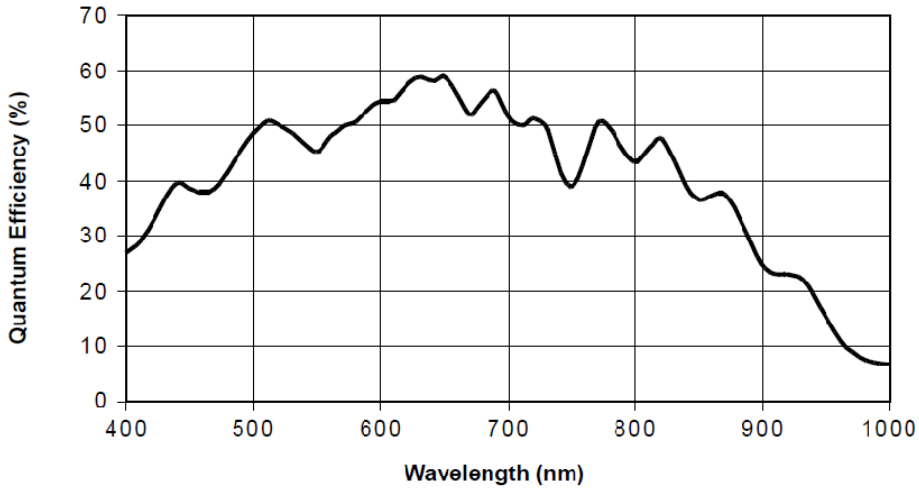

Figure 4.9: Spectral response of the Basler Sprint spL4096-104k camera. The image was captured from the manufacturer website: www.baslerweb.com.

4.4.4. Selection of the grating and focal length of collimator and objective

In the first order (m = 1) grating configuration the focal length necessary to image a spectral range of $\Delta\Lambda \simeq 70\text{nm}$ can be calculated using equations 4.2 and 4.4. Typical commercially-available transmissive gratings in the region around 800nm have groove frequencies of 800, 1200, 1500 and 1800 lines/mm. Table 4.3. reports the typical focal lengths needed to disperse a spectral range of $\Delta\Lambda \simeq 70\text{nm}$ over the Basler CMOS camera in function of the groove frequency of the grating.

g $(\frac{\text{lines}}{\text{mm}})$	f(mm)
800	689
1200	412
1500	303
1800	212

Table 4.3: Typical focal length values needed to disperse a spectral range of $\Delta\Lambda \simeq 70\text{nm}$ over the Basler CMOS camera in function of the groove frequency of the grating at $\lambda_0 = 836\text{nm}$ and with a first order (m=1) grating configuration.

Table 4.3 shows that several pairs of grating and focusing lens are usable. However, to produce high efficiency and reduce the effect of the sensitivity fall-off, the focal length needs to be selected also trying to minimize the spot size at the beam waist

$$2w = 2f\frac{\lambda_0}{\pi w_o} \qquad 4.9$$

where w and w_o are the beam waist radii ($1/e^2$) of the focused spot and the collimated beam. Figure 4.10 reports the diameter of the focused spot in function of the diameter of the collimated beam and the focal length reported in table 4.3.

To produce a spot diameter that fits the pixel size of the camera (10µm) with a long focal length (>300mm) requires a very large beam diameter (>16mm). The pair composed by the 1800 lines/mm grating and the 212mm focal length is preferable to produce high coupling efficiency and maintain a compact design.

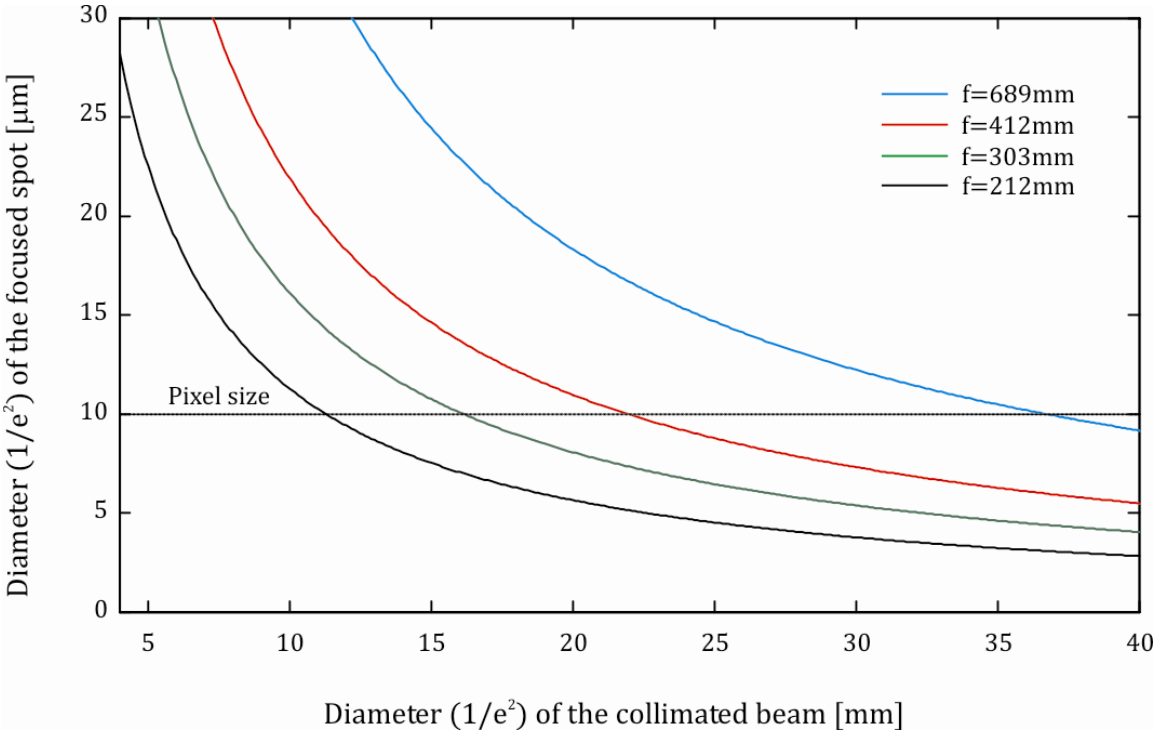

Figure 4.10: Diameter of the focused spot in function of the diameter of the collimated beam and four values of the focal length of the imaging lens. The pixel size of the Basler CMOS camera is marked in the graph.

From Figure 4.10, a collimated beam diameter ($1/e^2$) of approximately 12mm is needed to achieve a diffraction limited spot smaller than the pixel size. Commercial off the shelf components were selected with parameters near to the tradeoffs evaluated.

Focusing lens: In attempt to decrease the monochromatic aberrations a multi-element focusing lens (Axinon, Rolyn Optics, CA) was selected to image the dispersed spectrum onto the camera. The lens has a focal length f=210mm and a clear aperture of 45mm.

Grating: A volume phase holographic high density (1800 line/mm) transmission grating (HD1800, Wasatch Photonics, USA) was selected to disperse the spectral components. The grating has round shape with 50mm aperture. Figure 4.11 reports the response of the grating for the spectral range of interest. The grating has a relatively high average efficiency, which is important to optimize the overall efficiency and obtain high quality images.

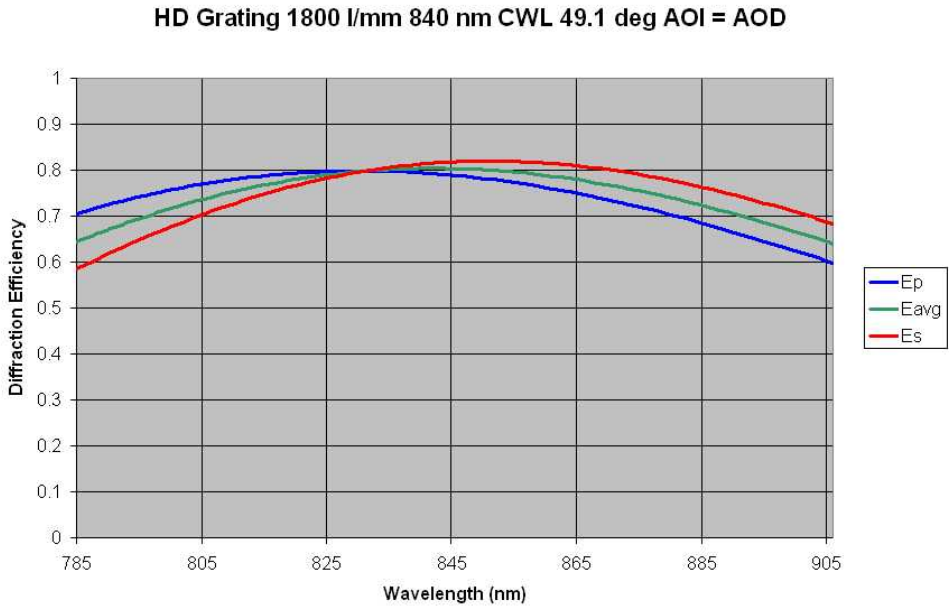

Figure 4.11: Spectral response of the HD1800 grating. The average efficiency in the range of interest spans from 60-80%. The efficiency for both p and s polarization is relatively flat over the wavelength range of interest. Plot obtained through personal communication with Wasatch, Inc.

The relatively flat response for both *p* and *s* polarization states allows the spectrometer to be less sensitive to polarization changes between the reference and the sample arms. A polarization mismatch between the arms can be induced, for instance, by a relocation or movement of one of the fiber arms during imaging.

Collimator: A fiber coupled collimating lens with focal length $f = 60mm$ (HPUCO-23AF-830-S-60AC, OZ Optics, Canada) was selected to both minimize the spot size at the camera plane and contain the diverging dispersed light into the aperture of the focusing lens. The detection fiber is directly connected to the collimating lens. The single mode fiber used in the fiber coupler (780-HP, Thorlabs, USA) has mode field diameter ($1/e^2$) (mfd) of 5μm at 850nm. With these parameters and according to equation 4.9, the collimator produces a Gaussian beam with diameter ($1/e^2$)

$$\mathrm{D} = 4\mathrm{f}\frac{\lambda_0}{\pi\ \mathrm{mfd}} = 4\ 60\mathrm{mm}\frac{836\mathrm{nm}}{\pi\ 5\mu\mathrm{m}} = 12.8\mathrm{mm} \qquad 4.10$$

The diameter of the collimated beam needs to be smaller than the aperture of the grating to avoid vignetting, and the aperture of the focusing lens needs to be wide enough so that the diffracted collimated beam is not vignetted. A software for optical system design (Zemax, Radiant Zemax LLC, USA) was used as a simulation tool to configure the spectrometer correctly and make sure that the dispersed beam fits into the multi-element lens aperture. With the selected collimator and multi-element lens, the diameter ($1/e^2$) of the focused spot at the beam waist is approximately $17.5\mu m$ ($\lambda_0 = 836mm$) and the dispersed beam completely fits the aperture of the imaging lens with no vignetting. The simulated diffraction limited beam diameter is 1.75 times larger than the pixel size.

4.4.5. Sensitivity fall-off

Sensitivity fall-off model

An important design parameter that affects the depth range of a SD-OCT system is the sensitivity fall-off. This parameter can reduce dramatically the effective depth range and needs to be carefully evaluated to optimize the spectrometer design when long depth range is needed. The main three causes of the sensitivity fall-off have been introduced in section 3.5.3. In reality, the spectral distribution in a spectrometer is also non-linearly distributed in λ, as shown by equation 4.3. Several models have been presented that do not take into account the non-linearity in k and λ (Leigeb et al, 2003; Yun et al, 2003). However, an accurate representation of the fall-off requires a comprehensive model. Hu et al (2007) reported a complete analytical model of signal formation in a spectrometer based interferometric system that includes the three mains causes of sensitivity roll-off and also the non-linearity in λ that is produced by the grating equation. The Hu et al model has been previously used to design spectrometer based OCT systems (Chan, 2010). Figure 4.12 shows the signal formation according to the Hu et al model. Assuming that the spectral distribution $s(k)$ is the same for the light returning from the two arms, the general expression of the signal intensity for the j^{th} pixel at the x_j coordinate is

$$I(x_j) = \frac{1}{4} Erf\left(\frac{\Delta y\sqrt{ln2}}{w}\right) \int_0^{\infty} \left[Erf\left(\frac{\Delta x - 2x(k) + 2x_j\sqrt{ln2}}{w}\right) + Erf\left(\frac{\Delta x + 2x(k) - 2x_j\sqrt{ln2}}{w}\right)\right] [2s(k)(1 + \cos 2\, kz_{MAX})]dk \quad 4.8$$

where $Erf(x) = \frac{2}{\sqrt{\pi}} \int_0^x e^{-t^2} dt$ is the error function, Δx and Δy are, respectively, the width and height of the individual pixel and w is the FWHM of the spot diameter of the focused beam. $x(k)$ is the non linear coordinate function along the direction of the array (horizontal) in function of the wavenumber. The detector is shown as illuminated by the point spread function of individual wavelengths in Figure 4.12. If the PSF of an individual wavelength crosses over more than one pixel, spectral cross-talk occurs. Thus, the intensity detected by the j^{th} pixel along x (Figure 4.12) contains contributions from several wavelengths. The integral in equation 4.8 accounts for this effect. The first error function in equation 4.8 accounts for the sensitivity loss generated if the finite size of the focused spot crosses over the pixel boundary along the y direction in Figure 4.12.

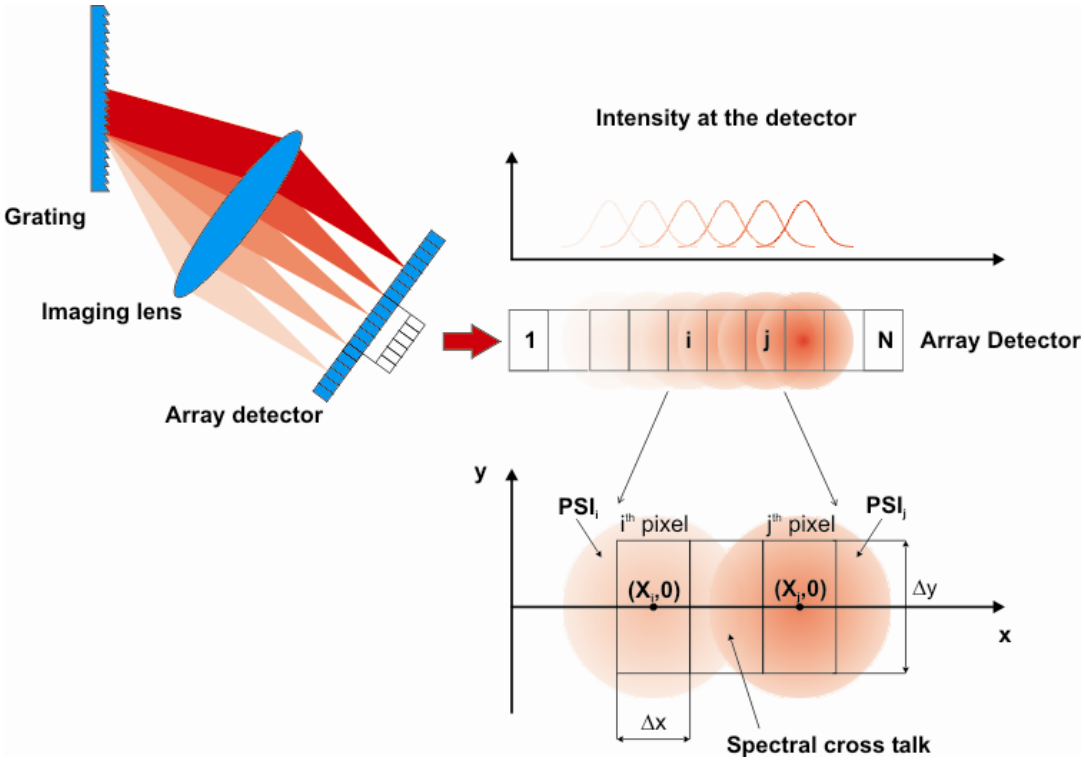

Figure 4.12: Schematic of the signal formation according to Hu et al. The intensity recorded by the j[th] pixel is the combination of all of the single wavelength PSFs, if the PSFs have finite size. The finite size of the pixel is $\Delta x \times \Delta y$ (horizontal × vertical).

In a real spectrometer, the expression of $x(k)$ can be calculated with the grating equation (equation 4.3) for the first order $m = 1$ as (Hu et al, 2007)

$$x(k) = f \tan\left[arcsin\left(\frac{2\pi g}{k} - \frac{\pi g}{k_0}\right) - arcsin\left(\frac{2\pi g}{k_{x=0}} - \frac{\pi g}{k_0}\right)\right] \qquad 4.9$$

where f is the focal length of the imaging lens used to image the light onto the array, $g = 1/d$ is the frequency of the grating, k_0 is the wavenumber at the center of the spectrum and $k_{x=0}$ is the wavenumber at the center of the first pixel of the array at the origin of the coordinate x. This expression can be substituted in the general formula in equation 4.8 so that $I(x_j)$ represents the partial signal recorded by the j^{th} pixel for a spectrum dispersed according to the distribution in equation 4.7. Numerical simulation of the interference fringes and the signal in the axial domain can be obtained for analysis of our current spectrometer by evaluating $\sum_j^N I(x_j)$ and its Fourier transform, respectively.

Simulation

The model was simulated using a numerical computing environment (Matlab, Mathworks, USA) to estimate the sensitivity roll-off with the design reported in the previous section. The parameters of the simulation are based on the off the shelf components that were selected in the previous section and are reported in table 4.4. The spectral distribution of light *s(k)* was chosen Gaussian for simplicity. The spot diameter of the focused beam 2*w* depends on the wavelength. Thus, the spot size along the camera sensor is not constant. In addition, off-axis optical aberration contributes to increase the spot size beyond the diffraction limit, and results in a bigger focused spot size near to the edges of the array sensor due to coma aberration. The simulation was run for a range of spot diameters where 2*w* is the "effective" spot size and is expressed in terms of the ratio

$2w/\Delta x$. Figure 4.13 shows the simulated sensitivity decrease vs. depth for six values of the ratio between the FWHM diameter of the effective focused spot $2w_{FWHM}$ and the size of the pixel Δx. For each ratio the roll-off was calculated for a spectral distribution that is linear and non linear in wavenumber. The analysis shows that for larger spot sizes the sensitivity decays more rapidly than for smaller spot sizes, as expected (Hu et al 2007, Chan 2010). Aside from the focused spot size, if the spectral distribution is not linear in k the sensitivity experiences a more rapid decay compared to the case of linear distribution. However, the effect of non linearity decreases for larger spot sizes because the spectral crosstalk dominates the sensitivity decay. The diffraction limited spot size of the dispersed light focused onto the camera is shown in Figure 4.14.

Parameter	Value
Focal length	210mm
Number of pixels (N)	4096
Pixel size	$10\ \mu m \times 20\ \mu m^{*}$
Δx	$10\ \mu m$
Δy	$20\ \mu m$
Grating frequency (g)	1800 lines/mm
Depth range	10.22mm
λ_0	836nm
$\Delta\lambda_{FHWM}$	50nm
$\Delta\Lambda$	70nm
$k_0 (=2\pi/\lambda_0)$	7.5158×10^{6} m^{-1}
$\lambda_{min} (=\lambda_0-\Delta\Lambda/2)$	801nm
$\lambda_{max} (=\lambda_0-\Delta\Lambda/2)$	871nm
$k_{x=0} (=2\pi/\lambda_{max})$	7.2138×10^{6} m^{-1}

Table 4.4: Design parameters of the SD-OCT spectrometer. *The camera can operate in summing mode between two lines so that the equivalent pixel height is twice the height of the individual pixels.

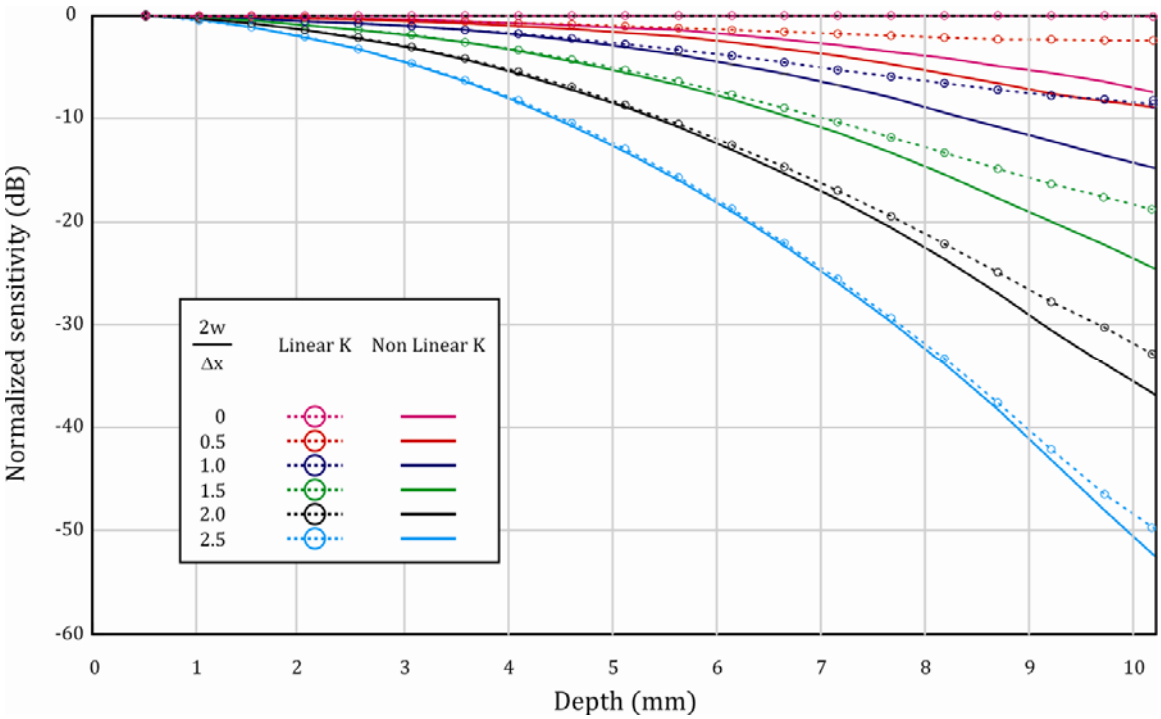

Figure 4.13: Normalized sensitivity decrease vs. depth in function of the ratio between the diameter of the effective focused spot $2w$ and the size of the pixel Δx. The legend shows six values of the ratio, from infinitesimal spot size to 2.5. The roll-off trend is reported for both linear and non linear spectral distributions function of the wavenumber *x(k)*.

The results were obtained using equation 4.7 and the following parameters: focal length $f = 210mm$, collimated beam diameter (1/e^2) $2w_0 = 12mm$ and wavelength range $\Delta\Lambda = 70\text{nm}$. The diameter (1/e^2) of the diffracted limited spot on the camera plane spans from 17.5µm to 19.5µm. In the model proposed by Hu et al, the spot size is calculated at the FWHM of the maximum intensity. To estimate the current configuration, the spot size in Figure 4.14 (blue line) was converted to the FWHM diameter using the conversion $w_{FWHM} = 0.85\, w_{1/e^2}$. The diameter (FWHM) spans from 14.9µm to 16.6µm and is reported in Figure 4.14 (red line). The spot size to pixel size ratio $\frac{2w_{FWHM}}{\Delta x}$ is calculated assuming $\Delta x = 10\mu m$ and an effective spot diameter $2w_{FWHM} = 15.7\ \mu m$, which is the average value of the spot size plotted in Figure 4.14.

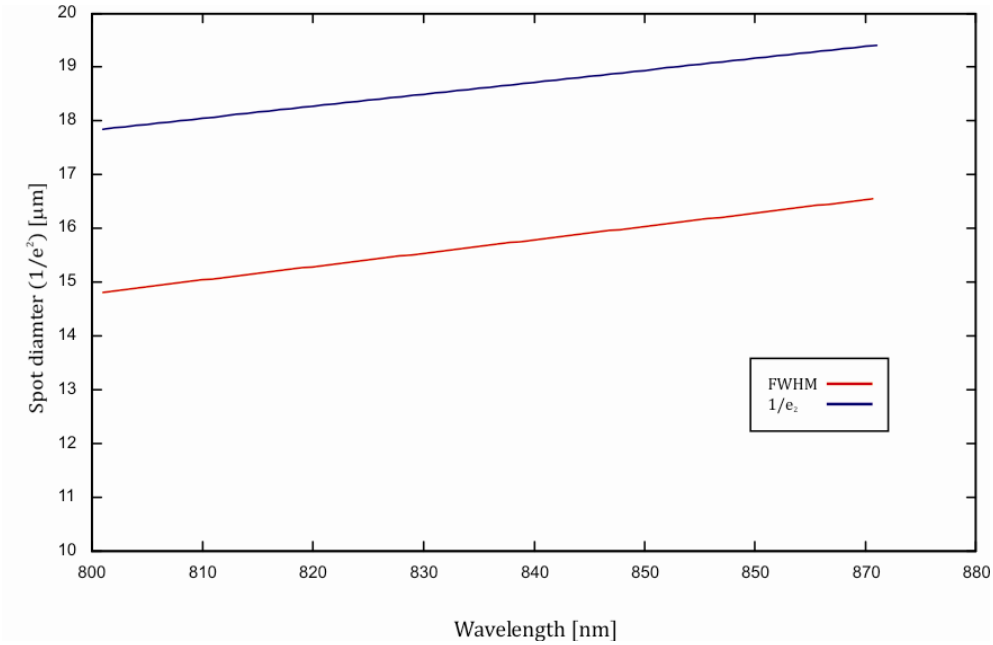

Figure 4.14: Diffraction limited spot diameter ($1/e^2$) for a focal length of 210mm, an incident beam diameter ($1/e^2$) of 12mm over a bandwidth of 70nm centered at 836nm (blue line). The spot diameter is also reported at the FWHM of its intensity(red line).

With these assumptions $\frac{2w_{FWHM}}{\Delta x} = 1.57$, which yields a sensitivity fall-off decay that is located in the area between the solid green and the solid black curve in Figure 4.13 and reaches a minimum of -24.9 dB at the end of the axial range.

In practice, the spot size will be larger than the diffraction limited one because of chromatic and monochromatic aberrations (spherical, coma, field curvature). The overall effect of the aberrations is an increase of the spot size especially at the edges of the lens. The roll-off evaluation was performed without taking into account the effect of optical aberrations. A more accurate analysis that considers these effects to the effective spot size needs to be performed if an accurate estimation of the sensitivity decay is needed. However, the roll-off estimation in the diffraction limited regime is useful to determine the general design specifications and to have rapid vision of the spectrometer

performance. We showed that with the selected components we expect a sensitivity fall-off inferior than -24.9 dB.

4.4.6. Spectrometer alignment

In order to achieve high efficiency and maximize the sensitivity a correct alignment of the spectrometer is key. Sensitivity roll-off is also strongly affected by the spot size that is focused on the array detector and therefore correct positioning is critical to achieve extended axial range. Alignment of the spectrometer is an iterative procedure that involves fine positioning of the multiple components to optimize the efficiency of the spectrometer and minimize aberrations. The feedback of alignment is given by readings of the acquired spectrum by the camera. A correct alignment is empirically obtained when the amplitude of the spectrum recorded with the sensor is maximized and when the shape of the spectrum resembles the original spectrum of the light source. The following strategy is one procedure that we adopted for aligning the spectrometer. The strategy assumes that only a limited number of parameters, such as distances between components and angles, are adjusted to perform fine alignment.

Figure 4.15 A, B and C report a summary of the key positioning parameters that are involved in the selected alignment procedure.

Figure 4.15 D shows the reference system that is used in Figure 4.15 A, B and C, which is based on the geometry of the array detector (D). In Figure 4.15D, D is the array detector and O is the center of its surface. The X axis is coincident with the array sensor plane, crosses its center O and it is parallel to its longest side. Y is perpendicular to detector plane and crosses the center O. The Z axis is perpendicular to the XY plane and crosses the center O.

Figure 4.15C reports the XY plane of the spectrometer. CL represents the collimator assembly and G the grating. According to the efficiency characteristic of the grating in Figure 4.11 and the Littrow condition (equation 4.2), to maximize the dispersion efficiency the optical axis of the collimated beam has to be angled at θ_L = 48.8º (at 836nm) with respect to the grating plane. The grating (G) plane is perpendicular to the XY plane and it is centered at O_G. In the Littrow condition, the angle between Y and the grating plane, θ_L' , is equal to θ_L. The focusing lens has the optical axis coincident with X. A requirement to reduce monochromatic aberrations is the telecentricity of the optical system composed by the grating and the lens. In case of telecentricity, all the chief rays corresponding to the dispersed wavelengths (Figure 4.15C) are perpendicular to the focal plane of the lens. Telecentricity is obtained when the lens is at a focal distance (f) from the origin of the diverging chief rays of the dispersed light. The position Y_L of the lens along the Y axis is set so that telecentricity is obtained by finely tuning the distance between the lens and O_G. The position of the detector Y_D along the Y axis is set to align the sensor plane with the focal surface. In reality, the focal surface for large apertures optics has a field that is usually curved. Field curvature produces defocus of the spot onto the array for certain wavelengths and makes the alignment of the sensor plane with the focal surface more complex. The focal surface of the focusing lens in the XY plane may also have a tilt with respect to the Y axis. This effect is caused by chromatic aberrations, which are due to the optical dispersion of the lens material. To compensate for tilts of the focal surface the sensor is tilted with roll angle θ_R.

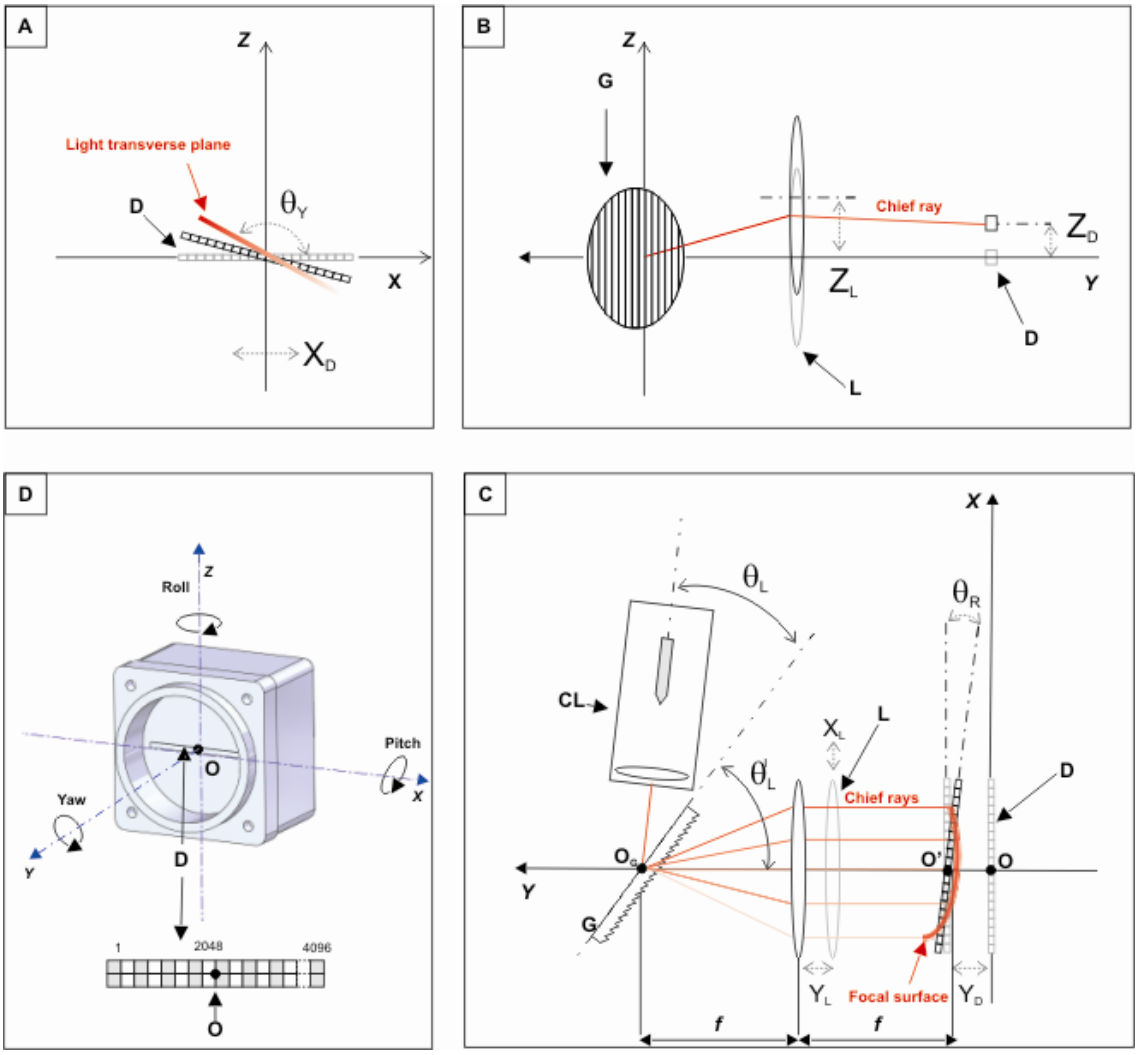

Figure 4.15: Alignment of the spectrometer in the XZ plane (A), in the YZ plane (B) and in the XY plane (C). The reference system, which is based on the geometry of the array detector, is reported (D).

In the YZ plane (Figure 4.15B) the lens height Z_L can be adjusted along the Z axis. This adjustment is needed to ensure that the dispersed light is focused at the center of the sensor array along Z. The position X_L of the lens along X is also adjusted in the XY plane (Figure 4.15C) to center the focused dispersed light onto the lens aperture.

In the XZ plane (Figure 4.15A), the array sensor can yaw by an angle θ'_Y to compensate for yaw misalignments of the transversal plane of the dispersed light.

Component	Adjustable Parameters	Number of Adjustable Parameters
Collimator - Grating	θ'_L	1
Imaging lens	X_L, Y_L, Z_L	3
Detector	X_D, Y_D, θ_R, θ_Y	4
		Total = 8

Table 4.5: Summary of the geometrical parameters that are adjustable in the bench prototype of the spectrometer.

A translation X_D of the sensor along X allows us to move the detector elements to center the array with the central wavelength of the light source. Table 4.5 summarizes the geometrical parameters that are adjustable for each component or assembly in the bench prototype of the spectrometer.

4.4.7. Optomechanical design

In order to configure and align the spectrometer based on the alignment technique proposed in the previous section, the optical components were mounted on custom supports and commercial precision positioning stages that allow adjustment of the eight parameters reported on Table 4.5. The collimator and the grating were mounted at a rigid angle θ_L on an assembly. The design of the mechanics was performed with a three dimensional mechanical CAD software (Solidworks, Dassault Systèmes SolidWorks Corp., USA) and it is shown in Figure 4.16A with the adjustable parameters. Figure 4.16B shows a picture of the spectrometer.

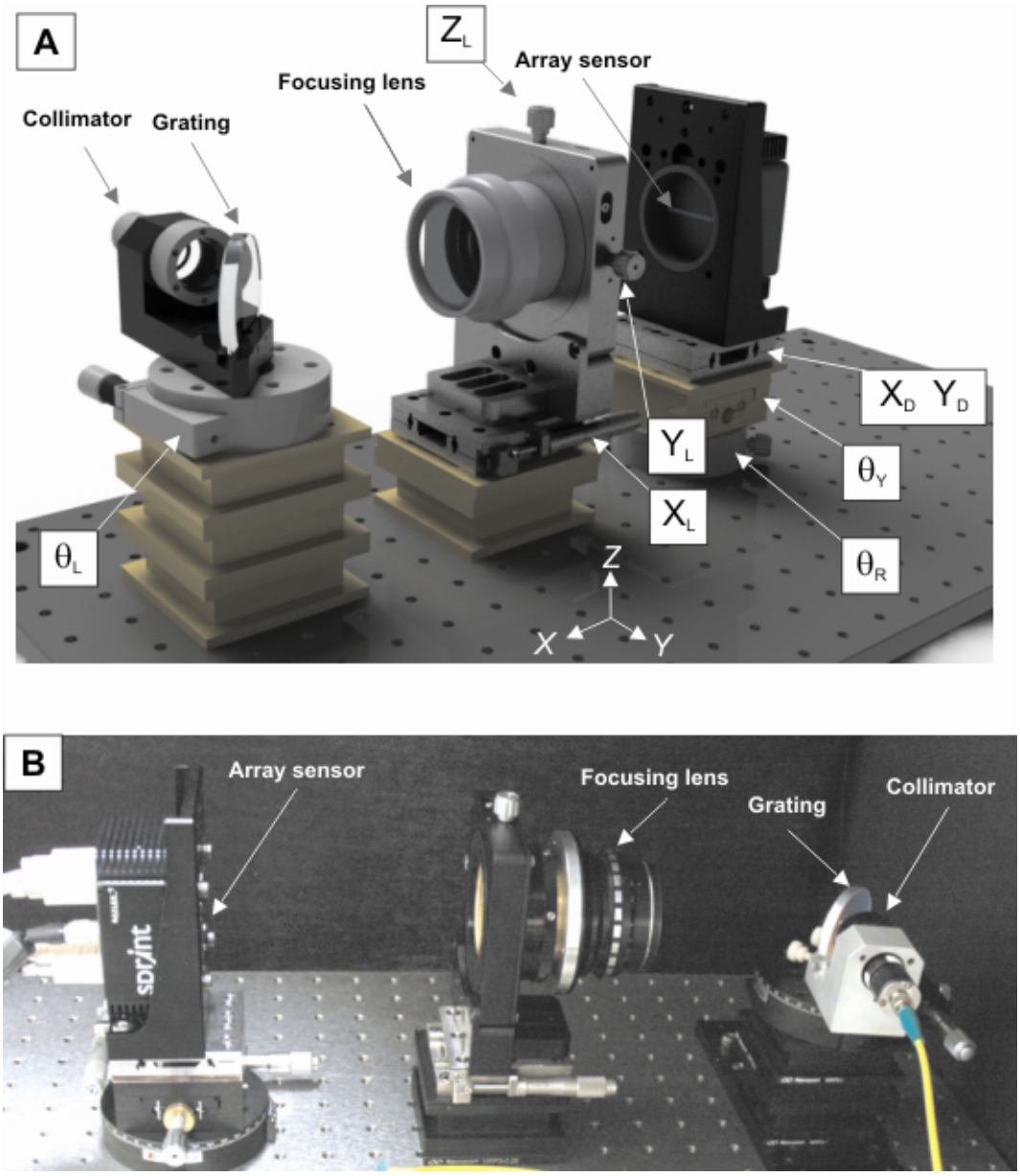

Figure 4.16: (A) Design of the spectrometer with the associated optical components: collimator, grating, lens and array sensor. Three rotation stages adjust for the parameters: $\theta_L, \theta_R, \theta_Y$ while five translation stages adjust for the parameters: X_L, Y_L, Z_L, X_D, Y_D. (B) Photograph of the spectrometer setup.

4.4.8. Spectrometer calibration

The distribution of wavelengths over the array is non-linear, and so a precise calibration must be performed to accurately map the pixel number to its corresponding

wavelength (Gaigalas et al, 2009; Dorrer et al, 2000). An imprecise spectrometer calibration will lead to errors when converting the spectral data to the depth-dependent reflectivity profiles that are used to construct a cross-sectional image, resulting in poor image quality (Dorrer et al, 2000). The non-linear distribution is approximated with a fourth-order polynomial, which maps the wavelength λ to the pixel location x across the array

$$\lambda = a_0 + a_1x^1 + a_2x^2 + a_3x^3 + a_4x^4 \qquad 4.11$$

where a_0, a_1, a_2, a_3, a_4 are the polynomial coefficients. Calibration of the spectrometer was performed with a gas discharge spectral calibration Neon lamp (6032, Newport, NJ). The neon lamp emits multiple spectral lines at known wavelengths over the spectral range of the spectrometer. A multimode optical fiber cable (50 µm core) delivered the light from the Neon lamp to the spectrometer. One end is coupled to the lamp and the other is coupled to the spectrometer. The spectral lines are dispersed onto the line scan camera. The camera was connected through a standard camera link interface and a high speed frame grabber (NI PCIe-1429, National Instruments, USA) in a workstation. A custom acquisition tool developed in a commercial graphical development environment (Labview, National Instruments, USA) enabled acquisition of the Neon lamp spectrum dispersed onto the line scan camera as a function of the pixel number. Fifteen spectral lines of known wavelength were selected in the recorded spectrum.

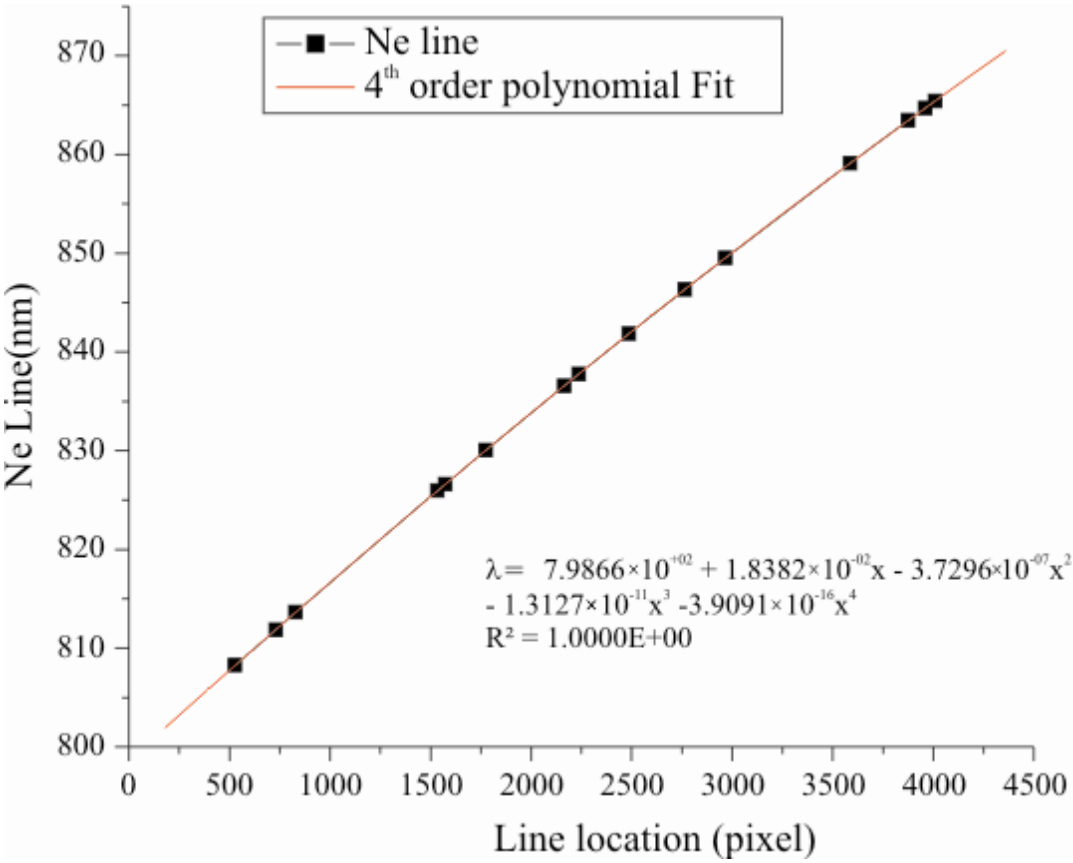

Figure 4.17: Spectrometer calibration. The graph displays the wavelength in function of the pixel index. The black dots represent the Neon lamp spectral lines recorded by the spectrometer and their relative pixel number. The formula of the calibration curve with the quartic fit coefficients is presented.

Their corresponding pixel positions were detected and a wavelength vs. pixel map was obtained. A fourth order polynomial interpolation function available in a commercial data analysis software (OriginLab, USA) (Figure 4.17) was applied to the wavelength-pixel map to compute the quartic fit coefficients a_0, a_1, a_2, a_3, a_4.

4.4.9. Optics and spectrometer performances

In this section the performance of the individual optical components and the overall spectrometer performance were tested and compared with the theoretical calculations.

Collimator beam profile

A beam profiler was setup to measure the beam intensity distribution produced by the collimator assembly in a plane perpendicular to its optical axis at 210mm from the lens surface. The beam profiler consisted of a 100 µm slit (58544, 100 micron mounted air slit, Edmund Optics, USA) that was placed in front of a power meter photodetector head (Power Meter 1930C, Newport). Two translation stages (UMR8.25, Newport) move the detector along the horizontal and vertical directions perpendicular to the optical axis of the collimator. The collimator was illuminated with the SLD light source selected in section 4.2. Once the center of the collimated beam was found, the detector was moved along the horizontal position at 250µm steps. The power was recorded at each step until the normalized power dropped below 1% of the maximum intensity (Figure 4.18). The shape of the intensity distribution is Gaussian with a diameter ($1/e^2$) of 11.7mm, which is in good agreement with the collimator specifications (12mm).

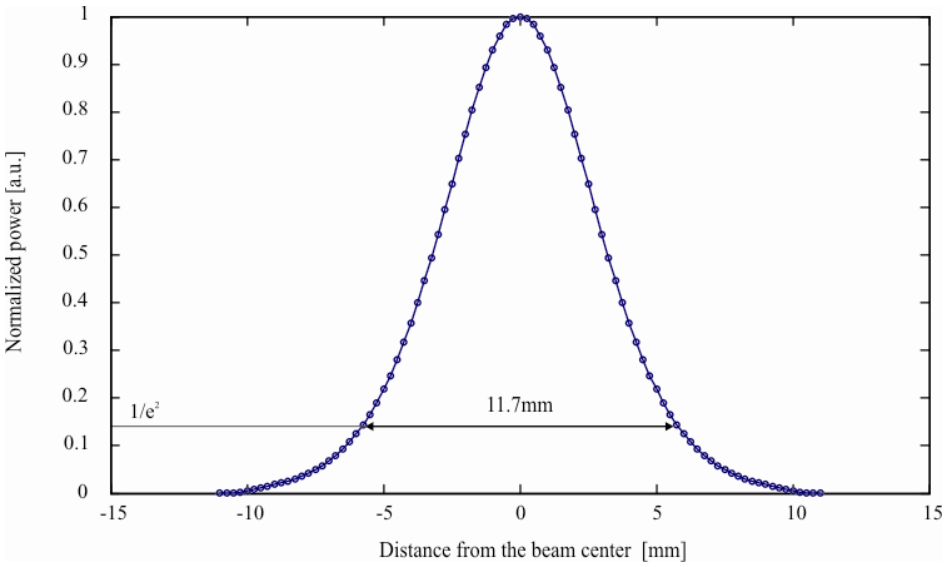

Figure 4.18: Measured intensity distribution of the collimator beam along a horizontal axis.

Focal spot size

The focusing lens and the collimator were tested together in order to measure the focused spot size using the selected light source. An optical setup was built that consisted of the collimator assembly and the focusing lens. The two optical components were aligned along the same optical axis. The distance between the collimator and the focusing lens surfaces was equal to the focal length of the lens (210mm). A CCD camera with 1024 × 786 pixels (Horizontal × Vertical) and pixel size 4.65µm × 4.65µm (XCD-X710 IEEE-1394 Firewire Camera, Sony, Japan) was placed at the focal plane of the lens to measure the profile of the focused beam. Unlike in the spectrometer, the profile measured in these conditions contains the contribution of all the wavelengths in the light source spectrum. Despite these differences, it provides an estimate of the difference between the real and the diffraction limited spot diameter produced by the lens system. Figure 4.19 shows the beam intensity profile of the wide band beam at the focal plane of the lens.

The measured diameter of the focused beam is approximately 27.9µm at $1/e^2$, which correspond to a FWHM diameter of 23.7 µm. As expected, the measured spot size is larger than the theoretical diffraction-limited value, which had an average diameter of 18.5 µm ($1/e^2$) or 15.7 µm (FWHM). The sensitivity roll-off of the current configuration can be simulated with the measured spot size, which yields a ratio $\frac{2w_{FWHM}}{\Delta x} = 2.3$. The simulated sensitivity fall-off is now located in the area between the solid light blue and the solid black curve in Figure 4.13 and reaches a minimum of -46 dB at the end of the axial range. This estimation was performed without taking into account diffraction grating and oblique incidence. Thus, the expected sensitivity fall-off will be lower than -46dB.

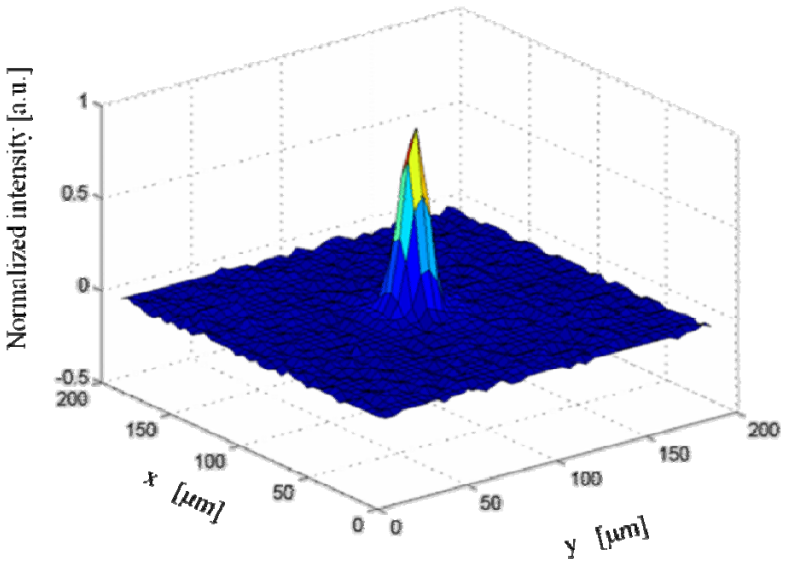

Figure 4.19: Normalized profile of beam at the focal plane of the multi-element lens. The lens and the collimator were aligned on the same optical axis and the collimator was illuminated with the SLD light source selected in section 4.2.

Sensitivity fall-off and axial resolution

After calibration of the spectrometer was performed, the sensitivity fall-off and axial resolution were measured using published methods (Lim et al, 2006). Two similar delay lines were built for the reference and the sample arms. Each arm fiber termination was interfaced to a collimator (PAF-X -11-B, Thorlabs, USA). In each arm, a silver mirror that reflects the light back to the collimator was mounted on a linear stage (UMR8.25, Newport USA). The linear stage is used to change the optical path length of the delay lines by changing the distance between the mirror and the collimator. A neutral density filter (OD = 4 single pass) was placed between the collimator and the mirror in the sample arm to attenuate the power. The power of the reference arm was adjusted to keep the camera near to saturation. The delay in the reference arm was then varied in 1mm increments.

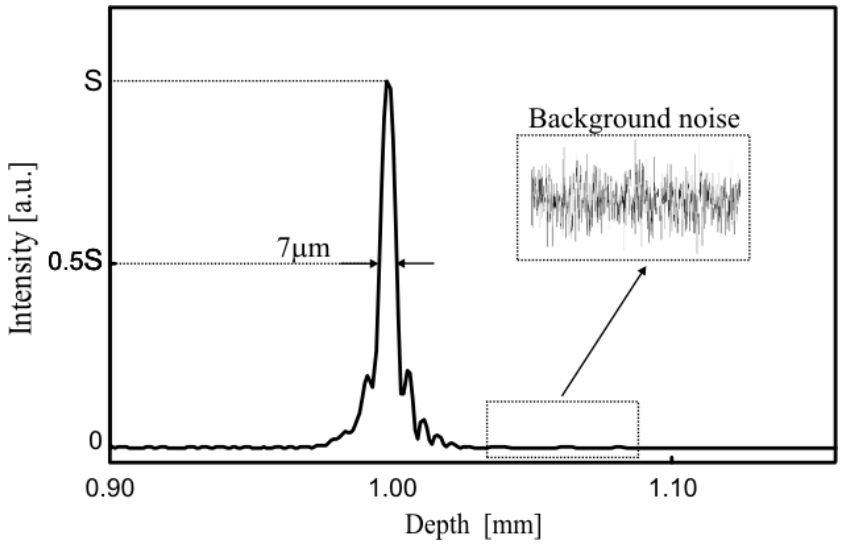

Figure 4.20: Measured interference signal in the depth domain for a free space arm displacement of 1mm. FWHM of the PSF and a close up of the background noise are shown.

At each increment the interference fringes were recorded and the interference signal in the space domain was calculated using a processing code developed in Matlab, which is based on the steps explained in section 4.6.1.

Figure 4.20 shows a typical recorded interference signal in the space domain for a OPD of 1mm. The sensitivity in function of depth was calculated with the following formula (Lim et al, 2006):

$$SNR_{SD-OCT} = 20\log\left(\frac{S}{\sigma}\right) + 20\ \mathrm{OD} \qquad 6)$$

where S is the signal peak and σ the standard deviation of the background noise, which was calculated on 400 samples recorded after the interference signal in the space domain. Figure 4.21A shows the normalized sensitivity as a function of the free space depth.

The measured sensitivity progressively decreases over the entire range from a peak of sensitivity of 98dB at 100µm from the zero delay to 51dB at a depth of 10mm, corresponding to a maximum sensitivity loss of about -47 dB. The free space axial range

was measured as the displacement between the sample and reference arm mirrors at which the interference peak is located at the last (2048th) point of the A-line. The last point of the A-line was reached when the linear stage micrometer reading was 10.43mm, which is in agreement with the theoretically predicted value of 10.22mm in section 4.4.2. Figure 4.21B shows the free space axial resolution as a function of depth. The resolution was measured as the FWHM of the PSFs of the interference signal in the depth domain, as shown in Figure 4.20. At depths below 7mm, the FWHM of the PSFs was approximately constant with an average value of 7.5µm. Beyond 7mm the free space axial resolution progressively degrades, until it reaches 14µm at the end of the axial range. The degradation of the axial resolution with depth is probably due to residue non linearity of the spectral fringes in the wavenumber and/or calibration errors (Wojtkowski, Leitgeb et al , 2002, Yasuno et al, 2005).

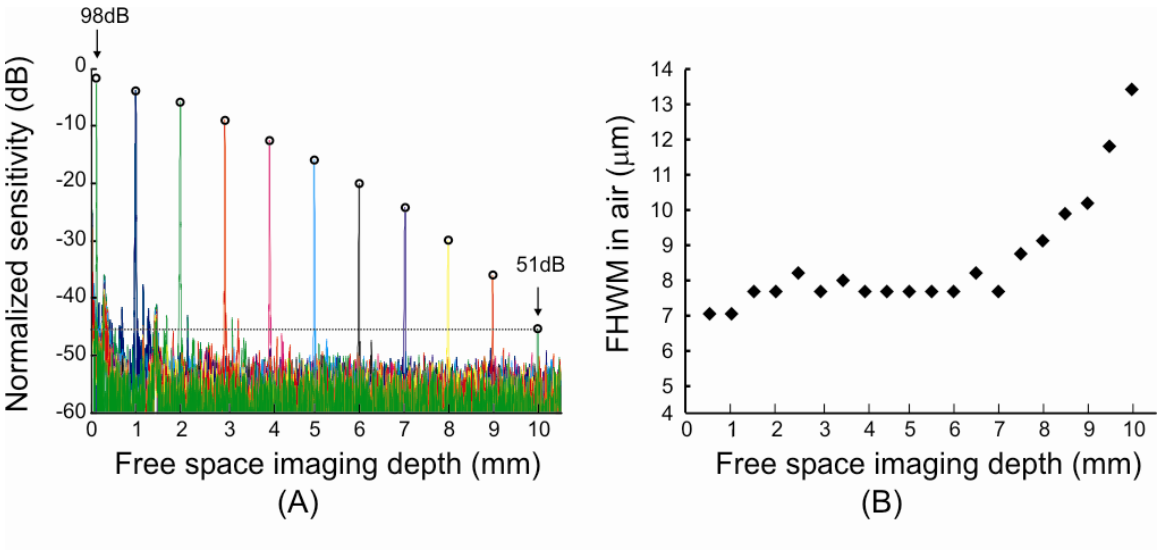

Figure 4.21: (A) Normalized sensitivity in function of depth. Plot of the interference signal as a function of depth is also reported. (B) FWHM of the axial point spread functions at different depth positions.

Fall-off simulation verification

A sensitivity decay of -46 dB was estimated in section 4.4.3 at the end of the axial range (z=10.22mm) using a spot size ($1/e^2$) of 27.9μm, which corresponds to a sensitivity decays of -44.8dB at 10mm. The measured roll-off at 10mm is -47 dB, which is in very good agreement with the prediction. The additional 2.2dB fall-off is probably due to aberrations (field curvature and coma). In order to quantify the effective spot size previously introduced, the experimental data of the sensitivity fall-off were fit to the model proposed by Hu et al over the axial range up to 10mm. The first experimental data point was at 1mm. The results of the best fit are shown in Figure 4.22. The best fit was obtained for an effective spot size of diameter of 24 μm (FWHM), or equivalently 28.3 μm ($1/e^2$) of the normalized intensity distribution, which is approximately equivalent to the measured spot size ($1/e^2$) of 27.9μm.

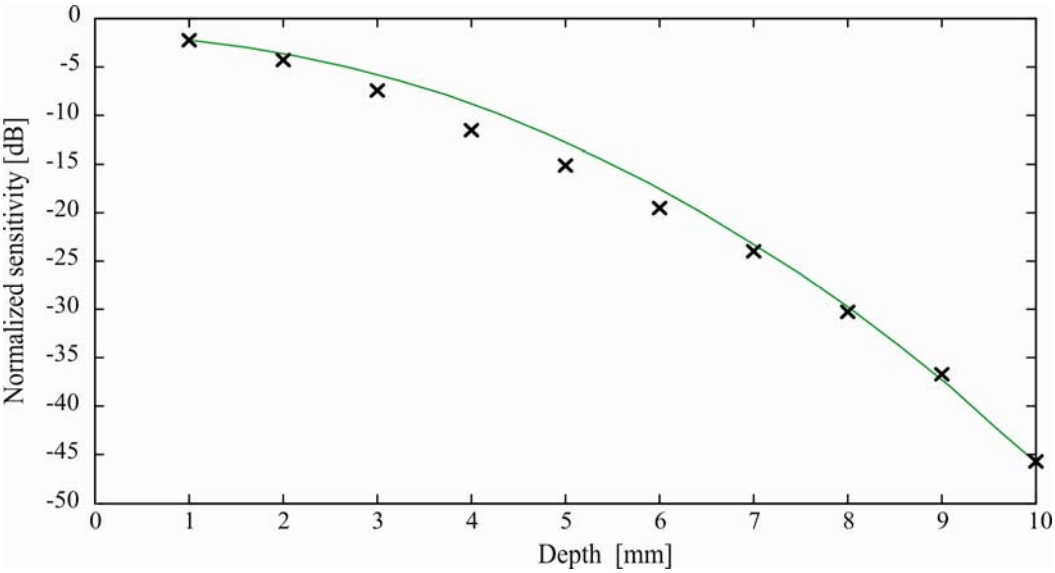

Figure 4.22: Experimental data points (black) were fit with theoretical data (green line) obtained with simulation.

Based on these results, the measured sensitivity performance of the spectrometer matches the performance calculated with the simulations.

4.5. Reference arm - delay line

4.5.1. Axial range extension using an optical switch

The current spectrometer is designed for imaging the entire thickness of the crystalline lens length at every age in a single frame with high speed. In a second stage of the project, the need to perform imaging of the entire anterior segment (cornea, anterior chamber and lens) emerged. One motivation of imaging the entire anterior segment is because information about the shape of the cornea and anterior chamber is needed in order to perform accurate biometry of the crystalline lens. To estimate the optical thickness of the anterior segment at all ages, published measurements of the anterior chamber depth (Fontana et al, 1980) and the central corneal thickness (Martola et al, 1968) measured over a broad population were used. According to these studies, the maximum geometrical length of the anterior chamber and central corneal thickness are 3.2mm and 0.6mm, respectively. The maximum optical thickness of the anterior chamber and the central cornea was calculated assuming an equivalent group refractive index of 1.34 for the aqueous humor and 1.38 for the cornea. Both refractive indices were obtained at 815nm (Drexler et al, 1998). The results lead to a optical anterior chamber depth of 4.2mm and an optical central corneal thickness of 0.8mm. Combining these values with the maximum optical thickness of the crystalline lens that has been estimated in the previous section, ideally, a maximum axial range of about 13mm would be necessary to image the whole anterior segment.

With the current detector and axial resolution the axial range is limited to 10.43mm, which is not sufficient to image the anterior segment along its entire length. One solution to extend the imaging range, other than using complex conjugate techniques, is to acquire two consecutive frames recorded at different depths that cover the entire anterior segment. An optical switching method similar to what has been reported before (Wang et al, 2008) was implemented to record the two frames. Figure 4.23A shows the custom-made optical switch. The switch uses a mirror mounted on a galvanometer scanner that rapidly switches the reference beam between two delay lines (M1 and M2) with calibrated optical path length difference. The optical path difference of the delay lines represents the axial offset between the two frames (F1 and F2) that are alternately recorded. By adequately selecting the offset between the delay lines, this configuration allows the nominal scan depth to cover the whole human anterior segment while the frame rate is halved.

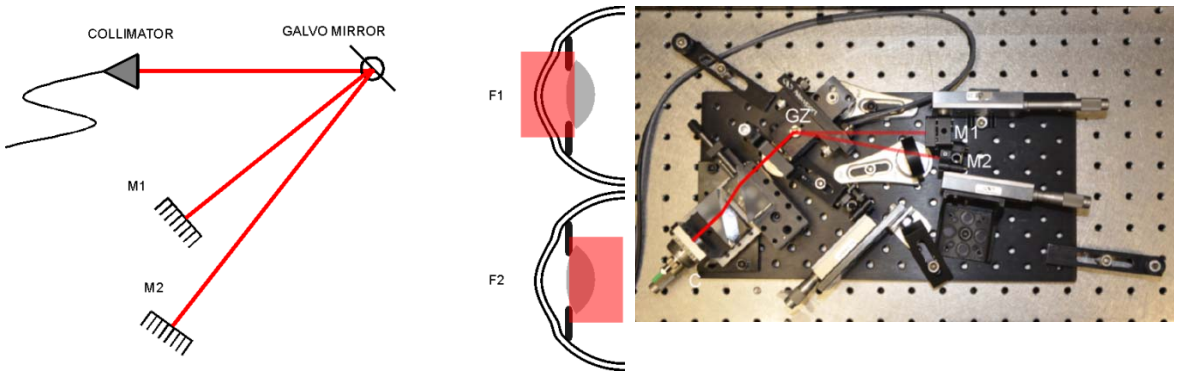

(A) (B)

Figure 4.23: (A) Scanning galvanometer delay line switching between the two mirrors M1 and M2. When the light beam is switched to the mirror M1 the frame F1 is acquired, which covers the anterior part of the anterior segment. When the light beam is switched to the mirror M2 the frame F2 is acquired, which covers the posterior part of the anterior segment. (b) Picture of the setup.

The offset was empirically determined, as described in section 5.5.1. The optical switch is shown in Figure 4.23B and consists of an aspheric lens collimator C (C220TME-B f=11mm, Thorlabs, USA), a Z galvanometer optical scanner GZ (6210H, Cambridge Technology, Inc., USA) and two silver mirrors used as retro-reflectors that are mounted on two linear stages. The optical switch features a short switching time of 300μs so that eye movements are negligible during the switching and that the two frames sit on the same transversal plane. The optical switch operations are controlled by a custom made electronic board.

4.5.2. Dispersion compensation

Normally, the fiber lengths of the two arms are different and different optics is used in the two arms of an OCT system. Dispersion mismatch between the sample and reference arms of the interferometer occurs, which degrades the axial resolution in OCT by broadening the signal peaks that are generated from reflections in the sample, as introduced in section 3.5.4. To optimize axial resolution, hardware dispersion compensation between the arms can be used (Al-Saeed et al 2009). An optical wedge is mounted in a fixed position and another optical wedge is mounted on a stage that translates the element laterally with respect to the optical beam (Figure 4.24). Movements of the translating wedge vary the amount of dispersion of the material in the optical path of the sample arm. Two BK7 wedges were used (NT43-649 Edmund Optics, NJ). Figure 4.24 shows the two glass blocks between the collimator and the galvanometer mirror. The dispersion tuning was accomplished by using perfect reflectors in the sample and the

reference arms. The length of both arms was matched by visually monitoring the spectral fringes generated by the interference of the back reflected light from both arms.

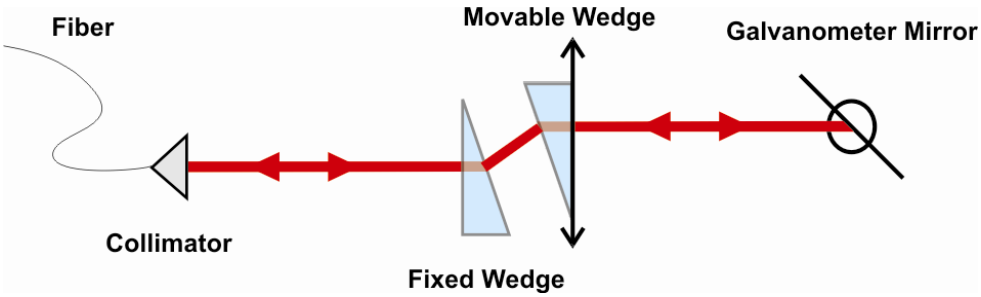

Figure 4.24: Optical wedges integrated in the reference arm.

In case the dispersion between the arms is imbalanced, a distortion of the interference spectrum occurs. The position of the wedge was tuned until the distortion of the spectrum disappeared. A slit with variable width (VA100, Thorlabs, USA) was also placed in the path of the light between the blocks and the galvanometer mirror to adjust the beam power and avoid to saturate the camera detector.

4.6. Image acquisition, processing and display

4.6.1. Spectral Domain data processing

The flowchart in Figure 4.25, shows the steps that are generally taken to process the raw pixel data from the array sensor and convert it to a depth scan. SD-OCT suffers from constant noise sources that manifest themselves as artifacts in the image. These noise sources are known as "fixed noise pattern" and usually arise from external sources, from the electronics and from the camera. The first step in the signal processing pipeline is to record the background. The recorded background is then subtracted from subsequent data to eliminate the fixed noise pattern. Data collected using the spectrometer is an interferogram as a function of wavelength. However, as it has been shown in section 3.4,

wavenumber and depth are conjugate variables so that the spectrum needs to be Fourier transformed in the wavenumber (or frequency) space in order to calculate the depth dependent intensity. The second step after acquisition is the resampling of the raw spectrum to produce a spectrum that is linear in wavenumber prior to inverse Fourier transformation. The wavelength array is inverted and resampled to linearize the wavenumber data. The sampling interval of the wavenumber data is the ratio between the detected spectral width in wavenumber and the number of pixels of the array. The new interferogram is then interpolated to produce the spectral interferogram that is linear in wavenumber. Software dispersion compensation is an extra step that is taken in case high quality imaging is needed and dispersion mismatch cannot be entirely compensated by adding the dispersive material in the reference arm.

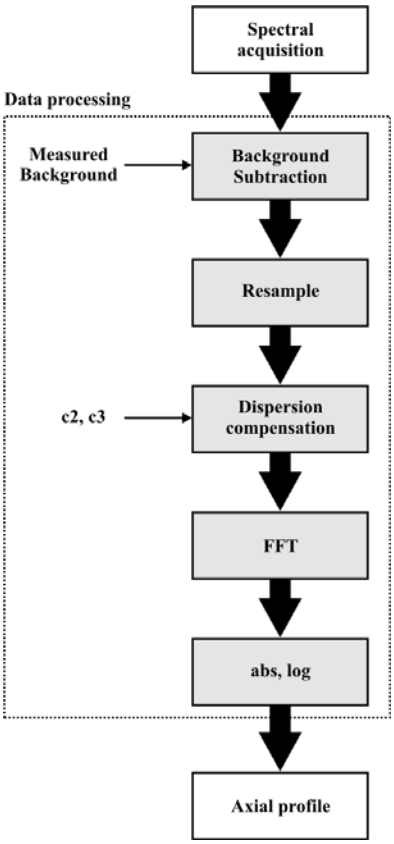

Figure 4.25: Data processing flowchart.

As discussed in section 3.5.4, compensation is achieved by tuning the second and third order distortion coefficients (shown as *c2* and *c3* in Figure 4.25). The tuning of the coefficients is performed off line manually or through iterative routines (Wojtkowski et al, 2004).

In the fourth step, the Fast-Fourier transform (FFT) of the signal is taken. This operation is followed by calculating the absolute value of the complex result of the FFT, to return the magnitude of the signal. The logarithm of the magnitude is calculated to compress the dynamic range of the signal, which results in the final intensity profile.

4.6.2. Software and control

An algorithm that is based on the previous steps was developed in Matlab to process the spectral data. The algorithm was used to process single camera recordings of the spectral data off-line and characterize the performance of the spectrometer reported in section 4.4.7. However, to build two and three dimensional images of the crystalline lens the beam must be scanned transversally across the sample to acquire multiple spectral interferograms that need to be processed at fast speed and displayed in real time. The transversal scanning in OCT is generally achieved by two galvanometer scanners similar to the one used in the delay line, which will be discussed in details in the next chapter. If the imaging requires to be extended to the entire anterior segment, two consecutive frames must be acquired at different depths by also controlling the optical switch in the reference arm. The operations of acquisition of the CMOS camera, transversal scanning and multi-frame scanning, need to be developed and synchronized. Figure 4.26 shows a diagram of the entire system. An image acquisition board (PCIe-1429; National Instruments, USA) was used to acquire the data captured by the CMOS camera and

transfer it to a computer workstation (Dell T5500, dual 3.6 GHz processor, 3 GB memory). A multifunction data acquisition board (PCI-6221; National Instruments, USA) was used to output the control signal for the transversal scanners. A control box with power supplies and drivers for the galvanometer scanners was built. A commercial software package (Bioptigen, Inc. Research Triangle Park, NC) was adapted to the hardware modules for hardware synchronization, real-time acquisition from the CMOS camera, scanning control, OCT processing and display of the OCT data. The data processing pipeline of the commercial software is similar to the one reported in Figure 4.25. The use of a commercial package was preferred rather than building a custom software to save time and take full advantage of the integrated database system that the commercial platform offers.

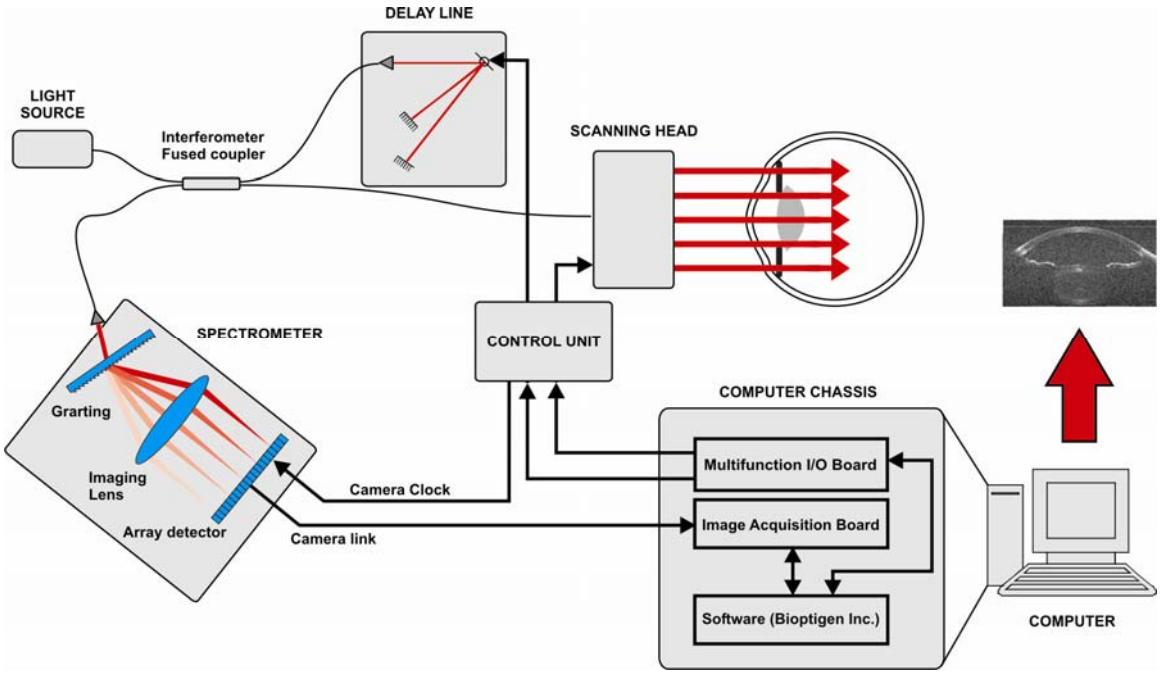

Figure 4.26: Configuration and connections of the SD-OCT system.

In order to acquire images of the entire anterior segment, two consecutive frames acquired at different depths are required. During the acquisition of one frame the optical

switch must remain stationary allowing the acquisition of all the A-lines of that frame. At the end of the frame acquisition, the switch in the reference arm must move the beam to the other delay line so another frame is acquired at a different depth, and so on. In order to synchronize the acquisition and the switching, the optical switch requires an end of frame acquisition signal. The commercial software does not provide such a signal. To overcome this limitation, an electronic circuit was designed and built to synchronize the frame switching operations with the end of frame acquisition.

4.7. Discussion, summary and conclusions

A SD-OCT system was developed with extended depth for in vivo imaging of the human crystalline lens along its entire depth at all ages. The axial resolution of the system varies between 7µm and 14µm, over an axial range of 10.43mm. The system features a fast scanning rate of 40,000 spectral recordings per second. While the axial resolution is well preserved along the depth range, the system suffer of an overall sensitivity loss of 47dB at the end of the axial range. The main sources of sensitivity decay are the finite width of the pixels of the array detector and the extended spot size of the spectrometer optics. SS-OCT allows recording of spectra that are linear in wavenumber by hardware triggering techniques (Huber et al, 2005; Zhang et al, 2004; Yun et al, 2004). Moreover, in SS-OCT the spectral lines are recorded by photodetectors with active area larger than the incident light. Thus, the sensitivity roll-off performance in SS-OCT is mainly determined by the finite instantaneous linewidth of the light source, which is the equivalent of the finite pixels size in SD-OCT. Recently, a SS-OCT implementation (Furukawa et al, 2010) at longer wavelengths (1310nm) has shown improved sensitivity performance compared to the SD-OCT implementation, thus making SS-OCT highly

suitable for extended depth imaging. However, swept sources in the spectral region around 800nm are not readily available. Few swept sources working at ~850 nm have been demonstrated (Lee et al, 2007; Lim et al, 2006) that show, respectively, low output power (~2mW) or broad linewidth, which results in significant sensitivity decay over depth.

In a second stage of the study the need to image the anterior segment along its entire length emerged, which requires an axial range of about 13mm. With the current detector and axial resolution requirements, the axial range limited by aliasing is 10.43mm. As reported in chapter 3, many approaches have been exploited that allow a twofold increase of the axial range and enhance sensitivity performance by removing the complex conjugate ambiguity of the spectral interference signal. However, these methods exhibit disadvantages in terms of speed or transversal scanning flexibility. To double the axial range an optical switching method was implemented in the reference arm. In the next chapter, the design and development of an OCT delivery unit for anterior segment imaging that connects to the sample arm of the OCT system will be discussed. The unit will also provide an accommodation stimulus so that imaging of the mechanism of accommodation can be performed with the SD-OCT system.

CHAPTER 5. DESIGN OF AN ANTERIOR SEGMENT DELIVERY SYSTEM

5.1. Objective

The first objective of this part of the project is the development of an optical probe mounted on a slit lamp that efficiently delivers the light from the sample arm of the SD-OCT system into the subject anterior segment. An optical system that provides a visible accommodation stimulus to the subject will be developed and combined with the slit-lamp optical probe. The goal is to implement an imaging system that enables biometry of the dynamic process of accommodation with the following design parameters:

- The transverse scanning mechanism has to provide enough lateral range for imaging the entire cornea (15mm)
- The focusing optics will produce high lateral resolution (100µm) and long depth of focus (~6mm) so that fine detail imaging of the anterior segment along its entire length can be performed with the SD-OCT system.
- The accommodation target will be designed to provide step stimuli from approximately 0D to 10D during imaging with the OCT.

5.2. OCT delivery system design

5.2.1. General design

The OCT delivery system consists of a transverse scanning device and focusing optics that are interfaced to the sample arm of the OCT system and are responsible of delivering and collecting the light from the sample. It is fundamental to support adequate lateral range, transverse resolution, depth of field and speed.

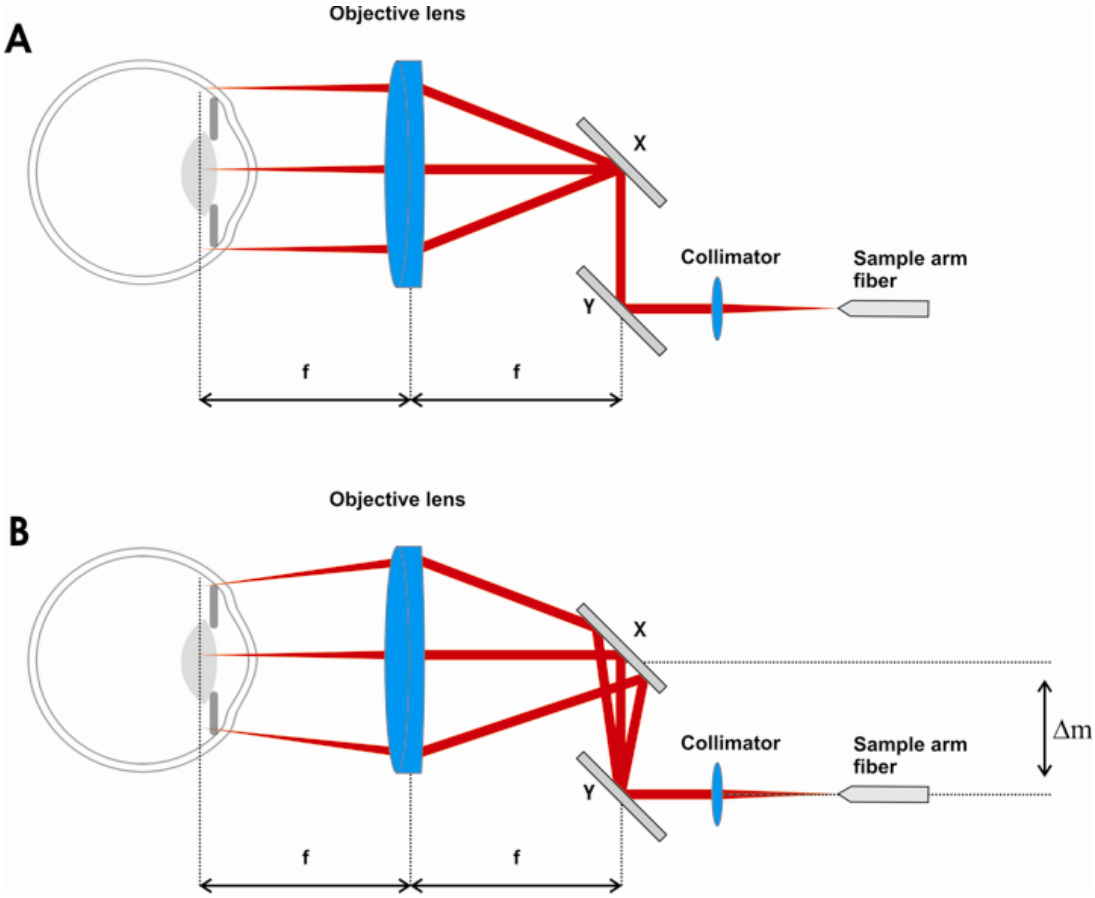

Figure 5.1: Configuration of the typical delivery setup used in a fiber based anterior segment OCT system. The system allows to scan the eye in the horizontal plane (A) and in the vertical plane (B).

The typical transverse scanning mechanism with two axes used in fiber based OCT systems for anterior segment imaging is shown in Figure 5.1. Two scanning mirrors are mounted on a galvanometer actuated axis (X,Y), that gives accuracy in angle positioning, low rotation inertia and high speed. The X axis scans the horizontal plane (Figure 5.1A) while the Y axis scans the vertical plane (Figure 5.1B). Light from the sample arm fiber is collimated before reaching the transversal galvanometer scanners. The objective lens (or focusing lens), is mounted in a telecentric configuration, for which the light beam is focused such that it is always perpendicular to the object to be scanned and the entire scanning has a flat imaging plane. The telecentric scan is ideal in anterior

segment imaging because it minimizes the distortions introduced by the scanning system (Ortiz 2009), which in turn reduces the amount of post processing needed to display geometrically correct images. For a telecentric design, the scanning mirrors are placed at the front focal point of the focusing lens. One common feature of the two mirrors scanning system is that the mirrors are spatially separated. Only one mirror can therefore be truly telecentric. In the current design, the X scanning mirror was aligned to the focal plane of the focusing lens so that the marginal beams in the horizontal plane are parallel to the optical axis (Figure 5.1A). The separation between the Y mirror and the focal plane of the focusing lens (Δm in Figure 5.1) generates off-axis beams that are not exactly parallel to the optical axis in the vertical plane (Figure 5.1B). Thus, field distortion is introduced by the Y axis scanner with consequent deformation of the image in the vertical plane (Ortiz et al, 2009; Xie et al 2005). Depending on the required measurement accuracy, field distortion may need to be corrected to obtain reliable biometric data such as surface curvature in the vertical plane.

5.2.2. Transverse resolution and depth of focus

The transverse resolution of the system and the depth of field are governed by the focal length of the collimator and the focusing lens (Figure 5.2). Assuming the OCT beam is Gaussian, the transverse resolution Δx is the diameter of the spot at the beam waist and the depth of field is twice the Rayleigh range z_R, respectively

$$\Delta x = \frac{4\lambda_0}{\pi}\frac{f_{obj}}{D}, \tag{5.1}$$

$$2z_R = \frac{\pi \Delta x^2}{2\lambda_0} \tag{5.2}$$

where f_{obj} is the focal length of the objective lens, D the diameter of the collimated beam and λ_0 the central wavelength of the light source.

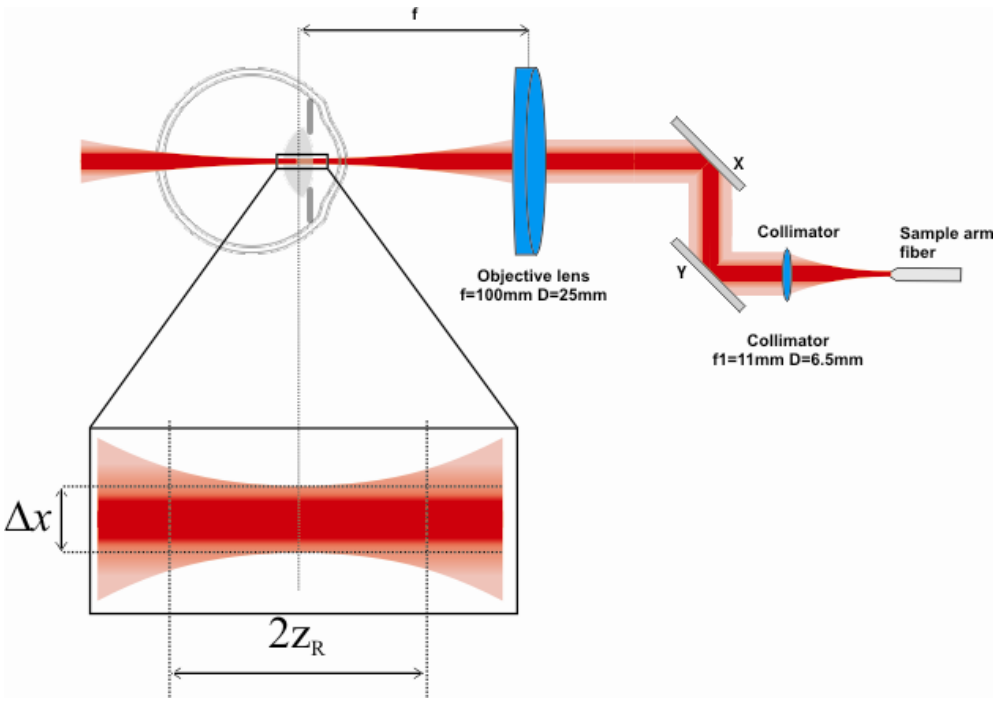

Figure 5.2: Configuration of the typical delivery setup used in a fiber based OCT system.

There is a trade-off between the transversal resolution and the depth of focus. If one optimizes the design to achieve long axial range with the OCT system, the depth of focus of the delivery optics needs to be large enough to efficiently collect the light backscattered by the sample while preserving lateral resolution. Several trade-offs need to be considered while designing this type of scanning scheme. The scanning mirror size needs to be relatively small to lower the actuator inertia and thus shorten the settling time to produce fast scanning speed and precise positioning. Mirrors mounted on fast galvanometer actuators have a typical clear aperture in the range from 3 to 6mm. The collimated spot size needs to be sufficiently small to fit the clear aperture of the mirrors. On the other hand, according to equation 5.1, a large collimated beam produces better

lateral resolution for a given focusing lens. The working distance of the focusing lens needs to be large (>100mm) to provide sufficient room for the imaging procedure. A long working distance is also needed to have enough space to couple the scanning head with an accommodation target device that will be described in the next section. Figure 5.3A and B report, respectively, the spot size and the depth of focus in function of objective focal length values larger than 100mm. In both graphs of Figure 5.3, three plots are reported for three values of the diameter of the collimated beam D=2,3 and 4mm that fit the typical clear aperture of galvanometer mounted mirrors. The graphs in Figure 5.3A shows that using a collimated beam with 2mm diameter produces a lateral resolution of 100µm if an objective lens with focal length shorter than 180mm is used. If the collimated beam has a larger diameter of 3 and 4mm the focal length necessary to produce a lateral resolution of 100µm increases. The graph in Figure 5.3B shows that to achieve a depth of focus of about 6mm using a collimated beam with a diameter of 2mm requires a focal length longer than 100mm. If the collimated beam diameter is increased to 3 and 4mm a longer focal length is needed.

5.2.3. Components

A scanning head was developed using off the shelf optics and scanner. An aspheric lens collimator C (C220TME-B, f=11mm, Thorlabs, USA) produces a collimated beam with a diameter equal to 2.3 mm that is focused on the sample by the objective lens. A X-Y galvanometer optical scanner (6210H, Cambridge Technology, Inc., USA) was selected with high speed (100µs small angle step response) and a 3mm clear aperture mirrors (at 45º respect to the incident beam) to ensure that the collimated beam is contained within the mirror during scanning.

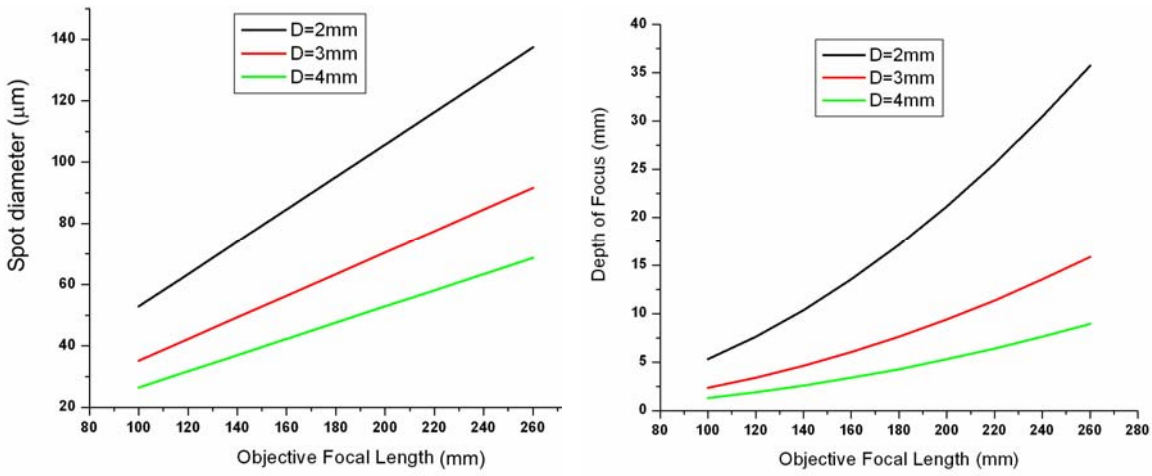

(A) **(B)**

Figure 5.3: (A) Spot size as a function of the objective focal length and the beam diameter. **(B)** Depth of focus as a function of the objective focal length and the beam diameter.

A NIR achromatic doublet lens with 100mm focal length (AC254-100-B, Thorlabs, USA) was used as objective lens to correct for chromatic aberrations due to the broad band of the light source. The objective lens and the collimator produce a spot size of 52μm and a depth of focus (two times the Rayleigh range) of 5.1mm in air (Figure 5.4). The beam gradually grows in either direction from the beam waist. From section 4.2, the maximum length of the anterior segment was estimated around 13mm. If the beam waist is placed at the center of the anterior segment, the beam reaches a diameter of ~140μm at the extremity of the anterior segment (Figure 5.4), which is enough to image the anterior segment with sufficient lateral resolution.

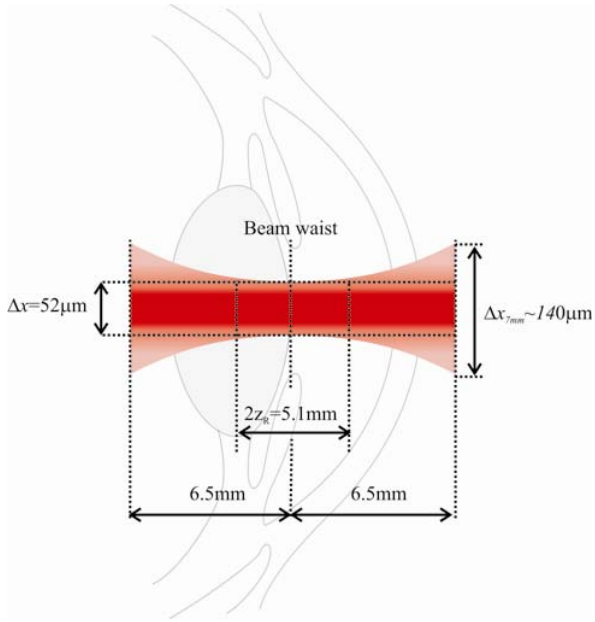

Figure 5.4: Approximate position of the beam waist with respect to the anterior segment. The axial resolution Δx and at the end of the axial range and the depth of focus $2z_R$ are reported together with the spot size at 6.5mm from the beam waist.

5.2.4. Lateral range

The cornea has an average diameter that reaches maximum 12mm in normal emmetropic subjects (Duke-Elder et al, 1961). The optical scanning range of the galvanometer actuator is ±20º. With the selected focal length (100mm) the maximum transverse scanning width provided by the scanners is 72mm. An objective lens with diameter of 25.4mm was chosen that limits the lateral scanning range to approximately 20mm, which is well above the lateral range needed to image the entire cornea.

5.2.5. Dichroic mirror

To image the real-time dynamic response of the lens a dichroic mirror DM (NT64-470, Edmund Optics, NJ) was placed in front of the objective lens to fold the OCT beam at 90 degrees into the subject's eye so that the subject is able to fixate the imaged eye on an accommodation target mounted straight across the dichroic mirror. The

accommodation target is described in the next section. The dichroic mirror was selected to reflect wavelengths of the OCT beam and transmit the visible wavelengths used to illuminate the target. Figure 5.5 show the schematic (A), the optomechanical design (B) and a photograph of the optical scanning system (C).

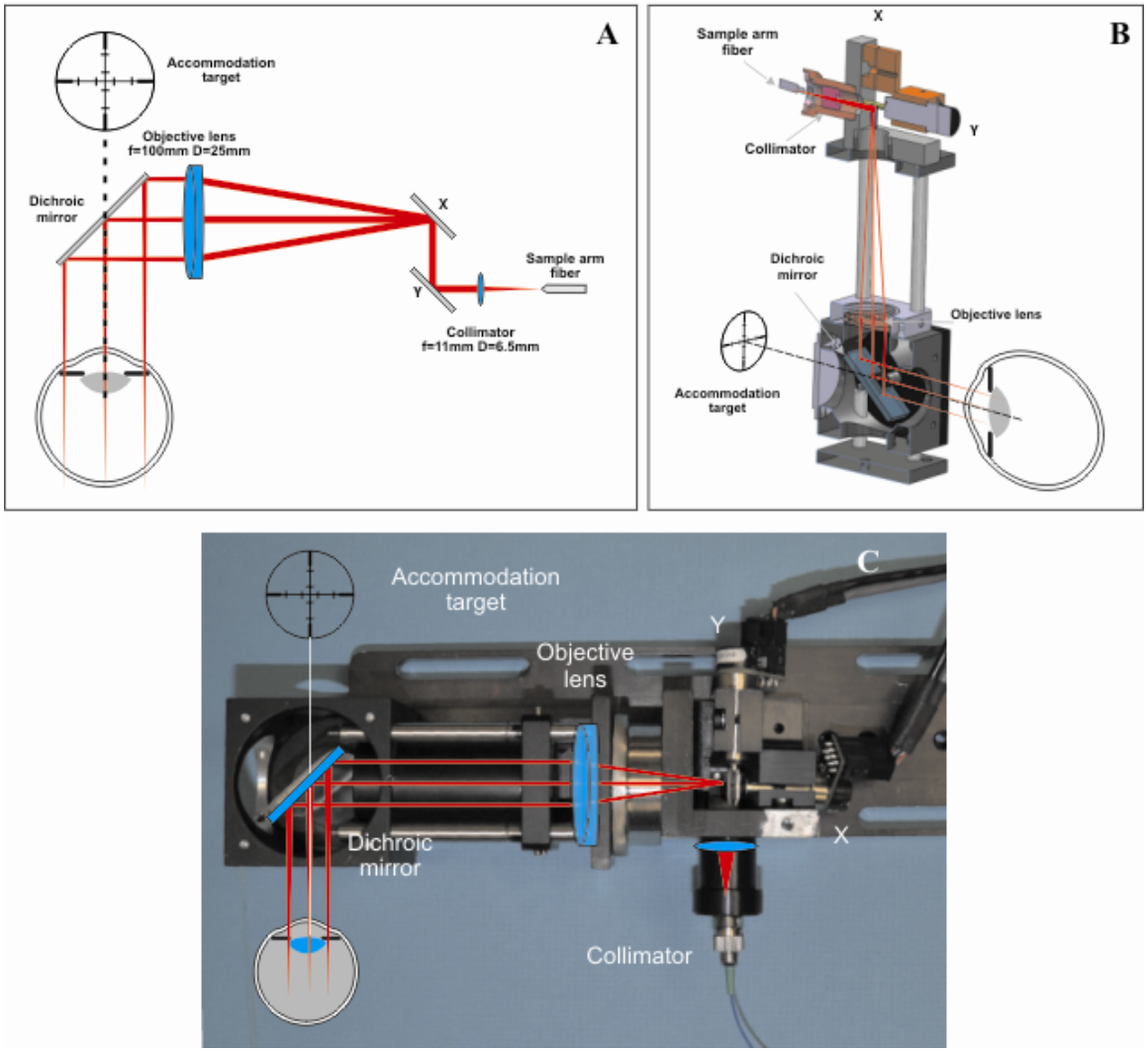

Figure 5.5: Schematic of the OCT scanning system. **(A)** Section of the delivery system optomechanical design showing the path of the OCT light is shown in red. **(B)** Picture of delivery system. The path of the OCT light is shown in red. **(C)**

5.3. Design of an accommodation target unit

5.3.1. Purpose and general requirements

The accommodation target unit is setup to provide an accommodation stimulus to the subject while images of the anterior segment along its entire length are recorded at video rate with the SD-OCT system. The unit needs to meet the following criteria

- monocular stimulus is provided to the eye that is imaged
- the unit provides fixed and step stimuli (far-to-near and near-to-far)
- the stimulus amplitude varies approximately between 0D and 10D
- correction lenses must be introduced to neutralize the eye's refractive error
- the step stimuli are synchronized with the OCT image acquisition
- the step stimuli need to be faster than the accommodative response
- the unit must not interfere with the OCT beam
- the combined OCT probe and accommodation target unit has to be compact and mounted on a slit lamp-mount

If a step stimulus is provided to one eye and imaging is performed in the contralateral eye, the OCT frames acquired at different time points will be misaligned because of the simultaneous convergence of both eyes during accommodation. If the stimulus is provided to the same eye that is imaged, the effect of accommodation convergence is reduced. Another reason behind stimulating and imaging the same eye is that accommodation experiments may be performed on subjects that have different visual refractive state and/or condition in one eye compared to the other eye. This may lead to inaccuracy if the observations are done in the eye that is not stimulated. During the experiments it would also be convenient to quickly switch the imaging procedure from

one eye to the other eye, which can be easily achieved if the OCT and the accommodation stimulus unit share co-axial paths.

Step stimuli in both directions are needed in order to study with OCT the dynamics of accommodation (from far to near) and disaccommodation (from near to far). The amplitude of the stimulus should be enough to allow the lens to go from relaxed (0D stimulus) to completely accommodated (10D) states and vice versa over a broad range of individuals.

5.3.2. Background

The simplest method to provide an accommodation stimulus is to vary the distance of a target placed in front of the eye. The stimulus magnitude (or stimulus vergence) in Diopters can be calculated as the reciprocal of the distance of the target from the eye in meters. Figure 5.6 and Table 5.1 report values of the stimulus vergence for a target that is placed at different distances.

Stimulus vergence(D)	Distance(m)
0.25	4
0.50	2
1.0	1
2.00	0.50
3.00	0.33
4.00	0.25
5.00	0.20
6.00	0.17
7.00	0.14
8.00	0.13
9.00	0.11
10.00	0.10

Table 5.1: The stimulus vergence for a target that is placed at different distances.

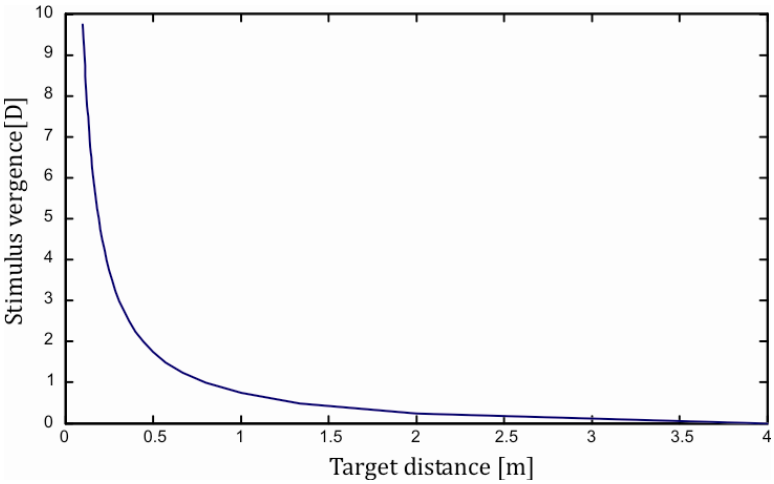

Figure 5.6: The values of the stimulus vergence in function of the target distance.

As a convention, when the target is moved closer to the eye, its vergence becomes more negative, whereas the stimulus vergence becomes more positive. Zero vergence occurs when the object is placed at infinity. Such an approach holds several drawbacks (Bennett and Rabbetts, 1989). First, the power scale is non linear with the target distance. Thus, the accuracy of the instruments is also inversely related to the distance. Second, in order to obtain zero vergence the target needs to be placed at a great distance, which increases the size and/or the complexity of the optical system. Third, magnification of the target changes with the angular size of the target, which itself changes reciprocally with the target distance. Changes in retinal image size affect the accommodation response. Instead of using a real target positioned at different distances, an accommodation unit based on the Badal Optometer can be used. The accommodation target based on the Badal Optometer consists of a movable target and a positive lens (Badal lens) that is placed at a focal distance away from the eye (Figure 5.7). The ocular vergence Q of the image of height h' at the back focal point of the Badal lens and the perceived angular size α can be written as (Bennett and Rabbetts, 1989, Atchison et al, 1994)

$$Q = -F_B(1 + F_B l), \quad 5.3$$

$$\alpha = hF_B \quad 5.4$$

where F_B is the equivalent power of the Badal lens ($F_B = \frac{1}{f_B}, with\ f_B\ focal\ length\ of\ the\ lens$) and l is the negative distance of the target of height h from the Badal lens. Equation 5.3 and 5.4 show that in the Badal Optometer, the vergence is linear with the distance between the target and the lens (l) and the angular size of the target is not affected by a target position change. However, a drawback of this setup is that the range of negative ocular vergences is limited to the equivalent power of the Badal lens F_B. To obtain a stimulus vergence of 10D a focal length of 100mm is needed. However, a longer working distance (>100mm) would be ideal to couple the Badal system with the OCT delivery.

Proximal vergence stimulus is an effect that occurs when the subject is aware that he/she is looking at a physically near test object and then stimulates an involuntary effort of accommodation. Proximal vergence may lead to inaccuracy of the experiments. The simple Badal Optometer used as an accommodation target is not immune to the proximal vergence stimulus.

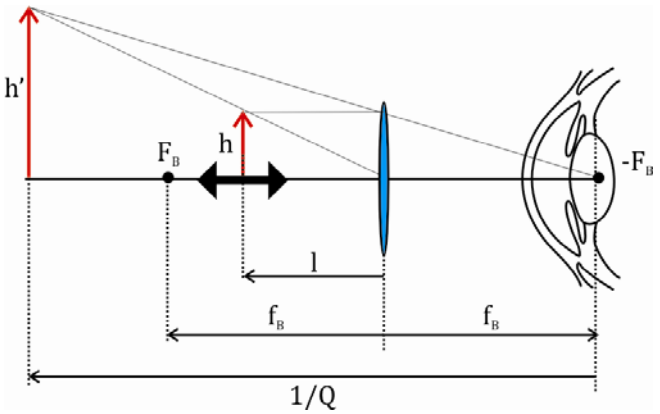

Figure 5.7: Schematic of the simple Badal Optometer.

Another drawback is that the target has to be physically moved axially, which can be difficult if the target includes an illumination system.

5.3.3. Optical design

The final stimulus unit is based on one of the variations of the simple Badal Optometer proposed by Atchison et al (1994) that overcomes the drawbacks of the simple Badal Optometer discussed in the previous section (Figure 5.7). An additional fixed collimating lens of equivalent power F_C is placed at a focal length distance from the real target *T*. This arrangement provides a convenient method to create an image *T′* of the real target *T* near infinity. The virtual image of the target *T′* with height *h′* is imaged by an auxiliary movable lens F_A placed in front of the Badal lens. Since the virtual target *T′* is at infinity its image *T″* will coincide with the back focal plane ($-F_A$) of the auxiliary lens.

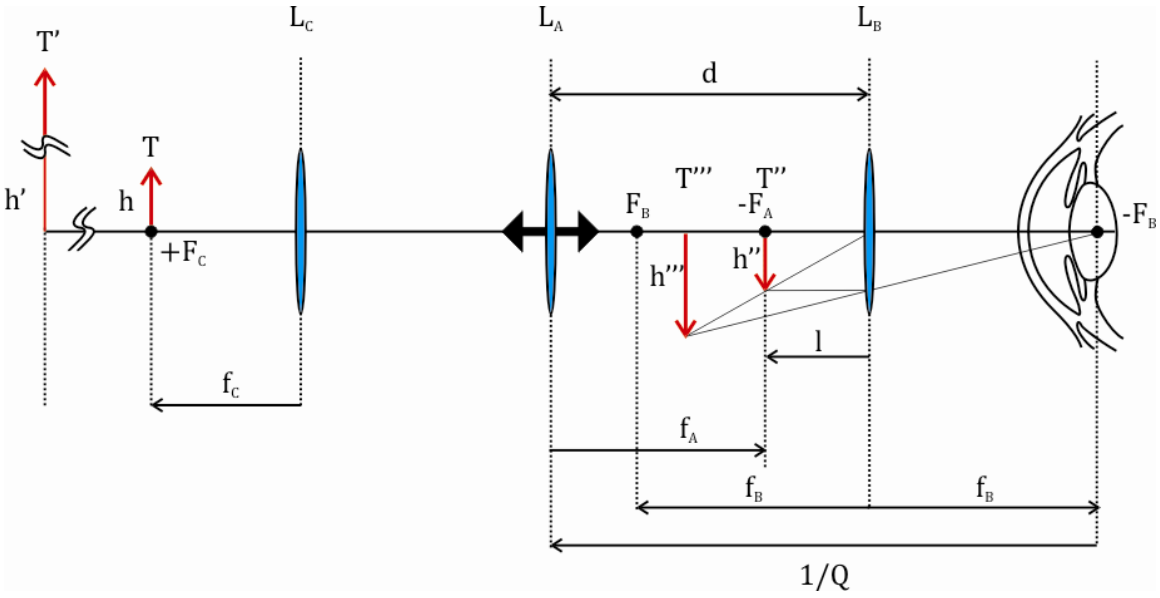

Figure 5.8: Schematic of the Badal Optometer modified by Atchison et al (1994)

A movement of the auxiliary lens produces an equal displacement of its image *T″*. Let us assume that the auxiliary lens is at a distance *d* from the Badal lens. From equation 5.3 the ocular vergence of the final image of the target (*T‴)* at the back focal point of the Badal lens is

$$Q = -F_B - {F_B}^2 l = -F_B - {F_B}^2(-d + \frac{1}{F_A}) \quad 5.5$$

The maximal ocular vergence equal to $-F_B - {F_B}^2/F_A$ is obtained when the distance between the auxiliary lens and the Badal lens (*d*) is near to zero. Zero ocular vergence is reached when the back focal length of the auxiliary lens coincides with the front focal length of the Badal lens, or $d = 1/F_B + 1/F_A$.

The angular size of the final image of the target can be written according to equation 5.4 as

$$\alpha = h'' F_B \quad 5.6$$

The system composed by the collimating and auxiliary lens is a telescope with magnification given by the ratio of their equivalent focal lengths F_C/F_A so that equation 5.6 can be rewritten as

$$\alpha = hF_B \frac{F_C}{F_A} \quad 5.7$$

Equation 5.7 shows that the angular size is constant. The goal of the design is to provide an ocular vergence from 0D to about 10D. This can be achieved with multiple combinations of focal lengths for the collimating, the auxiliary and the Badal lens. One of the goal of the design is to keep the design compact. In order to estimate the size of the system required to achieve the needed vergence range, several combinations were evaluated. Figure 5.9 reports the total length of the system *D* and the travel *d* of the

auxiliary lens at a vergence of 0D and 10D, in function of the focal length of the auxiliary and the Badal lenses. The collimating lens focal length was selected equal to the auxiliary lens focal length to simplify the optical design and achieve a unitary magnification of the target at the back focal point of the auxiliary lens. The working distance of the Badal lens has to be larger than 100mm to allow the coupling of the system with the OCT delivery head and at the same time shorter than 175mm to produce a compact accommodation target. Positive values of the distance d at 10D can be obtained only for values of f_A, approximately larger than 50mm and for values of f_B shorter than 150mm.

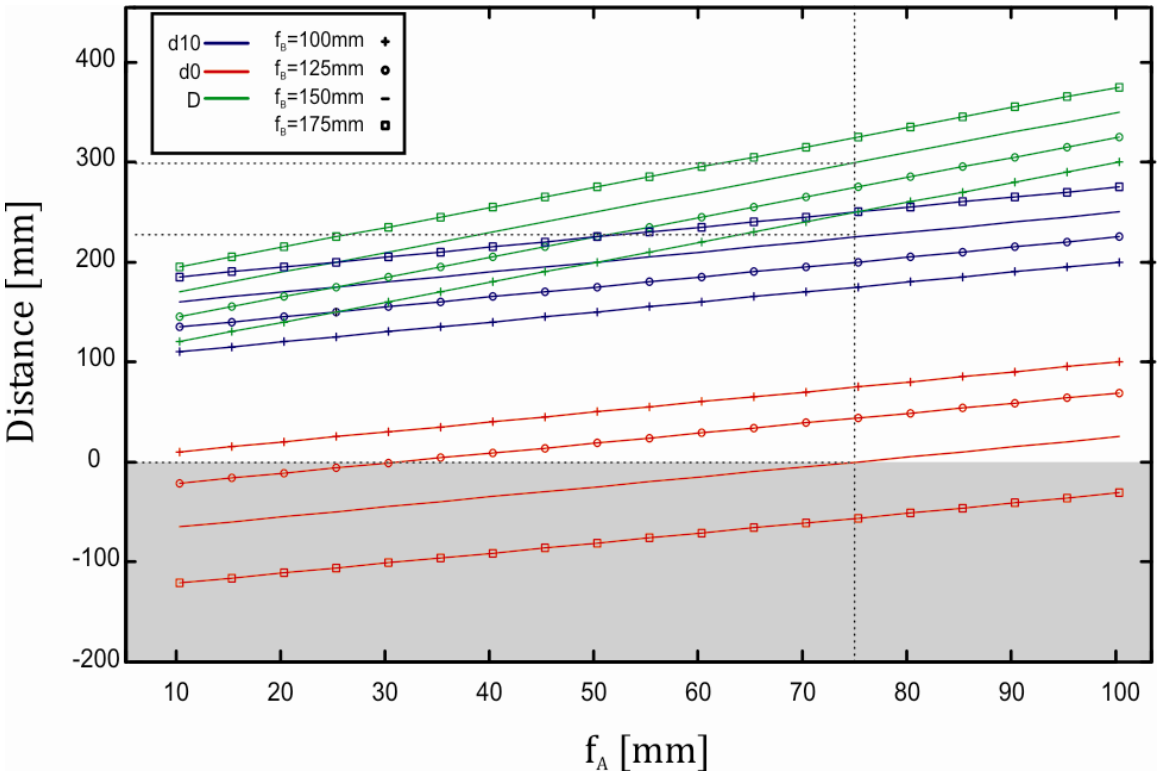

Figure 5.9: Length of the system D and travel d of the auxiliary lens at the stimulus vergence range ends (0D and 10D) in function of the focal length of the auxiliary and the Badal lenses.

Based on this consideration, two off the shelf achromatic doublets in the visible range (AC254-075-A, Thorlabs, USA) with f_A=75mm were selected for the collimating and auxiliary lenses and one off the shelf achromatic doublet in the visible range (AC254-150-A, Thorlabs, USA) with f_B=150mm was selected for the Badal lens. With these lenses, we obtained the following theoretical values: d=0mm at 10D, d =225mm at 0D and the overall length of the system is D=300mm (see black dotted lines in Figure 5.9). Real lenses have a finite thickness so the current setup cannot reach a distance d=0mm and consequently the practical stimulus vergence will be slightly less than 10D. Accounting for the thickness of the selected lenses, the minimum achievable distance d with the current components is about d=*10mm,* which leads to a maximum stimulus of 9.55D. The system has a linear scale with a high spatial resolution of about 0.044D/mm of displacement of the auxiliary lens.

With the proposed setup, the perceived angular size of the target can be calculated using equation 5.7 and assuming that the nodal point of the eye is approximately 17mm in front of the retina (Bennett and Rabbetts, 1989). The collimating and auxiliary lenses were selected with same focal length, thus the perceived angular size is only function of the Badal lens focal length. The target used is a high contrast, 5mm×5mm, 'X' letter printed on white paper that is placed at the focal plane of the collimating lens F_C. Figure 5.10 reports the height of the retinal image of a 5mm target in function of the focal length f_B. For f_B=150mm the retinal image is approximately 570µm in height. The smallest readable size for an emmetropic eye is approximately 4µm (Bennett and Rabbetts, 1989).

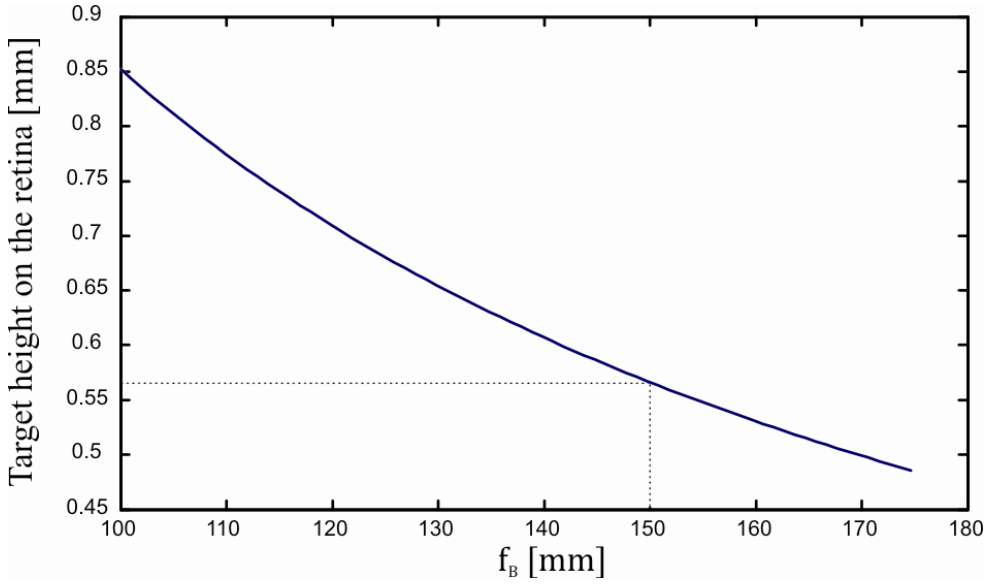

Figure 5.10: Retinal image height of a 5mm target in function of the focal length of the Badal lens.

With the proposed target size, the retinal image is about 140 times larger than the visual acuity, which makes the target well visible for the subject.

5.3.4. Accommodation unit

Figure 5.11A and B show the system that was built to provide the step stimuli. Two Badal targets similar to the one described in the previous section were built and coupled together using a 50/50 beam splitter cube (CM1-BS013, Thorlabs, USA) and a cube reflector (CM1-P01, Thorlabs, USA), respectively, BS and M in Figure 5.11A. The light from both arms becomes coincident at the beam splitter BS. One target provides low vergence stimuli (FAR target) and the other one provides high vergence stimuli (NEAR target). The targets were retro-illuminated using white light emitting diodes and ground glass diffusers (D) (DG10-220, Thorlabs, USA). Figure 5.12 shows the spectral distribution of the white LED.

The targets are visible to the subjects only when they are illuminated. A step stimulus is provided to the subject by alternatively illuminating the two targets. The step direction for an accommodation stimulus (far-to-near) is set by first illuminating the FAR target as in Figure 5.11B and then the NEAR target as in Figure 5.11A. The opposite sequence provides a disaccommodation step stimulus. The step stimulus is synchronized with the acquisition of the OCT and is triggered by an electronic system developed in the control unit of the system. The movable auxiliary lenses were manually moved to set the amplitude of the step stimulus. The distance from the Badal lens can be adjusted with a ruler mounted on the side of each arm. The amplitude of the step stimulus varies from 0 to 9.55D. Figure 5.13 shows the optomechanical design of the accommodation target system. The system was built using a customizable commercial cage system for optics (Thorlabs, USA) and custom made mechanical parts.

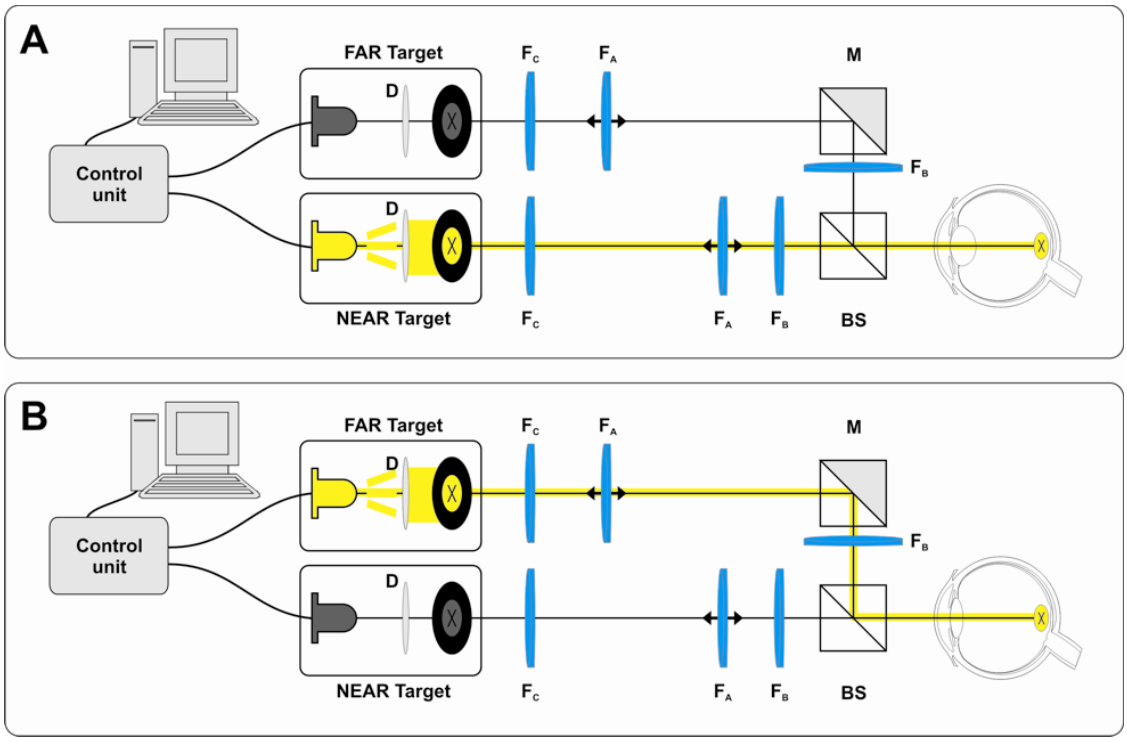

Figure 5.11: Schematic of the accommodation unit. The light path of the near target (A) and the far target (B) is shown in yellow.

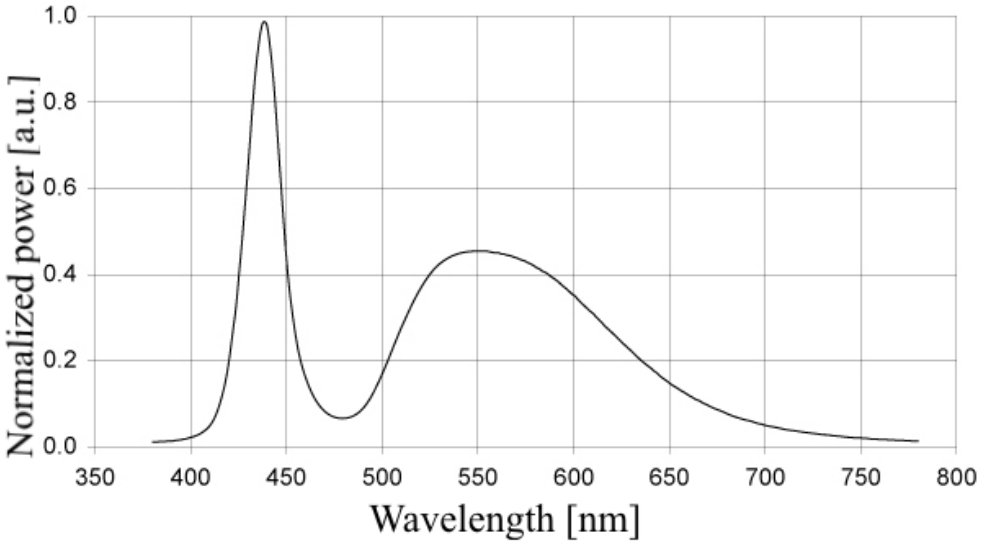

Figure 5.12: Spectral distribution of the White LED (The image was modified from technical datasheet of the components. www.ledsupply.com).

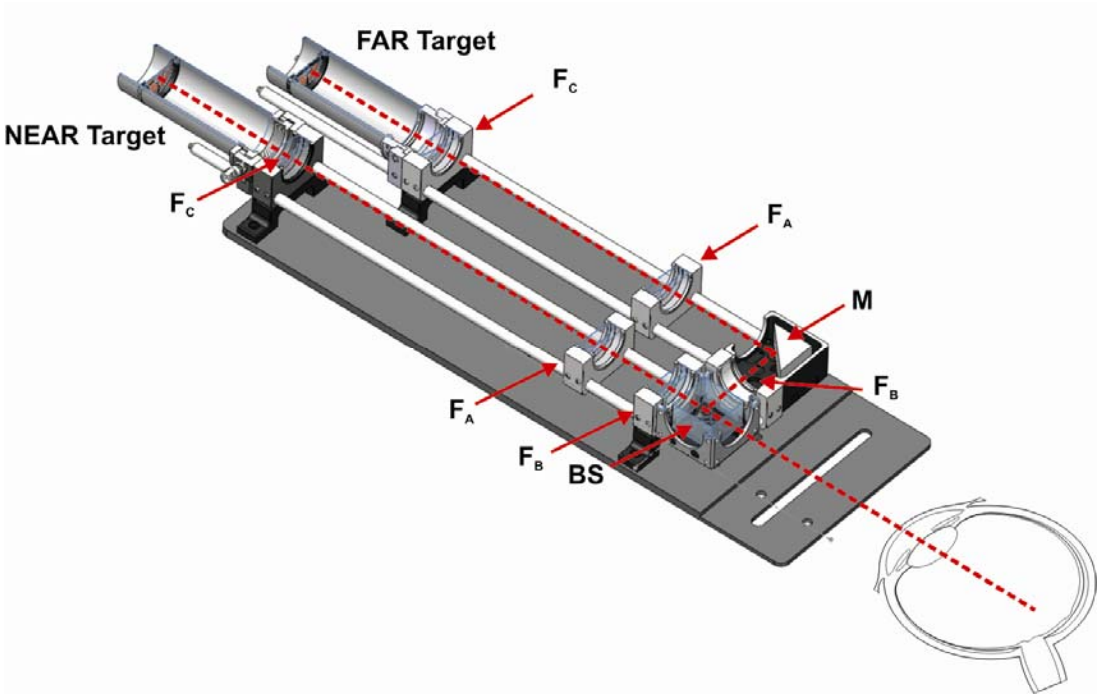

Figure 5.13: Section of the optomechanical design of the accommodation unit.

5.4. Slit-lamp mounted system design

Aligning the human eye with respect to the optical axis of the OCT imaging system and the accommodation unit is one of the challenging tasks of imaging accommodation. The human eye does not have a true optical axis because it is not a centered optical system (Bennett and Rabbetts, 1998). For simplicity, we will consider the schematic emmetropic eye reported in Figure 5.14A. For the schematic eye, the optical axis is defined as a straight line connecting the ocular surface vertices. The visual axis is the line that goes through the nodal points N and N' of the eye and reaches the fovea. Another axis connects the fovea via the centers E and E' of the entrance and the exit pupil, which is called line of sight (Figure 5.14A). The line-of-sight is generally the reference axis for retinal imaging systems or diagnostic systems, since it is easy to find the pupil center. Due to the foveal eccentricity (4º to 8º toward temporal and 2º toward inferior retina) the axes to the fovea are tilted of approximately 5º with respect to the optical axis, with a variability among the subjects of ±2º (Bennett and Rabbetts; 1998, Drexler 1997; Obstfeld et al, 1982). If the OCT delivery probe and the accommodation target unit share the same optical axis, the anterior eye segment of a subject fixating the target will appear tilted as in Figure 5.14B. Aligning the optical axis of the eye coincident with the optical axis of the OCT delivery optics is key to minimize the image distortion and to visualize the anterior segment surfaces with high contrast. Scanning rays parallel to the optical axis simplifies the post processing needed to display geometrically correct images. If the eye optical axis is angled as in Figure 5.14B, the principal direction of the light back reflected by the crystalline lens will not be coaxial with the incident light. Thus, the efficiency of light collected by the delivery probe, and therefore the sensitivity

of the system, will be lowered. The visibility of the parallel rays at the posterior surface of the crystalline lens is limited by the aperture width of the pupil. If the eye optical axis is angled, the aperture of the pupil narrows and limits further the visibility of the posterior lens. This effect is particularly detrimental during pupil constriction. Based on the previous consideration, the optical axes of the two instruments need to be tilted with respect to each other while imaging accommodation, with an angle that varies among subjects. In order to provide a variable angular displacement between the instruments optical axes, the OCT probe was coupled to the target unit so that it can be rotated during the imaging procedure to find the optimal alignment while the subject fixates the target.

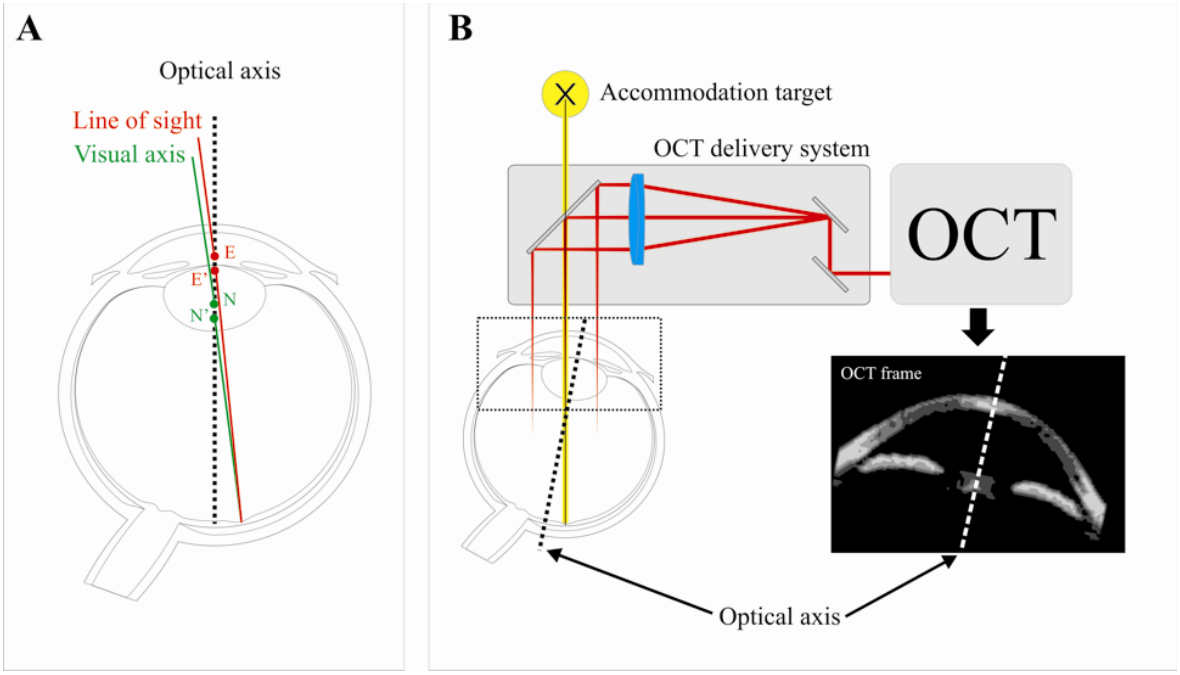

Figure 5.14: The schematic emmetropic eye with the optical axis, the visual axis and the line of sight. **(A)** Effect of the misalignment between the eye optical axis and the line of sight on the OCT image. **(B)**

Figure 5.15A shows the optomechanical design of the coupled systems. The red dotted lines in Figure 5.15A show the location where the OCT delivery system is placed on the base plate of the accommodation unit. Supports were included on the beam splitter mount to hold a trial case lens to neutralize the eye's refractive error (Figure 5.15B). The trial case lens does not interact with the optical path of the OCT delivery system. Figure 5.15C shows the paths of the OCT beam and the target illumination once the two instruments are combined. The dichroic mirror (DM) in the OCT probe allows the target light to be transmitted and the OCT light to be reflected into the anterior eye segment. The OCT probe can be rotated around the *z* axis and translated along the *x* axis in the image so that correct alignment of the OCT image can be achieved while the subject fixates the target. The light path of the near target is highlighted in Figure 5.15C (yellow dotted line). The system was adapted to a slit-lamp mount (Ocular Instrument Inc., USA) to allow precise positioning of the subject during the experiments. Figure 5.16 shows a photograph of the combined system.

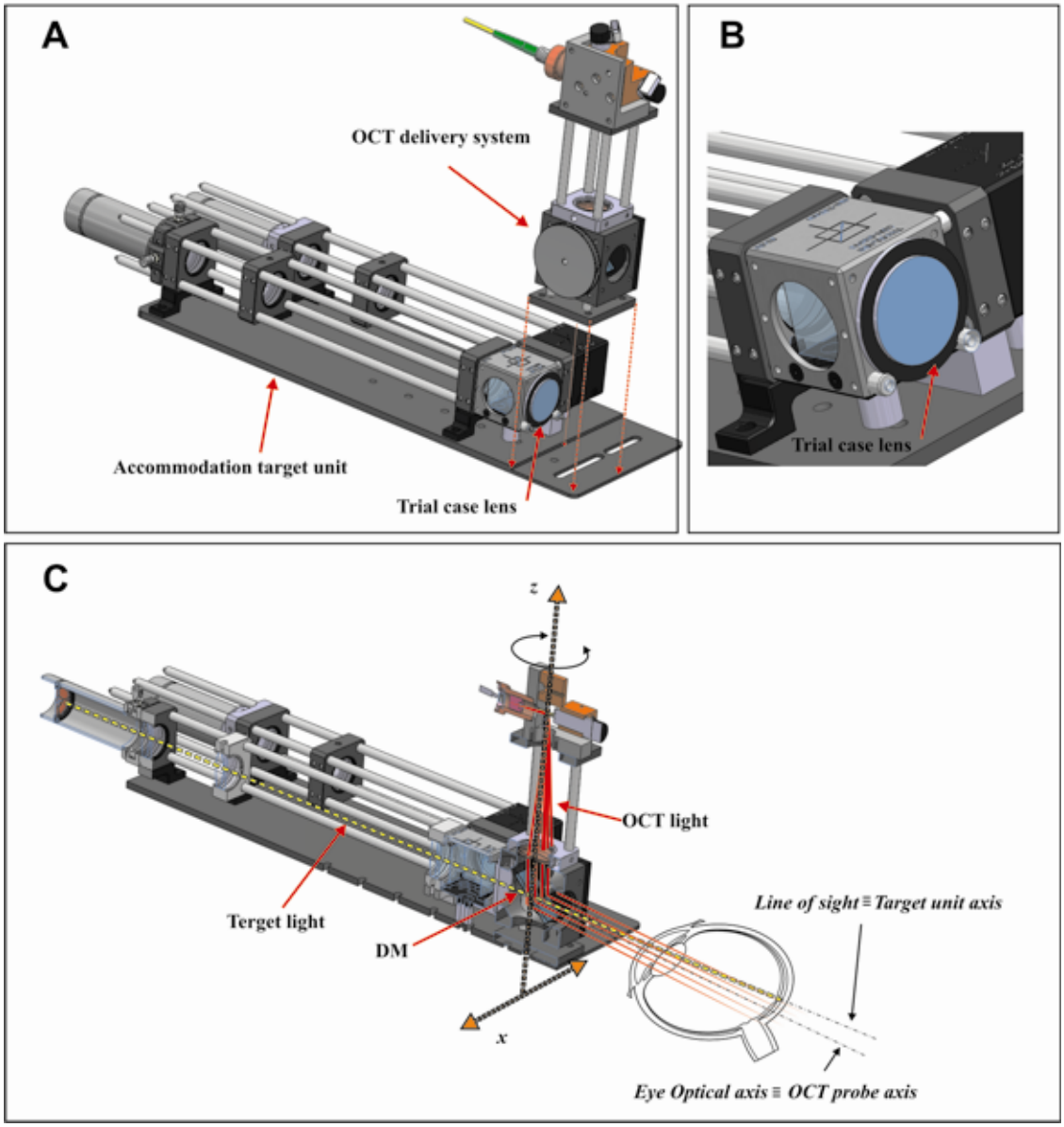

Figure 5.15: Optomechanical design of the accommodation target unit and OCT delivery probe coupled systems. The red dotted lines show the location where the OCT delivery system is mounted on the base plate of the accommodation unit. **(A)** Detailed view of the **s**upport holding a trial case lens to neutralize the eye's refractive error. **(B)** Section of the optomechanical design showing the light path of the near target arm of the accommodation unit and the OCT transverse scanning system. The OCT delivery head can be rotated around the *z* axis and translated along the *x* axis. **(C)**

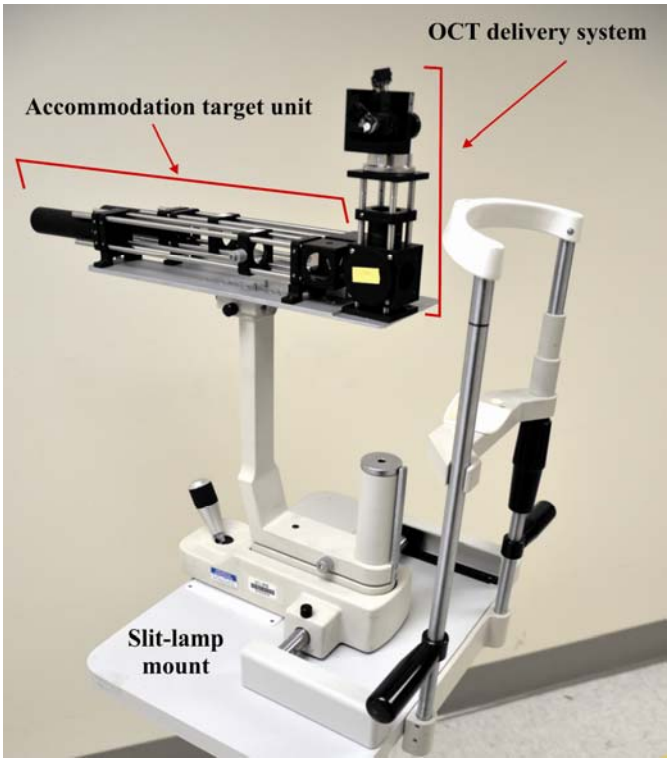

Figure 5.16: Photograph of the accommodation target unit coupled to the OCT delivery system and mounted on a slit-lamp stand.

5.5. Preliminary imaging tests

5.5.1. Anterior segment imaging

The imaging system was first tested without using the optical switch in the reference arm to assess the ranging capability of the spectrometer *in vivo*. Images were recorded on three subjects of age 24, 29 and 35 years. Figure 5.17A shows an OCT image of the anterior segment of the right eye of a 24 year-old subject acquired on the horizontal meridian crossing the apex of the cornea. The experiment was conducted with the subject fixating on the distant target of the accommodation system that was set at 0D (accommodation relaxed). The image consists of 1000 A-lines of 2048 pixels each, which corresponds to a frame size of 16mm × 7.6mm (lateral × axial) when the mean group

refractive index of the anterior segment is taken to be 1.37 at 840nm and it was acquired in 50ms. The system produced images of the whole anterior segment of this subject in one acquisition. The main structures of the anterior segment are recognizable from the bottom to the top of the image: cornea (C), anterior chamber (AC), crystalline lens (L), iris (I) and angle (A). The iris limits the lateral view of the crystalline lens. The effect of the sensitivity fall-off with depth is observable. The system was adjusted so that the zero delay position, which produces the highest sensitivity, corresponds to the posterior lens (bottom of the image in Figure 5.17A). The signal strength at the cornea, which is located at the end of the depth range, is significantly lower. The image was optimized during the imaging by displacing the zero delay and the beam waist of an amount Δ. We empirically found that the image was optimized for Δ~2mm.

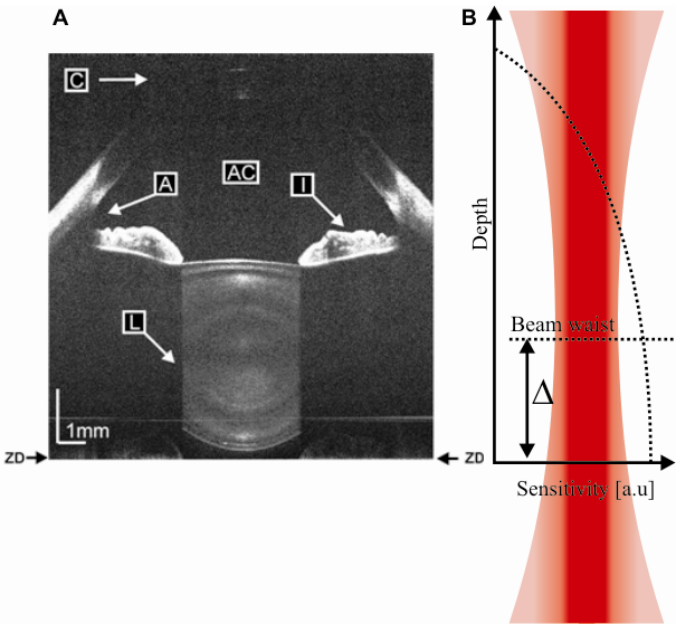

Figure 5.17: (A) Single frame OCT image of the whole anterior segment of a 24 year-old human eye. The main ocular structures are indicated: cornea (C), anterior chamber (AC), crystalline lens (L), iris (I) and angle (A). Image size: 16mm (lateral) × 7.8mm (axial). Zero delay location (ZD) is also indicated. The effect of the sensitivity fall-off with depth **(B)** is observable in the image. The beam waist of the focused delivery light is about 2mm above the zero delay location.

The bright line that can be seen about 1mm above the zero delay position is an artifact due to back reflections from optical fibers in the sample and reference arms.

5.5.2. Internal crystalline lens structure

The internal structures of the lens were identified in the OCT image. The crystalline lens zones of a 29 year-old subject were labeled according to the Oxford classification method (Sparrow et al, 1986) (Figure 5.18A). The outermost zone of the crystalline lens is the capsule, which can be distinguished as a narrow bright region. Moving toward the center, zones of low and high scattering can be distinguished, which correspond to the cortex and the nucleus. The cortex is arranged in anterior and posterior cortical zones. The anterior and posterior zones of the cortex are further divided in four sub-cortical zones defined as C1-C4 (Sparrow et al, 1986). Figure 5.18B shows a close up view of the anterior lens where the four cortical zones are labeled. C1 consists of two zones, one of low scattering ($C1_{\alpha}$) and the other one of high scattering ($C1_{\beta}$), that are displayed with a dark and a bright narrow region, respectively. C3 is a bright cortical zone that shows higher scattering, while the darker C2 and C4 show lower scattering. The cortex-nucleus boundary is displayed as a transition between the dark band C4 and the following narrow bright zone. The internal zones of the nucleus cannot be clearly visualized in Scheimpflug (Sparrow et al, 1986) images and are not distinguishable in the OCT image either. An alternative method to quantify the internal structure of the lens is to analyze the intensity profiles along the optical axis (Dubbelman et al, 2003). Five contiguous reflectivity profiles that approximately cover 120μm were extracted from the central region of the lens.

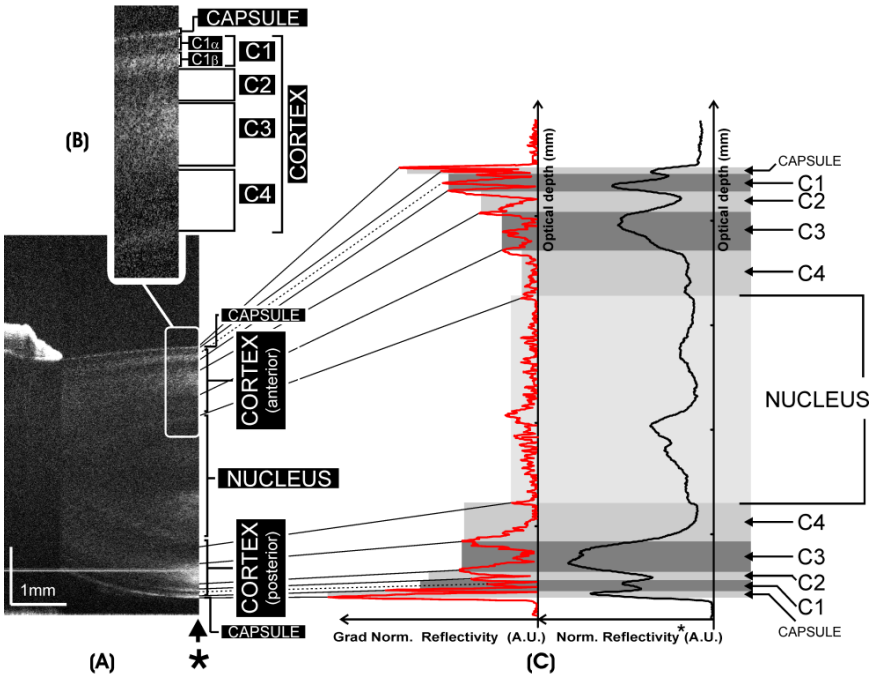

Figure 5.18: **(A)** Magnified section of an OCT image of the crystalline lens. The different zones of the lens are labeled according to a published classification method using Scheimpflug images. **(B)** Two-fold magnification of the marked area in **(A)**. The zones of the cortex were labeled from the top to the bottom as C1($C1_{\alpha}$,$C1_{\beta}$), C2, C3 and C4. **(C)** The average reflectivity (black profile) of five A-scans located at the center of the lens (see arrow in A). The gradient of the reflectivity (red profile).

The reflectivity profiles were averaged in order to reduce noise and their gradient was calculated (Figure 5.18B). Local maxima of gradient reflectivity correspond to boundaries between regions of different reflectivity. The gradient helps identify more accurately structures such as the capsule, and the main zones of the cortex and the nucleus. The thickness of the cortical zones and the nucleus of this subject in the relaxed state (0D) are summarized in Table 5.2. Geometrical distances were calculated assuming an average group refractive index equal to 1.40. These results are consistent with the results of reported before (Dubbelman et al, 2003), except for C4, which was not measured in their study.

Anterior Cortical Zones Thickness (mm)	Nucleus Thickness (mm)	Posterior Cortical Zones Thickness (mm)
C1=0.19	2.05	C1=0.12
C2=0.14		C2=0.09
C3=0.42		C3=0.39
C4=0.36		C4=0.21
Anterior Cortex=1.11		Posterior Cortex =0.81

Table 5.2: Thickness of the nucleus and the cortical zones of a 29 year-old subject in the relaxed state (0D). Total lens thickness is 3.97mm.

5.5.3. Anterior segment imaging with the switching delay line

When the spectrometer is combined with the optical switching method described in section 4.5 utilizing two switching arms, the free-space scan depth can be extended to a value greater the axial range of the spectrometer. The bottom of Figure 5.19 shows a representation of an anterior segment of an eye. Four different alignment schemes of the optical switch can be used to account for the sensitivity decay in imaging the anterior segment. The four alignments are based on the relative displacement between the two zero-delay locations provided by the optical switch, ZD1 and ZD2 and are displayed in Figure 5.19A,B,C and D. In Figure 5.19A reference arm mirror M1 is positioned such that its zero-delay location (ZD1) is approximately behind the lens anterior surface. Reference arm mirror M2 is positioned such that its zero-delay location (ZD2) is posterior to the posterior crystalline lens surface.

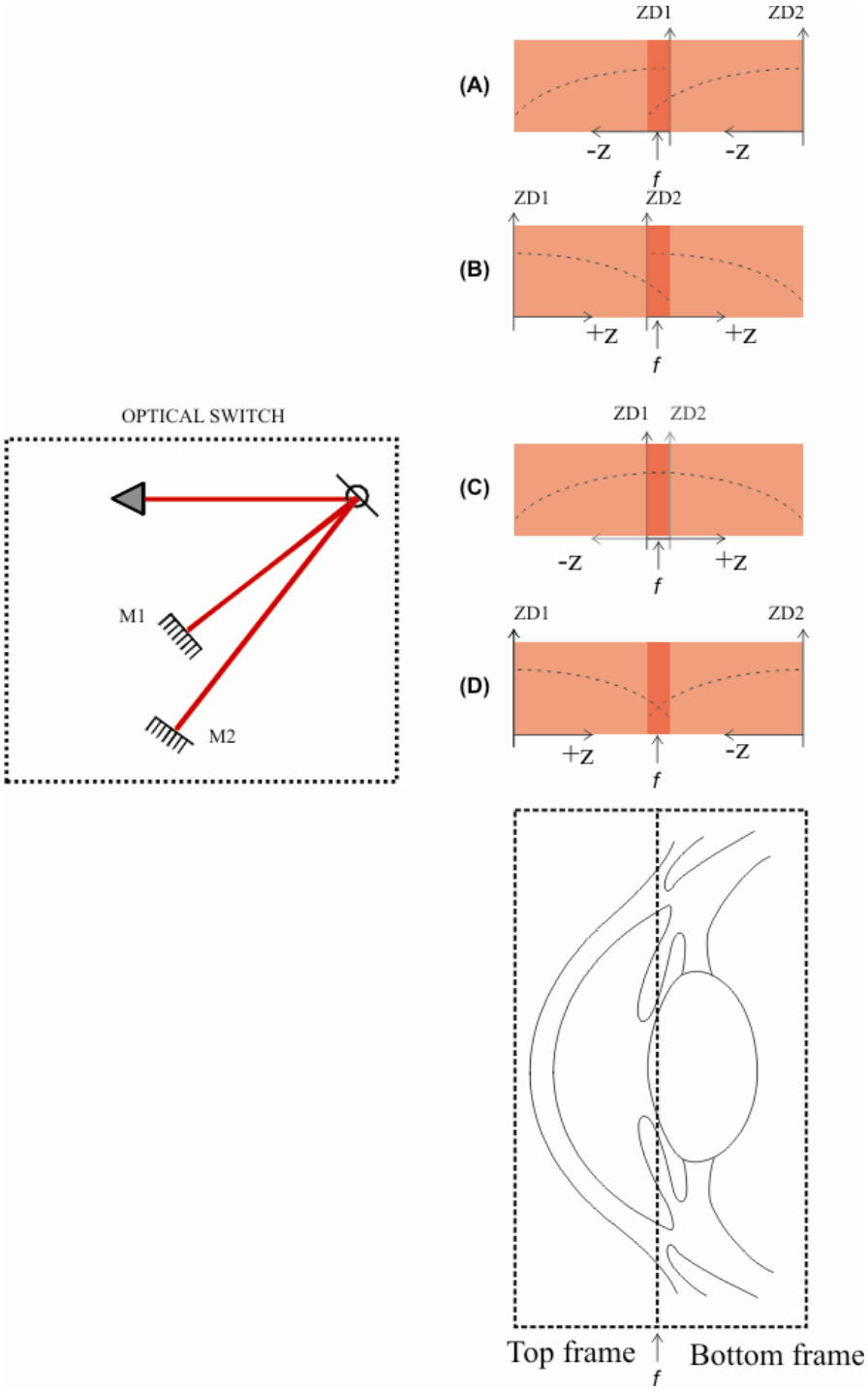

Figure 5.19: The four alignments of the optical switch are displayed (A,B,C and D) together with a schematic of the anterior segment. The anterior segment image is divided in a top and a bottom frame. The sensitivity decay is represented as a black dotted line in A, B, C and D. Alignment (D) provides the best overall sensitivity.

The first frame acquired extends from the cornea down through the anterior chamber up to the back of the anterior lens surface, which is captured on the negative side of the top frame. When the reference arm optical switch is activated, the zero-delay location shifts to ZD2, and the second frame captures the crystalline lens and the posterior lens, which is recorded on the negative side of the bottom scan. After the two frames are captured, they are combined in the computer by cropping the low-sensitivity end of each scan and creating a new image, where the two frames are joined together at the crop line *f*. The crop line *f* can be moved to make the signal transition between the two frames smooth so they can be merged into a new image with no artifacts. In order not to crop information out of the new image, the crop line *f* can be moved only within the frame overlap (see dark red region in Figure 5.19A). With this configuration, if the sensitivity roll-off is significant, there is a considerable sensitivity step in the transition between the two frames, despite the position of the crop line. The sensitivity step can be reduced by moving ZD1 closer to ZD2. However, this would shorten the overall axial range.

In Figure 5.19B reference arm mirror M1 is positioned such that ZD1 is approximately at the anterior cornea surface. Reference arm mirror M2 is positioned such that ZD2 is approximately at the center of the crystalline lens. Compared to the case in Figure 5.19A, the positive sides of the scans are taken instead of the negative ones and ZD1 and ZD2 are shifted to the left. The two solutions presented in Figure 5.19A and B are essentially equivalent, hence, all the considerations made for the previous case hold valid for this scheme as well.

In Figure 5.19C, initially the reference arm is positioned on mirror M2. The first frame recorded extends from the cornea down through the anterior chamber to the back of the anterior lens surface, which is captured on the negative side of the top scan. When the reference arm optical switch is activated, the zero-delay location shifts to ZD1, and the second frame captures the crystalline lens and the posterior lens, which is recorded on the positive side of the bottom scan. Although the sensitivity transition between the two frames seems smoother than the previous case, this schematic is not convenient because the new image is created by cropping the high-sensitivity end of each scan.

In Figure 5.19D, the delay line is initially positioned on mirror M1 such that ZD1 is approximately at the anterior cornea surface. The first frame recorded stretches from the cornea down through the anterior chamber to the back of the anterior lens surface, which is captured on the positive side of the top scan. When the reference arm optical switch is activated, the zero-delay location shifts to ZD2, and the second frame captures the crystalline lens and the posterior lens, which is recorded on the negative side of the bottom scan. In this configuration, the sensitivity transition between the two frames is smooth, and the schematic is convenient because the new image is created by cropping the lower-sensitivity end of each scan. For these reasons, this last alignment was selected for the optical switch.

Data acquisition using the switching delay line was performed on a 35 year-old healthy subject to test the delay line in the proposed configuration. Two images of the anterior segment were recorded at different depths using the optical switch. The optical switching time is about 250 μs. Figure 5.20A shows the image captured at a first zero-delay location ZD1 and Figure 5.20B shows the image captured at a second zero-delay

location ZD2. These two images are used to form a composite image in Figure 5.20C using the method described above. (Figure 5.20A and Figure 5.20B). The two frames together cover the entire anterior segment and the transition was not visible in the composite image. The free-space depth range of the spectrometer alone (10.6mm) could be extended to 12.7 mm, which is sufficient to image the entire anterior segment of a human eye, from anterior cornea surface to the posterior crystalline lens surface with increased sensitivity. The amount of distance that the two images overlap is adjustable using a custom post processing software that was developed in Matlab (Mathworks, Massachusetts, US). The overlapped region in Figure 5.20 (red region) is about 10mm. The two frames may also be combined with other methods such as, for instance, averaging (or summing) of the overlapping regions of both frames. Averaging (or summing) the overlapping regions in a limited dynamic range domain is beneficial only if the signals produced by the same anterior segment features in

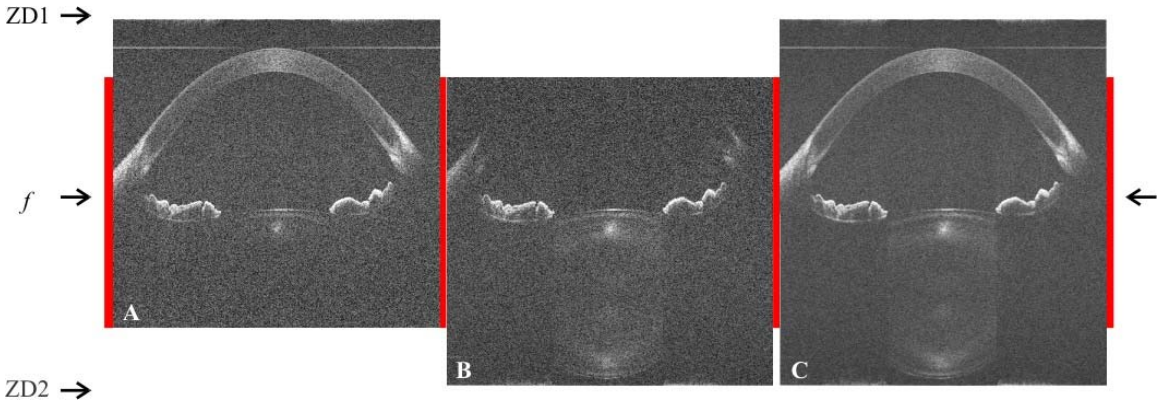

Figure 5.20: (A) OCT cross-sectional images of a 35 year old human eye from the anterior surface of the lens to the posterior lens capsule. The image was acquired using the switch positioned on M1. **(B)** OCT cross-sectional images of a 35 year old human eye from the anterior surface of the cornea to the anterior lens. The image was acquired with the switch positioned on M2. **(C)** The composite image was obtained by stitching and cropping along the line *f* the frame A and B. The red area displays the frame overlap.

the overlapping regions of both frames are above the noise floor level. The effect of averaging (or summing) is an increase of contrast in the overlapping regions that will make the image transition look uneven in the composite images. For this reason we preferred cropping the frames instead of averaging the frame overlap.

5.5.4. Accommodative response imaging

The accommodative response was imaged in the right eye of two subjects: a 24 year-old and a 35 year-old. The accommodation unit was set so that the near target produced a 7D stimulus and the far target a 0D stimulus. To align the system with the subject eye, the far and near target were alternately illuminated together so that the subject could look at both targets simultaneously from the beam splitter. The left eye of the subject was covered. The subject could rotate the slit-lamp mount until the two targets were aligned while the operator rotated the OCT delivery system until the iris in the real time OCT image provided by the software was oriented perpendicular to the direction of the incident light. The subjects were trained to know in which direction to accommodate before the step was provided. Once the system was aligned, a series of 30 cross-sectional images were acquired while a step stimulus from 0D to 7D was provided to the subject. The acquisition time per each composite frame was 50ms plus 250µs for the switching operation. The recording time was set long enough to allow the accommodation process to end. The images were acquired along the horizontal meridian crossing the apex of the cornea. Figure 5.21 shows OCT images before the step stimulus was provided (relaxed state) and at the maximum accommodation state after the step stimulus was provided for the 24 year-old (Figure 21A and B) and 35 year-old (Figure 21C and D). The images were composed of 1000 A-lines over a width of 16mm.

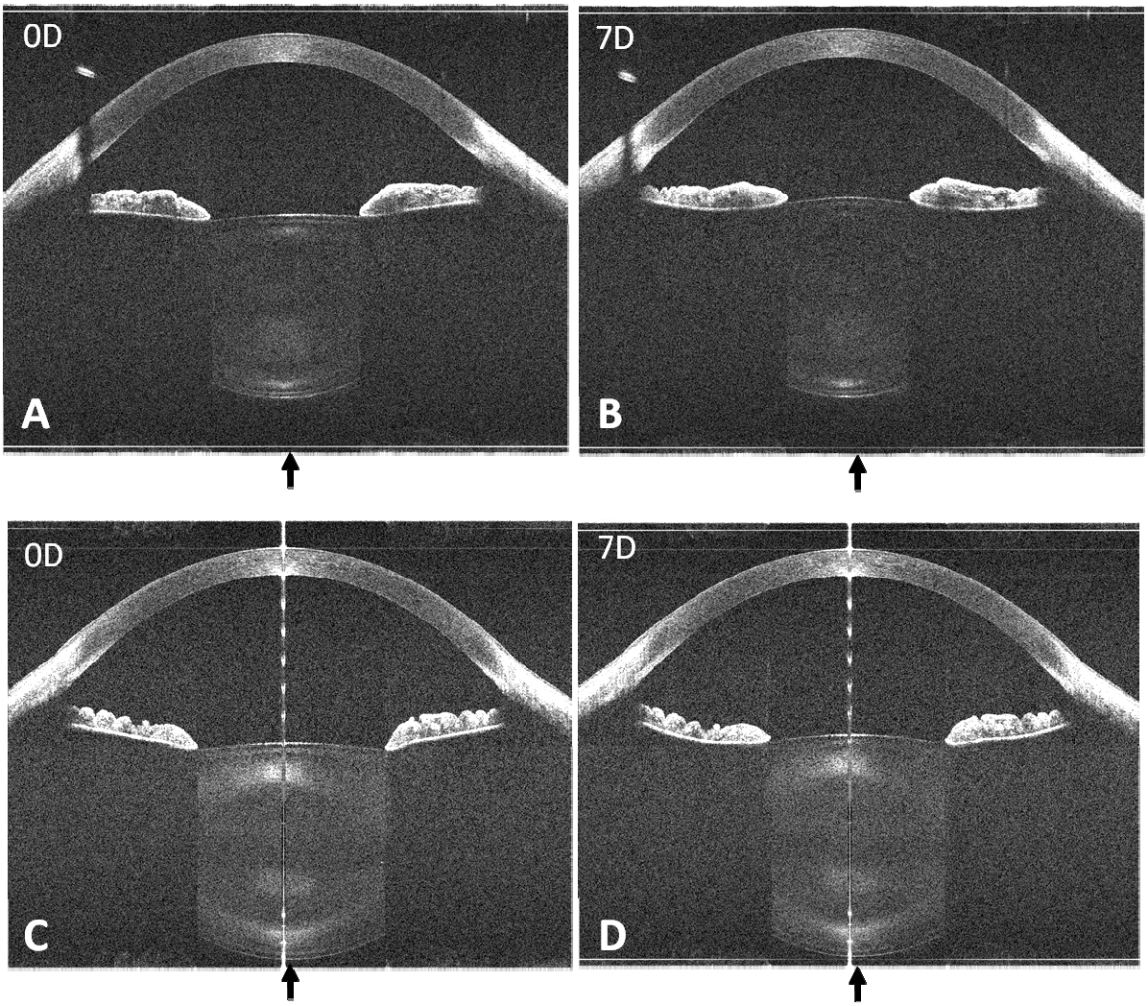

Figure 5.21: OCT cross-sectional images of the anterior segment acquired on a 24 year-old subject in the relaxed state **(A)** and in response to a 7D accommodative stimulus **(B)** and on a 35 year-old subject in the relaxed state **(C)** and in response to a 7D accommodative stimulus **(D)**.

Changes in curvature and thickness of the crystalline lens are observed in the 24 year-old subject. As expected, the lens is thicker and its surfaces are steeper in the accommodated state (7D stimulus) compared to the relaxed state (0D stimulus). For the 35 year-old subject, the changes in lens shape are minimal, a consequence of the loss of accommodation with age. The unaccommodated lens of the 35 year-old subject (Figure 5.21C) is also thicker than that of the 24 year-old lens (Figure 5.21A), due to the continuous growth of the adult lens. The OCT images also show that the pupil

contraction during accommodation is different in the two subjects. In addition, the backscattered signal strength is stronger in the 35 year-old lens, which corresponds to the progressive age-related changes in lens density (Said et al, 1959).

Movies were also captured from the processing and display software window during real-time display of the dynamic process of lens accommodation in the two subjects. The images in the movies were continuously displayed during the accommodative responses from the relaxed state (0D stimulus) to a 7D accommodative stimulus and back to the relaxed state with a frame rate of approximately 20 frames/sec.

The changes in thickness of the crystalline lens were quantified along the central A-line. Geometrical distances were calculated assuming an average group refractive index for both lenses equal to 1.40 at 840nm. These preliminary findings are consistent with the results of previous studies using Scheimpflug imaging (Dubbelman et al, 2003). The changes in thickness of the anterior chamber were also quantified along the central A-line. Geometrical distances were calculated assuming an average group refractive index for the anterior chamber equal to 1.34 at 840nm and an average refractive index for the cornea of 1.38 at 840nm. The preliminary findings are reported in Table 5.3 and are consistent with the results of previous studies (Fontana et al, 1980; Martola et al, 1968).

Age (years)	*Stimulus (Diopters)*	*Total Lens Thickness (mm)*	*Anterior chamber depth (mm)*	*Cornea Thickness (mm)*	*Total AS Thickness (mm)*
24	0	3.64	3.09	0.52	7.25
	7	3.91	2.83	0.52	7.26
35	0	4.24	3.20	0.53	7.97
	7	4.33	3.15	0.53	8.01

Table 5.3: Anterior segment structure length for a 24 and a 35 year-old subjects in the relaxed (0D stimulus) and accommodated (7D stimulus) states.

5.6. Discussion, summary and conclusion

An optical delivery system was developed for *in vivo* extended depth imaging of the anterior segment using the SD-OCT system. The delivery system features high lateral resolution (52 to 140μm), long transversal range (20mm) and long depth of focus (5.1mm).

The system was combined with a unit that provides accommodation and disaccommodation step stimuli with high spatial resolution of about 0.04D/mm over a power scale from 0D to 9.55D.

Accommodation is a response to an out of focus retinal image and it depends on several factors, such as the duration of the step stimulus, the contrast of the target, the size, the spatial frequency and the luminance (Bennett and Rabbetts, 1989). In this project we have setup an accommodation target unit that did not take into account all of these factors. The unit was built to perform preliminary studies on accommodation using OCT and provide a platform that can be used for further studies and can be improved taking into account the parameters of the target. Another effect that was not considered in the design of the accommodation unit is the accommodative lag, which is the difference between the accommodation demand and the accommodation response. Because of accommodation lag, the ocular vergence is lower than the stimulus vergence, with a difference that shows a great variability between individuals. Because of the accommodation lag variability, an objective measurement of the ocular vergence would be desired instead of referring to an equivalent dioptric distance. Simultaneous measurements of refraction and one dimensional biometry of the anterior segment during accommodation were demonstrated and used by others to investigate the thickness

changes in the anterior segment during accommodation (Ostrin et al, 2006). In the future, a refractometer can be coupled with the accommodation target to provide objective measurements of the ocular vergence.

The combined unit was mounted on a slit-lamp stand to perform imaging of accommodation on human subjects. The preliminary experiments show that the combination of the high resolution spectrometer and the optical delay line allows us to extend the axial range of the spectrometer from 10.63mm to 12.7mm. This axial range is enough to image the entire anterior segment. The abrupt deterioration of the signal due to the spectrometer fall-off limited the overall axial range longer to 12.7mm. Moreover, it significantly increased the width of the frame overlap to about 10mm. Any improvement to the sensitivity fall-off will immediately extend the imaging range further by reducing the frame overlap that is required to construct the final composite frame.

The feasibility of imaging the changes of the entire anterior segment during accommodation and with age was demonstrated. In this test, a relatively large step stimulus (0D-7D) was provided to two subjects at different ages (24 and 35 year-old) and OCT images of the anterior segment were acquired simultaneously. Thickness measurements of the anterior segment structures along the central A-line were performed, which compare well with published results. However, to obtain biometric data such as intraocular distances, surface curvature and asphericity in two- and three dimensions, correction of image distortion due to the refraction of the probe beam at the ocular surfaces is needed. In the next chapter, we report the development and validation of an algorithm for the correction of OCT image distortion in two-dimensions.

CHAPTER 6. BIOMETRY OF THE ANTERIOR SEGMENT AND ACCOMMODATION

6.1. Objective

The first objective of this part of the project is to test the capability of the system in quantifying the dynamic changes occurring in the crystalline lens during accommodation. Experiments will be conducted on one subject. A series of cross-sectional images at the same position will be acquired after a stimulus step of amplitude equal to 7D is provided in both directions, accommodation and disaccommodation. The dynamic changes in the lens thickness, corneal thickness, anterior chamber depth and anterior segment length will be measured.

The second objective of this chapter is to demonstrate the capability of the SD-OCT to provide accurate biometric data of the lens and the anterior segment in two-dimensions at different accommodative states. A method to correct the imaging distortions of the OCT images due to refraction of the beam through the consecutive ocular surfaces of the anterior segment will be developed. The correction method will be first validated on a custom built model eye with known geometry and optical properties. An experiment will be conducted on two subjects at different ages. For each subject, cross-sectional anterior segment images approximately at the same position into the eye will be acquired at different accommodative states (0D, 3D and 7D). The curvature of the lens surfaces will be extracted from the sections and compared.

6.2. Dynamic changes of thickness during accommodation

6.2.1. Purpose

Changes in lens thickness, anterior chamber depth and anterior segment length have been previously studied during accommodation. The anterior segment distances have been

previously measured at fixed accommodative states using A-scan ultrasonography (Storey et al, 1983, Beauchamp et al, 1985), partial coherence interferometry (Drexler et al, 1997) and Scheimpflug imaging (Dubbelman et al, 2003, Dubbelman, et al 2005). Dynamic one dimensional biometric changes of the anterior segment distances have been measured in response to accommodation and disaccommodation step stimuli in human (Storey et al, 1990, Beers and Van Der Heijde, 1994) and Rhesus monkeys (Vilupuru, 2003) using ultrasonography. The purpose of this test is to demonstrate the capability of the system to perform dynamic quantification of the anterior segment structures length in response to a step stimulus.

6.2.2. Methods

The accommodative response to a step stimulus in both directions was imaged in the right eye a 35 year-old subject. First, the accommodation unit was set to provide a step stimulus from 0D to 7D (accommodation). The far stimulus (0D) was illuminated and the subject was ask to fixate the target. The subject was trained to know which direction to accommodate before imaging was performed. Three frames were acquired at the relaxed states in 0.24ms. Immediately after three frames were acquired, the 7D accommodation step stimulus was provided and fifty frames were acquired in four seconds to image the dynamic response of the anterior segment (Figure 6.1A). The frames were acquired along the meridional horizontal plane of the anterior segment. The maximal optical thickness of cornea and the lens, the optical anterior chamber depth, and the optical length of the anterior segment were measured on each OCT image.

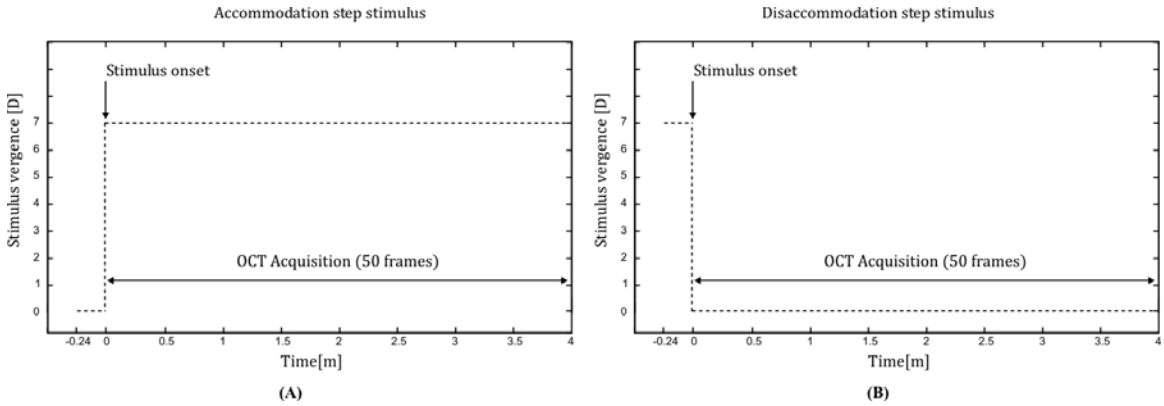

Figure 6.1: Timing and acquisition diagram for the accommodation step stimulus **(A)** and the disaccommodation step stimulus **(B)**.

The measurements were performed along the apex of the optical surfaces. The geometrical thicknesses of the anterior segment structures were obtained by dividing the optical length measurements by the group refractive index of the each ocular structure (cornea, aqueous humor and lens) at 840nm (Table 6.1). The group refractive index of the cornea and the lens were obtained by measurements performed on *ex vivo* samples by Uhlhorn et al (1998) and (2008), respectively. The refractive index of the aqueous humor was extrapolated for a wavelength of 840nm using a published method (Atchison and Smith, 2005). The same experiment was repeated by setting the accommodation target unit to provide a step stimulus from 7D to 0D (disaccommodation) as reported in Figure 6.1B.

Ocular tissue	Refractive index (at 840nm)
Cornea	n_C =1.387
Aqueous humor	n_A =1.342
Crystalline lens	n_L =1.415

Table 6.1: Group refractive index of the cornea (Uhlhorn et al, 1998), the crystalline lens (Uhlhorn et al, 2008) and the aqueous humor (Atchison and Smith, 2005) at 840nm.

6.2.3. Results

Figure 6.2 (Top) reports an OCT frame that was recorded at the time the accommodation step stimulus was provided to the subject (0s) and 1.2s and 3.7s after the stimulus was induced. Figure 6.2 (Bottom) reports an OCT frame that was recorded at the time the disaccommodation step stimulus was provided to the subject (0s) and 1.2s and 3.7s after the stimulus was induced. The red lines on the OCT images mark the location were the thickness measurements were performed.

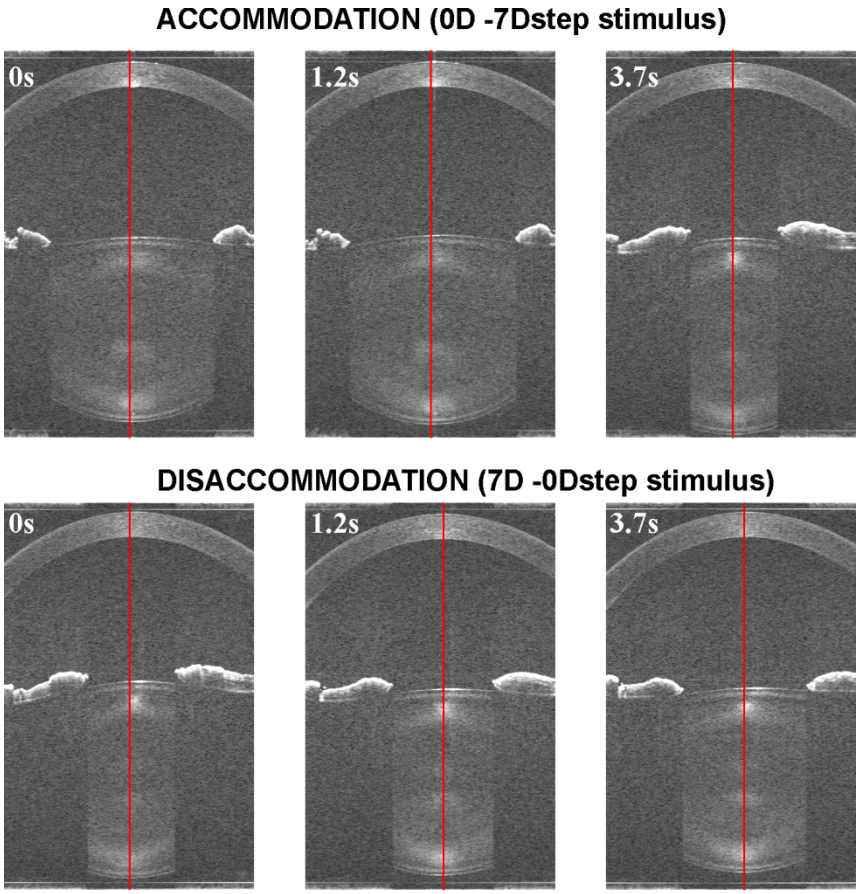

Figure 6.2: The OCT frame that was recorded at the time the accommodation step stimulus was provided to the subject (0s) and two frames recorded 1.2s and 3.7s after the stimulus was induced, are reported. **(Top)** The OCT frame that was recorded at the time the disaccommodation step stimulus was provided to the subject (0s) and two frames recorded 1.2s and 3.7s after the stimulus was induced, are reported. **(Bottom)** The red lines mark the location were the thickness measurements were performed.

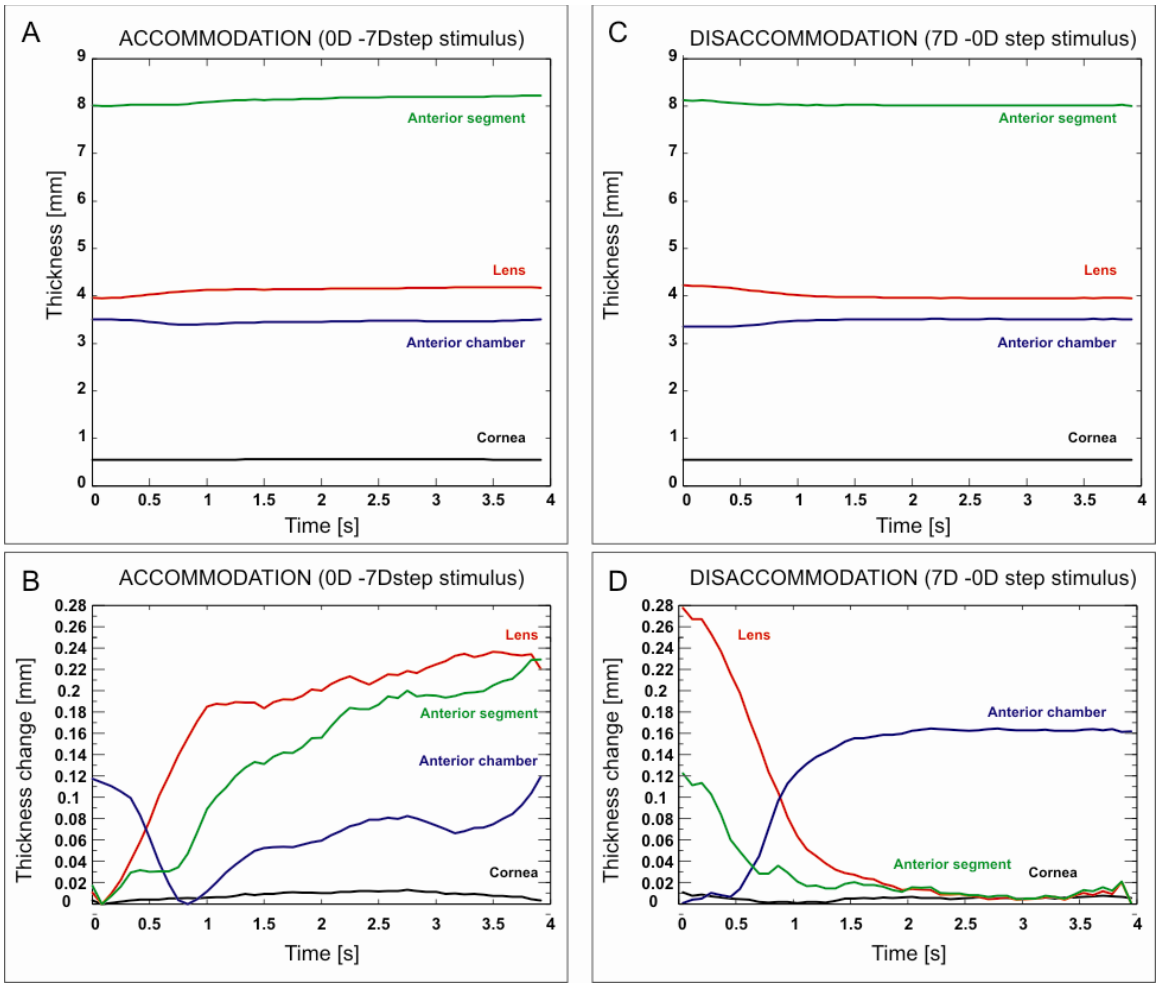

Figure 6.3: The dynamics anterior segment distances are reported in response to an accommodation step stimulus from 0D to 7D. **(A)** The dynamic changes in distance in response to the accommodation step stimulus are reported **(B)**. The dynamic distances are reported in response to a disaccommodation step stimulus from 7D to 0D. **(C)** The change in distance in response to the disaccommodation stimulus are reported **(D)**. The step stimulus was induced at the time t=0s.

The biometric distances of the anterior segment structures over time during accommodation are displayed in Figure 6.3A. Figure 6.3B shows the dynamic thickness changes of the ocular structures during accommodation. Figure 6.3C shows the dynamic thickness recordings of the anterior segment structures over time during disaccommodation. The dynamic changes are shown in Figure 6.3D.

The thickness of the cornea is expected to be constant during accommodation and disaccommodation. Figure 6.3B and D show minor corneal thickness changes during the dynamic responses. In both experiments, the maximal corneal thickness variation is about 10μm, which is comparable to the axial resolution of the OCT system. This variation is attributable to the measurements uncertainty and small eye movements. Thus, the thickness of the cornea assessed with our system can be assumed constant during accommodation and disaccommodation. The mean central corneal thickness was equal to 550 μm with a standard deviation of ±5μm, which agrees with the values reported by Martola et al (1968) and Dubbelman et al (2003).

The recordings show that crystalline lens thickness increases during accommodation (Figure 6.3B red line) and decreases during disaccommodation (Figure 6.3B red line), as expected. The dynamics of lens thickness changes in Figure 6.3A and B are similar to what has been reported before using continuous high-resolution A-scan ultrasonography to study the dynamic biometric changes in the human eye during accommodation (Storey et al, 1999) and during stimulated accommodation in Rhesus monkey eyes (Vilupuru et al, 2003). The thickness of the lens was 3.92mm in the relaxed state (0D) and the amplitude of the lens thickness increase was 0.32mm after the step stimulus was applied. During disaccommodation, the thickness decreased of about 0.32mm reaching a thickness of 3.76mm in the relaxed state (D). The average change of the lens thickness per Diopter for a ~35 year-old subject found by Dubbelman et al (2003) during accommodation was 0.045mm/D. According to this value, the change induced to the crystalline lens thickness upon an accommodative step stimulus with a 7D

amplitude is 0.315mm, which is in very good agreement with the change we found in our experiment (0.32mm).

It is known that the crystalline lens thickens and moves forward during accommodation. As a result, the anterior chamber depth decreases during accommodation, which is shown in our recording in Figure 6.3B (blue line). The dynamic thickness measurements show a decrease from about 3.51mm to 3.34mm. On the other hand, during disaccommodation the anterior chamber depth increases, which is shown in the recording of Figure 6.3B (blue line). The measurements show an increase from 3.35mm in the accommodated state to 3.51mm in the relaxed state. The anterior chamber depth values found are comparable with the ones reported by Fontana et al (1980). For a 35 year-old, the anterior chamber depth change per Diopter accommodation was measured by Dubbelman et al (2005) and it spans from -0.02 mm/D to -0.06mm/D. According to this range, the anterior chamber depth change for an accommodation stimulus amplitude of 7D varies between -0.14mm to -0.42mm. We found an anterior chamber depth change of -0.17mm during a 7D accommodation stimulus, which is within the depth range calculated above.

The dynamics of the anterior segment length is a result of the combination of the changes in lens thickness and lens shift during accommodation and disaccommodation. Figure 6.3B (green line) shows that the anterior segment length increases during accommodation and decreases during disaccommodation (Figure 6.3B and D - green line). The anterior segment length varies approximately between 7.99mm and 8.22mm during the response to the accommodation and disaccommodation step stimuli. Figure 6.3B shows a rapid decrease of the anterior segment length after the accommodation

stimulus was induced. This fast change is followed by a slow increase of the anterior segment length back to the initial depth, which is attributable to a slow movement of the lens back to the initial position.

6.2.4. Conclusion

The central anterior segment distances that were calculated dynamically during accommodation and disaccommodation, change in a manner well correlated with the amplitude of the accommodative stimuli induced to the subject's eye. The preliminary experiments demonstrate the ability of the current system to quantify the anterior segment distances dynamically during accommodation.

6.3. Changes of curvature during accommodation

6.3.1. Purpose

In principle, the high-resolution and high-speed cross-sectional and volumetric imaging capabilities of the SD-OCT system and its quantitative nature allow precise measurements of the changes in lens structure and in general the anterior segment, in two- and three-dimensions with aging and during accommodation. One of the major impediments in doing so is image distortion due to the refraction of the probe beam at the interface between ocular surfaces (Figure 6.4). In Figure 6.4, a depth scan in the object space is refracted at each ocular surface. When the depth scan is reconstructed in the OCT image space it is represented as a straight line. Thus, the OCT image does not represent the real geometry of the object. Image distortions due to refraction must be corrected in order to obtain reliable biometric data, such as surface curvature and asphericity.

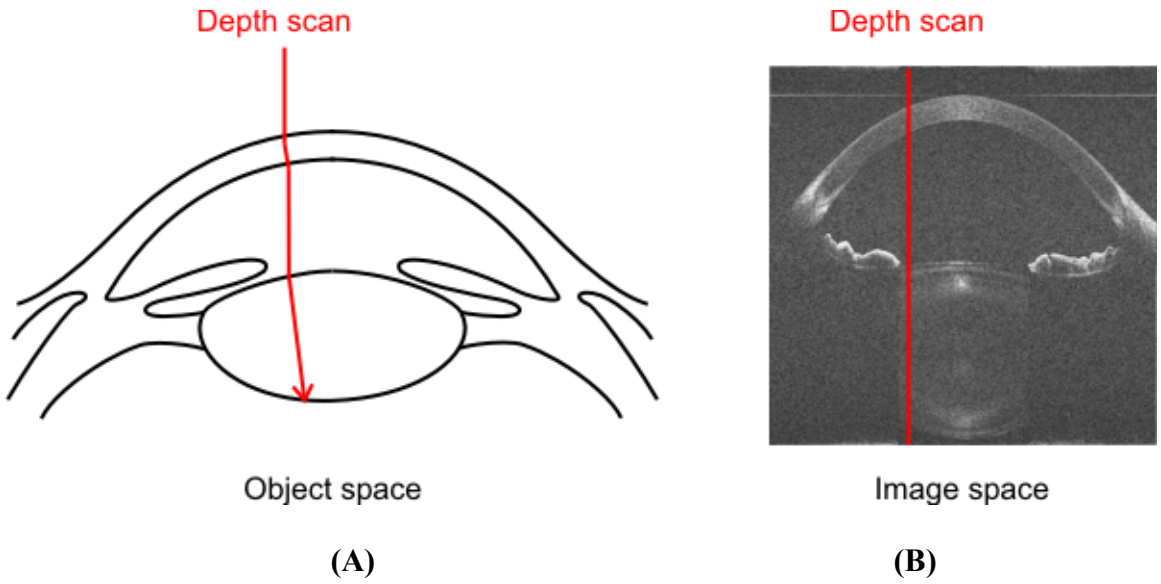

Figure 6.4: (A) Refraction of the beam due to refraction at the surfaces of the anterior segment. **(B)** The OCT depth scan is represented as a straight line in the OCT image space.

To correct for distortions of the crystalline lens in the OCT images, information about the structure of the cornea and anterior chamber is needed. Several previous reports have classified the sources of error and provided solutions for compensating for their effect in either two- or three-dimensional OCT datasets of human eyes (Ortiz et al, 2010; Ortiz et al, 2009; Podoleanu et al, 2004; Zawadzki et al, 2003; Westphal et al, 2002). A correction method based on two-dimensional ray-tracing is implemented in this work.

6.3.2. Tracing rays from the image plane to the object plane

The correction algorithm that was implemented in this project is designed to correct for refraction artifacts of OCT images acquired on horizontal meridional planes of the anterior segment. In this case, if the axial and depth range are not distorted, it is sufficient to trace incident rays successively through each surface of the human anterior segment using Snell's law.

The algorithm was developed in Matlab and it is based on the following steps:

Step 1: Segmentation

A segmentation tool was developed in Matlab. The program displays an image and allows manual selection of points in the image. A trained user uses a mouse to manually place a number of points (N>20) on the anterior segment boundaries of the OCT images, such as the anterior and posterior surfaces of the cornea, the iris and the anterior and posterior surfaces of the lens of the human eye (Figure 6.5). The user can crop the image to perform the analysis on a narrower lateral area of the OCT image centered at the apex of the ocular surfaces.

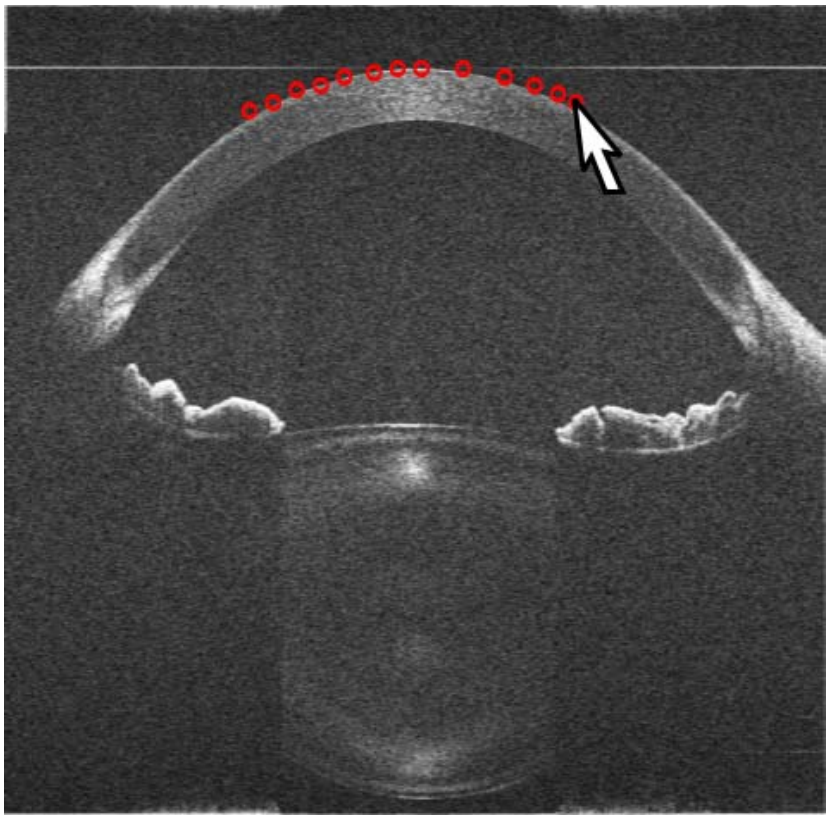

Figure 6.5: Schematic of the segmentation procedure. A number of points (red circles) are placed with the mouse pointer (white arrow) on the anterior segment boundaries. The outer cornea is segmented in the OCT frame displayed.

Step 2 - Curve fitting of the uncorrected surfaces

The points at each boundary that were manually selected by the user in the previous step (Figure 6.5) are fit with spherical functions over the central zone of the image using the fitting functions available in Matlab.

Step 3 - Ray tracing

The refraction correction algorithm is applied to the spherical functions representing the uncorrected boundaries. The basic principle of the ray tracing step is shown in Figure 6.6.

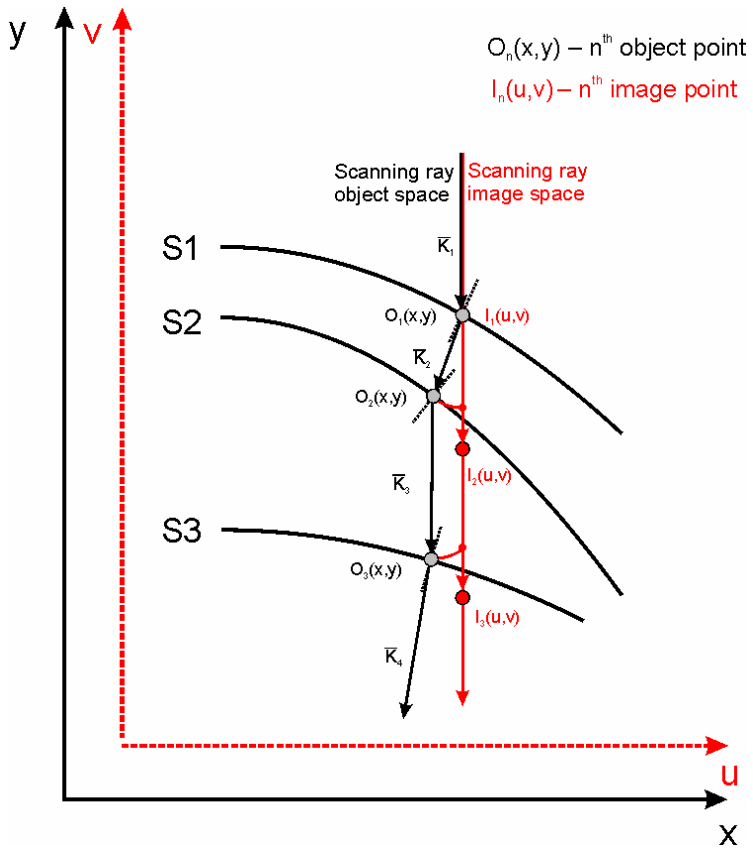

Figure 6.6: Schematic representation of the refraction correction method. The coordinate system *(u,v)* represents the uncorrected OCT image space (Red). The coordinate system *(x,y)* represents the real object space (Black). The scanning ray in the object and image space intersects with three surfaces S1, S2 and S3.

$S_1, S_2, \ldots S_K$ indicate a sequence of n curves representing the consecutive ocular boundaries in two dimensions. The telecentric scanning ray in the object space is reported for a generic position. For each consecutive curve, an object point $O_i(x,y)\ i = 1,2,\ldots,n$ (gray dots in Figure 6.6) was defined as the intersection of the refracted scanning ray and the actual ocular surface in the meridional plane. The coordinates of these intersections are undistorted in the object space defined as (x,y). The image point $I_i(u,v)\ i = 1,2,\ldots,n$ (red dots in Figure 6.6) was defined as the point with distorted coordinates that belongs to the uncorrected OCT image space defined as (u,v), which corresponds to the point $O_i(x,y)$ in the object space. The ray tracing algorithm consists in four subordinate steps that are repeated for each line of the image:

Sub-Step 3.1 Calculate the coordinates $O_1(x,y)$ of the intersection of the incident ray with the 1^{st} surface. $O_1(x,y)$ coincides with $I_1(u,v)$, the intersection of the incident ray with the first segmented surface in the image space.

Sub-Step 3.2 Once the coordinate of the generic point $O_1(x,y)$ are found, the direction of the refracted ray in the object space $\vec{K}_2$ is calculated using the vectorial form of the Snell's law:

$$n_2\left(\vec{K}_2 \times \bar{o}_1\right) = n_1\left(\vec{K}_1 \times \bar{o}_1\right) \qquad 6.1$$

where n_1 and n_2 are the refractive indices of the incidence and refracted medium, $\bar{o}_1$ is the unit vector that defines the normal vector at the point of incidence $O_1(x,y)$ with the 1^{st} surface (dashed lines in Figure 6.6) and $\vec{K}_1$ is the direction of the incident ray in the object space.

Sub-Step 3.3 Once $\vec{K}_2$ is calculated, the geometrical distance between two consecutive surfaces along the refracted ray in the object space is calculated by dividing

the optical distance $od_2 = I_2(u,v) - I_1(u,v)$ between two consecutive surfaces along the ray in the image space by the refractive index of the current refracting medium n_2.

$$gd_2 = \frac{od_2}{n_2} \tag{6.2}$$

Sub-Step 3.4 The coordinates of $O_2(x,y)$ are calculated by using the position $O_1(x,y)$, the distance calculated in Sub-Step 3.3 and the direction of the refractive ray $\vec{K}_2$

$$O_2(x,y) = O_1(x,y) + gd_2\vec{K}_2 \tag{6.3}$$

The same sub steps are repeated from Sub-step 3.2 for the next surface, and so on. The routine stops when the corrected coordinates of the posterior surface of the lens $O_4(x,y)$ are calculated.

Step 3.4 - Curve fitting of the corrected surfaces

The last step of the algorithm consists in fitting the cornea and lens corrected interfaces with spherical functions in order to calculate their radii of curvature over central zone.

6.3.3. Evaluation of manual segmentation

We performed an analysis to evaluate the variability of the anterior segment surface contours induced by boundaries determination using manual segmentation. An observer that was previously trained was asked to segment the outer cornea in an OCT image of the anterior segment (Figure 6.7A). The image was acquired on a 35 year-old subject. Segmentation was performed over a 3mm wide area (red rectangle in Figure 6.7A) that was centered at the apex of the cornea. The region was enlarged and a number of points

(N>10) were manually placed so that they were approximately evenly spaced along the outer cornea boundary (Figure 6.7B). The sampled data points were fit with a spherical function and the result was displayed to visually assess the quality of the fit. If the quality of the fit was satisfactory, the radius of curvature of the spherical function was collected and processed. The procedure was repeated twenty times and the mean radius of curvature was equal to 7.622mm with a standard deviation of ±0.143mm. Figure 6.8 reports the measurements error. This analysis shows that the 95% confidence interval for the radius of curvature is on the order of ±0.28mm.

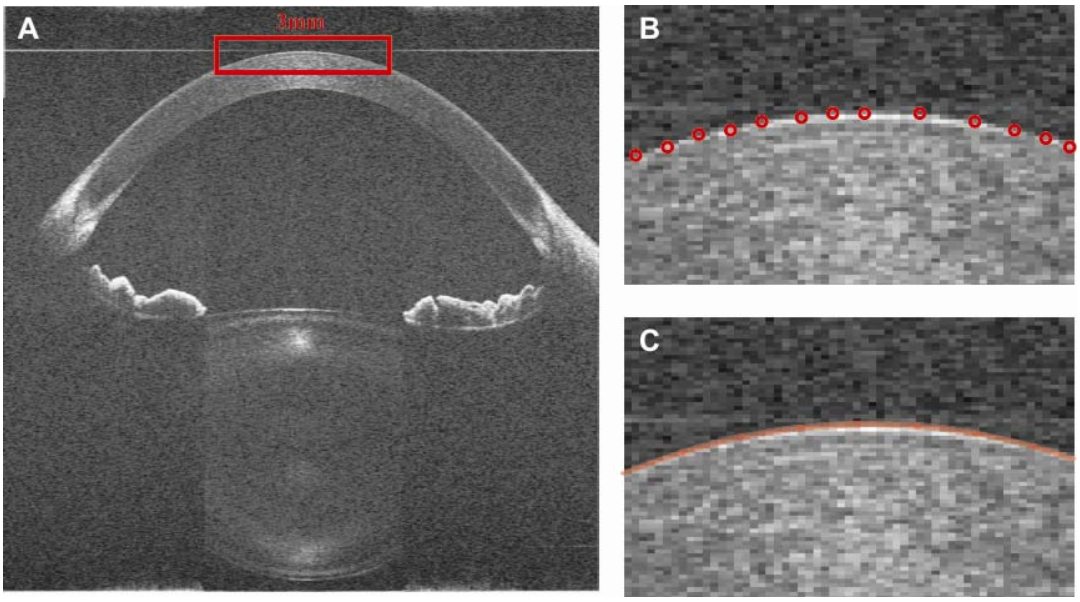

Figure 6.7: Segmentation was performed on the outer cornea over a 3mm wide region centered at the apex of the cornea. **(A)** Points were placed approximately evenly spaced on the outer cornea boundary. **(B)** Sample data points were fit with a spherical function **(C)**.

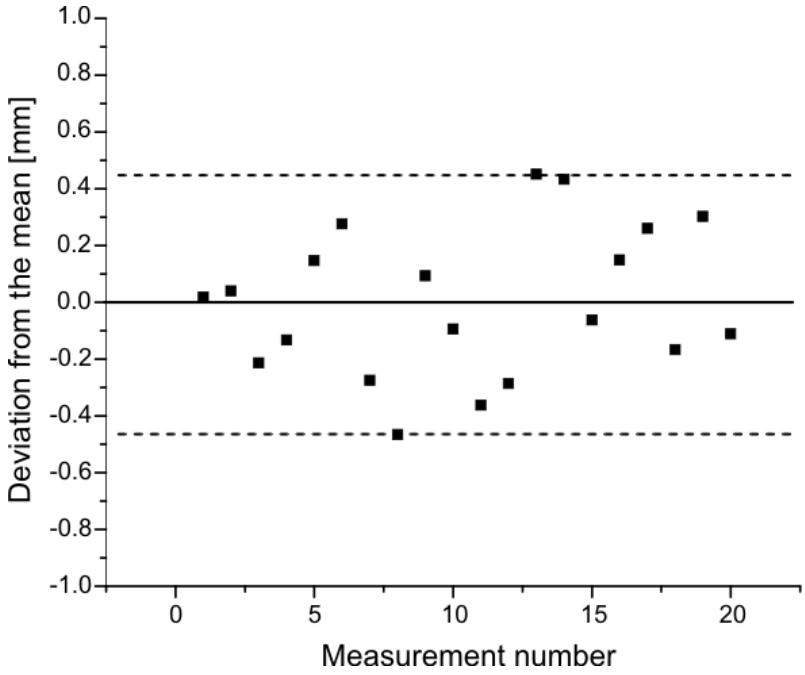

Figure 6.8: Image segmentation repeated twenty times on the outer cornea produced a mean radius of curvature of 7.622mm with a standard deviation of ±0.143mm. Deviation from the mean value is shown.

6.3.4. Repeatability produced by multiple measurements

We evaluated the repeatability of the outer corneal radius measurement for image acquisition of the same anterior segment performed at different times. The subject's eye was the same involved in the previous experiment. A trained operator performed ten separate OCT acquisitions of the same anterior segment. The operator realigned the scanning probe with the eye at each acquisition and acquired one image at the horizontal meridional plane of the anterior segment. For each of the ten images, manual segmentation of the outer cornea was performed once with the same modality of the previous experiment. The segmented data belonging to each frame was fitted with a spherical function and the radius of curvature of the outer cornea was calculated. The mean radius of curvature across the measurements was equal to 7.302mm with a standard deviation of ±0.133mm.

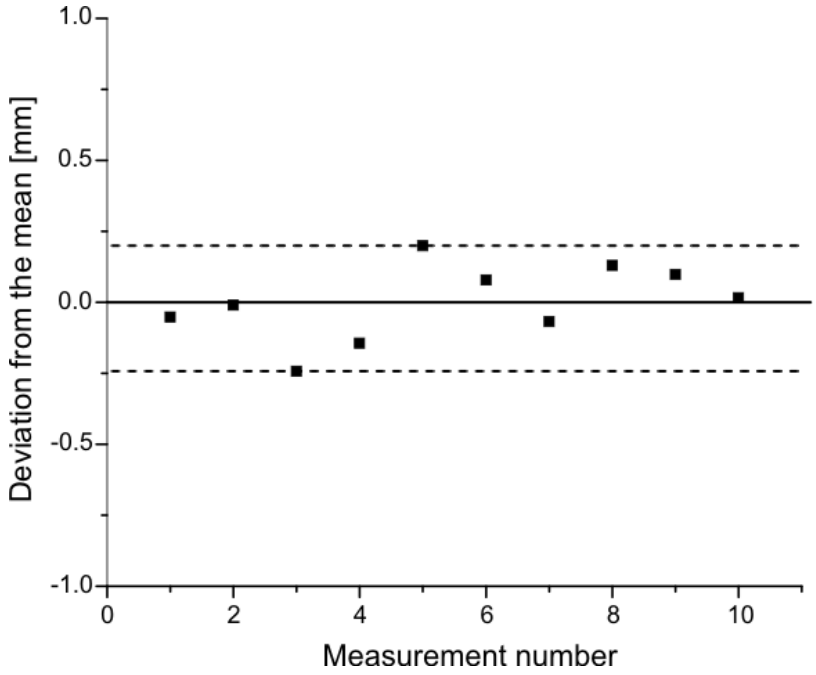

Figure 6.9: Ten OCT images acquired at different time on the same outer cornea produced a mean radius of curvature of 7.302mm with a standard deviation of ±0.133mm. Deviation from the mean value is shown.

Figure 6.9 reports the measurements error. The 95% confidence interval for the radius of curvature is on the order of ±0.26mm.

This analysis shows that the standard deviation of the anterior corneal radius measurements performed on different frames (±0.133mm) is comparable with the standard deviation of the measurements performed using the same frame (±0.143mm). Thus, the variability affecting the outer corneal radius of curvature measurements is mainly produced by the manual segmentation process.

6.3.5. Evaluation of the linearity of the axial and lateral ranges

Telecentricity of the transverse scan

The algorithm for distortion correction was implemented assuming that the transverse scan is telecentric. The further off the optical axis of the scanning system, the greater the field angle becomes, introducing field curvature in the horizontal and vertical planes. The

transversal scanner was design to produce a telecentric scan in the horizontal plane (section 5.2.1). Thus, field curvature occurs in the horizontal and vertical planes with a different degree. Field of curvature leads to differences in the measured optical path, which results in additional distortion of the image. Figure 6.10 displays an OCT image acquired along the horizontal (X) and the vertical (Y) planes of a flat mirror over a lateral width of 20mm, which is the maximal transversal scanning length of the scanning system. The images were enlarged and cropped in the vertical direction so that the height of the image is 0.75mm. The effect of field curvature can be observed as the flat surface of the mirror becomes curved in the image space. In the vertical plane (Y), the curvature is larger than in the horizontal plane (X), as expected. The arc produced by the image of the flat mirror in Figure 6.10 (X) has a radius of about 2.980m and a sag of approximately 12 μm. For the vertical plane, the arc produced by the image of the flat mirror (Figure 6.10(Y)) has a radius of 2.162m and a sag of approximately 26μm.

An image was considered non distorted when the sag of the arc corresponding to the flat mirror in the image space was comparable with the axial resolution of the system (~10μm). The sag of the arc produced by the 20mm wide scans along X and Y is above the axial resolution of the system and thus, according to the above criterion, the images in the horizontal and vertical planes are slightly distorted. The radius of curvature and sag of the arc were calculated for different lateral scan widths from 1mm to 20mm at 1mm steps. We found that the scan is telecentric in the horizontal direction up to a width of about 10mm and it is telecentric in the vertical direction up to a width of 3mm.

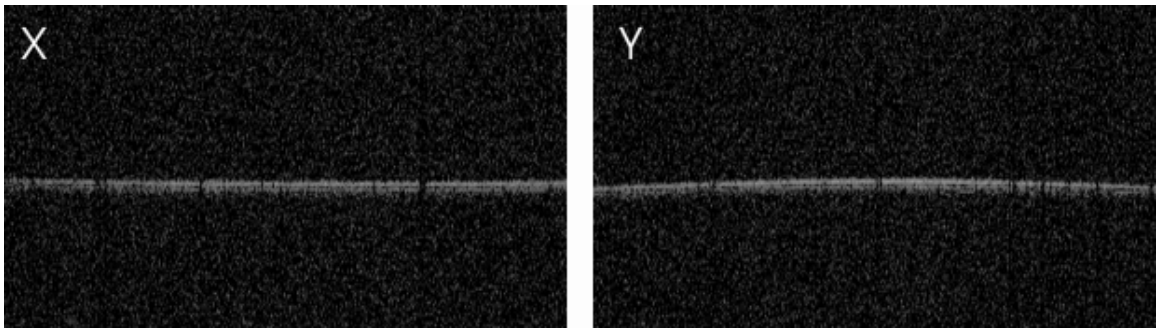

Figure 6.10: Image of a flat mirror using a scan width of 20mm along the horizontal plane of the scan (X). Image of a flat mirror using a scan width of 20mm along the vertical plane of the scan (Y).

Based on these results, to obtain reliable biometric data in two dimensions the algorithm can be applied to OCT images acquired in a meridional plane within the rectangular region of size 10mm × 3mm (Horizontal × Vertical) and centered at the optical axis of the scanning system, assuming that the apices of the anterior segment surfaces are centered with the optical axis of the scanning system.

Linearity of the axial range

The algorithm for distortion correction was implemented assuming that the depth range is linear. In the data processing, the Fourier transform is operated on a linear space in the wavenumber. Fourier transform is a linear function, thus we expect that the depth range is also linear. We experimentally assessed the linearity of the depth range using the same setup adopted in section 4.4.7 to calculate the sensitivity fall-off and the axial resolution of the system in function of depth. Two dispersion matched delay lines were connected to the reference and the sample arm. The optical path difference between the arms was matched. The delay in the reference arm was then varied in 1mm increments. The depth range is quantized in 2048 depth bins. At each 1mm increment, the depth bin position relative to the peak of the spread function was recorded.

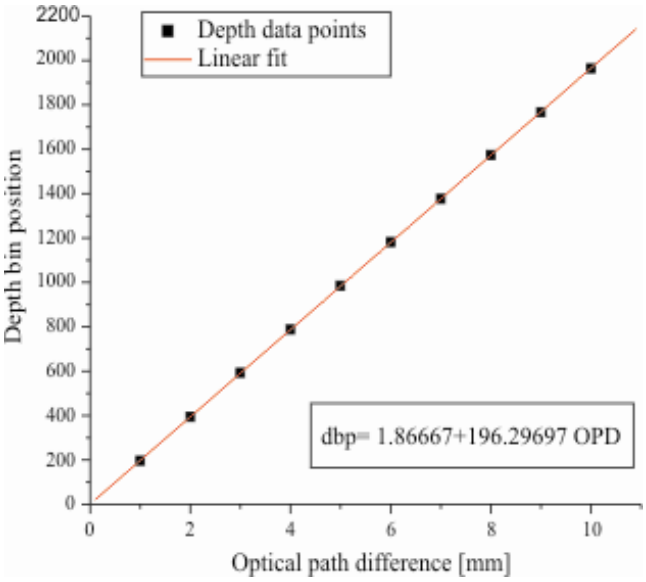

Figure 6.11: Depth bin position in function of the optical path difference between the reference and the sample arms. The data points were obtained by displacing the two arms in 1mm steps. The linear fit (R=1) of the data points is reported in red.

Figure 6.11 reports the depth bin position in function of the optical path difference between the two arms. The depth range is linear (R=1) in function of the depth bin position. By using the formula of the linear fit reported in the graph for the 2048th position, we found that the maximum imaging depth is 10.43mm, which agrees with the axial range measured in section 4.4.7.

6.3.6. Evaluation of the distortion correction on an eye model

Eye model

In order to validate the refraction correction algorithm we tested its performance on a model eye that was specifically built for this purpose. The model eye was exclusively intended to test the performance of the algorithm and not to reproduce an accurate representation of the human eye. Figure 6.12 shows the schematic of the model eye. The cornea surfaces were simulated by using a commercial plano convex lens *PCX*

(69497, Lens PCX f=40mm, Edmund Optics, USA) with known geometry and with specifications reported in Table 6.2. It is known that the human crystalline lens has a non-uniform refractive index distribution that increases from the lens surface toward the nucleus. To simulate the refractive index distribution of the crystalline lens a commercial lens with gradient refractive index *GRADIUM* (47453, Gradium lens f=60mm, Edmund Optics, USA) was chosen. The specifications of the lens with gradient refractive index are also reported in Table 6.2, as well as the other geometrical parameters of the model. The distance *d* between the lenses was set to 4.3mm.

In order to run the ray tracing correction on the eye model the group refractive index of both lenses has to be known. The refractive index of the PCX lens was measured with the OCT system. Figure 6.12 reports a cross-sectional OCT image of the PCX lens centered at its meridional plane. The image was acquired with the OCT light incident upon the back surface of the lens B_P. The central optical thickness T_P was calculated from the OCT image and was divided by the geometrical thickness t_P specified by the manufacturer in order to calculate its group refractive index n_P at 836nm.

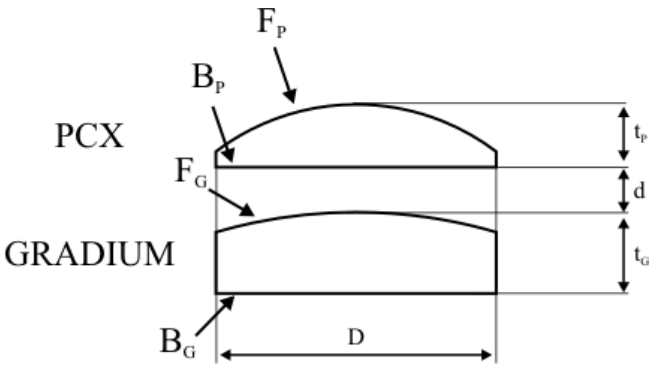

Figure 6.12: Schematic of the model eye design to validate the correction method. PCX and GRADIUM lens are shown that simulate the cornea and the human crystalline lens, respectively. The front and back surfaces of the PCX lens (F_P, B_P) and front and back surfaces of the Gradium lens (F_G, B_G) are indicated. The geometrical and optical parameters of the model are reported in Table 6.2.

Parameter	PCX	GRADIUM
Focal length	f_P=40mm	f_G=60mm
Diameter	D=25mm	D=25mm
Thickness	t_P=5.6±0.1mm	t_P=6.0±0.1mm
Radius of curvature	(F_P) 20.67mm (B_P) ∞	(F_G) 44.57mm (B_P) ∞
Distance B_P-F_G	d=4.3mm	
Group refractive index measured at 836nm	n_P=1.5615±0.028	n_G=1.7751±0.030

Table 6.2: Geometrical and measured optical parameters of the model eye.

The value of the group refractive index is reported in Table 6.2. The error affecting the measurement of the refractive index is associated to the tolerance on the geometrical thickness t_P provided by the manufacturer of the PCX lens (±0.1mm). The Gradium lens was imaged with the OCT light incident upon its front surface (Figure 6.13). The central optical thickness of the Gradium lens was too large to be measured in a single frame with the OCT system (Figure 6.13). However, the mirror image of the front surface (F_G-mirror) and the back surface (B_G) of the Gradium lens appeared in the same frame. The central optical thickness (T_G) of the Gradium lens can be calculated from the OCT image as the sum between the central optical distance of both surfaces from the zero delay location. The central optical thickness T_G was divided by the geometrical thickness t_P specified by the manufacturer to calculate the average group refractive index of the Gradium lens n_P along its optical axis at 836nm (Table 6.2). The error affecting the measurement of the refractive index is associated to the tolerance on the geometrical thickness t_G provided by the manufacturer of the Gradium lens (±0.1mm).

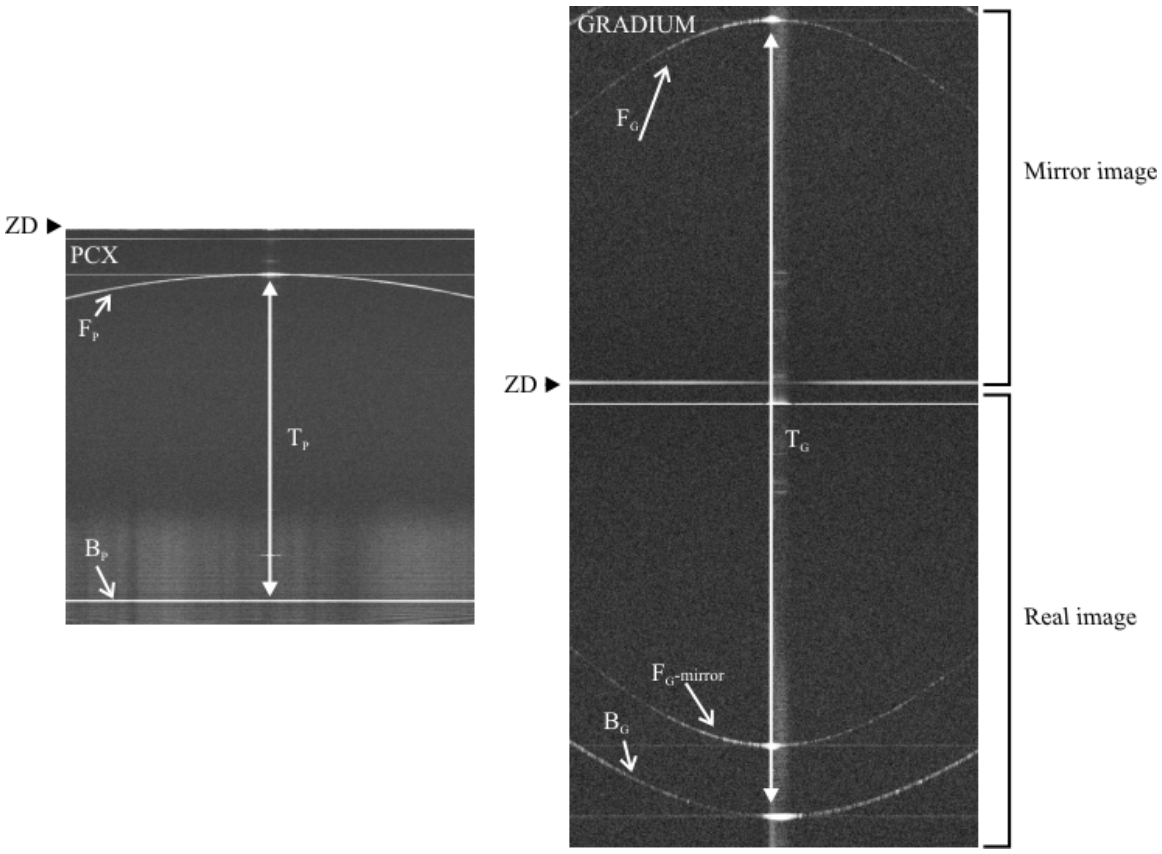

Figure 6.13: The OCT image of the PCX lens was acquired with the OCT light incident upon the flat surface of the lens (B_P). The central optical thickness T_P is reported **(PCX)**. The OCT image and the mirror image of the Gradium lens are reported. The surfaces (B_G,F_G) of the lens are indicated. F_G-mirror represents the mirror image of the surface F_G. The central optical thickness of the Gradium lens T_G is indicated.

Ray tracing correction validation

Validation of the ray tracing algorithm was performed on the model eye described in the previous section. The optical thickness of the model eye is about 24mm, which was calculated based on the geometrical and optical parameters in Table 6.2. The optical switch provides a free space axial range of 12.7mm when it is set in the configuration of section 5.5.3, which is too short to image the model eye along its entire thickness.

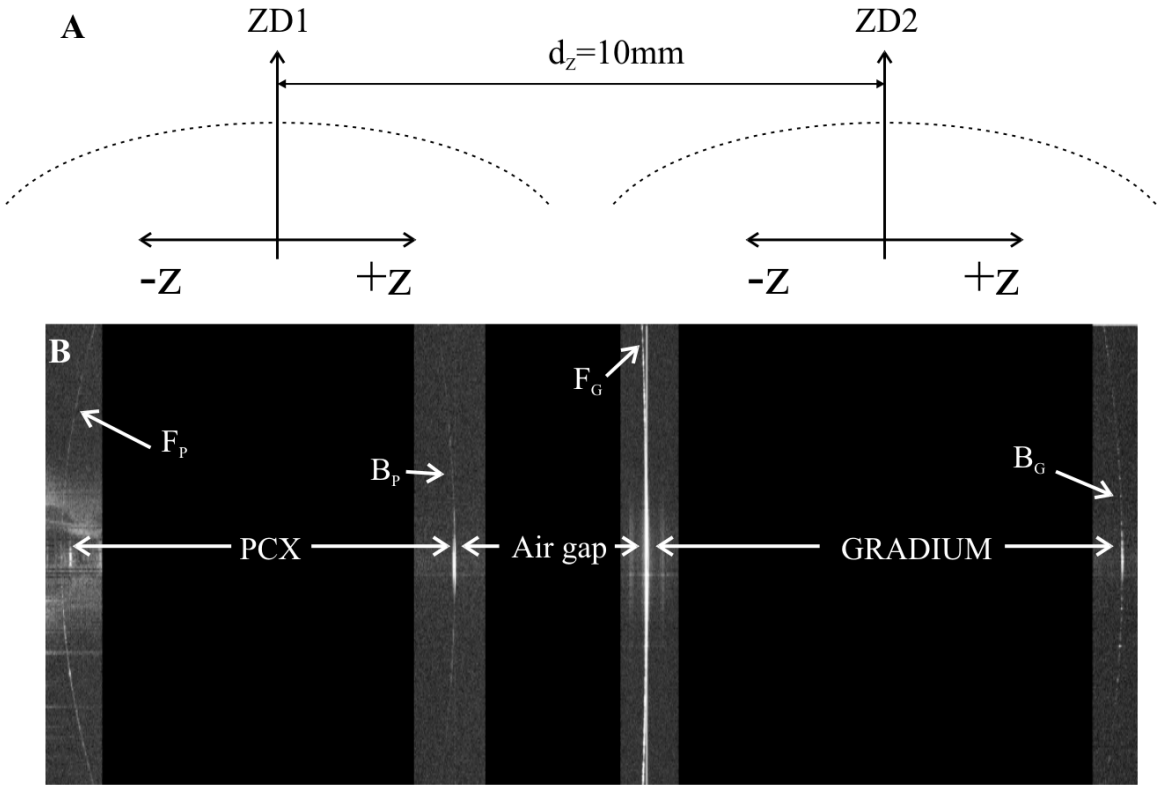

Figure 6.14: The configuration of zero delays ZD1 and ZD2 of the delay line adopted to image the whole model eye is reported. The zero delays were displaced of a distance d_Z=10mm **(A)**. The OCT image of the whole model eye was obtained by stitching the positive and negative depth scans acquired at the delays ZD1 and ZD2. The region inside and between the lenses were removed from the original section to suppress artifacts due to the presence of the zero delays and multiple reflections **(B)**.

The distance between the zero delays of the two mirrors of the delay line was changed to be able to acquire an OCT image of the whole model eye. Figure 6.14A shows the new alignment of the zero delays. Positive and negative sides of the axial scans were used to create a composite OCT image (Figure 6.14B) of the model eye. All the four surfaces F_P, B_P, F_G and B_G of the model eye are visible in the composite image. The region inside the lenses and the air gap were erased from the image to free the composite image from artifacts due to the zero delays and multiple reflections. The width of the

OCT image is 11mm (vertical direction in Figure 6.14B) and the depth is 24mm (Horizontal direction in Figure 6.14B).

Figure 6.15 reports the results of the first two steps of the ray-tracing algorithm, segmentation and fitting of the uncorrected surfaces, applied to the OCT image of the whole eye model. The images on the left were obtained by cropping, enlarging and rotating the regions of the OCT image containing the lens surfaces in Figure 6.14B. The segmentation and fitting of the model eye surfaces are reported as red lines on the right side of Figure 6.15. The transversal scan width of the OCT images is 11mm.

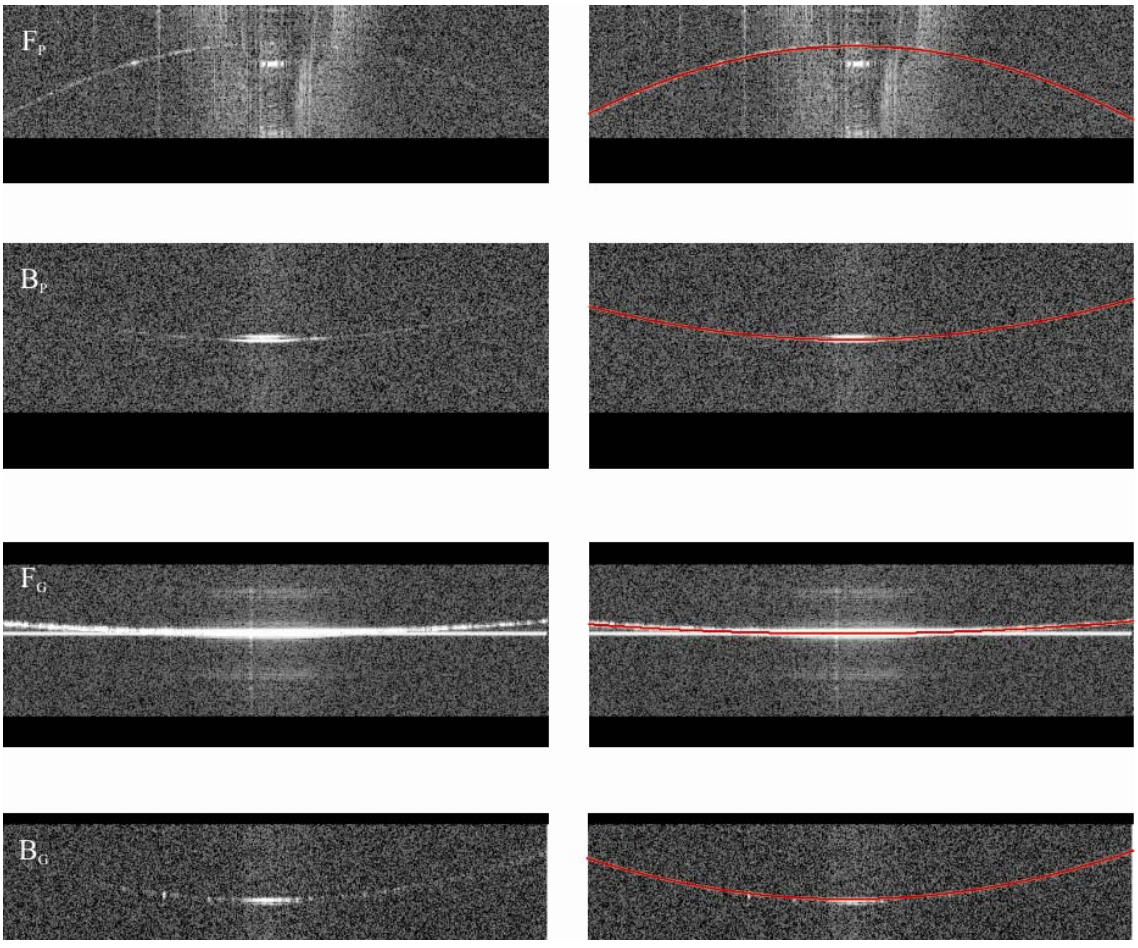

Figure 6.15: Cropped, enlarged and rotated sections of the model eye surfaces obtained from the OCT image of the whole model eye reported in Figure 6.14B (**Left**). The result of manual segmentation and curve fitting of the boundaries reported on the left is displayed in red (**Right**).

Figure 6.16 shows the result of the ray-tracing correction (left side) and the fitting (right side) of the corrected surfaces of the OCT image of the model eye reported in Figure 6.14B. The red lines on the *Ray tracing* graph represent the uncorrected boundaries while the blue lines are the corrected boundaries. On the right side of Figure 6.16 the corrected boundaries (blue lines) were fit with spherical functions (red lines). The corrected radii of curvature of the model eye boundaries were extracted and are reported in Table 6.3. Each radius of curvature was calculated for the mean refractive index of the two lenses, n_P and n_G, and for their extreme values reported in Table 6.2. The correction algorithm was also run on an narrower OCT scan of the model eye with width equal to 7mm (Table 6.3) to determine if there are changes depending on the optical zone of the OCT image. The measured radius of curvature of the anterior surface (F_P) of the PCX lens was 20.25mm for a scan width of 10mm and 19.73mm for a scan width of 7mm.

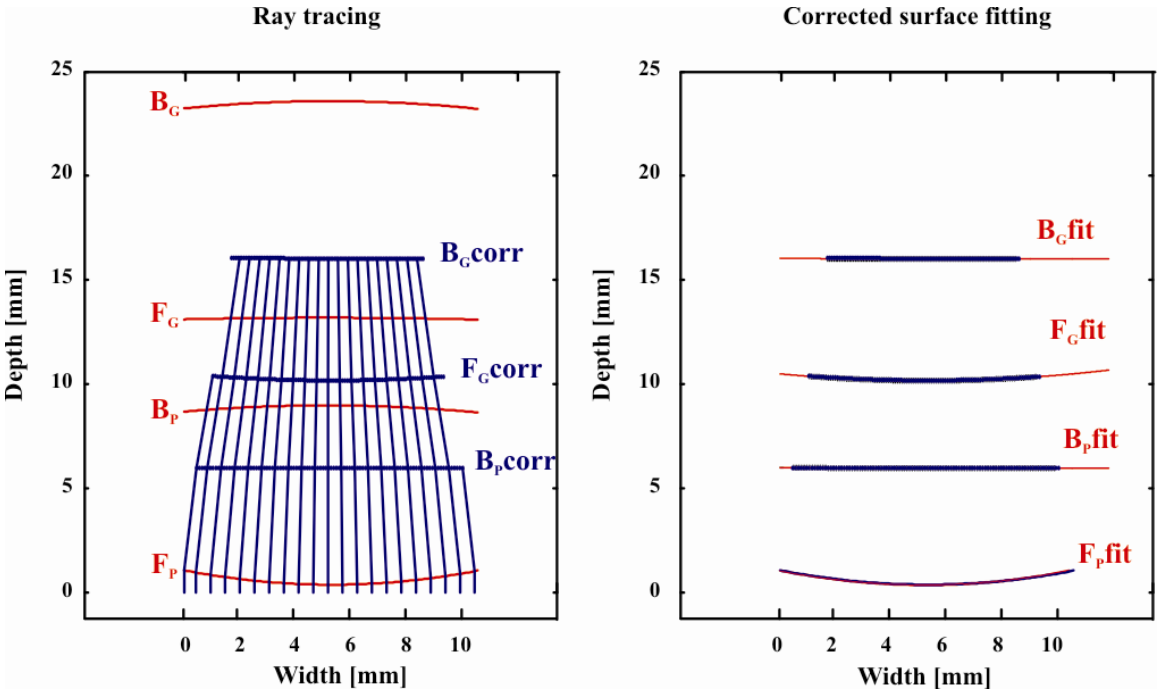

Figure 6.16: Ray tracing and fitting of the corrected surfaces of the model eye surfaces. The correction operation were performed on a 10mm wide region of the OCT scan.

OCT image width = 10mm				
Surface	***RI***	n_{Pmin}=1.5335	n_P=1.5615	n_{Pmax}=1.5895
F_P	-	20.25	20.25	20.25
B_P	-	2188	716	433
F_G	-	43.46	41.29	39.37
B_G	n_{Gmin}=1.7451	1674	702	447
	n_G=1.7751	849	493	349
	n_{Gmax}=1.8051	578	385	290
OCT image width = 7mm				
Surface	***RI***	n_{Pmin}=1.5335	n_P=1.5615	n_{Pmax}=1.5895
F_P	-	19.73	19.73	19.73
B_P	-	176579	2367	725
F_G	-	40.73	38.69	36.89
B_G	n_{Gmin}=1.7451	2041	761	471
	n_G=1.7751	880	503	354
	n_{Gmax}=1.8051	571	380	2879

Table 6.3: Corrected radii of curvature of the model eye surfaces in function of the measured refractive index of the PCX and Gradium lenses. Values are reported for two OCT scans of the model eye with width of 7mm and 10mm.

The radius of curvature provided by the manufacturer of the lens is 20.67mm (Table 6.2). The relative error of the measurements is 2% and 4.6% for a scan width of 10mm and 7mm, respectively. The relative error becomes higher for narrower scan width. This effect is due to a less accurate manual segmentation and curve fitting of the uncorrected boundaries. Manual segmentation becomes less accurate because it is harder to recognize boundaries for narrower scan widths due to the strong reflection band near the center. Curve fitting also becomes less accurate because the number of significant points belonging of the boundary is reduced over a narrower image width.

The posterior surface of the surface (B_P) of the PCX lens is flat. After correction, the measured radius of curvature ranges from 433mm to 176579mm, depending on the variability of the measured group refractive index of the PCX lens. Radii of curvature in

this range are very high compared to the width of the scan (7 mm and 10mm) so that the corrected B_P surface can be considered flat.

The measured radius of curvature of the anterior surface (F_G) of the Gradium lens ranges from 39.37mm to 43.46mm for the 10mm scan, depending on the measured group refractive index of the PCX lens. The radius of curvature provided by the manufacturer was 44.57mm (Table 6.2). The relative error of the measurements ranges from 2.5% to 16%. For the 7mm scan, the radius of curvature measurements ranges from 36.89mm to 40.73mm, with a relative error that spans between 8.6% and 17% depending on the refractive index of the PCX lens. The increase of relative error for the 7mm scan with respect to the 10mm scan occurs because of a less accurate manual segmentation and curve fitting, as previously explained.

The back surface of the Gradium lens B_G is flat. Depending on the variability of the group refractive index of both lenses, the measured radius of curvature of B_G varies from 290mm to 2879mm for both scan length. This range of values is high compared to width of the scan, thus the corrected surface can be considered flat.

In summary, the radius of curvature measurements are affected by an error that varies between 2% and 5% for undistorted surfaces, depending on the scan width. For distorted surfaces, we found a higher variability due to the propagation of the error throughout ray tracing procedure and the uncertainty affecting the refractive index measurements. For instance, the relative error affecting the calculation of the anterior surface of the Gradium lens varied from about 9% for a scan width of 10mm up to about 17% for a scan width of 7mm. The worsening of curvature measurements accuracy for narrower scan widths is strongly affected by the reflection band near the apex of the

model eye. The reflection band at the apex surfaces is an artifact in part produced by the background subtraction technique adopted in the commercial processing software. The detrimental effect of this artifact may be reduced by using other background subtraction techniques that were not available in the selected software.

6.3.7 Corneal and lens curvature measurements during accommodation

The accommodation unit was set to provide a static stimulus of vergence equal to 0D, 3D and 7D. At each stimulus vergence, a cross-sectional image was acquired along the meridional horizontal plane of the anterior segment of a 24 year-old and a 35 year-old subject. The cross-sectional images acquired at different accommodative states are reported in Figure 6.17 for the 24 year-old subject and in Figure 6.18 for the 35 year-old subject. The correction method introduced in section 6.3.2. was applied to a 3mm wide region centered approximately at the apex of the anterior segment surfaces (red rectangles in Figures 6.17 and 6.18). The results of manual segmentation and fitting of the ocular surfaces over the 3mm wide region of the anterior segment are reported in Figure 6.17 and 6.18 (red curves in the *ray tracing* section). Table 6.4 reports the group refractive index of the ocular structures used to ray trace the uncorrected surfaces of the two subjects at different ages. The average group refractive index of the cornea was obtained from measurement performed on *ex vivo* cornea samples by Uhlhorn et al (1998). The average group refractive index of the crystalline lens was used to correct the posterior surface of the lens (Borja et al, 2010). The average group refractive index of the lens for the two subjects was obtained by measurements performed on *ex vivo* lenses by Uhlhorn et al (2008). The group refractive index of the aqueous humor was estimated at 840nm with a published method (Drexler et al, 1998).

Ocular tissue	24 y/o RI (840nm)	35 y/o RI (840nm)
Cornea	n_C =1.387	n_C =1.387
Aqueous humor	n_A =1.342	n_A =1.342
Crystalline lens	n_L =1.415	n_L =1.417

Table 6.4: Group refractive index of the cornea (Uhlhorn et al, 1998), the crystalline lens (Uhlhorn et al, 2008) and the aqueous humor (Drexler et al, 1998) at 840nm.

The ray tracing was applied on the uncorrected surfaces and the resulting points with corrected coordinates are reported in black in the ray tracing section of Figure 6.17 and Figure 6.18. The data points were fitted with spherical functions, which are reported in red in the *fitting of the corrected boundaries* section of Figure 6.17 and Figure 6.18. The radii of curvatures of the ocular boundaries at different accommodative states produced by the correction algorithm are reported in Table 6.5.

Age (y/o)	24			35		
Vergence (D)	0	3	7	0	3	7
Radius AC(mm)	7.20	7.57	7.19	7.19	7.71	7.17
Radius PC (mm)	6.13	6.30	6.29	6.03	6.60	6.45
Radius AL (mm)	11.22	8.60	5.51	11.19	7.64	6.34
Radius PL (mm)	5.08	4.88	4.02	5.58	5.15	4.89
CT (mm)	0.53	0.52	0.53	0.53	0.54	0.54
ACD (mm)	3.05	2.91	2.79	3.05	3.35	3.39
LT (mm)	3.44	3.62	3.90	3.44	4.22	4.30

Table 6.5: Radii of curvature of the anterior segment surfaces are reported for three stimulus vergences (0D, 3D and 7D) and for two subjects at different age (24 y/o and 35 y/o). Geometrical thickness of the central cornea and the central lens and geometrical depth of the central anterior chamber are also reported. AC: anterior cornea; PC: posterior cornea; AL: anterior lens; PL: posterior lens; CT: corneal thickness; ACD: anterior chamber depth; LT: lens thickness.

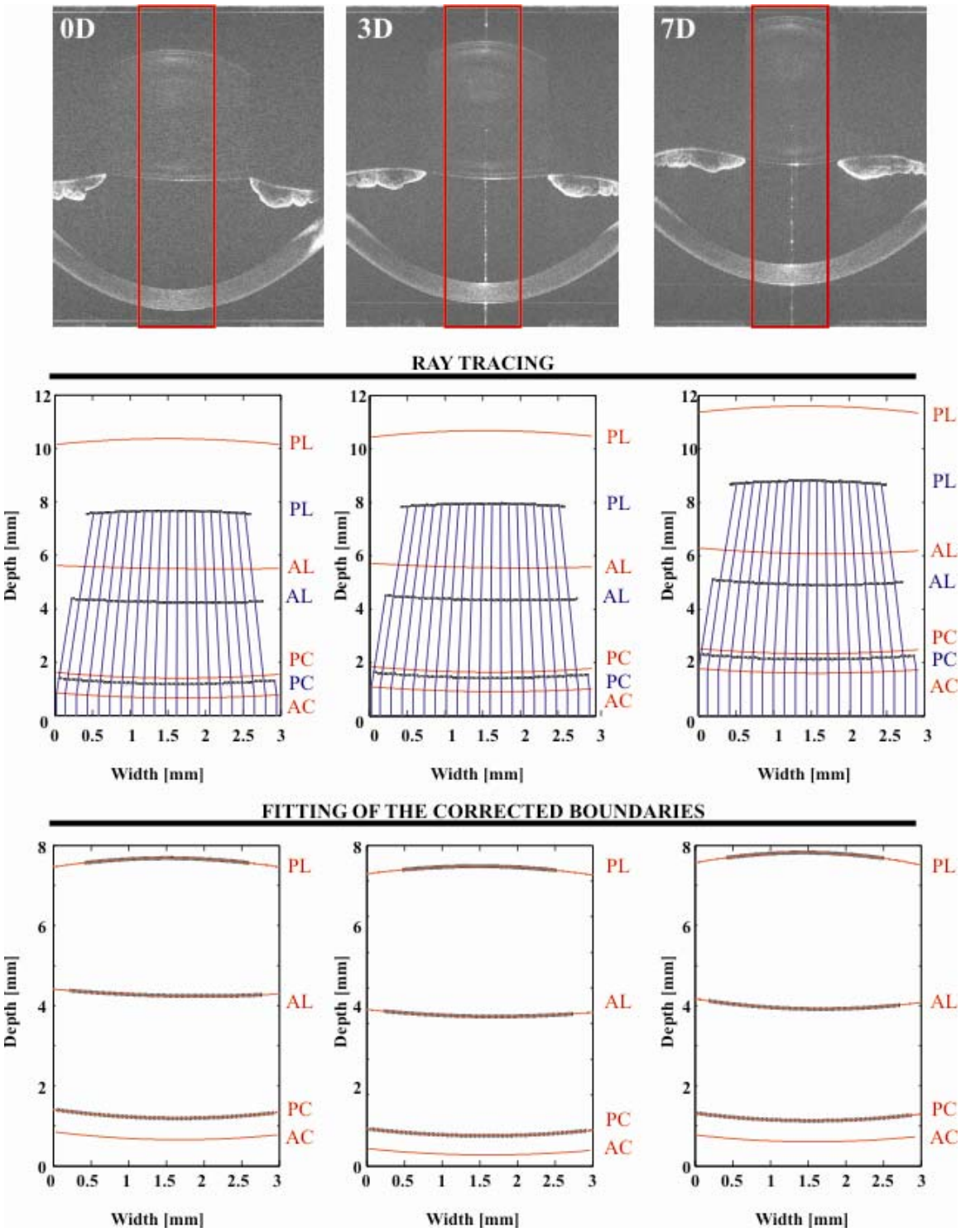

Figure 6.17: OCT images of the anterior segment are reported for a 24 y/o subject at three stimulus vergences (0D, 3D and 7D). The ray tracing and the fitting of the corrected boundaries are reported for an area on the OCT image of width equal to 3mm (red rectangles in the OCT images)

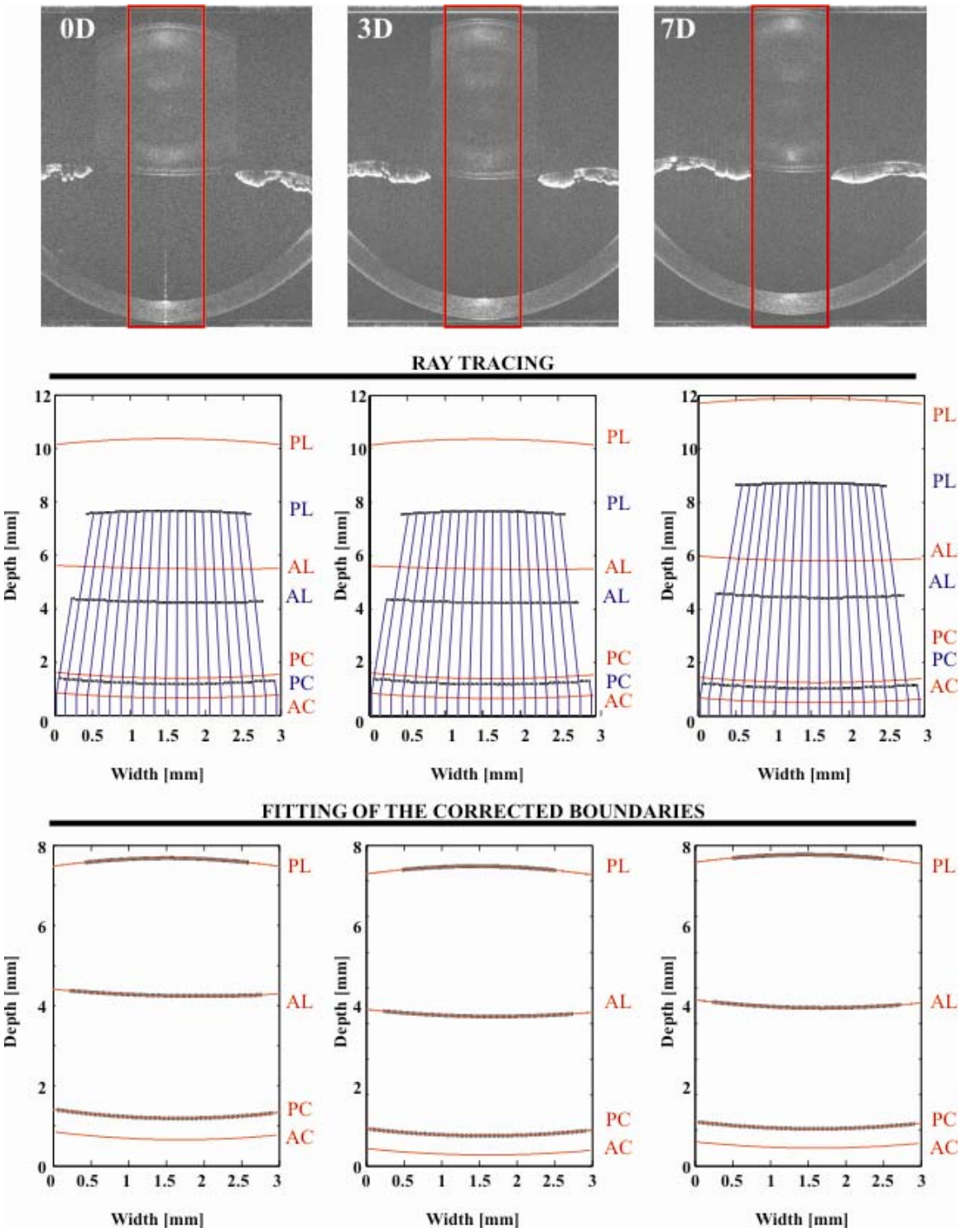

Figure 6.18: OCT images of the anterior segment are reported for a 35 y/o subject at three stimulus vergences (0D, 3D and 7D). The ray tracing and the fitting of the corrected boundaries are reported for an area on the OCT image of width equal to 3mm (red rectangles in the OCT images)

It is known that the anterior and posterior corneal radii of curvature are constant during accommodation. The average radius of curvature for the anterior human cornea is about 7.7mm while the average radius of curvature of the posterior cornea is about 6.8mm (Bennett and Rabbetts, 1998). The average radii of curvature of the anterior cornea measured with the system are 7.20mm and 7.35mm for the 24 year-old and for the 35 year-old subjects, respectively, with a relatively large variability over the three measurements. Although the average values are within the variability range of the anterior cornea radius of curvature of normal eyes (7.14mm to 8.46mm) (Høvding, 1983) they are well below the average anterior corneal curvature. The radius of curvature of the cornea of both subjects was also measured with two commercial devices: a Pentacam HR (Oculus, Germany), which is based on Scheimpflug imaging and a corneal topographer, TMS (Tomey, USA). Table 6.6 reports the radii of curvature of the anterior cornea measured with the commercial devices along the horizontal meridian. For both subjects, the radii of curvature of the anterior cornea that were measured with the two commercial devices matched. The average radius of curvature of the anterior cornea measured with the two commercial devices is 7.52mm for the 24 year-old subject and 7.78mm for the 35 year-old subject, which compare well with the average radius of curvature of the human cornea (7.7mm).

Age (y/o)	**24**		**35**	
DEVICE	**Pentacam**	**TMS**	**Pentacam**	**TMS**
Radius AC (mm)	7.52	7.51	7.78	7.78
Radius PC (mm)	5.96	-	6.43	-

Table 6.6: Radii of curvature of the anterior cornea are reported for the same two subjects (24 y/o and 35 y/o) of Table 6.5. The measurements were performed with two commercial devices, Pentacam HR (Oculus, Germany) and TMS (Tomey, USA).

A comparison of these data with the average values obtained with our system (7.20mm and 7.35mm for the 24 and the 35 year-old subject, respectively) confirms that our system underestimates the anterior corneal radius of curvature of about 0.32mm for the younger subject and 0.42mm for the older subject.

If we assume that the measurements produced by the two commercial devices are correct, the relative error affecting the measurements of the outer corneal diameter with our instrument is 4.2% for the 24 year-old subject and 5.4% for the 35 year-old subject. In the previous section, we found that our system underestimated the outer surface of the model eye with a relative error that varies between 2% and 5% depending on the scan width. Several factors may affect the calculation of the anterior cornea curvature with our system. In section 6.3.3. we showed that the estimation of the radius of curvature of the anterior cornea is mainly affected by the variability introduced with manual segmentation (SD ±0.143mm), which in part affects the measurements reported in Table 6.5. This error does not affect only the calculation of the radius of curvature of the cornea but, due to the ray tracing procedure, it propagates to the estimation of the radius of curvature of the deeper structures, such as the posterior cornea and the anterior and posterior lens. Another factor that affects the measurements is the alignment mismatch between cross-sectional images acquired at different stimulus vergences. There could be decentration or tilt of the ocular surfaces, which is not taken into account in the curve fit.

The radius of curvature of the posterior cornea at every stimulus vergence and for both subjects is within the variability range of the posterior lens curvature of normal eyes (Lowe and Clark, 1973). However, the mean values of 6.24mm and 6.36mm for the 24

and the 35 year-old subjects, respectively, are slightly below the average value. This may be in part due to the underestimation of the anterior corneal radius.

During accommodation, the crystalline lens anterior and posterior radii of curvature decrease (Helmoltz, 1962, Koretz et al, 1984). For both subjects, we measure a decrease of the radius of curvature of the anterior and posterior lens radii of curvature with accommodation (Table 6.5). The values reported at the relaxed stage are within the range previously measured with Scheimpflug and MRI (Dubbelman et al, 2005, Koretz et al, 2004). At the highest accommodative state (7D), the radii of curvature of both anterior and posterior lens are smaller in the younger subject, as expected. Dubbelman et al (2005) reported the radius of curvature of the anterior and posterior lens of a 29 year-old subject measured with Scheimpflug imaging. In their study they found an anterior lens radius of ~6.2mm with a 0D stimulus, ~6mm with a 3D stimulus and 5mm with a 7D stimulus. In the same study the posterior lens radius of the same subject was ~12mm with a stimulus of 0D, ~9.5mm with a stimulus of 3D and 5mm with a stimulus of 7D. The radius of curvature of anterior and posterior lens at different accommodative states calculated with our system (Table 6.5) are comparable with the values reported by Dubbelman et al (2005).

6.4. Discussion, summary and conclusion

The goal of these preliminary studies was to evaluate the basic functionality of the system for ocular biometry.

The capability of the system in quantifying the dynamic changes in thickness of the anterior segment structures (cornea, lens and anterior chamber) during

accommodation and disaccommodation was demonstrated. The results provided compare well with published results.

A method to correct the distortions of the OCT images was also developed that provides corrected two dimensional biometric data, as surface curvature and asphericity, at different accommodative states. Sources of optical distortion of the OCT images are due to the non linearity of the axial and transversal scanning systems and to the refraction of the OCT beam at successive boundaries. The linearity of the axial and transverse imaging ranges was assessed so that the only source of image distortion to correct was due to refraction. The method to correct for refraction of the light at the ocular boundaries consists of four steps: manual segmentation of the images, curve fitting of the uncorrected surfaces with conic functions, ray tracing and fitting of the resulting corrected data points with conic functions.

We first assessed how the variability associated to manual segmentation and multiple acquisitions reduced the accuracy in calculating the radii of curvature of the anterior corneal boundary. The experiments shows that manual segmentation dominates the radius of curvature measurements variability (SD±0.143mm). The measurement of the radii of curvature of deeper ocular boundaries, posterior corneal surface and anterior and posterior lens surfaces, are also affected by this type of inaccuracy. To correct an ocular surface boundary the ray tracing method makes use of the geometrical information measured on the previous ocular boundaries. Thus, the inaccuracy associated to the estimation of a surface is the combination of the uncertainty produced by manual segmentation of that boundary plus the uncertainty produced in estimating all the previous boundaries. The estimation of the deeper boundaries, such as the lens surfaces,

will be therefore affected by a greater measurement error compared to the corneal surfaces. Reducing the error associated to the inter-observer variability due to manual segmentation, for instance, using automatic or semi-automatic segmentation, will greatly improve the accuracy of ocular biometry of the crystalline lens. Although automatic structure segmentation of the OCT images is a more difficult task, it may reduce the inter-observer variability and also intra-observer variability, which was not estimated in this work, associated to manual segmentation. The time associated with manual segmentation of four boundaries, which was about 5 minutes, can be radically reduced by using a semi-automatic or automatic segmentation technique. These findings suggest that investigating a method for automatic detection of the ocular boundaries may greatly benefit the future development of this project.

The method to correct for distortion was validated on a custom built model eye with known optical and geometrical properties. The effect of the refractive index profile of the crystalline lens was simulated with a GRIN lens in the model eye. The corrective method retrieves the posterior boundary of the crystalline lens assuming a homogenous refractive index of the lens. The experiment conducted on the model eye shows that this assumption produces an error in the posterior curvature of the GRIN lens that is within the experimental variability of the system. For this reason, we believe that a homogenous refractive index can be used for the crystalline lens while performing ray tracing on OCT images of the anterior segment. A similar result was also found by Borja et al (2010). In their study, the estimation of the radius of curvature of the posterior surface of *ex vivo* crystalline lenses was performed by imaging them with OCT and then performing ray tracing using an equivalent refractive index for the lens. The crystalline lens was then

flipped, the posterior lens was imaged without refraction distortion and the radius of curvature was calculated and compared to the results found by imaging the crystalline lens with the OCT light incident upon its anterior surface. Their findings suggested that the average refractive index can be used for distortion correction of refraction of OCT images acquired on the crystalline lens.

The correction method was tested on two subjects at different ages (24 year old and 35 year old) and at different accommodative states induced by stimuli vergence of 0D, 3D and 7D. All the anterior segment surfaces were segmented and corrected. The posterior surface of the lens in the OCT images was retrieved using the ray tracing procedure and assuming a uniform refractive index equal to the average group refractive index of the lens. The average group refractive index of the lens used in our experiments was the one calculated before by Uhlhorn et al (2008) on *ex vivo* crystalline lens samples. The feasibility of measuring the radius of curvature of the anterior segment surfaces at different accommodative states was demonstrated with our instrument.

The radius of curvature of the anterior cornea estimated in our experiment is slightly smaller than the one measured with two commercial devices (Pentacam and TMS). The possible reasons of this underestimation are the variability associated with the manual segmentation of the OCT images and a possible tilt and decentration of the eye during the imaging. A tilt and/or decentration of the ocular surfaces with respect to the OCT scanning beam may cause the OCT frames to be consistently acquired in a plane that is not a meridional plane of the eye. This would lead to a constant underestimation of the radius of curvature of the corneal outer surface. The measurement accuracy of the anterior segment surfaces radius can be improved by performing three dimensional

biometry of the anterior segment. Biometry on a three dimensional dataset reduces the problem of tilt and/or decentration of the ocular surfaces and provides a larger amount of data, which in turn produce a more accurate spherical fit of the segmented surfaces. Commercial devices as Pentacam and TMS perform three dimensional biometry of the corneal surfaces to generate accurate measurements of the radii of curvature.

Due to the ray tracing procedure, an error on the estimation of the anterior cornea propagates to the estimation of the radius of curvature of the deeper structures, such as the posterior cornea and the anterior and posterior lens. However, although the radius of curvature of the anterior cornea measured with the OCT system is lower than expected, the radius of curvature of the posterior cornea and the anterior and posterior lens measured at different accommodative states and at different ages are reasonably within the expected range. To justify the correct estimation of the measured posterior corneal radius and anterior and posterior lens radii, we estimated the effect that a variation of the radius of curvature of the anterior cornea produces to the radius of curvature of the other anterior segment structures due to the propagation of the error through the ray tracing correction. In this simulation, the ocular surfaces were modeled with the parameters reported in Table 6.7.

Radius AC(mm)	7.7	**CT (mm)**	0.57
Radius PC (mm)	6.8	**ACD (mm)**	3.00
Radius AL (mm)	12.0	**LT (mm)**	4.00
Radius PL (mm)	6.0		

Table 6.7: Model eye parameters used to test the error that the ray tracing algorithm produces upon a variation of the radius of curvature of the anterior cornea to the curvature of the deeper surfaces. Corneal thickness (CT), anterior chamber depth (ACD) and lens thickness (LT) are also reported.

The anterior corneal radius was varied from 7.1mm to 8.1mm in 1mm steps. For each step, the ray tracing algorithm was run on the model eye of Table 6.7 and the corrected radii of curvature of the posterior cornea and anterior and posterior lens were calculated. Figure 6.19 shows the outcome of the simulation.

The radii of curvature of the posterior cornea and the anterior and posterior lens are reported in function of the radius of curvature of the anterior cornea. The data points were fitted with linear functions. The posterior corneal radius varies with a slope of ~0.25 millimeters per a millimeter deviation of the anterior corneal radius. The anterior and posterior lens radii vary, respectively, with a slope of ~1.14 and ~0.42 millimeters per millimeter deviation of the anterior corneal radius. The slope parameters shows that a variation of the anterior corneal radius produces a relatively small variation of the corrected posterior cornea and lens radii of curvature. The variation of the corrected anterior lens is larger. The maximum absolute error that affects the corneal radius estimation in our experiments is about ~0.43mm (Table 6.5 and Table 6.6). This error produces errors of the radius of curvature of the corrected posterior cornea and corrected anterior and posterior lens that, according to the slopes calculated above, are within the experimental variability. Segmentation and correction of the three dimensional images produced by the current OCT system is a future development of this work. However, although the speed of the system already produces static three dimensional frames of the anterior segment, imaging of dynamic of a process of the anterior segment such as accommodation in three-dimension will require to increase the speed of the system.

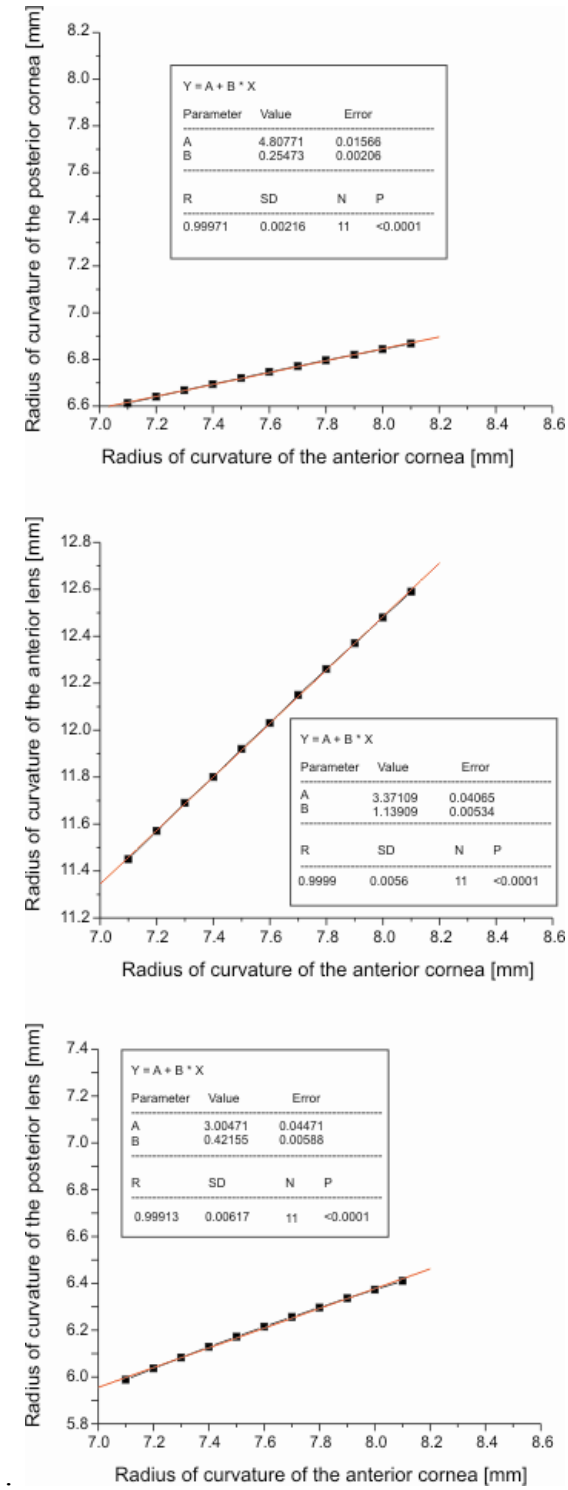

Figure 6.19: Corrected corneal posterior radius and corrected anterior and posterior lens radii variations produced by the ray tracing algorithm for the model eye of Table 6.7 and an anterior corneal radius that varies between 7.1mm and 8.1mm. The linear fits of the data points are reported.

CHAPTER 7. SUMMARY AND CONCLUSION

The changes in the human crystalline lens shape and its internal structure during accommodation and with aging are a fundamental component of the dynamic mechanism of accommodation and presbyopia, the loss of near vision with age. A better understanding of the crystalline lens changes during accommodation will help in developing new treatments to correct for presbyopia. There is currently a need of an instrument that provides high-resolution quantitative *in vivo* images of the human crystalline lens at video-rate to study the dynamic changes in lens shape during accommodative response.

In this study we proposed to develop an OCT system for imaging the human anterior segment and perform biometry during accommodation.

The goals of the dissertation were:

1. The development of a SD-OCT system with long axial range, high axial and lateral resolution and high speed for *in vivo* imaging of the anterior segment along its entire length at video-rate.
2. Development of a slit-lamp mounted optical delivery scanning system for the extended depth SD-OCT system combined with a custom made unit that provides accommodation and disaccommodation step stimuli.
3. Development of a method to correct the distortions of the OCT images that provides corrected two dimensional biometric data at different accommodative states.

A SD-OCT system with extended depth for *in vivo* imaging of the crystalline lens was developed and the feasibility of imaging the dynamic process of accommodation with

high resolution and high speed was demonstrated. A delay line that employs an optical switch was developed an coupled with the OCT system. The optical switch increased the axial range of the imaging system, and the feasibility of imaging the anterior segment along its entire length with high resolution and high speed was demonstrated. Experiments show that this system provides images of the anterior segment along its entire depth with higher resolution and higher speed compared to previously published systems.

We developed a slit-lamp mounted optical delivery scanning system with high transverse resolution and long depth of focus for the SD-OCT system. A unit that provides accommodation and disaccommodation step stimuli from 0D to about 10D was developed and coupled to the SD-OCT. Although OCT imaging of accommodation was demonstrated by previous investigators, to the best of our knowledge, this is the first system which has the capability to record OCT frames dynamically while an accommodation step stimulus is induced.

The feasibility to measure dynamically the length of the anterior segment structures during accommodation was demonstrated. To the best of our knowledge this is the first time that biometry of the anterior segment has been performed dynamically with OCT.

A method to correct for the distortion of the OCT images due to the refraction of the light at successive ocular surfaces that provides corrected two dimensional biometric data at different accommodative states was built. The method was assessed through validation using a custom made model eye. Experiments conducted on subjects at two different ages demonstrate the capability of performing measurements of the corrected radius of curvature of the anterior segment surfaces during accommodation. To the best of our

knowledge this is the first time that the radii of curvature of the anterior segment structures at different age and at different stimuli vergence has been provided with OCT.

There are several areas of potential improvement and further development:

- During the time of the project the performance of Swept Source based OCT systems was improved. The SS-OCT technology has improved the sensitivity fall-off at longer depths. In principle, the light source and the detection system of the SD-OCT imaging system can be replaced with a SS-OCT system. Together with the optical switch that can extend the imaging range further. However, adequate swept sources at ~800nm are still not readily available. When these sources become available, switching to SS implementations will help increase speed and sensitivity.
- The optical switch in the delay line uses two mirrors to extend the axial imaging range to the entire anterior segment of the human eye. Preliminary test shows that this system can be equipped with a third mirror with a zero delay located close to the vitreo-retinal surface to provide an image of the retina, without the need of dynamic focusing. Although retinal imaging with OCT is a well assessed and improved technology, this preliminary result is encouraging because it shows that biometry of the entire eye during accommodation could be accomplished.
- A semi-automatic or automatic method for image segmentation of the anterior segment images produced by the OCT system can be

implemented. This method would decrease the image analysis time and would improve the accuracy of measurements.

- The OCT system provides three dimensional imaging capabilities. The current method for correcting distortions of the OCT images can be extended from two dimensions to three dimensions. This would provide additional data and would provide more accurate data on the curvature of the anterior segment surfaces.
- The slit-lamp mounted delivery probe can be modified and a refractometer can be coupled with the accommodation target to provide objective measurements of the ocular change in vergence produced by the stimulus.
- Preliminary data shows that the delivery system could also be modified and mounted on a surgical microscope to provide surgeons with a cross-sectional imaging view during surgery. This could be particularly useful during Phaco-Ersatz procedures to control the injected volume.

REFERENCES

Abramowitz M, & Stegun IA. (1972). *Handbook of Mathematical Functions with Formulas, Graphs and Mathematical Tables* (9th ed.). New York: Wiley .

Al-Saeed, T. A., & Khalil, D. A. (2009). Dispersion Compensation in Moving-Optical-Wedge Fourier Transform Spectrometer. *Applied Optics*, *48*(20), 3979. OSA.

Allouch, C., Touzeau, O., Borderie, V., Puech, M., Ameline, B., Scheer, S., & Laroche, L. (2002). Orbscan: a New Device for Iridocorneal Angle Measurement. *Journal Français d'Ophtalmologie*, *25*(8), 799-806.

Anderson, H. A., Glasser, A., Manny, R. E., & Stuebing, K. K. (2010). Age-Related Changes in Accommodative Dynamics from Preschool to Adulthood. *Investigative Ophthalmology & Visual Science*, *51*(1), 614-22. doi:10.1167/iovs.09-3653

Arntz, A., Durán, J. A., & Pijoán, J. I. (2003). Subclinical Keratoconus Diagnosis by Elevation Topography. *Archivos de la Sociedad Española de Oftalmología*, *78*(12), 659-64.

Arora, R., Mehta, S., Goyal, J. L., Pahuja, S., Gupta, D., & Gupta, R. (2010). Pattern of Scheimpflug Imaging in Anterior Segment Foreign Bodies. *Eye (London, England)*, *24*(7), 1304-6. Royal College of Ophthalmologists.

Atchison, D. A., & Smith, George (200). *Optics of the Human Eye.* Butterwort-Heinnemann, Oxford, UK.

Atchison, D. a, Bradley, A., N Thibos, L., & Smith, G. (1995). Useful Variations of the Badal Optometer. *Optometry and Vision Science Official Publication of the American Academy of Optometry*, *72*(4), 279-284.

Atchison, D. A., & Smith, G. (2005). Chromatic Dispersions of the Ocular Media of Human Eyes. *Journal of the Optical Society of America A*, *22*(1), 29. OSA.

Avila, M., Li, Y., Song, J. C., & Huang, D. (2006). High-speed Optical Coherence Tomography for Management after Laser In Situ Keratomileusis. *Journal of Cataract and Refractive Surgery*, *32*(11), 1836-42. doi:10.1016/j.jcrs.2006.07.015

Baumann, B., Pircher, M., Götzinger, E., & Hitzenberger, C. K. (2007). Full Range Complex Spectral Domain Optical Coherence Tomography without additional Phase Shifters. *Optics Express*, *15*(20), 13375. OSA.

Beauchamp, R., & Mitchell, B. (1985). Ultrasound Measures of Vitreous Chamber Depth during Ocular Accommodation. *American Journal of Optometry and Physiological Optics*, *62*(8), 523-32.

Beers, A. P. A., & Van Der Heijde, G. L. (1994). In Vivo Determination of the Biomechanical Properties of the Component Elements of the Accommodation Mechanism. *Vision Research*, *34*(21), 2897-2905.

Bennett, A. G., & Rabbetts, R. B. (1998). *Bennett and Rabbetts' Clinical Visual Optics* (p. 451). Elsevier Health Sciences.

Bianciotto, C., Shields, C. L., Guzman, J. M., Romanelli-Gobbi, M., Mazzuca, D., Green, W. R., & Shields, J. A. (2011). Assessment of Anterior Segment Tumors with Ultrasound Biomicroscopy Versus Anterior Segment Optical Coherence Tomography in 200 cases. *Ophthalmology*, *118*(7), 1297-302.

Borja, D., Siedlecki, D., de Castro, A., Uhlhorn, S., Ortiz, S., Arrieta, E., Parel, J.-M., et al. (2010). Distortions of the Posterior Surface in Optical Coherence Tomography Images of the Isolated Crystalline Lens: Effect of the Lens Index Gradient. *Biomedical Optics Express*, *1*(5), 1331-1340. doi:10.1364/BOE.1.001331

Buehl, W., Stojanac, D., Sacu, S., Drexler, W., & Findl, O. (2006). Comparison of Three Methods of Measuring Corneal Thickness and Anterior Chamber Depth. *American Journal of Ophthalmology*, *141*(1), 7-12.

Chan, K. K. H. (2010). *Spectral Domain Optical Coherence Tomography System Design: Sensitivity Fall-off and Processing Speed Enhancement*. Master Degree Thesis in Biomedical Engineering. The University of British Columbia. Vancouver.

Chan, K. K. H., & Tang, S. (2010). High-speed Spectral Domain Optical Coherence Tomography using Non-Uniform Fast Fourier Transform. *Biomedical Optics Express*, *1*(5), 1309-1319. Optical Society of America.

Chinn, S. R., Swanson, E. A., & Fujimoto, J. G. (1997). Optical Coherence Tomography using a Frequency-Tunable Optical Source. *Optics Letters*, *22*(5), 340. OSA.

Choma, M. A., Hsu, K., & Izatt, J. A. (2005). Swept Source Optical Coherence Tomography using an All-fiber 1300-nm Ring Laser Source. *Journal of Biomedical Optics*, *10*(4), 44009.

Choma, M. A., Yang, C., & Izatt, J. A. (2003). Instantaneous Quadrature Low-Coherence Interferometry with 3 x 3 Fiber-Optic Couplers. *Optics Letters*, *28*(22), 2162-4.

Choma, M., Sarunic, M., Yang, C., & Izatt, J. (2003). Sensitivity Advantage of Swept Source and Fourier Domain Optical Coherence Tomography. *Optics Express*, *11*(18), 2183.

Coello, Y., Xu, B., Miller, T. L., Lozovoy, V. V., & Dantus, M. (2007). Group-velocity Dispersion Measurements of Water, Seawater, and Ocular Components using Multiphoton Intrapulse Interference Phase Scan. *Applied Optics*, *46*(35), 8394. OSA.

Dartt, D. A., Bex, P., D'Amore, P., Dana, R., Mcloon, L., & Jerry Niederkorn. (2011). *Ocular Periphery and Disorders*. (Darlene A. Dartt, Peter Bex, Patricia D'Amore, Reza Dana, Linda Mcloon, & Jerry Niederkorn, Eds.). Elsevier.

Davis, A. M., Choma, M. A., & Izatt, J. A. (2005). Heterodyne Swept-source Optical Coherence Tomography for Complete Conjugate Ambiguity Removal. *Journal of Biomedical Optics*, *10*(6), 064005.

de Boer, J. F., Cense, B., Park, B. H., Pierce, M. C., Tearney, G. J., & Bouma, B. E. (2003). Improved Signal-to-Noise Ratio in Spectral-Domain compared with Time-Domain Optical Coherence Tomography. *Optics Letters*, *28*(21), 2067. OSA.

Dorrer, C., Belabas, N., Likforman, J.-P., & Joffre, M. (2000). Spectral Resolution and Sampling Issues in Fourier-Transform Spectral Interferometry. *Journal of the Optical Society of America B*, *17*(10), 1795. OSA.

Drexler, W., K Hitzenberger, C., Baumgartner, A., Findl, O., Sattmann, H., & F Fercher, A. (1998). Investigation of Dispersion Effects in Ocular Media by Multiple Wavelength Partial Coherence Interferometry. *Experimental Eye Research*, *66*(1), 25-33.

Drexler, W., Baumgartner, A., Findl, O., Hitzenberger, C. K., & Fercher, A. F. (1997). Biometric Investigation of Changes in the Anterior Eye Segment During Accommodation. *Vision Research*, *37*(19), 2789-800.

Dubbelman, M., Van der Heijde, G. L., & Weeber, H. A. (2005). Change in Shape of the Aging Human Crystalline Lens with Accommodation. *Vision Research*, *45*(1), 117-32.

Dubbelman, M., Van der Heijde, G. L., Weeber, H. A., & Vrensen, G. F. J. M. (2003). Changes in the Internal Structure of the Human Crystalline Lens with Age and Accommodation. *Vision Research*, *43*(22), 2363-75.

Duke-Elder, S. and Y Bar, K. (1961). *Cornea. System of Ophthalmology. Vol 2. The Anatomy of the Visual System*. (H. Kimpton, Ed.) (pp. 92-94).

Duker, J., James, F., Witkin, A., & Wojtkowski, M. (2005). OCT3 and Beyond: New Developments Managing the Open Globe Calls for Creativity and Flexibility of Surgical Approach Tailored to the Specific Case.

de Sanctis, U., Loiacono, C., Richiardi, L., Turco, D., Mutani, B., & Grignolo, F. M. (2008). Sensitivity and Specificity of Posterior Corneal Elevation Measured by Pentacam in Discriminating Keratoconus/Subclinical Keratoconus. *Ophthalmology*, *115*(9), 1534-9.

de Sanctis, U., Missolungi, A., Mutani, B., & Grignolo, F. M. (2007). Graft Central Thickness Measurement by Rotating Scheimpflug Camera and Ultrasound Pachymetry after Penetrating Keratoplasty. *Ophthalmology*, *114*(8), 1461-8.

Fercher, A. (1995). Measurement of Intraocular Distances by Backscattering Spectral Interferometry. *Optics Communications*, *117*(1-2), 43-48. Elsevier.

Fercher, A. (2002). Dispersion Compensation for Optical Coherence Tomography Depth-Scan Signals by a Numerical Technique. *Optics Communications*, *204*(1-6), 67-74.

Fercher, A. F. (1996). Optical Coherence Tomography. *Journal of Biomedical Optics*, *1*(2), 157.

Fontana, S. T., & Brubaker, R. F. (1980). Volume and Depth of the Anterior Chamber in the Normal Aging Human Eye. *Archives of Ophthalmology*, *98*(10), 1803-8.

Fukuda, S., Kawana, K., Yasuno, Y., & Oshika, T. (2009). Anterior Ocular Biometry using 3-Dimensional Optical Coherence Tomography. *Ophthalmology*, *116*(5), 882-9.

Furukawa, H., Hiro-Oka, H., Satoh, N., Yoshimura, R., Choi, D., Nakanishi, M., Igarashi, A., et al. (2010). Full-range Imaging of Eye Accommodation by High-speed Long-depth Range Optical Frequency Domain Imaging. *Biomedical Optics Express*, *1*(5), 1491-1501. Optical Society of America.

Gaigalas, A. K., Wang, L., DeRose, P., & He, H.-J. (2009). Procedures for Wavelength Calibration and Spectral Response Correction of CCD Array Spectrometers (July 2009). *Journal of Research of the National Institute of Standards and Technology*, *114*(4), 215.

Geerling, G., Müller, M., Winter, C., Hoerauf, H., Oelckers, S., Laqua, H., & Birngruber, R. (2005). Intraoperative 2-Dimensional Optical Coherence Tomography as a New Tool for Anterior Segment Surgery. *Archives of Ophthalmology*, *123*(2), 253-7.

Genevois, O., Benzerroug, M., Gardea, E., Brasseur, G., & Muraine, M. (2007). Macular Edema after Corneal Graft: a Prospective Study by Optical Coherence Tomography. *Cornea*, *26*(6), 683-4.

Goldsmith, J. A., Li, Y., Chalita, M. R., Westphal, V., Patil, C. A., Rollins, A. M., Izatt, J. A., et al. (2005). Anterior Chamber Width Measurement by High-speed Optical Coherence Tomography. *Ophthalmology*, *112*(2), 238-44.

Gora, M., Karnowski, K., Szkulmowski, M., Kaluzny, B. J., Huber, R., Kowalczyk, A., & Wojtkowski, M. (2009). Ultra High-speed Swept Source OCT Imaging of the Anterior Segment of Human Eye at 200 kHz with Adjustable Imaging Range. *Optics Express*, *17*(17), 14880. OSA.

Grulkowski, I., Gora, M., Szkulmowski, M., Gorczynska, I., Szlag, D., Marcos, S., Kowalczyk, A., et al. (2009). Anterior Segment Imaging with Spectral OCT System using a High-speed CMOS Camera. *Optics Express*, *17*(6), 4842. OSA.

Haberland, U. (1997). Optical Coherence Tomography of Scattering Media using Frequency-modulated Continuous-wave Techniques with Tunable Near-infrared Laser. *Proceedings of SPIE* (Vol. 2981, pp. 20-28). SPIE.

Hale, G. M., & Querry, M. R. (1973). Optical Constants of Water in the 200-nm to 200-µm Wavelength Region. *Applied Optics*, *12*(3), 555. OSA.

Hamblin, M., & Demidova, T. (2006). Mechanisms of Low Level Light Therapy – an Introduction. *Proceedings of SPIE*, *6140*(61001), 1-12.

Hashemi, H., & Mehravaran, S. (2007). Corneal Changes after Laser Refractive Surgery for Myopia: Comparison of Orbscan II and Pentacam Findings. *Journal of Cataract and Refractive Surgery*, *33*(5), 841-7.

Helmholtz, H. (1962). *Helmholtz's Treatise on Physiological Optics.* New York: Dover Publications.

Heron, G., Charman, W. N., & Schor, C. (2001). Dynamics of the Accommodation Response to Abrupt Changes in Target Vergence as a Function of Age. *Vision research*, *41*(4), 507-19.

Hockwin, O., Weigelin, E., Laser, H., & Dragomirescu, V. (1983). Biometry of the Anterior Eye Segment by Scheimpflug Photography. *Ophthalmic Research*, *15*(2), 102-8.

Hofer, B., Považay, B., Hermann, B., Unterhuber, A., Matz, G., & Drexler, W. (2008). Dispersion Encoded Full Range Frequency Domain Optical Coherence Tomography. *Optics Express*, *17*(1), 7. OSA.

Høvding, G. (1983). A Clinical Study of the Association Between Thickness and Curvature of the Central Cornea. *Acta Ophthalmologica*, *61*(3), 461-6.

Hu, Z., Pan, Y., & Rollins, A. M. (2007). Analytical Model of Spectrometer-based Two-beam Spectral Interferometry. *Applied Optics*, *46*(35), 8499. OSA.

Huang, D., Swanson, E., Lin, C., Schuman, J., Stinson, W., Chang, W., Hee, M., et al. (1991). Optical Coherence Tomography. *Science*, *254*(5035), 1178-1181.

Huber, R., Wojtkowski, M., Taira, K., Fujimoto, J. G., & Hsu, K. (2005). Amplified, Frequency Swept Lasers for Frequency Domain Reflectometry and OCT Imaging: Design and Scaling principles. *Optics Express*, *13*(9), 3513. OSA.

Häusler, G., & W Lindner, M. (1998). ”Coherence Radar” and ”Spectral Radar”— New Tools For Dermatological Diagnosis. *Journal of Biomedical Optics*, *3*(1).

Izatt, J A, Hee, M. R., Swanson, E. A., Lin, C. P., Huang, D., Schuman, J. S., Puliafito, C. A., et al. (1994). Micrometer-scale Resolution Imaging of the Anterior Eye In Vivo with Optical Coherence Tomography. *Archives of Ophthalmology*, *112*(12), 1584-9.

Jungwirth, J., Baumann, B., Pircher, M., Götzinger, E., & K Hitzenberger, C. (2009). Extended In Vivo Anterior Eye-segment Imaging with Full-range Complex Spectral Domain Optical Coherence Tomography. *Journal of Biomedical Optics*, *14*(5). SPIE.

Kasthurirangan, S., Vilupuru, A. S., & Glasser, A. (2003). Amplitude Dependent Accommodative Dynamics in Humans. *Vision Research*, *43*(27), 2945-56.

Koretz, J. E., Strenk, S. A., Strenk, L. M., & Semmlow, J. L. (2004). Scheimpflug and High-resolution Magnetic Resonance Imaging of the Anterior Segment: a Comparative Study. *Journal of the Optical Society of America. A, Optics, Image Science, and Vision*, *21*(3), 346-54.

Koretz, J. F., Handelman, G. H., & Brown, N. P. (1984). Analysis of Human Crystalline Lens Curvature as a Function of Accommodative State and Age. *Vision Research*, *24*(10), 1141-51.

Kulkarni, M. D., Thomas, C. W., & Izatt, J.A. (1997). Image Enhancement in Optical Coherence Tomography using Deconvolution. *Electronics Letters*, *33*(16), 1365.

Lee, E. C., de Boer, J. F., Mujat, M., Lim, H., & Yun, S. H. (2006). In Vivo Optical Frequency Domain Imaging of Human Retina and Choroid. *Optics Express*, *14*(10), 4403. OSA.

Lee, S.-W., Kim, C.-S., & Kim, B.-M. (2007). External Line-Cavity Wavelength-Swept Source at 850 nm for Optical Coherence Tomography. *IEEE Photonics Technology Letters*, *19*(3), 176-178.

Lehman, B. M., Berntsen, D. A., Bailey, M. D., & Zadnik, K. (2009). Validation of Optical Coherence Tomography-based Crystalline Lens Thickness Measurements in Children. *Optometry and Vision Science: Official Publication of the American Academy of Optometry*, *86*(3), 181-7.

Leitgeb, R. A., Hitzenberger, C. K., Fercher, A. F., & Bajraszewski, T. (2003). Phase-Shifting Algorithm to Achieve High-speed Long-depth-range Probing by Frequency-domain Optical Coherence Tomography. *Optics Letters*, *28*(22), 2201. OSA.

Leitgeb, R., Hitzenberger, C., & Fercher, A. (2003). Performance of Fourier Domain vs. Time Domain Optical Coherence Tomography. *Optics Express*, *11*(8), 889. OSA.

Leung, C. K.-S., & Weinreb, R. N. (2011). Anterior Chamber Angle Imaging with Optical Coherence Tomography. *Eye (London, England)*, *25*(3), 261-7. Royal College of Ophthalmologists.

Li, Y., Netto, M. V., Shekhar, R., Krueger, R. R., & Huang, D. (2007). A Longitudinal Study of LASIK Flap and Stromal Thickness with High-speed Optical Coherence Tomography. *Ophthalmology*, *114*(6), 1124-32.

Lim, H., de Boer, J. F., Park, B. H., Lee, E. C., Yelin, R., & Yun, S. H. (2006). Optical Frequency Domain Imaging with a Rapidly Swept Laser in the 815-870 nm Range. *Optics Express*, *14*(13), 5937. OSA.

Lim, H., Mujat, M., Kerbage, C., Lee, E C, Chen, Y., Chen, Teresa C, & de Boer, J F. (2006). High-Speed Imaging of Human Retina In Vivo with Swept-Source Optical Coherence Tomography. *Optics Express*, *14*(26), 12902-8.

Loewen, E. G., & Evgeny, P. (1997). *Diffraction Gratings and Applications - Erwin G. Loewen, Evgeny Popov - Google Books*. New York.

Lowe, R. F., & Clark, B. A. (1973). Posterior Corneal Curvature. Correlations in Normal Eyes and in Eyes Involved with Primary Angle-Closure Glaucoma. *The British Journal of Ophthalmology*, *57*(7), 464-70.

Maldonado, M. J., Ruiz-Oblitas, L., Munuera, J. M., Aliseda, D., García-Layana, A., & Moreno-Montañés, J. (2000). Optical Coherence Tomography Evaluation of the Corneal Cap and Stromal Bed Features after Laser In Situ Keratomileusis for High Myopia and Astigmatism. *Ophthalmology*, *107*(1), 81-87.

Manns, F. (2004). Customized Visual Correction of Presbyopia. In S. Inc (Ed.), *Wavefront Customized Visual Corrections: the Quest for Super Vision II*. NJ.

Martola, E.-L., & Baum, J. L. (1968). Central and Peripheral Corneal Thickness: A Clinical Study. *Arch Ophthalmol*, *79*(1), 28-30.

Muscat, S., McKay, N., Parks, S., Kemp, E., & Keating, D. (2002). Repeatability and Reproducibility of Corneal Thickness Measurements by Optical Coherence Tomography. *Investigative Ophthalmology & Visual Science*, *43*(6), 1791-5.

Müller-Breitenkamp, U., & Hockwin, O. (1992). Scheimpflug Photography in Clinical Ophthalmology. A Review. *Ophthalmic Research*, *24 Suppl 1*, 47-54.

Nassif, N. A., Cense, B., Park, B. H., Pierce, M. C., Yun, S. H., Bouma, B. E., Tearney, G. J., et al. (2004). In Vivo High-resolution Video-rate Spectral-domain Optical Coherence Tomography of the Human Retina and Optic Nerve. *Optics Express*, *12*(3), 367. OSA.

Nolan, W. (2008). Anterior Segment Imaging: Ultrasound Biomicroscopy and Anterior Segment Optical Coherence Tomography. *Current Opinion in Ophthalmology*, *19*(2), 115-21.

Nolan, W. P., See, J. L., Chew, P. T. K., Friedman, D. S., Smith, S. D., Radhakrishnan, S., Zheng, C., et al. (2007). Detection of Primary Angle Closure Using Anterior Segment Optical Coherence Tomography in Asian Eyes. *Ophthalmology*, *114*(1), 33-9.

Ortiz, S., Siedlecki, D., Grulkowski, I., Remon, L., Pascual, D., Wojtkowski, M., & Marcos, S. (2010). Optical Distortion Correction in Optical Coherence Tomography for Quantitative Ocular Anterior Segment by Three-Dimensional Imaging. *Optics Express*, *18*(3), 2782. OSA.

Ortiz, S., Siedlecki, D., Remon, L., & Marcos, S. (2009). Optical Coherence Tomography for Quantitative Surface Topography. *Applied Optics*, *48*(35), 6708. OSA.

Ozdal, M. P. C., Mansour, M., & Deschênes, J. (2003). Ultrasound Biomicroscopic Evaluation of the Traumatized Eyes. *Eye (London, England)*, *17*(4), 467-72.

Palanker, D. V., Blumenkranz, M. S., Andersen, D., Wiltberger, M., Marcellino, G., Gooding, P., Angeley, D., et al. (2010). Femtosecond Laser-assisted Cataract Surgery with Integrated Optical Coherence Tomography. *Science Translational Medicine*, *2*(58),

Pan, Y., Birngruber, R., Rosperich, J., & Engelhardt, R. (1995). Low-coherence Optical Tomography in Turbid Tissue: Theoretical Analysis. *Applied Optics*, *34*(28), 6564. OSA.

Parel, J. M., Gelender, H., Trefers, W. F., & Norton, E. W. (1986). Phaco-Ersatz: Cataract Surgery Designed to Preserve Accommodation. *Graefe's archive for Clinical and Experimental Ophthalmology = Albrecht von Graefes Archiv für Klinische und Experimentelle Ophthalmologie*, *224*(2), 165-73.

Pavlin, C. J., & Foster, F. S. (1995). *Ultrasound Biomicroscopy of the Eye*. Springer.

Pavlin, C. J., Harasiewicz, K., Sherar, M. D., & Foster, F. S. (1991). Clinical Use of Ultrasound Biomicroscopy. *Ophthalmology*, *98*(3), 287-95.

Pekmezci, M., Porco, T. C., & Lin, S. C. (2009). Anterior Segment Optical Coherence Tomography as a Screening Tool for the Assessment of the Anterior Segment Angle. *Ophthalmic Surgery, Lasers & Imaging: the Official Journal of the International Society for Imaging in the Eye*, *40*(4), 389-98.

Podoleanu, A. G. (2000). Unbalanced Versus balanced Operation in an Optical Coherence Tomography System. *Applied Optics*, *39*(1), 173. OSA.

Podoleanu, A., Charalambous, I., Plesea, L., Dogariu, A., & Rosen, R. (2004). Correction of Distortions in Optical Coherence Tomography Imaging of the Eye. *Physics in Medicine and Biology*, *49*(7), 1277-1294.

Potsaid, B., Baumann, B., Huang, D., Barry, S., Cable, A. E., Schuman, J. S., Duker, J. S., et al. (2010). Ultrahigh Speed 1050nm Swept Source / Fourier Domain OCT Retinal and Anterior Segment Imaging at 100,000 to 400,000 Axial Scans per Second. *Optics Express*, *18*(19), 20029. OSA.

Prasher, P., Muftuoglu, O., Bowman, R. W., Cavanagh, H. D., McCulley, J. P., & Mootha, V. V. (2010). Corneal Power Measurement with a Rotating Scheimpflug Imaging System after Descemet-stripping Automated endothelial Keratoplasty. *Journal of Cataract and Refractive Surgery*, *36*(8), 1358-64.

Radhakrishnan, S., Huang, D., & Smith, S. D. (2005). Optical Coherence Tomography Imaging of the Anterior Chamber Angle. *Ophthalmology Clinics of North America*, *18*(3), 375-81, vi.

Rao, S. N., Raviv, T., Majmudar, P. A., & Epstein, R. J. (2002). Role of Orbscan II in Screening Keratoconus Suspects before Refractive Corneal Surgery. *Ophthalmology*, *109*(9), 1642-6.

Rollins, A. M., & Izatt, J. A. (1999). Optimal Interferometer Designs for Optical Coherence Tomography. *Optics Letters*, *24*(21), 1484. OSA.

Rosales, P., Dubbelman, M., Marcos, S., & van der Heijde, R. (2006). Crystalline Lens Radii of Curvature from Purkinje and Scheimpflug imaging. *Journal of Vision*, *6*(10), 1057-67. Association for Research in Vision and Ophthalmology.

Said, F. S., & Weale, R. A. (1959). The Variation with Age of the Spectral Transmissivity of the Living Human Crystalline Lens. *Gerontologia*, *3*, 213-31.

Sarunic, M. V., Applegate, B. E., & Izatt, J. A. (2006). Real-time Quadrature Projection Complex Conjugate Resolved Fourier Domain Optical Coherence Tomography. *Optics Letters*, *31*(16), 2426. OSA.

Sarunic, M. V., Asrani, S., & Izatt, J. A. (2008). Imaging the Ocular Anterior Segment with Real-time, Full-range Fourier-domain Optical Coherence Tomography. *Archives of Ophthalmology*, *126*(4), 537-42.

Sarunic, M. V., Choma, M. A., Yang, C., & Izatt, J. A. (2005). Instantaneous Complex Conjugate Resolved Spectral Domain and Swept-source OCT using 3x3 Fiber Couplers. *Optics Express*, *13*(3), 957. OSA.

Schmitt, J. M. (1999). Optical Coherence Tomography (OCT): a Review. *IEEE Journal of Selected Topics in Quantum Electronics*, *5*(4), 1205-1215.

Schnopper, H. W., Van Speybroeck, L. P., Delvaille, J. P., Epstein, A., Källne, E., Bachrach, R. Z., Dijkstra, J., et al. (1977). Diffraction Grating Transmission Efficiencies for XUV and Soft X Rays. *Applied Optics*, *16*(4), 1088-1091. OSA.

Silverman, R. H. (2009). High-resolution Ultrasound Imaging of the Eye - a Review. *Clinical & Experimental Ophthalmology*, *37*(1), 54-67.

Sparrow, J. M., Bron, A. J., Brown, N. A., Ayliffe, W., & Hill, A. R. (1986). The Oxford Clinical Cataract Classification and Grading System. *International Ophthalmology*, *9*(4), 207-25.

Storey, J. K., & Rabie, E. P. (1983). Ultrasound: a Research Tool in the Study of Accommodation. *Ophthalmic & Physiological Optics: the Journal of the British College of Ophthalmic Opticians (Optometrists)*, *3*(3), 315-20.

Storey, J., Tromans, C., & Rabie, E. (1990). Continuous Biometry of the Crystalline Lens During Accommodation. *Ultrasonography Ophthalmology*, *12*, 117-23.

Tang, M., Li, Y., & Huang, D. (2010). An Intraocular Lens Power Calculation Formula Based on Optical Coherence Tomography: a Pilot Study. *Journal of Refractive Surgery*, *26*(6), 430-7.

Targowski, P., Gorczyńska, I., Szkulmowski, M., Wojtkowski, Maciej, & Kowalczyk, Andrzej. (2005). Improved Complex Spectral Domain OCT for In Vivo Eye Imaging. *Optics Communications*, *249*(1-3), 357-362.

Uhlhorn, S. R., Manns, F., Tahi, H., Pascal, R. O., & Parel, J.-M. (1998). Corneal Group Refractive Index Measurement using Low-coherence Interferometry. *SPIE Proceedings*, *3246* (Ophthalmic Technologies VIII,), 14-21.

Uhlhorn, S. R., Borja, D., Manns, F., & Parel, J.-M. (2008). Refractive Index Measurement of the Isolated Crystalline Lens using Optical Coherence Tomography. *Vision Research*, *48*(27), 2732-8.

Vakhtin, A. B., Peterson, K. A., & Kane, D. J. (2006). Resolving the Complex Conjugate Ambiguity in Fourier-domain OCT by Harmonic Lock-in Detection of the Spectral Interferogram. *Optics Letters*, *31*(9), 1271. OSA.

Vakoc, B. J., Yun, S. H., Tearney, G. J., & Bouma, B. E. (2006). Elimination of Depth Degeneracy in Optical Frequency-domain Imaging through Polarization-based Optical Demodulation. *Optics Letters*, *31*(3), 362-4.

Vilupuru, A. S., & Glasser, A. (2003). Dynamic Accommodative Changes in Rhesus Monkey Eyes Assessed with A-scan Ultrasound Biometry. *Optometry and Vision Science: Official Publication of the American Academy of Optometry*, *80*(5), 383-94.

Wang, H., Pan, Y., & Rollins, A. M. (2008). Extending the Effective Imaging Range of Fourier-domain Optical Coherence Tomography using a Fiber Optic Switch. *Optics Letters*, *33*(22), 2632. OSA.

Westphal, V., Rollins, A., Radhakrishnan, S., & Izatt, J. (2002). Correction of Geometric and Refractive Image Distortions in Optical Coherence Tomography applying Fermat's Principle. *Optics Express*, *10*(9), 397-404. OSA.

Wojtkowski, M., Kowalczyk, A., Leitgeb, R., & Fercher, A. F. (2002). Full Range Complex Spectral Optical Coherence Tomography Technique in Eye Imaging. *Optics Letters*, *27*(16), 1415. OSA.

Wojtkowski, Maciej, Leitgeb, Rainer, Kowalczyk, Andrzej, Bajraszewski, T., & Fercher, Adolf F. (2002). In Vivo Human Retinal Imaging by Fourier Domain Optical Coherence Tomography. *Journal of Biomedical Optics*, *7*(3), 457-63.

Wojtkowski, Maciej, Srinivasan, V. J., Ko, T. H., Fujimoto, J. G., Kowalczyk, Andrzej, & Duker, J. S. (2004). Ultrahigh-resolution, High-speed, Fourier Domain Optical Coherence Tomography and Methods for Dispersion Compensation. *Optics Express*, *12*(11), 2404. OSA.

Wykoff, C. C., Berrocal, A. M., Schefler, A. C., Uhlhorn, S. R., Ruggeri, M., & Hess, D. (2010). Intraoperative OCT of a Full-thickness Macular Hole Before and After Internal Limiting Membrane Peeling. *Ophthalmic Surgery, Lasers & Imaging: the Official Journal of the International Society for Imaging in the Eye*, *41*(1), 7-11.

Xie, J., Huang, S., Duan, Z., Shi, Y., & Wen, S. (2005). Correction of the Image Distortion for Laser Galvanometric Scanning System. *Optics & Laser Technology*, *37*(4), 305-311.

Yasuno, Y., Hong, Y., Makita, S., Yamanari, M., Akiba, M., Miura, M., & Yatagai, T. (2007). In Vivo High-contrast Imaging of Deep Posterior Eye by 1-um Swept Source Optical Coherence Tomography and Scattering Optical Coherence Angiography. *Optics Express*, *15*(10), 6121. OSA.

Yasuno, Y., Madjarova, V. D., Makita, S., Akiba, M., Morosawa, A., Chong, C., Sakai, T., et al. (2005). Three-dimensional and High-speed Swept-source Optical Coherence Tomography for In Vivo Investigation of Human Anterior Eye Segments. *Optics Express*, *13*(26), 10652. OSA.

Yun, S. H., Tearney, G. J., de Boer, J. F., & Bouma, B. E. (2004). Removing the Depth-degeneracy in Optical Frequency Domain Imaging with Frequency Shifting. *Optics Express*, *12*(20), 4822. OSA.

Yun, S., Tearney, G., de Boer, J., Iftimia, N., & Bouma, B. (2003). High-speed Optical Frequency-domain Imaging. *Optics Express*, *11*(22), 2953. OSA.

Yun, S., Tearney, G., Bouma, B., Park, B., & de Boer, J. (2003). High-speed Spectral-domain Optical Coherence Tomography at 1.3 μm Wavelength. *Optics Express*, *11*(26), 3598. OSA.

Zhang, J., Jung, W., Nelson, J. S., & Chen, Z. (2004). Full Range Polarization-sensitive Fourier Domain Optical Coherence Tomography. *Optics Express*, *12*(24), 6033. OSA.

Zhang, J., Nelson, J. S., & Chen, Z. (2005). Removal of a Mirror Image and Enhancement of the Signal-to-noise Ratio in Fourier-domain Optical Coherence Tomography using an Electro-optic Phase Modulator. *Optics Letters*, *30*(2), 147. OSA.

Zawadzki, R.J., Leisser, C., Leitgeb R., Pircher M. & Fercher A. F. (2003). Three-dimensional Ophthalmic Optical Coherence Tomography with a Refraction Correction Algorithm. Proc. SPIE. In W. Drexler (Ed.), *Optical Coherence Tomography and Coherence Techniques* (Vol. 5140, p. 5140_20). Optical Society of America.